MSc Thesis

Magnetic Drug Targeting in Human Airway Geometry

Author:
Jimmy Leroy TJIN

Supervisor:
Dr. S. KENJERES, Dipl.-Ing.

Reviewers:
Prof. Dr. Ir.C.R. KLEIJN
Dr. Ir. J.R. VAN OMMEN
Ir. B.W. RIGHOLT

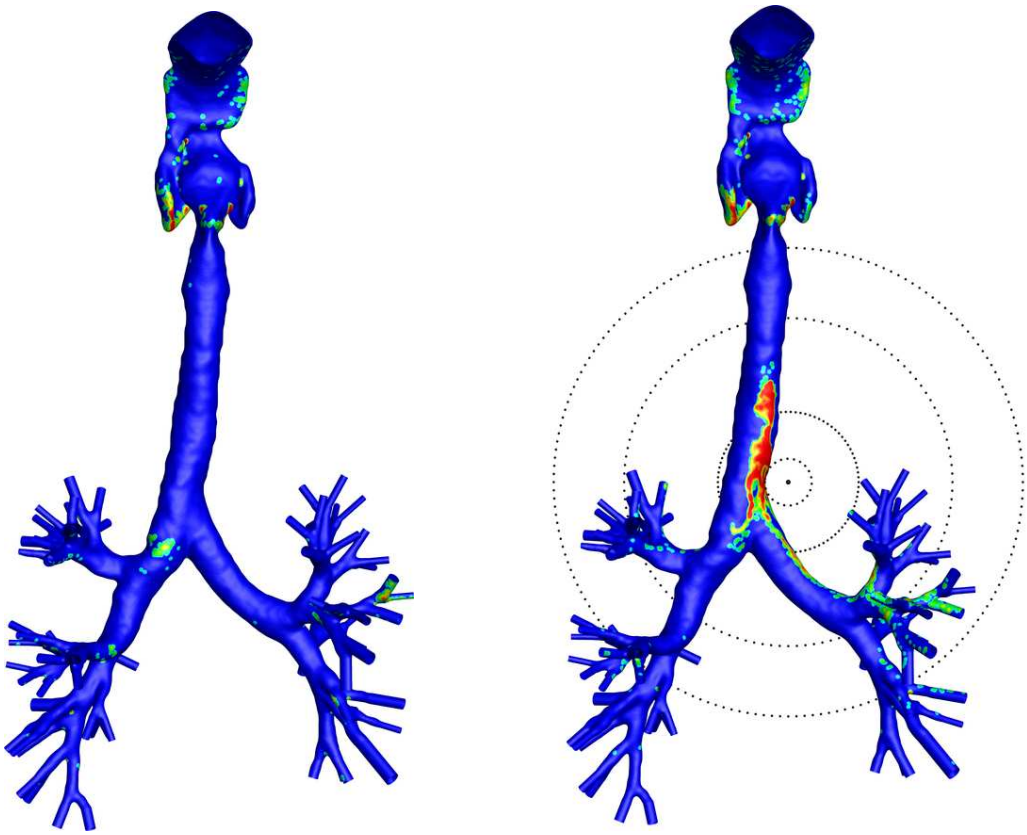

Delft University of Technology, Department of Chemical Engineering
Transport Phenomena Group

Examination Date: April 25, 2014

TU Delft Delft University of Technology

Abstract

Patient specific drug delivery may improve the efficiency of the medicine and reduce the side-effects. In addition to different medicines and dosages, the target site of the medicine can differ from patient to patient. By using drug particles with a magnetic core, and under the influence of a magnetic field, the particles may be steered towards the point of interest.

In the present study, computational fluid dynamics is used to study air flow and particle deposition in human airway geometry. In the first case study, passive particle deposition was carried out in a 90° bend to represent a simplified throat. Random-uniform and deterministic-uniform particle inlet distributions were used. Both the total and cumulative deposition efficiencies showed good agreement with literature.

The second case study is again a 90° bend simulation but this time represents a simplified artery. Although the curvature ratio was the same the dimensions of the geometry were much smaller. In addition to passive particle deposition, magnetically enhanced particle deposition was studied and good agreement was obtained with both reference cases.

The third case study features a simplification of the conducting airways: a triple bifurcation geometry. The geometrical parameters are obtained from literature and correspond to an 'average' male adult lung. The region of the bifurcation is geometrically different from the reference case, this affected both the flow structures and particle deposition. While the axial velocity profiles and stream traces did show agreement, and the same effect of different inlet distributions were observed, a quantitative agreement was not obtained. Most notably the particle deposition in the second generation was lower than in the reference case. An extra comparison was performed in a double bifurcation geometry where the reference paper used the same bifurcation geometry as in the present study; there a good agreement is obtained. It was shown that magnetic core-shell particles can be steered towards one side in the triple bifurcation geometry by using a magnetic field generated by a straight current carrying wire. Not only is the deposition on the side of the magnetic source increased but the number of particles which leave the domain on that side relative to the other side was also increased.

In the final case study a patient specific geometry obtained from Banko et al. (2014) was used to perform fluid and particle simulations. Several turbulence models were applied and compared. These turbulence models are: large eddy simulations two different subgrid scale models, Shear Stress Transport Transition (SST-Transition), k-ε Realisable and k-ω Low Reynolds Number. Based on velocity profiles and vorticity contours the large eddy simulations showed the best agreement of all models. Between the RANS models the SST-Transition was the most accurate. Since no velocity fluctuations were available for the experimental data, the turbulent kinetic energy (TKE) profiles were compared between the models only. The levels of the TKE in the LES were higher than those in the RANS models. This may be due to the first order discretisation used in the RANS models and a difference in the models; other authors have observed higher TKE levels for LES in for example stenosed tubes (Zhang and Kleinstreuer, 2011). The flow field obtained from the SST-Transition model was used for particle deposition studies and the steerability of particles in a patient specific human airway geometry was displayed by comparing magnetic particle deposition to passive particle deposition. Particle deposition studies were performed both with and without isotropic turbulent dispersion. Additionally, the need for better turbulent dispersion models is displayed.

Samenvatting

Om bij-effecten te verminderen en de efficientie van behandelingen te verhogen kunnen de medicijnen gestuurd toegediend worden. Niet alleen het medicijn en de dosis verschilt van persoon tot persoon, maar de locatie van de ziekte kan ook nog patient afhankelijk zijn. Door medicijnen te gebruiken waarvan de kern bestaat uit magnetisch material kan het medicijn, onder invloed van een aangelegd magnetisch veld, gestuurd worden daar waar het nodig is.

In de huidige studie is numerieke vloeistofmechanica gebruikt om de luchtstroming en het neerslaan van de medicijn deeltjes te simuleren in menselijke luchtwegen. Als eerst is er een passieve deeltjes studie in een versimpelde keel uitgevoerd. In de versimpelde keel is er geen vernauwing meegenomen en is de keel opgevat als een ronde buis met een hoek van 90 graden. Zowel willekeurig-uniforme als deterministisch-uniforme deeltjes verdelingen zijn gebruikt om de deeltjes te injecteren in de geometrie. De totale en cumulatieve deeltjes neerslag komen goed overeen met de literatuur.

Na het uitvoeren van de passieve deeltjesneerslag studie is in de tweede studie, in een geometrie die representatief is van een ader, een deeltjesneerslag studie uitgevoerd waarbij er een magnetisch veld aanwezig is. Het verschil in de geometrie ten opzichte van de eerste studie is de veel kleinere diameter en het gebruik van bloed als vloeistof in plaats van lucht.

In de derde studie was een versimpeling van de vertakkende luchtwegen gebruikt om daarin de deeltjesneerslag te bestuderen, het betreft hier drie opeenvolgende vertakkingen. De constructie parameters komen overeen met een 'gemiddelde' volwassen man. De geometrie van het gebied in de vertakking is anders dan de referentie studie, dit heeft zowel effect op de stroming als de paden die de deeltjes afleggen. Alhoewel de snelheidsprofielen kwalitatief overeenkwamen met de referentie studie was er geen kwantitatieve overeenkomst gevonden. Het effect van de verschillende deeltjes distributie in de ingang van de geometrie kwam, voornamelijk voor de eerste vertakking, kwalitatief overeen met de referentie studie. Er was een extra studie uitgevoerd in een soortgelijke geometrie, maar dit keer met een dubbele vertakking, waarin de geometrie van de vertakking wel overeenkwam met de referentie studie. In deze extra studie was er een goede overeenkomst gevonden. Tevens kunnen deeltjes die een magnetische kern bevatten gestuurd worden in een vertakkende geometrie door middel van een magnetisch veld. Het magnetisch veld was gegenereerd door een elektrische stroom die door de draad stroomt. Zowel de totale neerslag als het aantal deeltjes die aan de zijde van het draad het domein verlaten ten opzichte van de andere zijde zijn toegenomen.

In de laatste studie zijn in een gescande luchtwegen geometrie stroming en deeltjes simulaties uitgevoerd. Verschillende turbulentie modelled zijn gebruikt en vergeleken met elkaar en experimentele data verkregen van MRI metingen (Banko et al., 2014). Deze turbulentie modellen zijn: large eddy simulation, Shear Stress Transport Transition (SST-Transition), k-ε Realisable and k-ω Low Reynolds Number. Daarbij vallen de laatste drie modellen onder de zogeheten Reynolds gemiddelde Navier-Stokes modellen (afgekort als RANS naar het Engelse Reynolds Averaged Navier-Stokes). Op basis van snelheidsprofielen en vorticiteit contouren vertoonde de LES de beste overeenkomst tussen alle modellen. Onder de RANS modellen presteerde het SST-Transition model het beste. Vanwege het gebrek aan experimentele snelheidsfluctuaties konden de turbulente kinetische energie (TKE) profielen alleen onder de turbulentie modellen onderling worden vergeleken.

De niveaus van TKE waren in de LES hoger dan die in de RANS modellen wat kan worden toegekend door de eerste orde discretisatie die is toegepast bij de RANS modellen en een verschil in de modellen zelf; in de literatuur voor een vernauwde buis voorspelt de LES een hogere TKE dan bijvoorbeeld het SST-Transition model (Zhang and Kleinstreuer, 2011). Het snelheidsveld van het SST-Transition model was gebruikt om de deeltjes studie uit te voeren, daarbij werd er ook gekeken naar het effect van de deeltjes dispersie die door de turbulentie veroorzaakt werd. Uit de vergelijking van de deeltjesneerslag met en zonder magnetisch veld was gebleken dat de deeltjes gestuurd konden worden door de magnetische kracht. Tevens wordt er duidelijk gemaakt dat er of een alternatief op het huidige turbulente dispersie model gebruikt moet worden of een deeltjes simulatie moet worden uitgevoerd door middel van LES in de tijd uit voeren.

List of Symbols

Roman Symbols

Symbol	Description	Units
a^*	Model coefficient, k-ω LRN	-
A_f	Cell face area	m^2
B	Magnetic field strength	T
B^n	Bounding parameter used to limit a certain transported quantityfrom the contribution at time-step n	-
C_L	Diffusion correction constant in turbulent dispersion model	-
C_s	Smagorinsky constant	-
C_w	WALE constant	-
C_c	Cunningham slip factor, used to correct the drag force for submicron particles	-
D	Diameter	m
D_ω	k-ε/k-ω blending term in the omega transport equation of the SST model	$kg\,m^{-3}s^{-2}$
d_m	Diameter of magnetic core	m
d_p	Particle diameter	m
$E_{\gamma,1-2}$	Sink terms of the intermittency equation	$kg\,m^{-3}s^{-1}$
f	Drag factor	-
F_1	Blending function used in the SST model to turn on the epsilon formulation of omega near the wall	-
$\vec{F}_b$	buoyancy force	N
$\vec{F}_{Basset}$	Basset force	N
$\vec{F}_{Faxen}$	Faxen force	N
$\vec{F}_D$	Drag force	N

Symbol	Description	Units
$\vec{F}_g$	Gravitational force	N
$\vec{F}_M$	Magnetic force	N
$\vec{F}_{p.grad}$	Pressure gradient force	N
$F(\phi)$	Part of transport equation of ϕ which contains every term except for the time derivative	Depends on ϕ
$\vec{F}_{Saffman}$	Saffman lift force	N
$G_{f,a}$	Area growth factor	-
G_{prop}	Production of transported property (in k-omega LRN model)	Depends on transported property
$\vec{H}$	Auxiliary magnetic field	$A\,m^{-1}$
I	Current	A
IP	Impaction parameter	$\mu m^2 L min^{-1}$
k	Turbulent kinetic energy	$m^2 s^{-2}$
L	Length	m
L_s	Subgrid mixing length	m
m_p	Particle mass	kg
M_{sat}	Saturation magnetisation	$A\,m^{-1}$
$\vec{M}$	Magnetisation concentration	$A\,m^{-1}$
R_c, i	Radius of curvature of the carinal ridge in bifurcation I	m
R_k	Model constant of k-ω LRN	-
R_b	Bend radius	m
S_{ij}	Mean rate of strain tensor	s^{-1}
SF_L	Steering factor left side	-
SF_pen	Penetration steering factor	-
$\overline{S}$	Strain rate magnitude	s^{-1}
t	Time	s
T_L	Integral time scale of the fluid	s
$\vec{u}$	Fluctuating velocity component	$m\,s^{-1}$
$\vec{U}$	Average velocity	$m\,s^{-1}$
$\vec{u}_f$	Fluid velocity vector	$m\,s^{-1}$

Symbol	Description	Units
$\vec{u}_p$	Particle velocity vector	$m\,s^{-1}$
$\breve{u}$	Instaneneous velocity	$m\,s^{-1}$
$\hat{u}$	Instaneneous velocity	$m\,s^{-1}$
u'	Unfiltered velocity component	$m\,s^{-1}$
$\tilde{u}$	Filtered velocity component	$m\,s^{-1}$
$\vec{v}$	Velocity	$m\,s^{-1}$
V_cv	Volume of computational cell	m^3
V_p	Particle volume	m^3
V_{cell}	Volume of computational cell	m^3
$\vec{x}$	Coordinate vector	m
x_d	Fractional drug loading	-
Y_{prop}	Sink term of transported property	Depends on transported property
Z	Sample from gaussian distribution	-

Greek Symbols

Symbol	Description	Units
α_{1-3}	Model constants of the Morsi & Alexander drag law	-
β_i	Model constant of k-ω LRN	-
γ	Intermittency	-
ε	Dissipation rate	$m^2 s^{-3}$
ζ	Surface concentration of particles	-
η_k	Kolmogorov lengthscale	m
κ	von Karman constant	-
μ_f	Dynamic viscosity	$kg\,m^{-1}s^{-1}$
μ_t	Turbulent viscosity	$kg\,m^{-1}s^{-1}$
μ_0	Permeability of free space	$T\,m\,A^{-1}$
ν_f	Kinematic viscosity	$m^2 s^{-1}$
ν_{sgs}	Sub grid viscosity	$m^2 s^{-1}$
ν_t	Turbulent viscosity	$m^2 s^{-1}$
ρ	Density	$kg\,m^{-3}$
ρ_f	Fluid density	$kg\,m^{-3}$
ρ_p	Particle density	$kg\,m^{-3}$
τ_e	Eddy timescale	s
τ_{ij}	Reynolds stress tensor	$kg\,m^{-1}s^{-2}$
τ_p	Particle relaxation time	s
τ_{wall}	Wall shear stress	$kg\,m^{-1}s^{-2}$
Φ	Variable (used in chapter num)	Depends on ϕ
Φ_{cv}	Value of the variable at the cell centre	Depends on ϕ
Φ_f	Value of the variable at a cell face	Depends on ϕ
χ_p	Particle magnetic susceptibility	-
ω	Specific dissipation rate	s^{-1}
Ω_{ij}	Rate of rotation tensor	s^{-1}

Dimensionless Quantities

Symbol	Description	Definition
Co	Courant number	$Co = \frac{u\Delta t}{\Delta x}$
d^*_{mp}	Ratio of magnetic core diameter to total particle diameter	$d^*_{mp} = \frac{d_m}{d_p}$
De	Dean number	$De = Re\sqrt{R_0}^{-1}$
Fr	Froude number	$Fr = \frac{U_p^2}{Lg}$
Fr_{Mag}	Magnetic Froude number	$Fr_{Mag} = \frac{U_p^2 m_p}{F_m D_{char}}$
l_{ratio}	Ratio of grid length scale to Kolmogorov length scale	$l_{ratio} = \frac{V_{cell}^{1/3}}{\left(\frac{\nu_f^3}{\varepsilon}\right)^{1/4}}$
Mnp	Magnetic particle number	$Mnp = \frac{d_{mp}^3 d_p^2 \mu_0 M \cdot \nabla H}{18\mu_f U_{char}}$
Pe	Peclet number (can also be seen as cell Reynolds number)	$Pe = \frac{u\Delta x}{\nu}$
R_0	Curvature ratio	$R_0 = \frac{R_b}{R_{tube}}$
Re	Reynolds number	$Re = \frac{\rho U D}{\mu_f}$
Re_p	Particle Reynolds number	$Re_p = \frac{\rho_f d_p}{\mu_f}\lvert\vec{u}_f - \vec{v}_p\rvert$
Re_υ	Strain-rate Reynolds number	$Re_\upsilon = \frac{\rho y^2}{\mu_f} S$
Re_θ	Momentum thickness Reynolds number	$Re_\theta = \frac{\max(Re_\upsilon}{2.193}$
St	Stokes number	$St = \frac{C_c \rho_p d_p^2 U_m}{18\mu_f D/2}$
σ_{prop}	Prandtl number of transported property	$\sigma_{prop} = \frac{\nu_f}{D_{prop}}$
t_i	Turbulent intensity	$t_i = \sqrt{2k/3}U^{-1}$
v_τ	Friction velocity	$v_\tau = \sqrt{\frac{\tau_{wall}}{\rho_f}}$
y^+	Dimensionless cell height	$y^+ = \frac{v_\tau y}{\nu_f}$

Abbreviations

Abbreviation	Definition
CDS	Central differencing scheme
LES	Large Eddy Simulation
LL	Left lung
LRN	Low Reynolds number
MF	Magnetic force
MRI	Magnetic Resonance Imaging
PLGA	Poly(lactic-co-glycolic-acid)
RANS	Reynolds averaged Navier-Stokes
RL	Right lung
RMS	Root mean square
RNG	Re-normalisation group
SST	Shear Stress Transport
STL	STereoLitography
TD	Turbulent dispersion
UDS	upwinding differencing scheme
VR	Ventilation ratio
WALE	Wall Adapting Local Eddy Viscosity

Contents

Chapter 1

Introduction

The airway system is crucial for human life, since its function is to deliver oxygen to, and remove carbon dioxide from, the blood, diseases or other defects may greatly alter lifestyle or quality of life. Therefore increased knowledge of the human airway system may lead to more advanced and better treatments.

One way of looking at this complex biological system is from a physics point of view. In such a view the air flow inside the lungs can be modelled and drug particles can be injected to study their behaviour and possible alter their behaviour to aid treatment.

Roughly speaking there are two types of drugs, systemic and non-systemic drugs. Systemic drugs affect the entire body, this is convenient if the disease is present throughout the entire body, an example of this is diabetes treatment with insulin; gene therapy and vaccines may also be delivered via this route (Sanjar and Matthews, 2001; Laube, 2005; Bellary and Barnett, 2006). For pneumal drug delivery of systemic drugs the preferred site of deposition is in the respiratory region which features a large surface area. Some diseases are only present at a certain location, like large cell lung carcinoma (see figure 1.1) and the medicines used typically have serious side-effects. Therefore, it is preferred that the total amount of medicine is reduced and that the majority of the drug ends up at the site of the disease.

The aim of this study is to establish whether or not drugs can be steered in the human airways by making use of magnetic cores and a magnetic field. Since it is reported in literature that the narrowing of the oropharynx and larynx can cause the flow to transition from laminar to turbulent flow a suitable turbulence model should be applied. Since the goal is to ultimately provide patient specific procedures and time may be of essence using direct numerical simulations or large eddy simulations may be too computationally intensive. Therefore, one can question if a Reynolds averaged Navier-Stokes (RANS) model would be good enough and if these models can predict what is experimentally observed. From these topics the research questions can be extracted:

- Is it possible to steer magnetic particles in the human airways by using a magnetic field?
- Due to the throat geometry, the flow can transition from laminar to turbulent. Do the turbulence models predict this behaviour and is a Reynolds Averaged Navier-Stokes model good enough?
- Do the simulations agree with the flow structures and/or particle deposition behaviour observed in experiments?

Before delving straight into the complicated geometries of real lungs simulations were performed in simplified geometries to see whether or not particles can be steered at all. If the conclusion was that it is impossible to steer particles in simplified geometries then performing the same simulations in real lung geometries would not make a lot of sense.

Perhaps so far it seems like drug delivery is the only application, and while this is the scope of the present study, this is certainly not the case in general. Toxic particles may also end up in the airway system, and therefore to determine more precisely where these end up, and thus which area is more prone to exposure, may yield important information for toxicologists, health practitioners and instances alike. Ultimately, the goal of this field is to achieve patient specific drug delivery and risk analysis.

In chapter 2 the reader is introduced to the physiology of the lungs to provide insight into the important features of the lungs and some basic terminology. In chapters 3 and 4 the physical background of the simulations are

detailed. Chapter 5 details the numerical methods used to discretise the equations and what the solving algorithm looks like. In chapter 6 the results of particle deposition in a simplified throat and artery are given (sections 6.1 and 6.2 respectively). In the simplified artery a magnetic force is introduced while in the simplified throat only passive particle deposition is performed. In chapter 7 the flow structures and passive particle deposition in a triple bifurcation geometry is compared to literature and magnetic targeting of core-shell particles is illustrated. Since the goal of this project was to study whether or not particles can be steered in patient specific geometry both passive and magnetically enhanced particle deposition was carried out in patient specific geometry the results of which can be found in chapter 8. Finally the report is wrapped up with conclusions of the case studies (chapter 9) and recommendations for future studies (chapter 10).

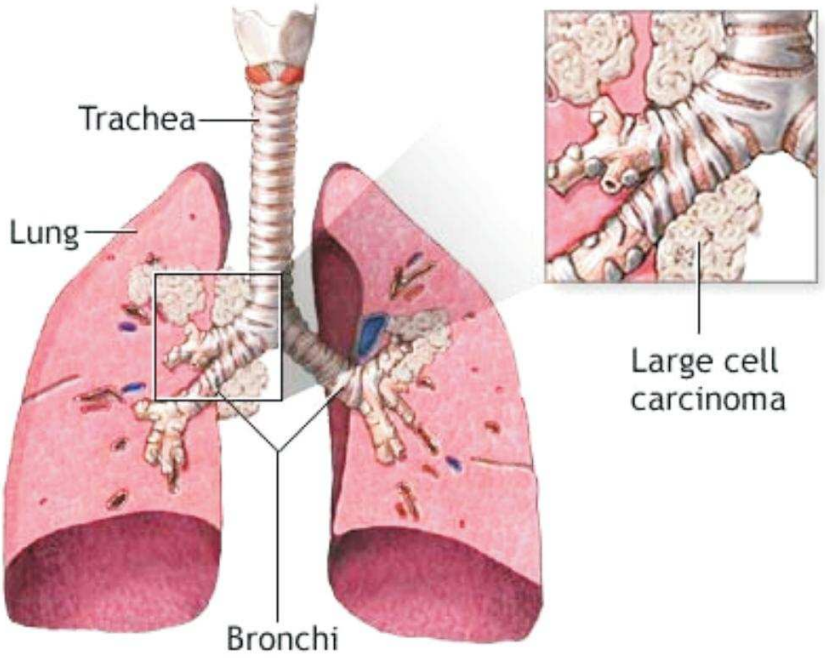

Figure 1.1: Example large-cell lung carcinoma, one of the types of lung cancer (source:`www.asktmc.com`).

Chapter 2

Physiology of the Human Airways

2.1 Physiology of the Human Airway System

The human respiratory system is a complex gas exchange system which contains many interesting geometrical features such as bifurcations, highly curved domains and narrowing. Moreover, the lung contains a thin layer of sticky fluid, called lining fluid, which makes it easy for particles to stick to the surface of the lung. The following sections provide more information on the physiological aspects of the human airway system and will be indicative of how complex the human airway system is (figure 2.1). First the upper airways, comprised of the mouth, nose and throat are described. Second, the conducting airways which entails many generations of bifurcations are detailed. Third, the respiratory region with its large collection of small alveolar sacs is described briefly.

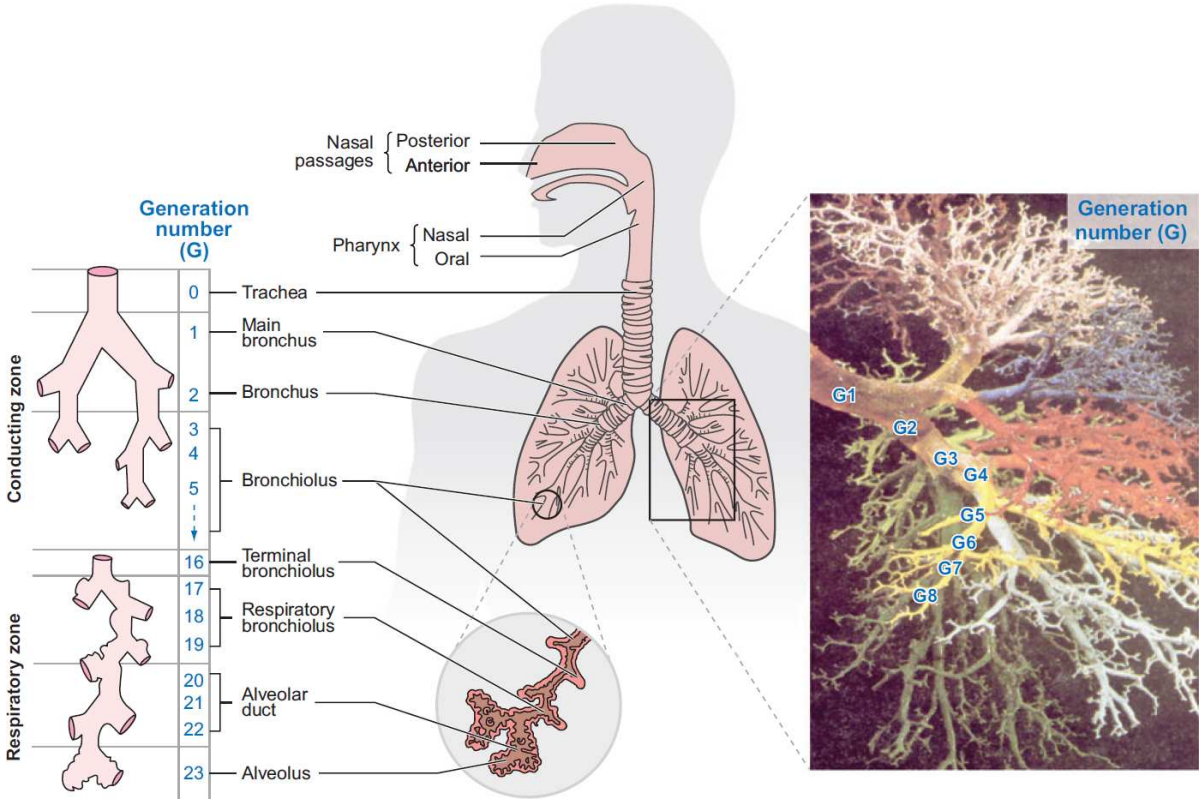

Figure 2.1: Schematic representation of the human airway system, copied from Kleinstreuer et al. (2008).

2.1.1 Upper Airways

The upper airways consist of the mouth, nose, throat and trachea (see figure 2.2). Air usually enters the upper airways via the mouth or nose (although it may enter the throat directly after a medical procedure) after which it goes through the highly bent and narrowing pharynx. This can give rise to a turbulent jet. After the pharynx the air passes through the larynx is again a narrowing and like the pharynx can introduce turbulence (Kleinstreuer and Zhang, 2003a). After passing the larynx, the air flows through the trachea and into the next region of the human airway system, the conducting airways.

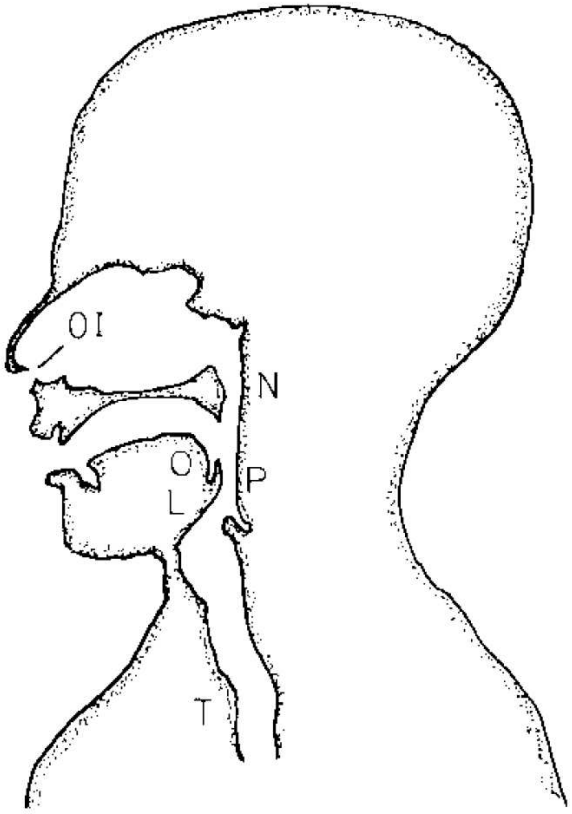

Figure 2.2: Schematic representation of the upper airway system (Pedley, 1977). Abbreviations: Ostium Internum (OI), Nasopharynx (N), Oropharynx (O), Pharynx (P), Larynx (L), Trachea (T).

2.1.2 Conducting Airways

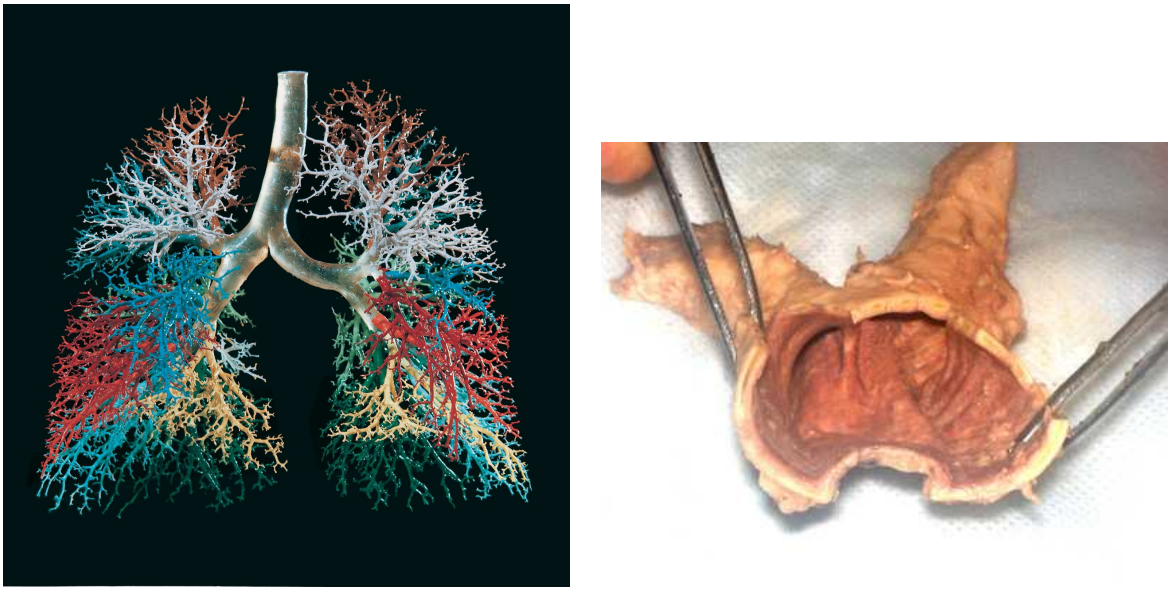

(a) (b)

Figure 2.3: (a) Cast of a human lung (taken from Ralph Hutchings, Visuals Unlimited, Inc.), (b) Photograph of a bifurcation where the carina (flow divider) is visible (source: Martino `http://academic.amc.edu/martino/grossanatomy/site/INDEX.HTM`).

The conducting airways, depicted in figure 2.3a, is the region between the trachea (of the upper airway) and the gas exchanging region (respiratory region) and features roughly twenty generations of typically asymmetric bifurcations (Pedley, 1977). The daughter branches of a bifurcation often feature a smaller diameter than the parent branch and do not have to lie in the same plane, moreover the branches can be curved which in turn may give rise to flow separation (Pedley, 1977). Of course, since they are bifurcations they cause flow division and the introduction of a 'new' wall causes boundary layers to grow on the wall after the flower divider, the flow dividers in the lung are called carina and a photograph of a carina is given in figure 2.3b.

Some diseases such as asthma, bronchitis and cancer can cause a narrowing or clogging (see figures 2.4 and 1.1) of some of these branches resulting in less or no airflow into the respiratory region, reducing the amount of oxygen delivered to the blood.

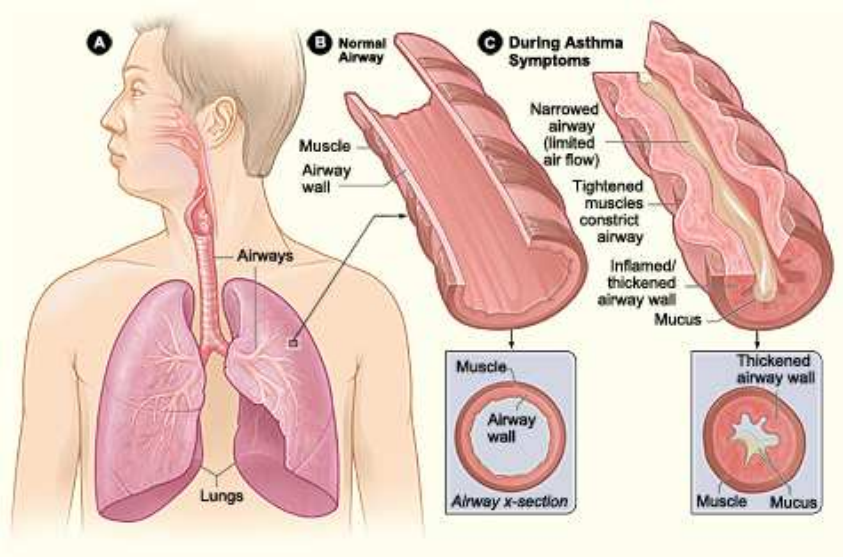

Figure 2.4: Effect of asthma on the lung, the airway is narrowed by contracted muscles and there is a significant amount of mucus present (source:`www.nhlbi.nih.gov`).

2.1.3 Respiratory Region

After the air has moved through the conduction airways the velocity has been decreased considerably (the cross sectional area has hugely increased) and ends up in the respiratory region. The respiratory region or alveolar region consists of the last few generations of the lung which have many alveolar sacs at the walls (see figure 2.5) which can expand and contract during respiration cycles due to lack of cartilage. It is in this alveolated region where the gas exchange takes place. The sheer amount of alveoli and their high surface area are what makes the lung such an efficient gas exchange system, but also a very suitable drug delivery system.

Although very interesting, the respiratory region is not studied in the present report.

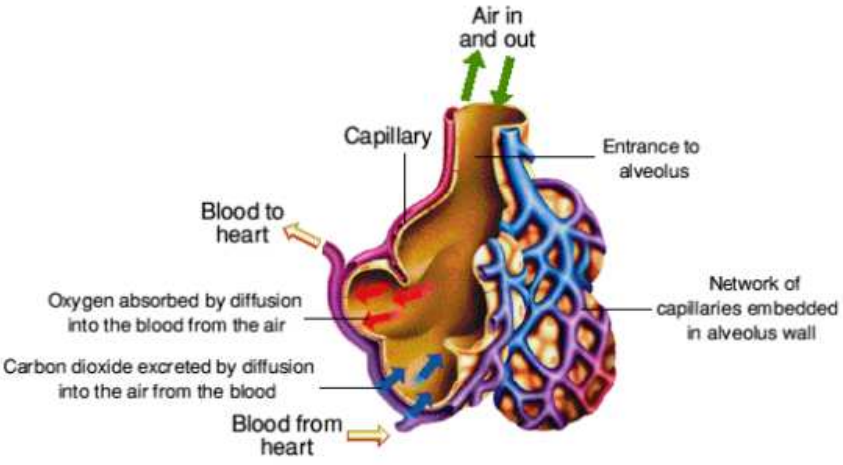

Figure 2.5: Depiction of the gas exchange process in an alveolar sac (source:`http://www.mcqueens.net/mcqueen-ntl/dis/toc_/Pt20.html`).

Chapter 3

Fluid Dynamics

The fluid, in this case air, is modelled by solving the momentum equation known as the Navier-Stokes equations, these equations stem from the conservation of momentum. The conservation of mass is described by the continuity equation. If the fluid is assumed to be incompressible then continuity equation is reduced to:

$$\nabla \cdot \vec{v} = 0 \tag{3.1}$$

And the Navier-Stokes equation is reduced to:

$$\rho \left(\frac{\partial \vec{v}}{\partial t} + \vec{v} \cdot \nabla \vec{v} \right) = -\nabla p + \nabla \cdot (\mu \nabla \vec{v}) + \vec{F} \tag{3.2}$$

To solve the underlying transport phenomena in (complex) geometries, the equations above are discretised (chapter 5), or modified and subsequently discretised for turbulent models (section 3.1), and solved in a domain consisting of many control volumes.

3.1 Closure Models

In the human airway system the flow can transition from laminar to turbulent and vice versa. Therefore, a turbulence model is required to capture the local turbulence. Preferably the model should be able to capture the relaminarisation of the turbulent flow. Several RANS models and two closure models for LES have been used and are briefly explained in the following sections. The following notations are defined as follows.

The instantaneous velocity $\hat{u}_i$ can be represented by the average of the velocity U_i plus the fluctuations u_i (for RANS):

$$\hat{u}_i \;=\; U_i + u_i \tag{3.3}$$

For Large Eddy Simulations the instantaneous velocity is given by the sum of the filtered, or resolved, velocity $\tilde{u}_i$ plus the unfiltered velocity u_i':

$$\breve{u}_i \;=\; \tilde{u}_i + u_i' \tag{3.4}$$

3.1.1 RANS

In the Reynolds averaged Navier-Stokes (RANS) method, the conservation equations are time averaged. The time-averaging can be performed on a long interval such that $\dfrac{\partial U_i}{\partial t} \;=\; 0$ (steady state) or over an interval smaller than that to capture some transient effects. The time-averaged continuity and momentum equations are given below. ν_t stems from the assumption that the unknown quantities, the Reynolds stresses $\tau_{ij} \;=\; -\rho\overline{u_i u_j}$, can be modelled as an extra diffusion term due to the eddies. The Reynolds stresses are then modelled by the product of a the turbulent viscosity μ_t and the mean strain rate (Boussinesq approximation):

$$\tau_{ij} \;= \mu_t \left(\frac{\partial U_i}{\partial x_j} + \frac{\partial U_j}{\partial x_i} \right) - \frac{2}{3}\delta_{ij} \left(\rho k + \mu_t \frac{\partial U_k}{\partial x_k} \right) \tag{3.5}$$

where k is the turbulent kinetic energy $k = \frac{1}{2}\overline{u_i u_i}$.

$$\frac{\partial U_i}{\partial x_i} = 0 \tag{3.6}$$

$$\frac{\partial U_i}{\partial t} + U_j \frac{\partial U_i}{\partial x_j} = -\frac{1}{\rho}\frac{\partial P}{\partial x_i} + \frac{\partial}{\partial x_j}\left((\nu + \nu_T)\frac{\partial U_i}{\partial x_j}\right) \tag{3.7}$$

3.1.2 RANS: K-epsilon Realisable

In the standard k-ε model, the turbulent viscosity is defined as $\mu_t = C_\mu \rho \frac{k^2}{\varepsilon}$ where k is the turbulent kinetic energy (TKE) and ε the dissipation rate. The transport equations for the TKE and ε for the standard model are given by:

$$\frac{\partial(\rho k)}{\partial t} + \frac{\partial(\rho k U_i)}{\partial x_i} = \frac{\partial}{\partial x_i}\left[\left(\mu_f + \frac{\mu_t}{\sigma_k}\right)\frac{\partial k}{\partial x_i}\right] + G_k + G_b - \rho\varepsilon - Y_M \tag{3.8}$$

$$\frac{\partial(\rho \varepsilon)}{\partial t} + \frac{\partial(\rho \varepsilon U_i)}{\partial x_i} = \frac{\partial}{\partial x_i}\left[\left(\mu_f + \frac{\mu_t}{\sigma_\varepsilon}\right)\frac{\partial \varepsilon}{\partial x_i}\right] + C_{1\varepsilon}\frac{\varepsilon}{k}(G_k + C_{3\varepsilon}G_b) - C_{2\varepsilon}\rho\frac{\varepsilon^2}{k} \tag{3.9}$$

$G_k = 2\mu_t S_{ij} S_{ij}$ is the production of turbulent kinetic energy (TKE) due to mean velocity gradients. G_b is the production of TKE due to buoyancy. Y_M is a model for dilatation dissipation (dissipation of turbulence due to compressibility of the medium). σ is the turbulent Prandtl number for the transported property. $C_{1\varepsilon}$ to $C_{3\varepsilon}$ are model constants.

In the traditional k-ε equation and the RNG k-ε, the normal Reynolds stresses $\overline{u^2}$ can become negative (which is unphysical) when the strain rate is large enough (see equation 3.10), the realisable model thus alters the turbulent viscosity to make sure that the normal stresses remain positive by redefining C_μ, see equation 3.11.

$$\overline{u^2} = \frac{2}{3}k - 2\nu_t \frac{\partial U}{\partial x} \tag{3.10}$$

$$C_\mu = \left(A_0 + A_s \frac{k}{\varepsilon} U^*\right)^{-1} \tag{3.11}$$

where U^* (equation 3.12) is a function of the mean rate of strain and the mean rate of rotation tensors (see section A.2.2).

$$U^* = \sqrt{S_{ij}S_{ij} + \tilde{\Omega}_{ij}\tilde{\Omega}_{ij}} \tag{3.12}$$

The modified transport equation for the dissipation rate is:

$$\frac{\partial(\rho \varepsilon)}{\partial t} + \frac{\partial(\rho \varepsilon U_i)}{\partial x_i} = \frac{\partial}{\partial x_i}\left[\left(\mu_f + \frac{\mu_t}{\sigma_\varepsilon}\right)\frac{\partial \varepsilon}{\partial x_i}\right] + C_1 S \varepsilon \rho - C_{2\varepsilon}\rho\frac{\varepsilon^2}{k + \sqrt{\nu\varepsilon}} + C_{1\varepsilon}\frac{\varepsilon}{k}C_{3\varepsilon}G_b \tag{3.13}$$

where $S = \sqrt{2S_{ij}S_{ij}}$, and C_1 is defined as:

$$C_1 = max\left(0.43, \frac{\eta}{\eta + 5}\right) \tag{3.14}$$

with η defined as:

$$\eta = S\frac{k}{\varepsilon} \tag{3.15}$$

3.1.3 RANS: K-omega LRN

The k-ω model, like the k-ε model is a two-equation model for which the first transported property is the same in both. The second property differs from the k-ε in that the k-ε model describes the transport of the dissipation rate ε (units $m^2 s^{-3}$) and the k-ω model describes the specific dissipation rate ω (dissipation per unit TKE, units s^{-1}). The additional transport equations for the regular k-ω model are:

$$\frac{\partial(\rho k)}{\partial t} + \frac{\partial(\rho k U_i)}{\partial x_i} = \frac{\partial}{\partial x_i}\left[\left(\mu_f + \frac{\mu_t}{\sigma_k}\right)\frac{\partial k}{\partial x_i}\right] + G_k - Y_k \tag{3.16}$$

.

$$\frac{\partial(\rho\omega)}{\partial t}+\frac{\partial(\rho\omega U_i)}{\partial x_i} \;=\; \frac{\partial}{\partial x_i}\left[\left(\mu_f+\frac{\mu_t}{\sigma_\omega}\right)\frac{\partial\omega}{\partial x_i}\right]+G_\omega-Y_\omega \tag{3.17}$$

where G_{prop} is the production of the transported property, Y_{prop} the dissipation of that property.

Because the flow in the throat is transitional the k-ω low Reynolds number (LRN) model is expected to be more suitable than the standard model for this problem. The difference in these models lies in the turbulent viscosity μ_t, in the LRN approach the definition of μ_t is modified to dampen the turbulent viscosity when the Reynolds number is low. The μ_t is defined as:

$$\mu_t = a^*\rho\frac{k}{\omega} \tag{3.18}$$

where the model coefficient $a^*=1$ for the standard k-ω model, in the low Reynolds modification this $a^*=1$ has been modified to dampen the turbulent viscosity when the Reynolds number is low. The exact modification, namely the new definition of a^* is given by:

$$a^* = a^*_\infty\left(\frac{\beta_i\_3+Re_t\_R_k}{1+Re_t\_R_k}\right) \tag{3.19}$$

where β_i=0.072, a^*_∞=1, R_k=6 and $Re_t=\dfrac{\rho_f k}{\mu_f\omega}$.

3.1.4 RANS: SST-Transition

The SST-Transition model is a modified SST model created by Menter et al. (2006) and has two additional transport equations to model transitional flow. These additional transport equations describe the transport of intermittency (γ, equation 3.23) and the Reynolds momentum thickness ($R\tilde{e}_{\theta t}$, equation 3.24). It can be used both with and without wall functions with the latter requiring that the dimensionless first cell height (y^+) be around 1 and not higher than 5 to resolve the viscous sublayer. The advantage of modelling this layer is that pressure gradients are more accurately captured and thus providing higher accuracy when adverse pressure gradients are present (which is likely in the case of a highly curved geometry like the human airway) and the disadvantage is the increased computational cost associated with a denser mesh.

$$\frac{\partial(\rho k)}{\partial t}+\frac{\partial(\rho kU_i)}{\partial x_i} \;=\; \frac{\partial}{\partial x_i}\left[\left(\mu_f+\frac{\mu_t}{\sigma_k}\right)\frac{\partial k}{\partial x_i}\right]+\tilde{G}^*_k-Y^*_k \tag{3.20}$$

$$\frac{\partial(\rho\omega)}{\partial t}+\frac{\partial(\rho\omega U_i)}{\partial x_i} \;=\; \frac{\partial}{\partial x_i}\left[\left(\mu_f+\frac{\mu_t}{\sigma_\omega}\right)\frac{\partial\omega}{\partial x_i}\right]+G_\omega-Y_\omega+D_\omega \tag{3.21}$$

where $\tilde{G}^*_k$ is the production term for the turbulent kinetic energy defined as $\tilde{G}^*_k=\gamma_{eff}\tilde{G}_k$ where $\tilde{G}_k$ is the production term from the original SST model and γ_{eff} the effective intermittency (equation A.17). Y^*_k the sink term from the original SST model times a factor which depends on the γ_{eff}. The transport equation for the specific dissipation also contains a production (G_ω), sink (Y_ω) but is different from that in the standard k-ω model. Several of the terms are defined slightly different and equation 3.21 is a blend of the k-ε model (for which the transport equations have been transformed to k and ω transport equations) in the free stream and k-ω near the wall; the blending term is defined as:

$$D_\omega \;=\; 2(1-F_1)\rho\frac{1}{\omega\sigma_{\omega,2}}\frac{\partial k}{\partial x_i}\frac{\partial\omega}{\partial x_i} \tag{3.22}$$

where the $(1-F_1)$ is the blending function and the rest is the term which pops up when transforming the k-ε equation to ω, called the cross diffusion term.

The additional equations employed by Menter et al. (2006) to model transitional flow are the transport equation for the intermittency γ (equation 3.23) and the transport equation for the Reynolds momentum thickness $R\tilde{e}_{\theta t}$ (equation 3.24). The intermittency is used to turn on the transition locally by enabling the modified production term in the k-equation downstream of this transition. The transport equation for γ is defined as:

$$\frac{\partial(\rho\gamma)}{\partial t}+\frac{\partial(\rho\gamma U_i)}{\partial x_i} \;=\; \frac{\partial}{\partial x_i}\left[\left(\mu_f+\frac{\mu_t}{\sigma_\gamma}\right)\frac{\partial\gamma}{\partial x_i}\right]+P_{\gamma1}-E_{\gamma1}+P_{\gamma2}-E_{\gamma2} \tag{3.23}$$

where $P_{\gamma 1}$ and $E_{\gamma 1}$ are the transition source and sink terms respectively, $P_{\gamma 2}$ and $E_{\gamma 2}$ the source and sink terms of laminarisation respectively. The transport equation for $R\tilde{e}_{\theta t}$ is given by:

$$\frac{\partial(\rho R\tilde{e}_{\theta t})}{\partial t}+\frac{\partial(\rho R\tilde{e}_{\theta t}U_i)}{\partial x_i} \;=\; \frac{\partial}{\partial x_i}\left(\sigma_{\theta t}\left(\mu_f+\mu_t\right)\frac{\partial R\tilde{e}_{\theta t}}{\partial x_i}\right)+P_{\theta t} \tag{3.24}$$

where $P_{\theta t}$ is the source term for the Reynolds momentum thickness (equation A.16) which is modelled such that it in the free stream the transported scalar $R\tilde{e}_{\theta t}$ matches the local value $Re_{\theta t}$ and is turned off in the boundary layer such that the property is transported from the free stream to the boundary layer.

The parameters $Re_{\theta t}$, F_{length} and $Re_{\theta c}$ (equations A.13-A.15) are defined through correlations which are proprietary to Ansys and thus this model can only be used with Ansys Software (Menter et al., 2006). The model constants applied throughout this study are the Fluent standard settings. The full model description can be found in Menter et al. (2006).

3.1.5 Large Eddy Simulations

In contrast to the previous models, where the turbulence is modelled in its entirety, large eddy simulations (LES) fully resolves the large scales of the flow down to a certain length scale which is usually the grid length scale $\Delta = V_{cell}^{1/3}$, below the grid scale a subgrid scale (SGS) model is used to model the small scale turbulence. This subgrid model in the form of a turbulent viscosity models the subgrid turbulence isotropically.

A LES acts as an implicit low pass filter by resolving the longer length scale turbulence but modelling the very short time and length scale turbulence (subgrid, $l < V_{cell}^{1/3}$). Additionally, explicit filtering can be applied on top of the implicit filter to increase the accuracy of the simulation but the filter length of the explicit filter needs to be larger than the grid length scale (filter Lent for the implicit filter). In the present report no explicit filtering is applied.

The filtered continuity and Navier-Stokes equations are:

$$\frac{\partial\tilde{u}_i}{\partial x_i} \;=\; 0 \tag{3.25}$$

$$\frac{\partial\tilde{u}_i}{\partial t}+\tilde{u}_j\frac{\partial\tilde{u}_i}{\partial x_j} \;=\; -\frac{1}{\rho}\frac{\partial\tilde{p}}{\partial x_i}+\frac{\partial}{\partial x_j}\left((\nu+\nu_{sgs})\frac{\partial\tilde{u}_i}{\partial x_j}\right) \tag{3.26}$$

where ν_{sgs} is the subgrid scale viscosity which is a model for the nonlinear unresolved scales (high frequency) which is a similar approach to the RANS models. There are multiple models for the subgrid scale viscosity in equation 3.26, the models employed in the present study are the standard Smagorinsky-Lilly model and the Wall-Adapting Local Eddy Viscosity (WALE) model.

3.1.5.1 Smagorinsky-Lilly Subgrid Model

In the Smagorinsky-Lilly model the SGS turbulent viscosity is modelled by:

$$\nu_{SGS} \;=\; L_S^2|\overline{S}| \tag{3.27}$$

where ρ_f is the fluid density, L_S the subgrid mixing length and $|\overline{S}|$ the strain rate magnitude defined as $|\overline{S}| = \sqrt{2S_{ij}S_{ij}}$. And the subgrid mixing length is defined as:

$$L_s \;=\; min(\kappa d, C_s\Delta) \tag{3.28}$$

where κ is the von Karman constant, d the distance to the closest wall, $\Delta = V_{cell}^{1/3}$ the length scale of a control volume and C_s the Smagorinsky constant of which the value depends on the type of problem you are solving. C_s=0.1 has been used in the simulations performed in the present report.

3.1.5.2 WALE Subgrid Model

In the WALE subgrid model definition of the subgrid turbulent viscosity the strain rate magnitude is replaced by a more detailed expression (equation 3.29) which makes sure that the model returns a zero turbulent viscosity for laminar shear flows.

$$\nu_{SGS} = L_S^2 \frac{\left(S_{ij}^d S_{ij}^d\right)^{3/2}}{\left(\overline{S}_{ij}\overline{S}_{ij}\right)^{5/2} + \left(S_{ij}^d S_{ij}^d\right)^{5/4}} \tag{3.29}$$

where

$$\overline{S}_{ij} = 1/2\left(\frac{\partial \tilde{u}_i}{\partial x_j} + \frac{\partial \tilde{u}_j}{\partial x_i}\right) \tag{3.30}$$

and

$$S_{ij}^d = 1/2\left[\left(\frac{\partial \tilde{u}_i}{\partial x_j}\right)^2 + \left(\frac{\partial \tilde{u}_j}{\partial x_i}\right)^2\right] - 1/3\delta_{ij}\left(\frac{\partial \tilde{u}_k}{\partial x_k}\right)^2 \tag{3.31}$$

Additionally the subgrid mixing length term is slightly modified in that the Smagorinsky constant is replaced by the WALE constant C_w which is 0.3 in the present study.

$$L_s = min(\kappa d, C_w \Delta) \tag{3.32}$$

Chapter 4

Particle Dynamics

Since the problem is assumed to be one-way coupled due to low particle loading, the particles can be modelled after modelling the air flow inside the geometry. The method with which the particles are modelled is by solving the equation of motion for each particle. Newton's second law of motion for each particle.

$$m_p \frac{d\vec{u}_p}{dt} = \sum \vec{F}_i \tag{4.1}$$

Where $\sum \vec{F}_i$ is sum of all forces acting on the particles. These forces will be discussed in the following sections starting with the drag force and finishing with the excluded forces. After integrating the particle velocity with respect to time, the position can be calculated by performing another integration:

$$\frac{d\vec{x}}{dt} = \vec{u}_p \tag{4.2}$$

4.1 Drag Force

The drag force on a spherical particle is given by equation 4.3

$$\vec{F}_D = \frac{m_p f}{\tau_p}(\vec{u}_f - \vec{u}_p) \tag{4.3}$$

where f is the drag factor which depends on the particle Reynolds number:

$$Re_p = \frac{\rho_f d_p}{\mu_f}|\vec{u}_f - \vec{v}_p| \tag{4.4}$$

and τ_p is the particle relaxation time defined as:

$$\tau_p = \frac{C_c \rho_p d_p^2}{18\mu_f} \tag{4.5}$$

The Cunningham slip correction factor (C_c) is taken to be one in all of the case studies to match the reference cases. Because several reproduction studies were performed in the present study, different drag forces are used in different case studies. Equation 4.6 is used in all three cases whereas equation 4.8 (Cohen Stuart, 2009) is used in case one and two and equation 4.7 (Zhang et al., 2001) is used in case three. In chapters B and 8 the Morsi and Alexander drag law (Morsi and Alexander, 1972) in equation 4.9 is used where the coefficients α_1-α_3 depend on the Re_p (see equation A.18 or the original paper for the values).

$$f = 1 \text{ if } Re_p \leq 1 \tag{4.6}$$

$$f = Re_p^{0.354} \text{ if } 1 < Re_p \leq 400 \tag{4.7}$$

$$f = 1 + 0.15Re_p^{0.687} + 0.0175(1 + 4.25 \cdot 10^4 Re_p^{-1.16})^{-1} \text{ if } 1 < Re_p \leq 3 \cdot 10^5 \tag{4.8}$$

$$f = \frac{Re_p}{24}\left(\alpha_1 + \frac{\alpha_2}{Re_p} + \frac{\alpha_3}{Re_p^2}\right) \tag{4.9}$$

An often reported dimensionless number found in literature and also this report, is the Stokes number (equation 4.10). This dimensionless number pops up when scaling the equation of motion and represents the ratio of the particle relaxation time and the fluid relaxation time and indicates the particles 'ability' to follow the fluid motion: low stokes numbers indicate particles that deviate only slightly from a steamtrace.

$$St = \frac{C_c \rho_p d_p^2 U_m}{18\mu_f D/2} \tag{4.10}$$

Because the flow is bifurcated in the conducting airways, it may be of interest to estimate the St in one of the lower generations. To do this a few assumptions are made: the daughter branches have the same diameter, the flow divides evenly and the total cross sectional increase (area daughter A + area daughter B) due to the bifurcation called the area growth factor $G_{f,a}$ is the same for each bifurcation. Then the characteristic length scale in a daughter branch is (see section A.4.2 for the derivations):

$$D_{daughter} = D_{parent}\sqrt{\frac{G_{f,a}}{2}} \tag{4.11}$$

The velocity in a daughter branch is:

$$U_{daughter} = \frac{U_{parent}}{G_{f,a}} \tag{4.12}$$

The St_N in generation N then becomes:

$$St_N = \frac{\rho_p d_p^2 U_0}{18\mu_f D_0/2} G_{f,a}^{-3N/2}(1/2)^{-N/2} = St_0 G_{f,a}^{-3N/2}(1/2)^{-N/2} \tag{4.13}$$

For example, if the area of generation N is 40% larger than that of generation N-1 the $G_{f,a} = 1.4$ (which is the case for example in chapter 7) then in the sixth generation $St_6 = 0.4St_0$.

4.2 Gravity and Buoyancy

Gravity and buoyancy effects for a particle with mass m_p can be added by adding the force given in equation 4.14 to the right hand side of equation 4.1. Due to the relatively large particle density compared to the fluid density the buoyancy effect can be neglected.

$$\vec{F}_{g+b} = m_p \vec{g}\left(1 + \frac{\rho_f}{\rho_p}\right) \tag{4.14}$$

The ratio F_g/F_D scales as $F_g/F_D \sim \left(\frac{\rho_p d_p^2 g}{18\mu_f U_m}\right)$ and thus becomes more important when the particle size and density increase. When scaling the equation of motion, a dimensionless number for the effect of gravity pops up. This dimensionless number is called the Froude number (Fr) and is the ratio of inertia and gravitational forces. The Fr is defined as:

$$Fr = \frac{U_p^2}{Lg} \tag{4.15}$$

Where the capital U_p and L indicate the scales of the particle velocity and geometry size respectively. Now, for relatively large velocities the Fr becomes larger indicating that gravity plays a smaller role. The gravitational effects are reported to be of interest in the more distal branches, therefore an estimate can be made to assess whether the gravity should be used or not. When a branch bifurcates, the total cross sectional area increases and the velocity drops correspondingly (equation 4.12). Lets dub the cross sectional area increase for one generation $G_{f,a}$ (growth factor of area). If we assume the same growth factor holds for all generations (not very likely but good enough for an approximation) then the Fr in generation N, $\mathrm{Fr_N}$ becomes (by applying equation 4.11 for the length scale):

$$Fr_N = \frac{U_{p,0}^2}{L_0 g G_{f,a}^{2.5N} (1/2)^{N/2}} = Fr_0 G_{f,a}^{-2.5N} (1/2)^{-N/2} \tag{4.16}$$

For the patient specific geometry (chapter 8) there are 6-8 (total number of outlets is 72 so primarily consists of 6 generations) generations of branches, if we assume a 40% area increase ($G_{f,a} = 1.4$, same as for the St_N) the Froude number in the sixth generation Fr_6 is then 20 times smaller than Fr_0. Since $Fr_N \sim G_{f,a}^{-2.5N}(1/2)^{-N/2}$ and $St_N \sim G_{f,a}^{-3N/2}(1/_2)^{-N/2}$ (equation 4.13) the Fr drops much more rapidly.

4.3 Magnetic Force

For magnetic core-shell particles subject to a magnetic field $\vec{H}$ the following magnetic force can be calculated:

$$\vec{F}_M = d_{mp}^3 V_p \mu_0 \vec{M} \cdot \nabla \vec{H} \tag{4.17}$$

Where d_{mp}^* is the ratio of the magnetic core diameter to the total particle diameter, U_p is the particle volume, μ_0 is the magnetic permeability of free space, $\vec{M}$ is the magnetisation concentration. The magnetisation concentration depends on the saturation of the particle, if it is fully saturated then the magnetisation concentration no longer increases. This magnetisation concentration is determined as follows (Cohen Stuart, 2009):

$$\vec{M} = \begin{cases} \chi_m \vec{H} & \text{if } \vec{H} < M_{sat} \chi_m^{-1}, \\ \dfrac{\chi_m}{|\chi_m|} M_{sat} \hat{H} & \text{if } \vec{H} \geq M_{sat} \chi_m^{-1} \end{cases} \tag{4.18}$$

Where χ_m is the particle susceptibility. The auxiliary magnetic field $\vec{H}$ depends on the configuration of the current carrying wire. For a straight current carrying wire, which is used in the present study, the magnetic field is given by:

$$\vec{H} = \frac{I}{2\pi s} \hat{\phi} \tag{4.19}$$

Where I is the current through the wire, s the radial distance between the wire and evaluation point and $\hat{\phi}$. A dimensionless number to determine the relative importance of the magnetic force compared to the drag force was defined by Cohen Stuart (2009); Haverkort (2008) as the magnetic number Mnp:

$$Mnp = \frac{d_{mp}^3 d_p^2 \mu_0 M \cdot \nabla H}{18 \mu_f U_{char}} \tag{4.20}$$

where M depends on the saturation of the particle, throughout this report the Mnp is based on saturated particles, for a current carrying wire and a saturated particle located at distance ΔL_{wire} away from the wire the Mnp is given by:

$$Mnp = \frac{(d_{mp}^*)^3 d_p^2 \mu_0 M_{sat} I}{18 \mu_f U_{char} 2\pi \Delta L_{wire}^2} \tag{4.21}$$

Instead of describing the ratio of the magnetic force to the drag force, we can also look at the non-dimensionalised equation of motion to see how the magnetic force equivalent of the Froude number scales.

$$Fr_{Mag,N} = \frac{U_p^2 m_p}{F_m D_{char}} \tag{4.22}$$

$$Fr_{Mag,N} = -\frac{\rho_p 2\pi U_{p,0}^2 \Delta L_{wire}^2}{(d_{mp}^*)^3 I M_{sat} D_0 G_{f,a}^{2.5N} (1/2)^{N/2}} = -Fr_{Mag,0} \frac{\Delta L_{wire,*}^2}{G_{f,a}^{2.5N} (1/2)^{N/2}} \tag{4.23}$$

where ΔL_{wire} is the distance between the point of interest and the wire and $\Delta L_{wire,*} = \Delta L_{wire} / \Delta L_{wire,ref}$. This dimensionless number scales like the gravity IF the distance to the wire is always equal which is clearly not the case. Since the geometry is bifurcated some distal branches can be much closer to the wire than other branches of the same generation or even previous generations therefore a locally defined $Fr_{Mag,N}$ is not as general as the St_N or Fr_N. For example, the $Fr_{Mag,6} = Fr_{Mag,0}/20$ at the same distance as the reference distance but when the distance is increased by a factor 10 $Fr_{Mag,6} = 5 Fr_{Mag,0}$

4.4 Saffman Lift Force

The lift caused by an asymmetric velocity field around a particle can be incorporated by using the Saffman lift force. The lift force is given by equation 4.24 where $Re_G = \frac{\rho_f d_p^2}{\mu_f}\frac{du}{dy}$:

$$\vec{F}_{Saffman} = 1.61\mu_f d_p \left|\vec{u}_f - \vec{u}_p\right| \sqrt{Re_G} \tag{4.24}$$

Dividing by the stokes drag and scaling gives a ratio that scales as $\frac{F_{Saffman}}{F_{drag}} \sim \sqrt{Re_L}\frac{d_p}{L}$, which means that the Saffman lift force is relatively weak and can be neglected. However, it was used in chapter B since it was used in the reference paper.

4.5 Virtual Mass Force

The virtual mass force, or added mass force, can be added to model the effect of displacement of the fluid by the particle as the particle is accelerated. The displaced mass is equal to a sphere of the fluid with the same volume as the particle. The virtual mass force is modelled by equation 4.25. Since the density of the particles is three orders of magnitude larger than that of the fluid the virtual mass force can be neglected.

$$\vec{F}_{virtualmass} = \frac{\rho_f V_p}{2}\frac{D(\vec{u}_f - \vec{u}_p)}{Dt} \tag{4.25}$$

4.6 Pressure Gradient Force

The force which acts on the particle due to pressure gradients in the flow surrounding the particle is the pressure gradient force (equation 4.26) and becomes important when the density ratio ρ_f/ρ_p becomes larger.

$$\vec{F}_{p.grad} = V_p \rho_f \frac{D\vec{u}_f}{Dt} \tag{4.26}$$

4.7 Faxen Force

To incorporate the drag force caused by a non-uniform flow field, the drag force is expended by adding the Faxen force:

$$\vec{F}_{Faxen} = \mu_f \, \pi \, \frac{d_p^3}{8} \nabla^2 \vec{u}_f \tag{4.27}$$

The ratio of the Faxen force and Stokes drag force scales with $\frac{F_{Faxen}}{F_{Drag}} \sim \left(\frac{d_p}{L}\right)^2$, because the particles used in this study are on micrometre scale and the geometries are on the centimetre scale, the Faxen force is negligibly small compared to the drag force and is thus not considered.

4.8 Basset Force

As the particle accelerates through the fluid, a boundary layer is formed on its surface. This boundary layer is not formed instantaneously and of course has an effect on the shear stress on the surface. The Basset force is used to model this lagging boundary layer and is given by equation 4.28. This force is neglected in all of the reference cases as it is difficult to implement (Cohen Stuart, 2009).

$$\vec{F}_{Basset} = \frac{3}{2} d_p^2 \sqrt{\pi \rho_f \mu_f} \left(\int_0^t \frac{\frac{D\vec{u}_f}{Dt'} - \frac{\partial \vec{u}_p}{\partial t'}}{\sqrt{t - t'}} \mathrm{d}t' \right) \tag{4.28}$$

4.9 Turbulent Dispersion in RANS Models

Since in RANS models the calculated flow field is time averaged, no fluctuations are present and thus if particles were injected in this flow field the particles would behave like they would in laminar flow. To account for this, there is a model which, based on the turbulent kinetic energy in each cell, adds velocity fluctuations to the flow field and thus make the particle behaviour more like they would in turbulent flow where local velocity fluctuations cause deviations from the stream traces of the time averaged velocity field. This discrete random walk can be described as follows:

$$\begin{aligned} \hat{u} &= U + u \\ u &= \sqrt{\frac{2}{3}kZ} \end{aligned} \tag{4.29}$$

where k is the turbulent kinetic energy and Z is a pick from a standard Gaussian distribution. A fluctuation is kept constant during a time period corresponding to the characteristic eddy time-scale τ_e (equation 4.30). After this this time has been reached a new set of picks are made from the normal distribution.

$$\tau_e = 2T_L \tag{4.30}$$

T_L is the fluid integral time scale defined as:

$$T_L = C_L \frac{k}{\varepsilon} \tag{4.31}$$

where C_L is a constant determined by matching the diffusivity of tracer particles to the prediction of the diffusion rate of a scalar by the turbulence model. For the SST model $C_L = 0.15$ (Ansys, 2011).

In Fluent the number of tries can also be specified, which indicates that the initial picks from the probability density function are re-picked for a new set of particle injections. The effect of turbulent dispersion on the particle deposition in patient specific geometry is studied in section 8.3.

4.10 Overview of Forces Used

The forces used throughout the report are not the same therefore an overview was made to identify which forces are being used in which simulation. The virtual mass force, Faxen and Basset force were not used in any of the simulations and are therefore omitted from the overview.

Table 4.1: Overview of the particle forces used in each of the studies.

Case Study	Chapter	F_d	F_g and F_b	F_m	F_{Saffman}	$F_{\text{p.grad.}}$	Turbulent Dispersion
1	6.1	+	-	-	-	-	-
2	6.2	+	-	+	-	-	-
3	7	+	-	+	-	-	-
4	B	+	+	-	+	+	-
5	8	+	+	+	-	-	+

4.11 Core-Shell Particles

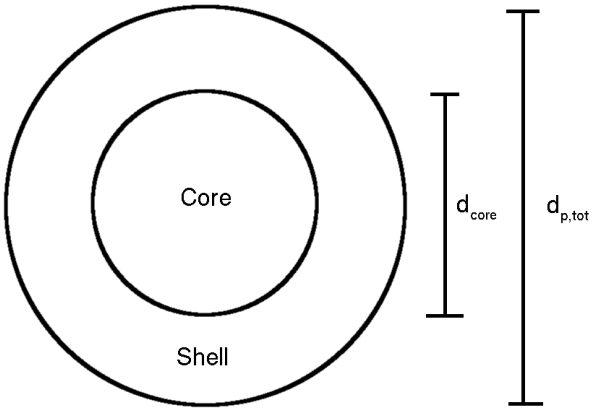

Figure 4.1: Schematic drawing of a core-shell particle.

For magnetic drug delivery a magnetic core is used (typically iron oxides) and because these materials themselves are not medicinal the drug has to be delivered somehow. What can be done is coating these magnetic cores with a layer which contains the drug, creating a shell. This shell can be made from all sorts of materials but typically are made from biodegradable materials. More specifically, in the present study the material will be taken to be poly(lactic-coglycolic acid) (more commonly referred to as PLGA). To incorporate these effects into the forces seen above, some terms have to be modified. More specifically, the magnetic force is dependent only on the magnetic core and the drag force is dependent only on the surface. The core shell method of the particle was previously used by Righolt (2010) to more accurately model the particles that would be used in practise.

The density of the materials is also important, since this changes the mass of the particle (with a constant volume). In the present study this is incorporated as follows.

There is a magnetic core of diameter d_m, around this is a shell with thickness $d_s = d_p - d_m$ to give a total particle diameter d_p. The following ratio is defined: $d^*_{mp} = \dfrac{d_m}{d_p}$. If d^*_{mp} is zero then no core is present, if it is one then the entire particle is made of magnetic material.

To determine the combined density the following formula can be derived:

$$\rho_{combined} = \rho_{core}\,(d^*_{mp})^3 + \rho_{shell}\,(1-(d^*_{mp})^3) \tag{4.32}$$

However, since the shell contains both carrier and drug, the density of the shell is dependent on the loading of the drug. The loading is the mass percentage of drug in the shell. The following formula is used to determine the density of the shell:

$$\rho_{shell} = \left(\frac{x_d}{\rho_{drug}} + \frac{1-x_d}{\rho_{core}}\right)^{-1} \tag{4.33}$$

Where x_d is the fractional loading of the drug in the shell (based on the mass). In the present study this was taken to be 30% which is based on data available for anti-tubercular drugs (Pandey and Khuller, 2005).

For the core in chapters 7and 8 the material is taken to be maghemite (γFe_2O_3) with a density of 4860 kg·m^{-3} (Anthony et al., 2001), particle susceptibility χ_m=3 (Cullity and Graham, 2011) and saturation magnetisation of roughly $3.9 \cdot 10^5\ A \cdot m^{-1}$ (Moskowitz, 1991). The PLGA density is 1300 $kg\,m^{-3}$ (Polysciences, 2013) and the drug density is taken to be 1610 $kg \cdot m^{-3}$ after Righolt (2010).

Chapter 5

Numerical Methods

In this chapter the numerical methods for the discretisation, solving and meshing are given. The software package used to perform the simulations is Ansys Fluent (12,13,14), therefore the following section will address some of the methods found in this package.

5.1 Discretisation

5.1.1 Finite Volume Method

The domain is subdivided into smaller control volumes which may have different shapes and sizes. For each of these control volumes, the conservation equations should hold. By integrating the Navier Stokes equation over the control volume and doing this for all control volumes in the domain, the flow problem can be solved (approximately).

$$\rho\left(\frac{\partial\vec{v}}{\partial t}+\vec{v}\cdot\nabla\vec{v}\right)=-\nabla p+\nabla\cdot(\mu\nabla\vec{v})+\vec{F} \tag{5.1}$$

$$\int_V \nabla\cdot\vec{v}dV=\oint_S \vec{v}\cdot\hat{n}dS \tag{5.2}$$

Starting with the Navier Stokes equation for an incompressible fluid (equation 5.1) and integration over a control volume V and applying Gauss' divergence theorem yields:

$$\rho\left(\int_V\frac{\partial\vec{v}}{\partial t}+\oint_S\vec{v}(\vec{v}\cdot\hat{n})dS\right)=-\int_V\nabla pdV+\oint_S\mu\nabla\vec{v}\cdot\hat{n}dS+\int_V\vec{F}dV \tag{5.3}$$

Since the cells are made up of several well defined faces (with surface area A_f) enclosing a volume V, the surface integral along the cell can be replaced by the sum of flux times face area (A_f) for all the faces and the equation can now be rewritten in terms of the face values of variables (e.g. velocity at certain face $\vec{v}_f$, and area A_f).

$$\rho\left(V\frac{\partial\vec{v}}{\partial t}+\sum_{faces}\vec{v}_f(\vec{v}_f\cdot\hat{n})A_f\right)=-\nabla pV+\sum_{faces}\mu_f\nabla\vec{v}_f\cdot\hat{n}A_f+\vec{F}V \tag{5.4}$$

However, as the fluid variables are defined at the centre of the cell, the face value has to be determined.

5.1.2 Discretisation

To calculate the face values between neighbouring cells an interpolation method is used to interpolate between the values of the variable at the centre of the cells. Different techniques (or schemes) exist to perform this interpolation, in the next few paragraphs a few of these schemes are explained.

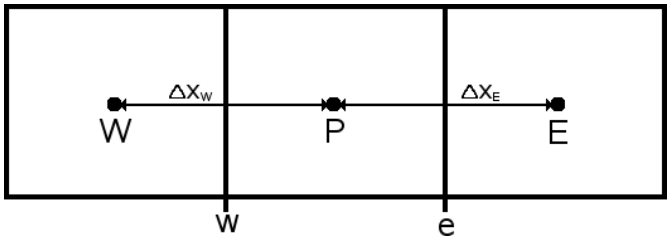

Figure 5.1: Schematic drawing of three control volumes.

5.1.2.1 Spatial Discretisation

5.1.2.1.1 Upwinding Differencing Scheme

In the Upwinding Differencing Scheme (UDS) the face value is set to be equal to the value at the control volume centre which is located upstream of that face (see equation 5.5 and figure 5.1).

$$\begin{aligned} if\, U > 0 \rightarrow\ \Phi_w = \Phi_W,\ \Phi_e = \Phi_P, \\ if\, U < 0 \rightarrow\ \Phi_w = \Phi_P,\ \Phi_e = \Phi_E \end{aligned} \tag{5.5}$$

5.1.2.1.2 Second Order Upwinding Differencing Scheme

In a higher order upwinding differencing scheme a Taylor expansion around the cell centre is performed and in case of the second order UDS (which is applied in the present study) the following expression is found for the face value of a variable ϕ_f:

$$\Phi_f = \Phi + \nabla\Phi \cdot \delta\vec{s} \tag{5.6}$$

Where $\delta\vec{s}$ is the position vector from the cell centre to the face centre. The gradient can be determined by the Green Gauss gradient evaluation (another application of equation 5.2):

$$\nabla\Phi_{cv} = \frac{1}{V_{cv}} \sum_{faces} \bar{\Phi}_f \vec{S}_f \tag{5.7}$$

Where V_{cv} is the volume of the control volume for which the gradient $\nabla\Phi_{cv}$ is to be determined, $\vec{S}_f$ is the surface vector and $\bar{\Phi}_f$ is the value of the variable at the face evaluated by either a arithmetic average of the neighbouring cell centres the face (cell-based Green Gauss method) or from the arithmetic average of the nodal values (node-based Green Gauss method). For unstructured meshes built from tetrahedrals Ansys recommends the node-based Green Gauss method for the gradient evaluation.

5.1.2.1.3 Central Differencing Scheme

In the Central Differencing Scheme (CDS), a linear interpolation is used to calculate the face value between two control volumes. The formula for the two faces adjacent to the central control volume P is given in equation 5.8. The CDS is stable if the Peclet number ($Pe = \frac{u\Delta x}{\nu}$) is lower than 2.

$$\begin{aligned} \Phi_w &= \tfrac{1}{2}(\Phi_W + \Phi_P) \\ \Phi_e &= \tfrac{1}{2}(\Phi_P + \Phi_E) \end{aligned} \tag{5.8}$$

5.1.2.1.4 Bounded Central Differencing Scheme

The bounded central differencing scheme employs three options to ensure boundedness. Based on local criteria, it can either be a full CDS, a blend of CDS and second order UDS or first order UDS. The first order UDS is only used if the CBC cannot be met otherwise (Ansys, 2011).

5.1.2.2 Temporal Discretisation

In the following explanation of the temporal discretisations the differential equations are rewritten to the form of:

$$\frac{\partial\phi}{\partial t} = F(\phi) \tag{5.9}$$

where ϕ stands for the transported property and $F(\phi)$ contains the convective and diffusive transport as well as possible sources and sinks and thus contains the spatially discretised quantities. By using either a one sided or central differencing scheme for the left hand side the new values can be evaluated.

5.1.2.2.1 Explicit Temporal Discretisation

In the explicit scheme, a backward differencing scheme is applied to the left hand side and ϕ_i^{n+1} is explicitly expressed on current values of ϕ only. The explicit temporal discretisation scheme has the drawback that it is not unconditionally stable and as such the time step should be taken such that the Courant number is lower than 0.5 everywhere.

$$\frac{\phi_i^{n+1} - \phi_i^n}{\Delta t} = F(\phi_i^n) \tag{5.10}$$

5.1.2.2.2 Implicit Temporal Discretisation

The implicit method differs from the explicit method in that the right hand side of equation 5.9 is not evaluated at the current time step but rather the next time step. This method is unconditionally stable and thus the time step does not have to be lower than dictated by $\mathrm{Co} < 0.5$ for stability. It is not 'unconditionally accurate', certain phenomena occur on a certain time-scale and if the time-step is much larger these phenomena are not captured, and as such even though the solution is stable it may not be accurate.

$$\frac{\phi_i^{n+1} - \phi_i^n}{\Delta t} = F(\phi_i^{n+1}) \tag{5.11}$$

5.1.2.2.3 Bounded Second Order Implicit Temporal Discretisation

Another unconditionally stable method is the second order implicit temporal discretisation method displayed in equation 5.12. Additionally a bounded second order scheme can be used to limit the values of some properties, for example limiting the turbulent kinetic energy to positive values, the bounded second order scheme is given in equation 5.13 where the regular second order scheme is returned when $B^{n+3/2} = B^{n+1/2} = 1$.

$$\frac{3\phi_i^{n+1} - 4\phi_i^n + \phi_i^{n-1}}{2\Delta t} = F(\phi_i^{n+1}) \tag{5.12}$$

$$\frac{2(\phi^{n+1} - \phi^n) + B^{n+3/2}(\phi^{n+1} - \phi^n) - B^{n+1/2}(\phi^n - \phi^{n-1})}{2\Delta t} = F(\phi_i^{n+1}) \tag{5.13}$$

5.1.3 Solving Algorithm

The algorithm used to solve the flow problem is briefly described below. The very first step is to provide a first guess, the initialisation. The standard initialisation is to patch (set) values for the variables throughout the domain. Another approach, which provides a better first guess especially for complex geometry, is the hybrid initialisation method. This method is different from the standard initialisation in that instead of patching the velocity and pressure instead the Laplace equation is solved for both the velocity potential and for the pressure; other variables such as turbulent kinetic energy are patched (Ansys, 2011).

All derived properties are calculated before solving the momentum equations. Pressure gradients are required when solving the momentum equations 3.2 and in the case of compressible flows the pressure can be calculated by applying an equation of state to the density field obtained from the continuity equation. For incompressible flows the density is constant and thus a different method is required; a solution can be to couple the pressure to the velocity from which a pressure correction equation can be derived which when solved satisfies the continuity equation. One such pressure-velocity coupling methods is the SIMPLE method (section A.1). Then, depending on which method is used, the momentum and pressure correction equations are solved either sequentially (segregated method, figure 5.2) or at the same time (coupled method). Then the mass fluxes at the faces are updated, after which the other transport equations, such as turbulent kinetic energy or dissipation, are handled.

For transient simulations the scheme in figure 5.2 is modified such that if convergence is achieved for the current time, the time is advanced.

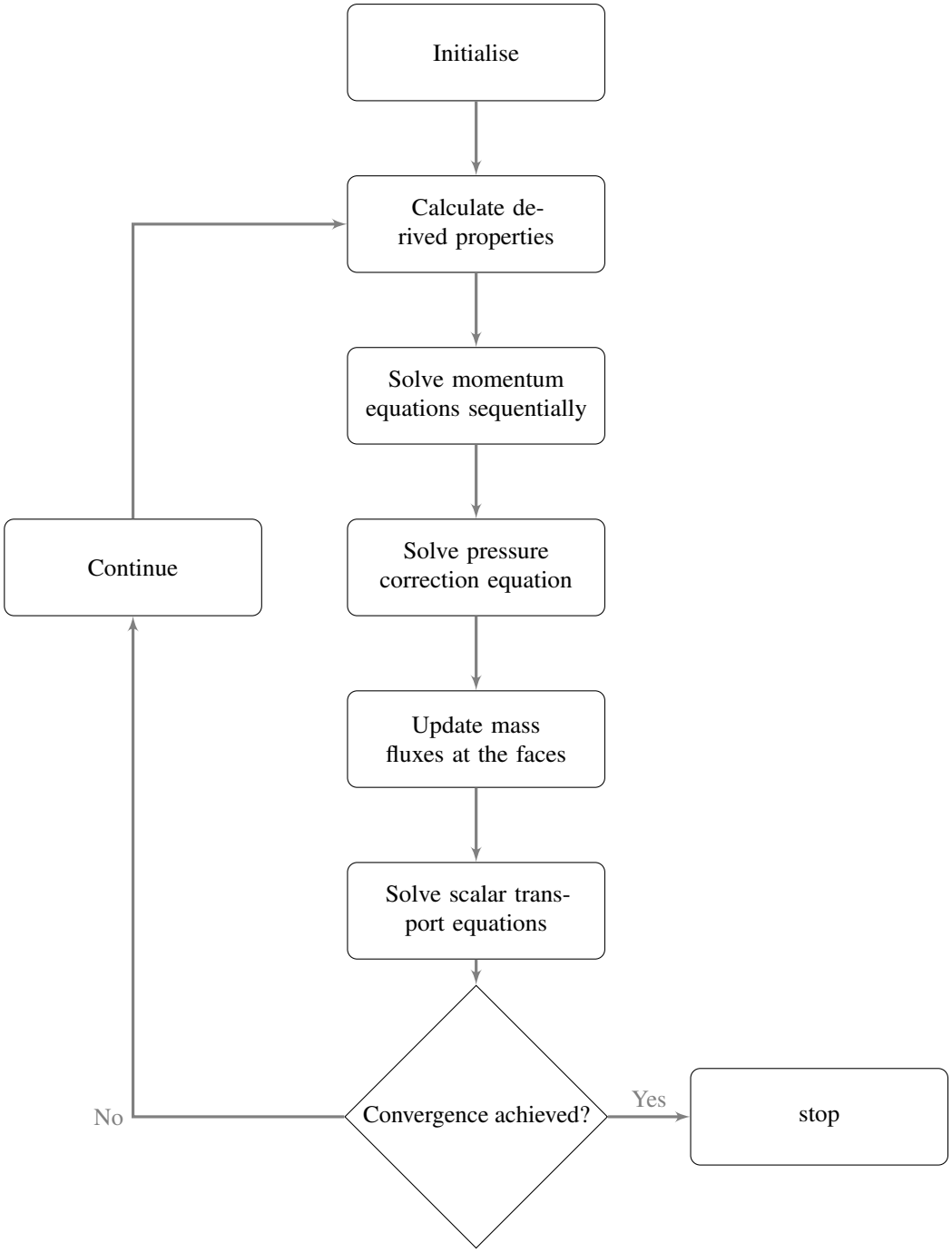

Figure 5.2: Pressure-based segregated solver algorithm.

Chapter 6

Drug Delivery in 90 Degree Bends

6.1 Passive Particle Deposition in a Simplified Human Throat

To model particle deposition in a representation of the human throat, the geometry can be simplified to a 90° bend Breuer et al. (2006). In such simplified geometry, the particle deposition depends on several parameters: the Reynolds number based on the diameter of the tube Re_D or more precisely the Dean number $De = Re \cdot \sqrt{R_0}^{-1}$ (which is the Reynolds number scaled by one over the square root of the curvature ratio R_0) and the Stokes number. In the present chapter, the effect of the Stokes number (varied by varying the particle diameter) on particle deposition is determined and compared with previous studies by Breuer et al. (2006); Cohen Stuart (2009). To compare with the other authors, first the velocity field is compared to those simulated by Breuer et al. (2006); Cohen Stuart (2009). After a proper flow field is obtained the particles can be added. In literature and the present study particles stick to the wall on contact with the wall, the reason for this stems from the fact that the epithelial layer in the lungs have a layer of lining fluid which makes it sticky. It must be noted that Breuer et al. (2006) uses a more realistic deposition rule: particles deposit when the point particle is closer to the wall than the centroid of the first control volume. Since Fluent does not have such an option, the deposition rule used in the present study is particle entrapment of the point particle on collision with the wall.

6.1.1 Case Study Overview

The geometry is a 90° bent tube with radius $R_{tube} = 1\,cm$ and a curvature ratio of $R_0 = R_b/R_{tube} = 5.6$. The straight inlet of the bend is $2 \cdot R_{tube}$ long, the outlet is $4 \cdot R_{tube}$ long. A schematic overview can be found in figure 6.1a. The mesh, as described in chapter 5 is an O-block face mesh (figure 6.1b), swept along the tube for 260 grid points: 20 at the inlet, 200 in the bend and 40 at the extended outlet. This yields a total of 1.66 million grid cells and is the approximately the same as the mesh used by Cohen Stuart (2009).

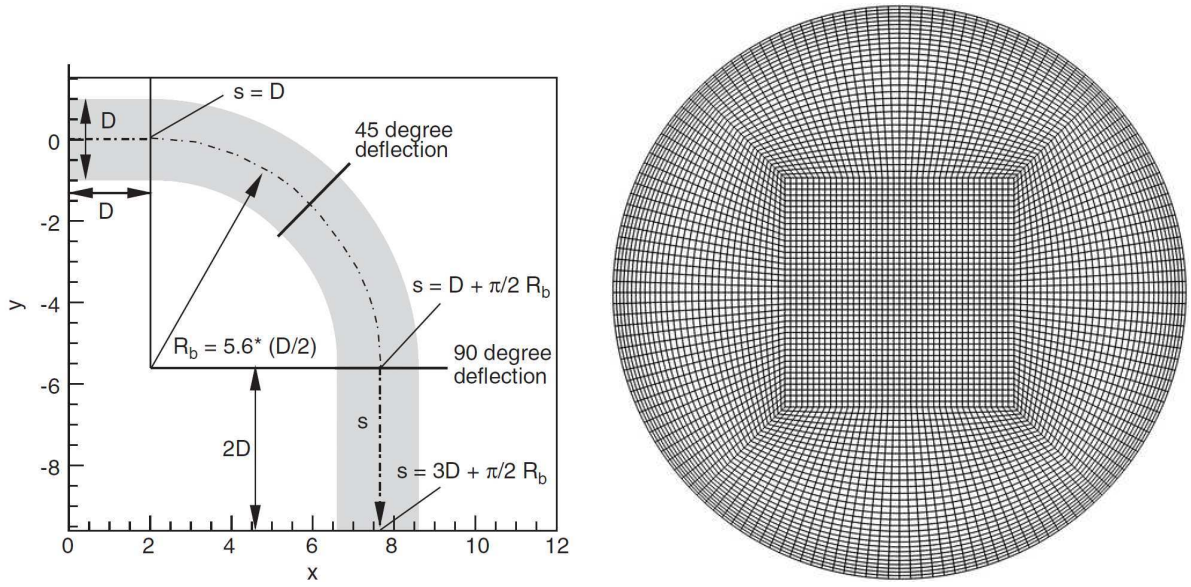

Figure 6.1: (a) Schematic drawing of the geometry non-dimensionalised by the radius of the tube (R_{tube}) (source: Breuer et al. (2006)) and (b) depiction of the face mesh.

Since this is a reproduction study the boundary conditions are taken to be the same as those from Breuer et al. (2006); Cohen Stuart (2009). For the fluid this entails a fully developed velocity profile with $Re_D = 1000$ (this yields a Dean number of $De = 423$), a no-slip condition for the fluid at the wall and an outflow boundary condition. The particles are distributed random-uniformly or deterministic-uniformly over the inlet with the same velocity as the fluid at that position and the particle trap boundary condition is used to trap the particles when they touch the wall. An overview of the parameters is given in table 6.1 below.

Table 6.1: Overview of the parameters used in the 90° bent tube simulation.

Boundary Conditions	
Inlet	Fully developed velocity profile, $Re_D = 1000$, $De_D = 423$
Wall	No-slip condition for fluid, trap condition for particles
Outlet	Outflow
Particle distribution	1:random-uniform, 2: deterministic-uniform
Fluid Properties	
Density	$1.185\,kg \cdot m^{-3}$
Dynamic viscosity	$1.82 \cdot 10^{-5} Pa \cdot s$
Particle Properties	
Density	$895\,kg \cdot m^{-3}$
Diameter	$21.8\,\mu m - 84.5\,\mu m$
St	$0.1 - 1.5$

Table 6.2: Overview of the particle forces used in this chapter.

F_d	F_g and F_b	F_m	F_{Saffman}	$F_{\text{p.grad.}}$	Turbulent Dispersion
+	-	-	-	-	-

6.1.2 Comparison of Flow Field

In this geometry the secondary velocities that originate due to centrifugal force are important for particle deposition. Thus, to qualitatively compare the flow field the streamtraces can be compared to those of Cohen Stuart (2009); Breuer et al. (2006). In figure 6.2 the streamtraces found by Breuer et al. (2006); Cohen Stuart (2009), in a 45° and 90° deflection plane respectively, are given together with the streamtraces found in the current case study. It can be seen that, qualitatively, they agree quite well.

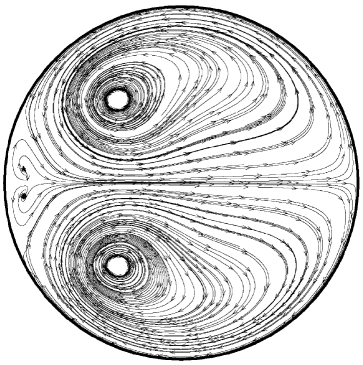

(a) Stream traces for the 45° deflection plane found by Breuer et al. (2006).

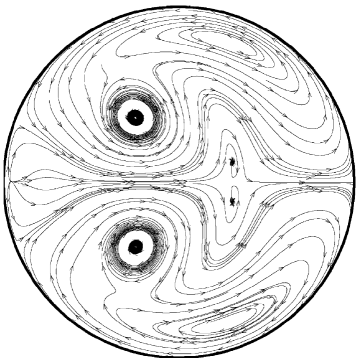

(b) Stream traces for the 90° deflection plane found by Breuer et al. (2006).

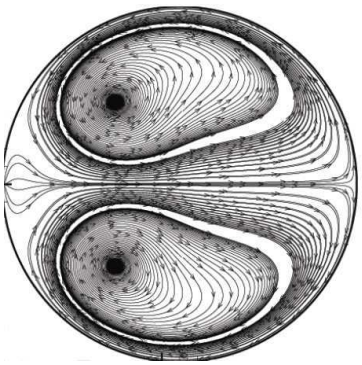

(c) Stream traces for the 45° deflection plane found by Cohen Stuart (2009).

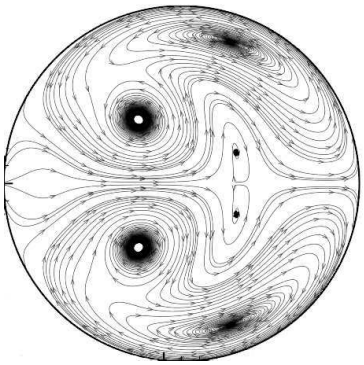

(d) Stream traces for the 90° deflection plane found by Cohen Stuart (2009).

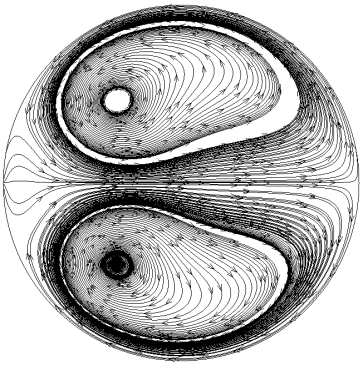

(e) Stream traces for the 45° deflection plane (present study).

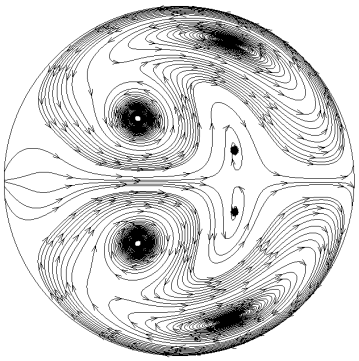

(f) Stream traces for the 90° deflection plane (present study).

Figure 6.2: Overview of the stream traces in a 45° and 90° cross-sectional deflection plane (see figure 6.1a) for the different authors: (a,b) Breuer et al. (2006), (b,c) Cohen Stuart (2009), (d,e) present study.

However, a quantitative agreement of the velocities should be obtained for higher accuracy of the deposition study therefore velocity profiles along lines in the 45 and 90 degree deflection planes are compared in figure 6.3. It can be seen that in the present study, where a second order upwinding differencing scheme is employed, the velocities show more agreement with Cohen Stuart's central differencing scheme (CDS) than his second order UDS (which was stated to be inaccurate for his case) (Cohen Stuart, 2009). Based on the agreement found with Breuer et al. (2006); Cohen Stuart (2009), the particles can be added to study the deposition in the idealised throat geometry.

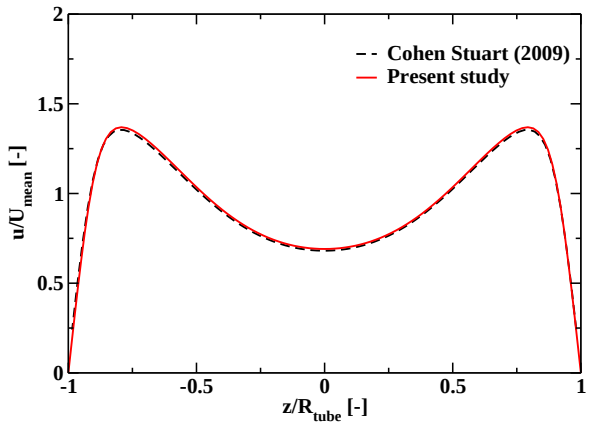

(a) Profile of the u-velocity in a 45° cross-sectional deflection plane.

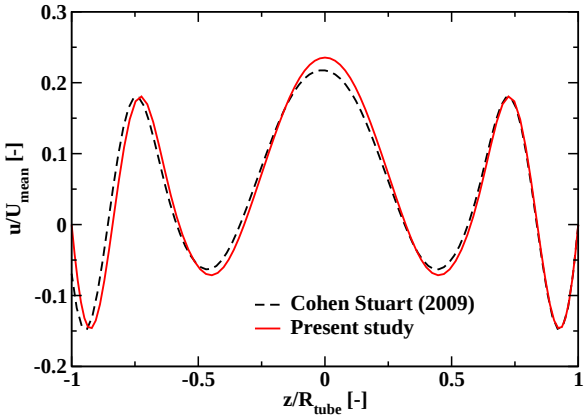

(b) Profile of the u-velocity in a 90° cross-sectional deflection plane.

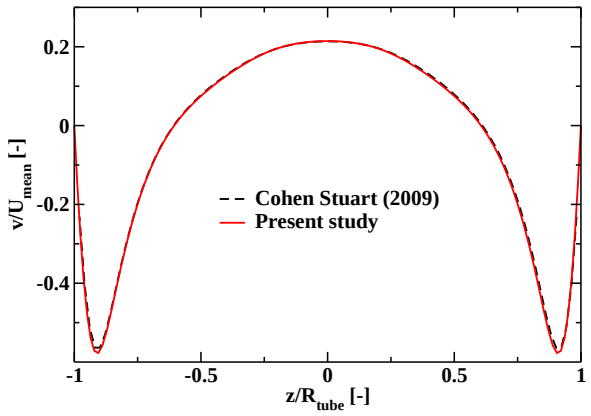

(c) Profile of the v-velocity in a 45° cross-sectional deflection plane.

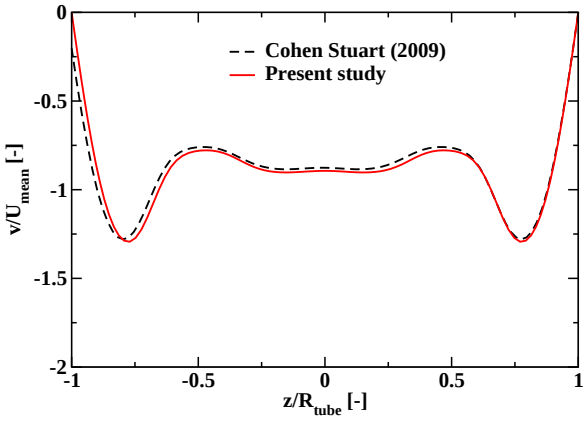

(d) Profile of the v-velocity in a 90° cross-sectional deflection plane.

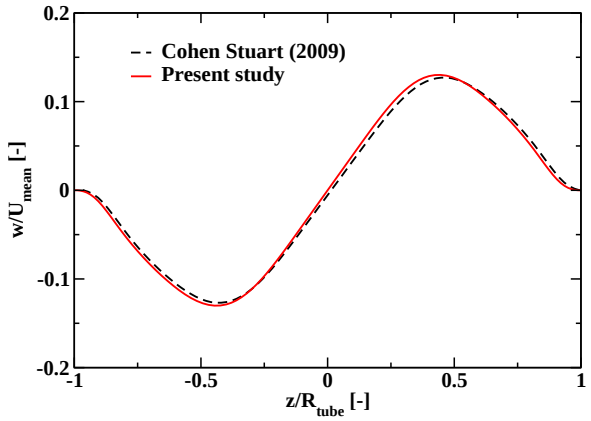

(e) Profile of the w-velocity in a 45° cross-sectional deflection plane.

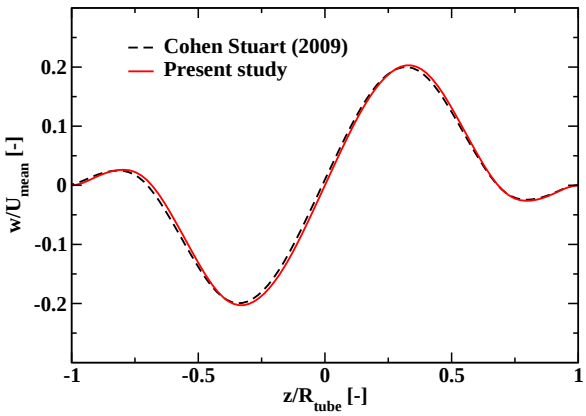

(f) Profile of the w-velocity in a 90° cross-sectional deflection plane.

Figure 6.3: Comparison of the velocity profiles obtained in the present study and those of Cohen Stuart (2009)

6.1.3 Particle Deposition

The particles used in this study have the same properties as those used by Breuer et al. (2006); Cohen Stuart (2009), the Stokes number ranges from 0.1 to 1.5 and the particle density is $\rho_p = 895\,kg \cdot m^{-3}$. Important factors to compare are not only the total deposition in the geometry but also the local deposition since deviations in local values can indicate errors in the geometry or flow field. To study the local deposition the cumulative particle deposition efficiency based on the total number of particles is plotted and compared with the results from Breuer et al. (2006) (figure 6.5a).

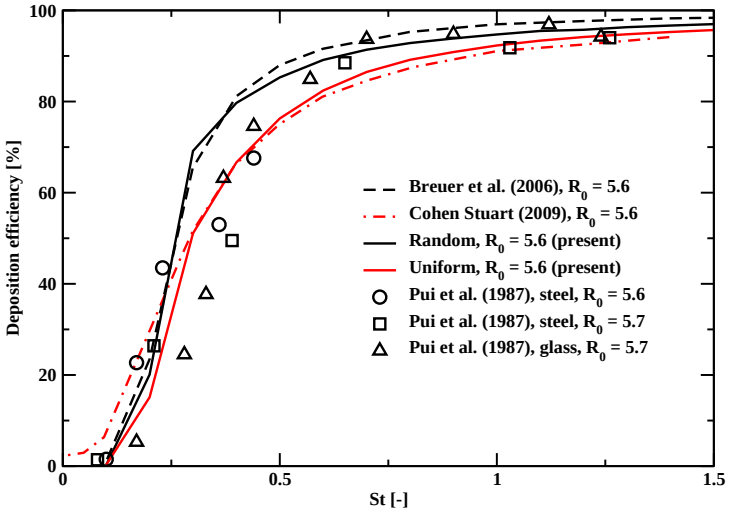

Figure 6.4: Comparison of the results obtained in the present study (with a uniform distribution and a random distribution) and the results from Pui et al. (1987); Breuer et al. (2006); Cohen Stuart (2009).

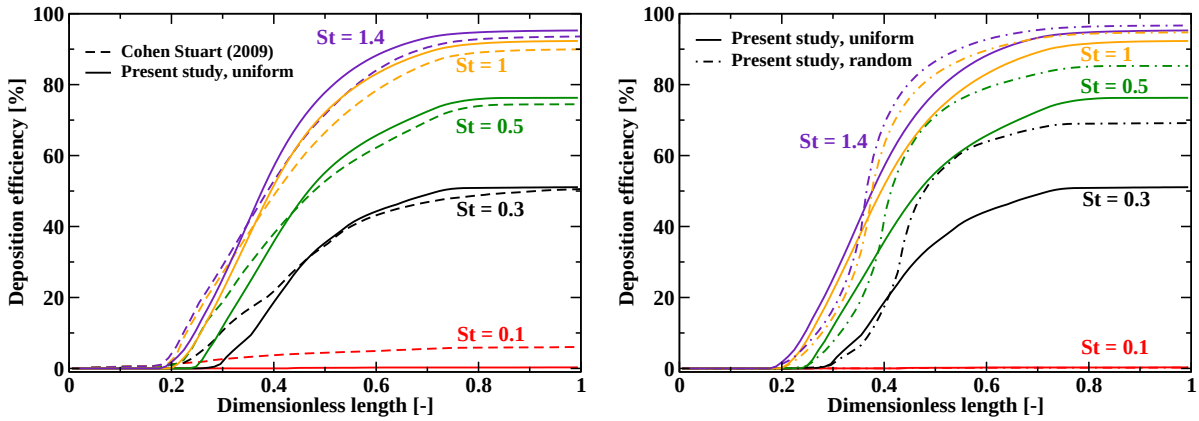

Figure 6.5: Comparison of the cumulative particle deposition as a function of the non-dimensionalised length of the tube between (a) Cohen Stuart (2009) and a uniform distribution, (b) a uniform distribution and a random distribution.

It can be seen from figure 6.4 that the total deposition for both inlet distributions is lower than found by Breuer et al. (2006), this is expected to be caused by the more realistic particle deposition rule employed by Breuer et al. (2006) (who used a random inlet distribution) because in their the particles deposit when they are further away from the wall than in the present study. Furthermore, the particle inlet distribution by Cohen Stuart (2009) was not mentioned, which was the main motivation behind performing an alternative simulation with a uniform distribution. In general what can be seen from the total deposition is that the uniform distribution has better agreement with Cohen Stuart (2009) than the random distribution while for Breuer et al. (2006) it is the other way around. Indicating that it is likely that the two others used different particle distribution profiles.

One significant difference is the particle deposition for low stokes numbers; Cohen Stuart (2009) found much higher deposition for $St = 0.1$ than all the other simulations and experiments. This may indicate a problem in his flow field, this can also be seen from the cumulative deposition where particles deposit before the bend begins and in his report are some figures which show that particles deposit right after entering the tube. Another interesting result is that the slope of the cumulative deposition curve is different for the random and uniform distributions.

6.2 Magnetically Enhanced Particle Deposition in a Simplified Artery

This case study serves as a validation of the implementation of a magnetic force acting on the particles and is a reproduction of Haverkort (2008); Cohen Stuart (2009). In contrast to the other case-studies the fluid is blood ($\mu_f = 3.5 \times 10^{-3}\, Pa \cdot s$, $\rho_f = 1000 kg \cdot m^{-3}$). This case study also has relevance towards patient specific drug delivery although is not in line with the rest of the report. It must be noted that magnetically enhanced drug delivery via the blood has been studied before and could be a powerful tool in the future to cure cancers, for example, locally(Haverkort, 2008; Cohen Stuart, 2009; Righolt, 2010). The magnetic field is generated by a straight current carrying wire which acts on ferromagnetic particles.

6.2.1 Case Study Overview

The geometry has similarities with the previous case study since the curvature ratio is the same ($R_0 = 5.6$), but features a smaller tube radius ($R_{tube} = 3.5\ mm$) moreover, the inlet and outlet extensions are both $10 \cdot R_{tube}$ long. The mean velocity entering the tube is $0.1\ m \cdot s^{-1}$ meaning that the Reynolds number is $Re = 200$ and the Dean number is $De = 84.5$. The particles are distributed uniformly along the inlet of the pipe with the same velocity as the fluid at that point. The magnetic force is caused by the magnetic field from a straight current carrying wire ($I = 1 \times 10^5\, A$), and acts on the particles with a susceptibility χ_m=3 and saturation magnetisation of $M_{sat} = 4.85 \times 10^6 A \cdot m^{-1}$. The density of these particles is 6450 $kg \cdot m^{-3}$ and the diameter is varied from 0.25 μm to 2 μm (Haverkort, 2008; Cohen Stuart, 2009). The wire is positioned such that the closest point between the wire and the centre line of the tube is 1 cm. Cohen Stuart (2009) took the particles to be below their saturation point and as such the same assumption is made in this chapter.

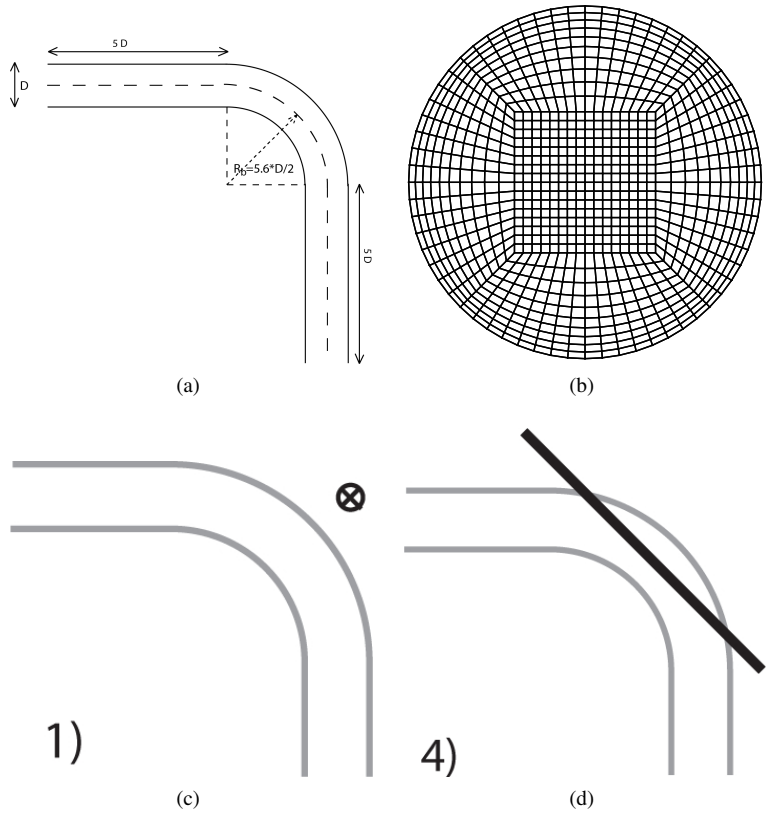

Figure 6.6: (a) Schematic drawing of the geometry and the parameters of construction (Cohen Stuart, 2009), (b) depiction of the face mesh, (c) schematic drawing of wire position 1 (Cohen Stuart, 2009), (d) schematic drawing of wire position 4 (Cohen Stuart, 2009).

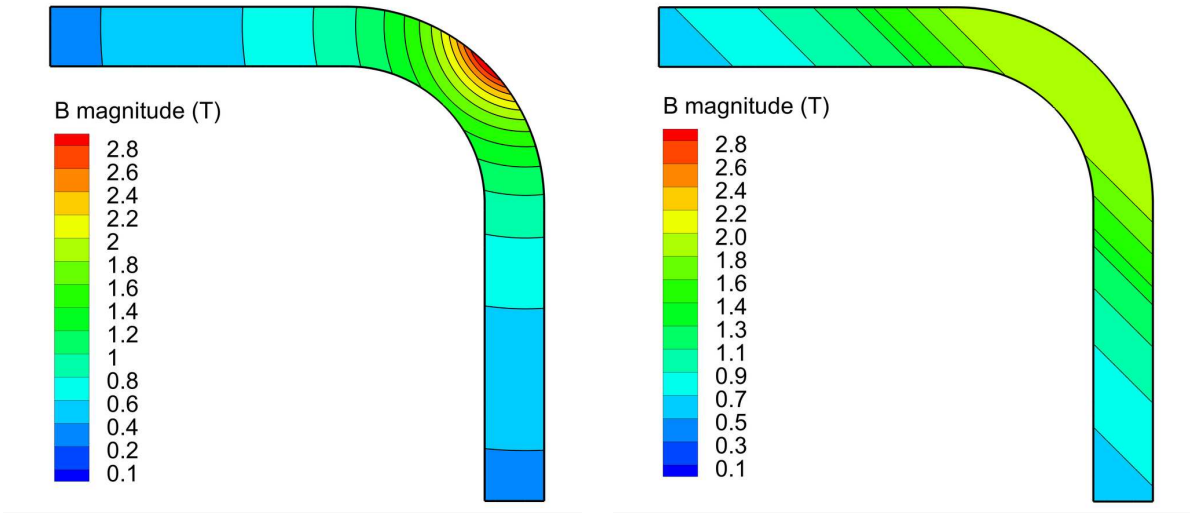

(a) (b)

Figure 6.7: Resulting magnetic field strengths for (a) wire position 1 and (b) wire position 4.

Table 6.3: Overview of the parameters used in the 90° bent tube simulation.

Boundary Conditions	
Inlet	Fully developed velocity profile, $U_m = 0.1\,m \cdot s^{-1}, Re_D = 200$, $De_D = 84.5$
Wall	No-slip condition for fluid, trap condition for particles
Outlet	Outflow
Particle distribution	Uniform
Fluid Properties	
Density, ρ_f	$1000\,kg \cdot m^{-3}$
Dynamic viscosity, μ_f	$3.5 \times 10^{-3} Pa \cdot s$
Particle Properties	
Density, ρ_p	$6450\,kg \cdot m^{-3}$
Diameter, d_p	$0.25\,\mu m - 2\,\mu m$
St	$1.8 \times 10^{-7} - 1.2 \times 10^{-5}$
Susceptibility, χ_m	3
Mnp	$5.3 \times 10^{-3} - 3.4 \times 10^{-1}$

Table 6.4: Overview of the particle forces used in this chapter.

F_d	F_g and F_b	F_m	F_{Saffman}	$F_{\text{p.grad.}}$	Turbulent Dispersion
+	-	+	-	-	-

6.2.2 Flow Field Validation

Before particle deposition can be simulated, the flow field has to be solved first. In figure 6.8 velocity profiles along three deflection planes (0°, 45°, 90°) are given. Since these velocities show good agreement with Haverkort (2008); Cohen Stuart (2009) particles can be added to study the particle deposition.

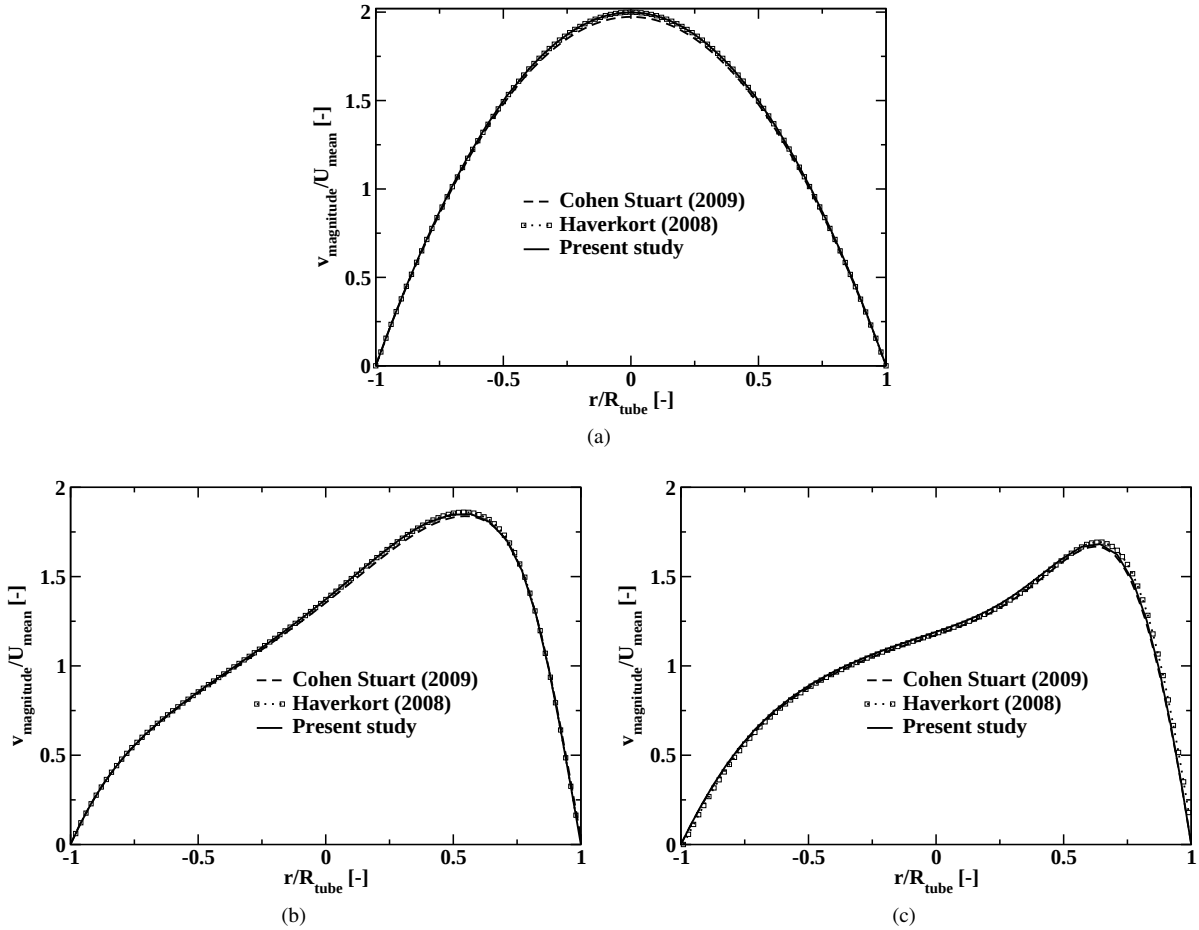

Figure 6.8: Velocity magnitude profiles in a: (a) 0° degree deflection plane, (b) 45° degree deflection plane, (c) 90° degree deflection plane.

6.2.3 Particle Deposition

Since this case study serves as a validation of the implementation of the magnetic field, and thus force on the magnetic particles, not all positions are simulated. Rather, the two most different (in cumulative deposition) positions are compared to determine the level of agreement. The positions that will be compared with those of Haverkort (2008); Cohen Stuart (2009) are without magnetic force, position 1 and position 4.

For the cases with magnetic force, the total deposition (figure 6.10)shows a good agreement with both Haverkort (2008); Cohen Stuart (2009). Not only the total deposition but also the cumulative deposition shows good agreement for the cases with magnetic force. However, without the magnetic force an error can be seen: particles deposit even though the Stokes number is very low (see table 6.3). This is the case for both the present study and the reference case. This can be due to errors in the velocity field since the mesh used in both cases is relatively coarse (compared to the first case study). It must be noted that the mesh used in the present study was modelled after the mesh displayed by Haverkort (2008). Despite the fact that the total deposition is lower, in the present study a few particles deposit before they enter the bend. This may be explained by the fact that the particles are possibly injected closer to the wall and that the particles that are already close to the wall need only a small error in the flow field to deposit. Since less than 1% of the particles deposits before the bend and the final deposition for the particles is lower than in the study by Cohen Stuart (2009), combined with the agreement of the velocity profiles

the accuracy is deemed to be close enough to the reference cases.

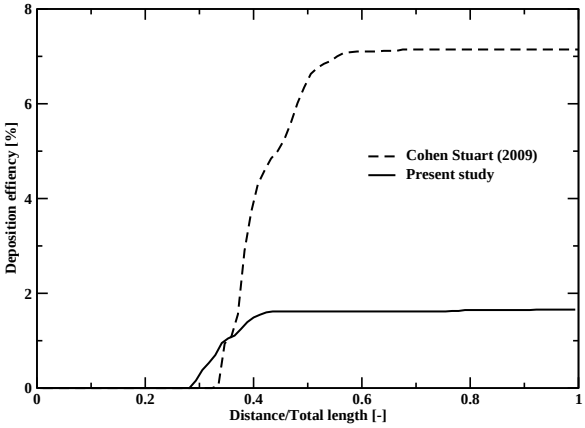

(a)

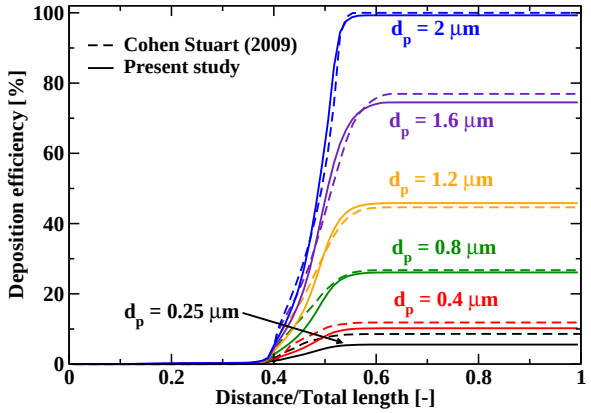

(b)

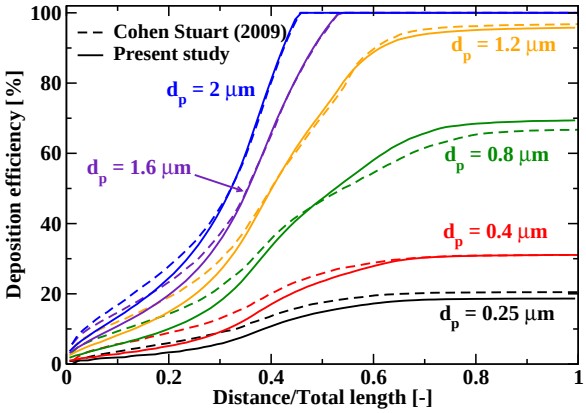

(c)

Figure 6.9: Overview of the accumulative particle deposition for the three configurations: (a) without magnetic force, (b) wire position 1, (c) wire position 4.

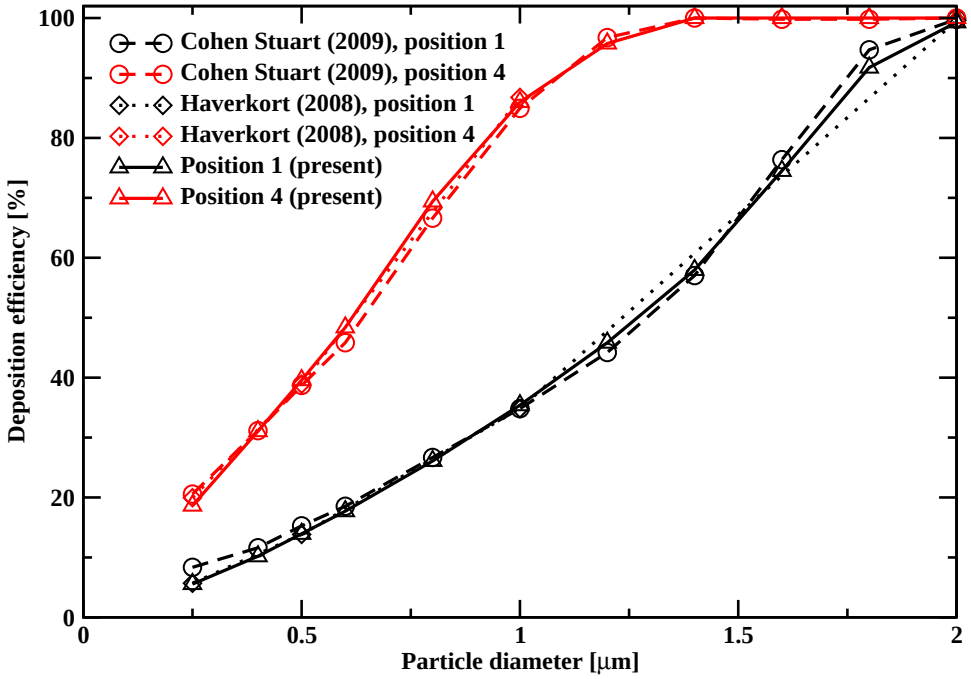

Figure 6.10: Total deposition as a function of the particle diameter.

Chapter 7

Magnetic Drug Targeting in Bifurcating Geometries

The conducting airways consists of many generations of bifurcations; fully resolving the entire conducting airways would be challenging. Not only would it require a great number of computational cells to perform the simulation, the results should be compared to experimental data. In the more distal branches the length scales are very small thus making it difficult to perform measurements here. Steering of particles in a single bifurcation with the aid of a magnetic field has been studied before (Dames et al., 2007) but not in a sequential bifurcation geometry. To assess the steerability of particles in a sequentially bifurcating geometry an idealised geometry, modelled after the third till sixth generation of the conducting airway, was used. The geometry was not identical to the reference paper in the bifurcation region and therefore the flow structures are only compared qualitatively to Zhang et al. (2001). After obtaining a converged solution, passive particle deposition was performed and compared against Zhang and Kleinstreuer (2001). Finally, the steerability of magnetic core-shell particles in a triple bifurcation geometry is assessed.

7.1 Geometry and Mesh Generation

The geometry consists of an idealised representation of three subsequent bifurcations, starting from the third generation, see figure 7.1. In this model the details necessary to describe one bifurcation are: length of the parent tube, parent diameter, diameter of the children, bend angle, bend radius, length of children tubes and the smoothing radius for carina (flow divider). The basic geometry (with a sharp carina) can be easily made in a lot of software such as Gambit and Ansys Designmodeler. A smoothed carina however is difficult to make in some software if one is limited to that software's tools. In Gambit the smoothing would be very tedious thus for smoothing of the carina geometry it is advised to perform the geometry generation in software, such as Ansys Designmodeler, where the carina can be smoothed without much effort.

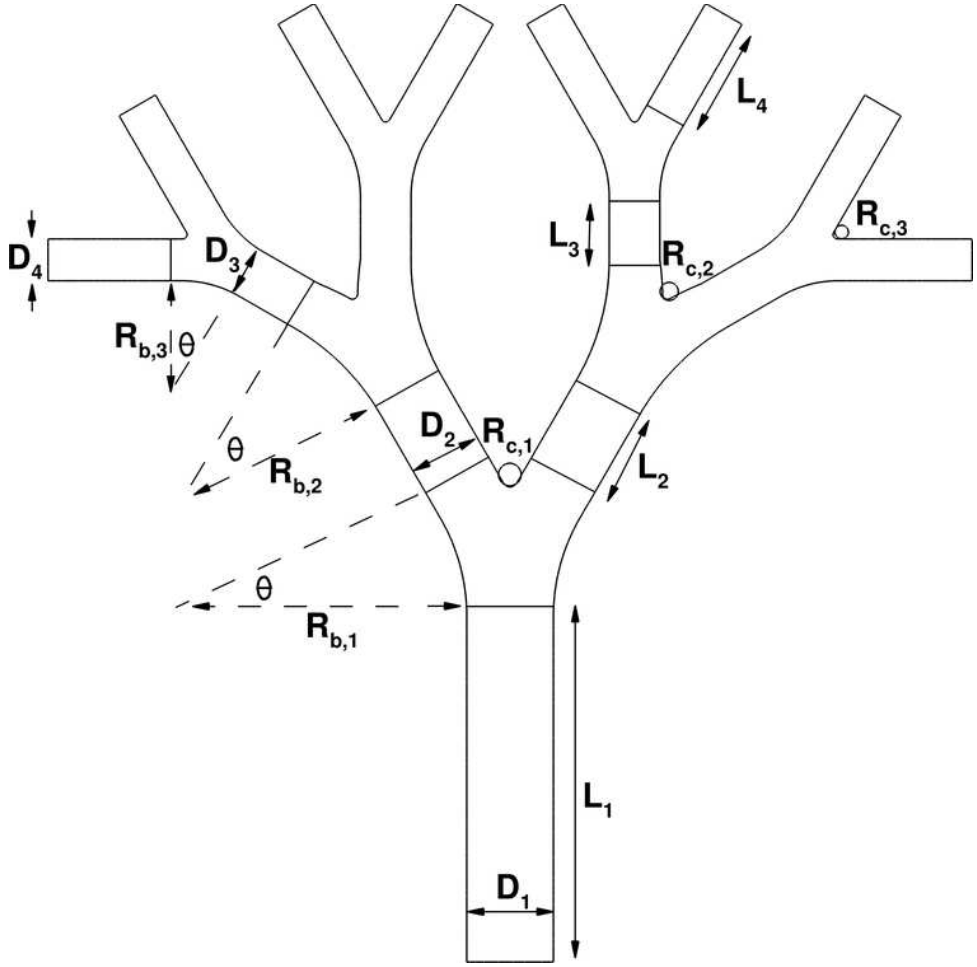

Figure 7.1: Schematic drawing of the triple bifurcation geometry along with the parameters determining the geometry, for the values of these parameters see table 7.1.

The geometry used in the present study is not identical to Zhang et al. (2001); Zhang and Kleinstreuer (2001) (see figure 7.2). With the number of parameters provided by Zhang et al. (2001) their geometry cannot be recreated and further research lead to another paper, by the same author, which showed that they indeed used more parameters (Comer et al., 2001). However, such geometry cannot easily be made in Ansys Designmodeler and therefore the bifurcation region is modelled similar to the style used by Longest and Vinchurkar (2007) (figure 7.2b, compare with figure 7.2c). Because their cross sectional area transition is different, the flow field is expected to be different but still feature some similarities. For particle deposition, since this is dependent on the velocity field, a difference is also expected.

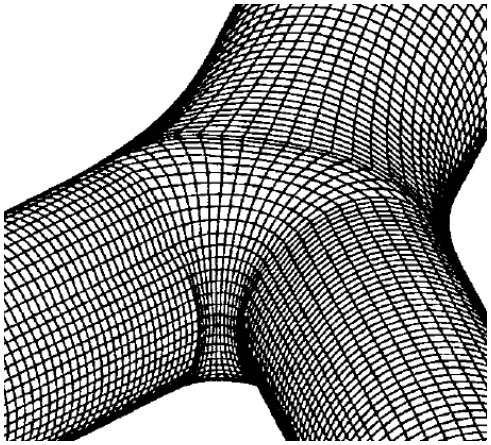

(a) Comer et al. (2001)

(b) Longest and Vinchurkar (2007)

(c) Present

Figure 7.2: (a) Mesh at the bifurcation region in the geometry by Comer et al. (2001). (b) Mesh at the bifurcation region in the geometry by Longest and Vinchurkar (2007). (c) Mesh used in the present study.

The meshing of the geometry was performed in Ansys Meshing which provides a low control but highly automated method of unstructured meshing. Since for patient specific geometry it can be very time consuming and difficult to create a structured mesh it is expected that tools which provide a more automated meshing method will be utilised for such endeavours. Very important to note here is that Zhang et al. (2001); Zhang and Kleinstreuer (2001) used a blocking grid to create a mesh consisting only of hexahedrals and thus requires much less cells to achieve similar results. Longest and Vinchurkar (2007) showed the effects of different meshing methods on the resulting flow structures and based on their results the flow structures obtained with the tetrahedral mesh employed in the current study is expected to show deviations from a hexahedral mesh if the geometry would be the same. Since the

hexahedral mesh created by Zhang et al. (2001) has a different bifurcation region further deviations are expected.

After obtaining the mesh (with roughly 3×10^6 cells), it was refined in Fluent (to roughly 6×10^6 cells) to study if the coarser grid is good enough. To compare the meshes, the cumulative deposition along a line normal to the inlet was calculated. In figure 7.3 this deposition is compared for a Stokes number of $St = 0.04$ (figure 7.3.a) and $St = 0.12$ (figure 7.3.b). Due to the level of agreement, the mesh with 3 million cells was used for the other calculations.

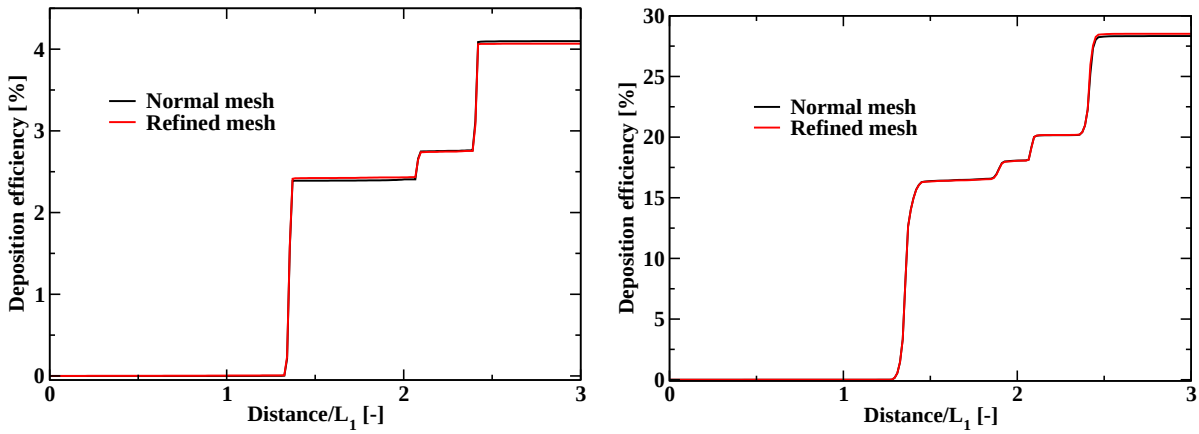

Figure 7.3: Comparison of the deposition along a line normal to the inlet for two different Stokes numbers: (a) $St = 0.04$, (b) $St = 0.12$.

Table 7.1: Overview of the geometrical parameters used to construct the geometry. All dimensions are in cm unless stated otherwise.

Bifurcation	**First**		**Second**		**Third**	
Parent tube diameter	D_1	0.6	D_2	0.5	D_3	0.35
Daughter tube diameter	D_2	0.5	D_3	0.35	D_4	0.29
Tube lengths	L_1	2.4	L_3	0.437	L_4	0.928
	L_2	0.836				
Carinal ridge radius of curvature	$R_{c,1}$	$0.1D_2$	$R_{c,2}$	$0.1D_3$	$R_{c,3}$	$0.1D_4$
Bifurcation bend radius	$R_{b,1}$	$2.7D_2$	$R_{b,2}$	$4.7D_3$	$R_{b,3}$	$2.7D_4$
Bifurcation half angle	θ 30 degrees					

7.2 Case Study Overview

Because the particle deposition is expected to differ from from Zhang et al. (2001) an additional factor, namely the type of particle distribution, is compared. Zhang and Kleinstreuer (2001) found that between a deterministic parabolic and random-uniform inlets, especially in the first bifurcation, a major difference in particle deposition is to be observed (deposition in the first bifurcation of 16.8% vs 26.76% respectively for a $St_{D1} = 0.12$). This was used to qualitatively compare the results to see if the same trend can be observed here.

The boundary conditions applied at the outlets, namely zero gauge pressure, means that, if the geometry is truly symmetrical,the flow will be divided evenly at the first flow division.

Gravity was not implemented by Zhang et al. (2001); Zhang and Kleinstreuer (2001) as the dominant deposition determining factor is inertial impaction since the local St numbers are relatively high. If another sequence of bifurcations was studied say from generation 16 till 20 then due to the huge increase of area the velocities would have dropped far enough that gravitational settling starts to dominate the inertial impaction.

To study the effect of the position of the magnetic wire, several positions along one side of the geometry were studied. Generally patients who would undergo such a magnetically enhanced drug targeting therapy suffer from terrible diseases and can be weakened by these diseases, as such preferably the patient should not undergo surgery to do this targeting and thus placing a wire in close proximity of the geometry should be avoided during actual practise. However, for educational purposes such a placement is possible in a simulation or lab experiment. A schematic drawing of the positions and the magnetic field strength are given in figure 7.4, the position, direction and current through the wire and the target magnetic field strength at the centre of the tube closest to the wire is given for each position in table 7.2.

Please note that the *St* used in the reference papers is different from the rest of the report, this was done to match the definition used by the reference papers. The St in the present chapter is defined as (in the other chapters R is used instead of D):

$$St = \frac{\rho_p d_p^2 U_m}{18 \mu_f D_1} \tag{7.1}$$

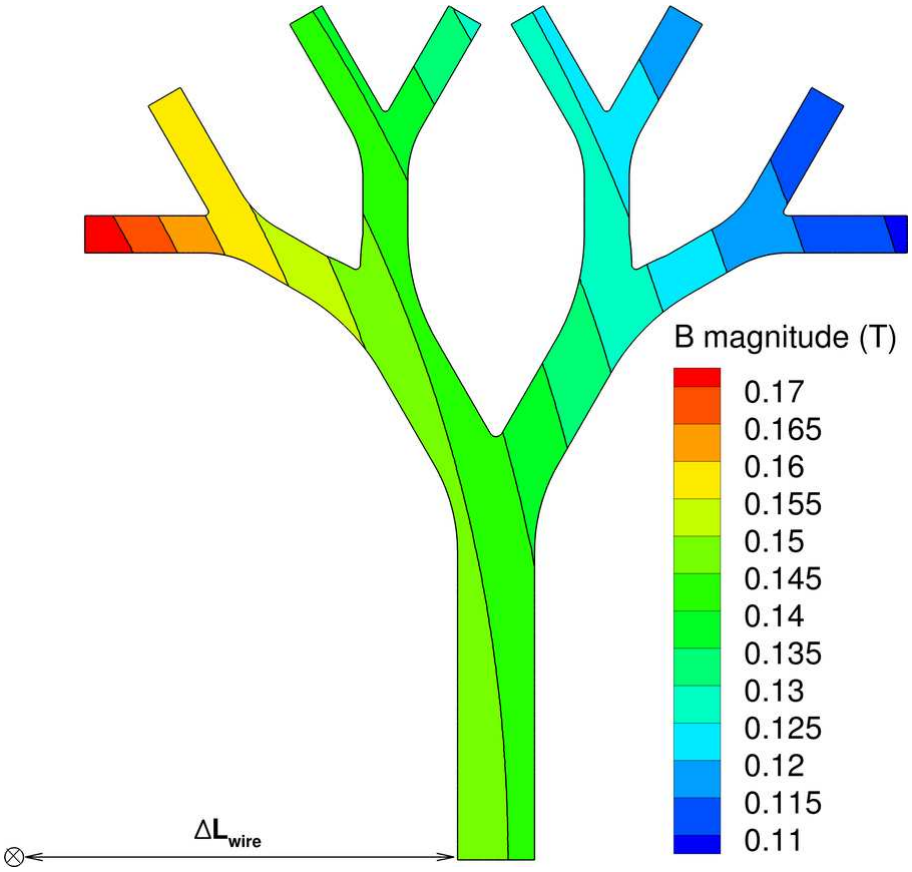

Figure 7.4: Overview of the magnetic field strength for a current of $8.55 \times 10^4 A$ through a wire positioned at distance $\Delta L_{wire} = 11.4cm$ from the leftmost side of the inlet and pointing into the paper. Note that the position of the wire has not been drawn to scale and that the side where the magnetic wire is positioned is called the left side.

Table 7.2: Overview of the parameters used in the triple bifurcation case study.

Boundary Conditions	
Inlet	Fully developed velocity profile, $Re_{D_1} = 500$
Wall	No-slip condition for fluid, trap condition for particles
Outlet	Zero gauge pressure
Particle distribution	Deterministic parabolic, random-uniform
Fluid Properties	
Density, ρ_f	$1.185\,kg \cdot m^{-3}$
Dynamic viscosity, μ_f	$1.82 \times 10^{-5}\,Pa \cdot s$
Particle Properties	
Combined density, ρ_p	$3413\,kg \cdot m^{-3}$
Diameter, d_p	$3\,\mu m - 7.35\,\mu m$
magnetic core diameter ratio, d^*_{mp}	0.836
St	$0.1 - 0.12$
Susceptibility, χ_m	3
Saturation magnetisation, M_{sat}	$3.9 \times 10^5 A \cdot m^{-1}$
Mnp	$4 \times 10^{-5} - 5 \times 10^{-2}$

Table 7.3: Overview of the particle forces used in this chapter.

F_d	F_g and F_b	F_m	F_{Saffman}	$F_{\text{p.grad.}}$	Turbulent Dispersion
+	-	+	-	-	-

7.3 Flow Field

To get a rough comparison of the velocities throughout the domain, the scaled velocity magnitude in the mid plane is given in figure 7.5 together with the axial velocity contours reported by Zhang et al. (2001) in figure 7.5b. It must be noted that they divided the geometry into its constituent bifurcations and applied a local coordinate system for each. Similar patterns are observed in each of the figures indicating that the qualitative behaviour of the triple bifurcation system is captured in the geometry used in the present study.

However, since the geometry is not the same (the bifurcation region is modelled differently) the velocities in several planes are compared. Axial velocity contours and secondary velocity plots are obtained at stations 1, 2, 4 and 6 and compared with those obtain by Zhang et al. (2001) in figures 7.6 and 7.7. A qualitative agreement of the presence of secondary velocities is obtained, and the axial velocity contours show some agreement. However, there are certainly differences present which can be attributed to two factors previously described in section 7.2: the geometrical difference in the bifurcation region and the difference in meshing method. Based on these figures, adding particles in a similar fashion to the reference paper, observed deposition should show similarities but will not be the same since inertial impaction is the mechanism by which the particle deposit, and the velocity fields are not identical.

A small additional study was preformed in a double bifurcation geometry after Longest and Vinchurkar (2007) which featured the same bifurcation style as used in the present study. In the double bifurcation case study the Re=1780 and only St=0.25 was used to study the deposition. A fully developed velocity profile was prescribed at the inlet and particles were distributed using a deterministic parabolic distribution. The full overview of this study can be found in chapter B.

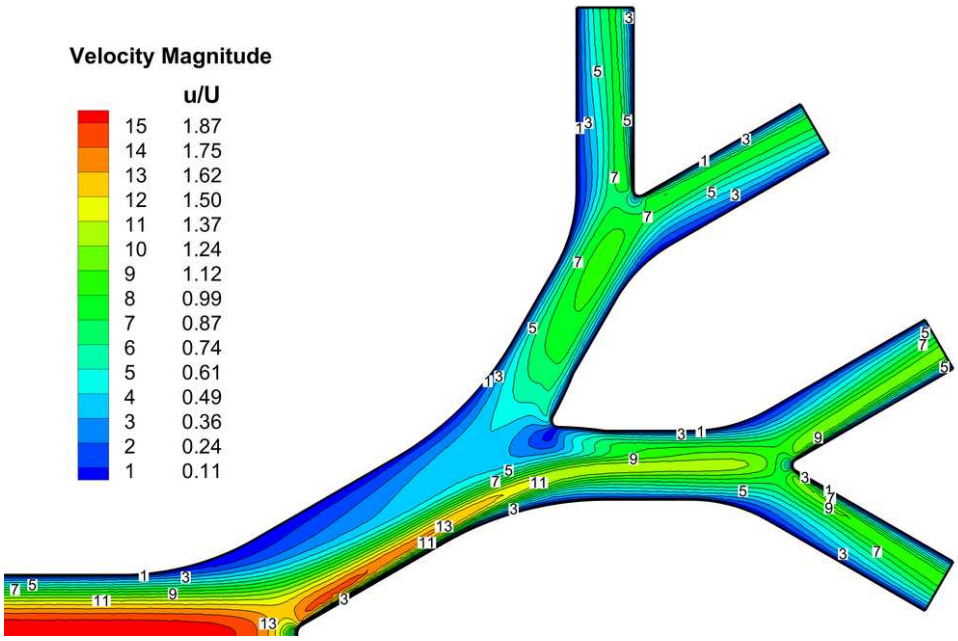

(a) Present Study

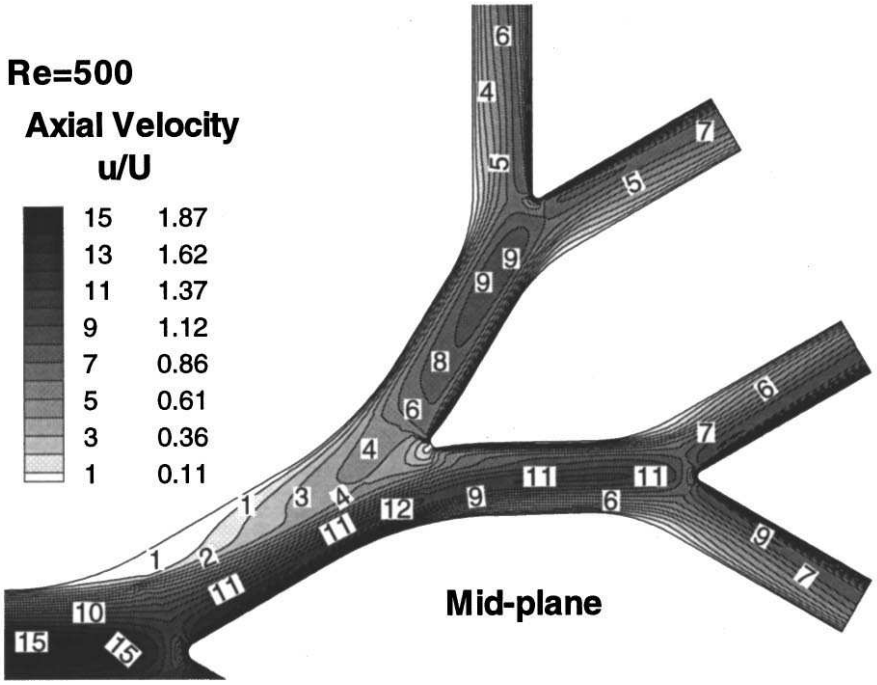

(b) Zhang et al. (2001)

Figure 7.5: (a) Contours of velocity magnitude in one half of the mid plane of the triple bifurcation system, (b) contours of axial velocity found by Zhang et al. (2001) note that they used a local coordinate system for each bifurcation.

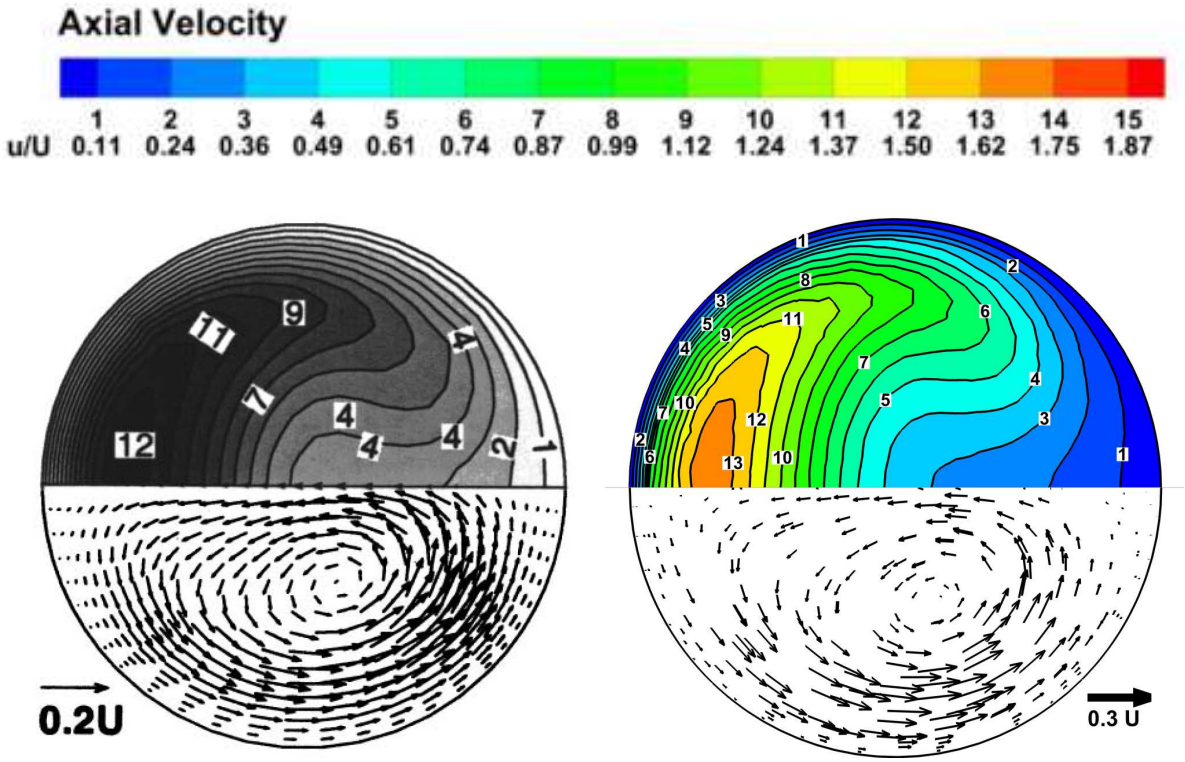

(a) Axial velocity contour and secondary velocity plot for station 1 from Zhang et al. (2001).

(b) Axial velocity contour and secondary velocity plot for station 1.

(c) Axial velocity contour and secondary velocity plot for station 2 from Zhang et al. (2001).

(d) Axial velocity contour and secondary velocity plot for station 2.

Figure 7.6: Flow field panel

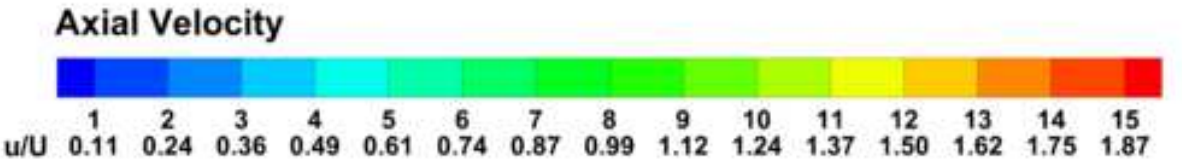

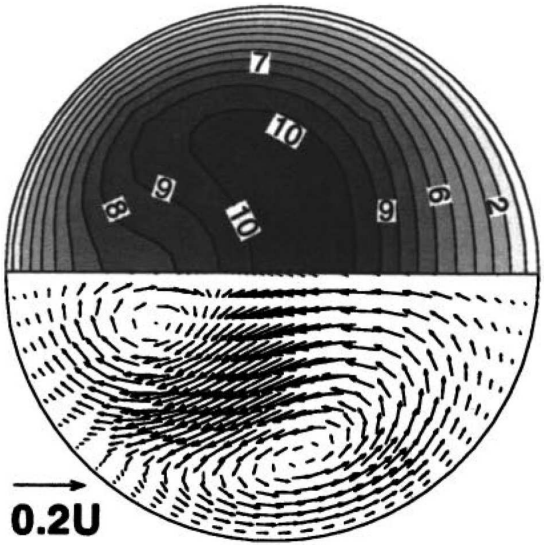

(a) Axial velocity contour and secondary velocity plot for station 4 from Zhang et al. (2001).

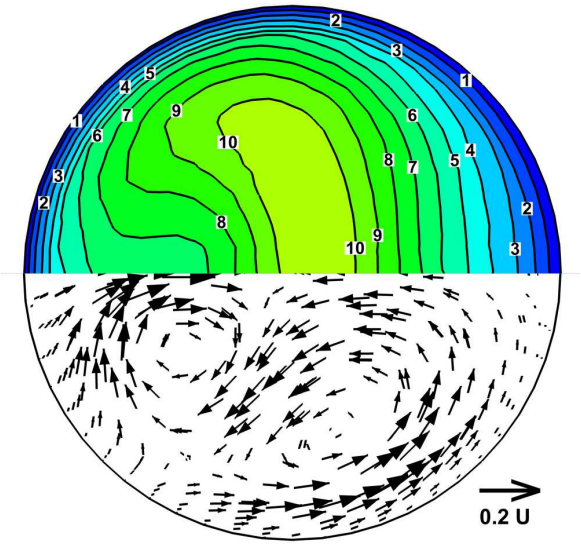

(b) Axial velocity contour and secondary velocity plot for station 4.

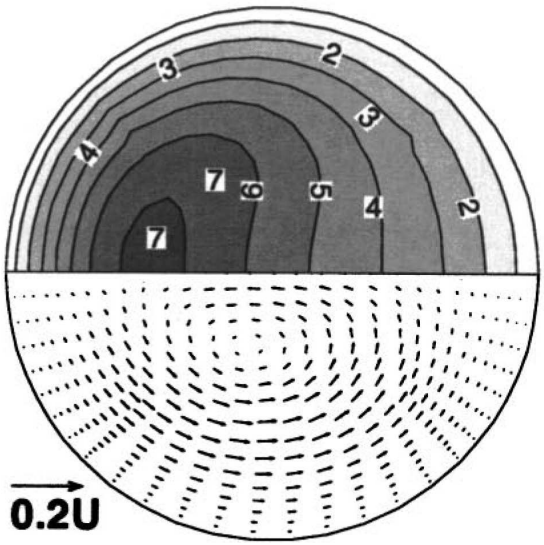

(c) Axial velocity contour and secondary velocity plot for station 6 from Zhang et al. (2001).

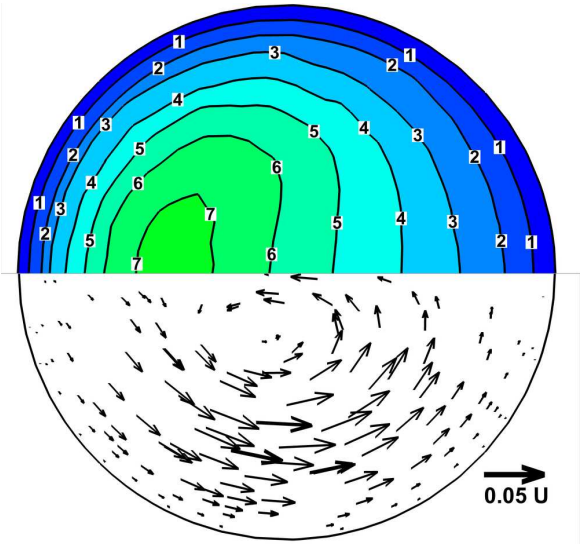

(d) Axial velocity contour and secondary velocity plot for station 6.

Figure 7.7: Flow field panel

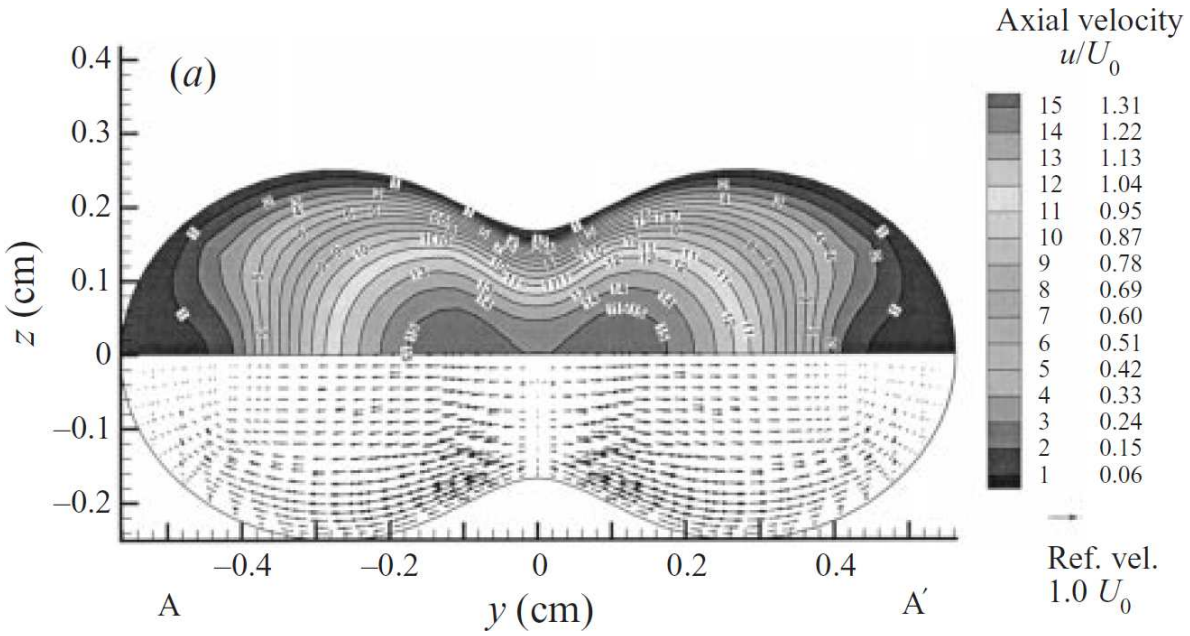

(a) Comer et al. (2001)

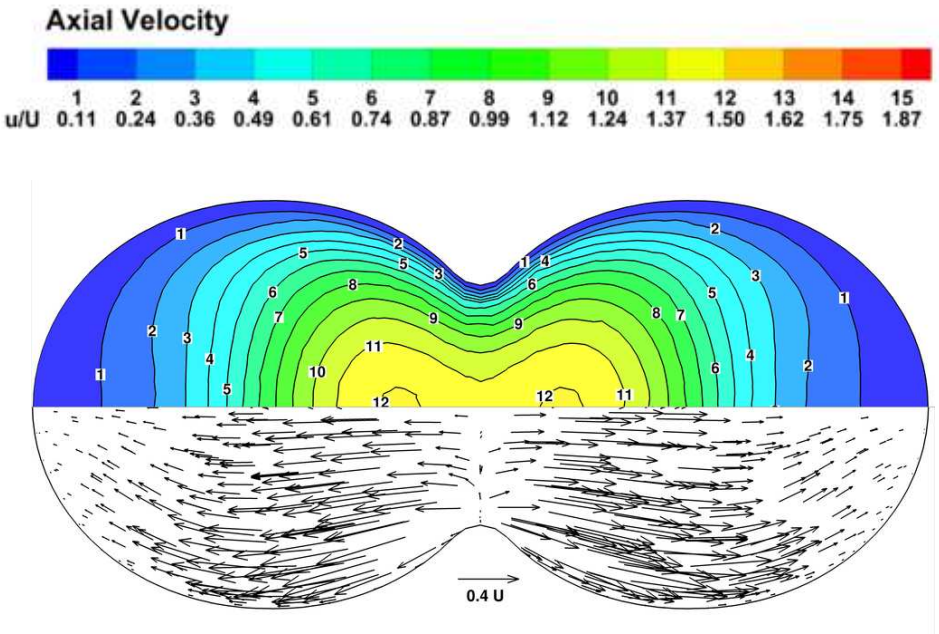

(b) Present

Figure 7.8: Velocity magnitude and vectors in a cross-section in the region of the first bifurcation. (a) Comer et al. (2001).

7.4 Particle Deposition Without Magnetic Force

Before a magnetic force is implemented and applied on the particles a baseline should be made so that the effects of magnetic force can be compared. Nevertheless, this also serves as a piece of the validation: as seen in the previous section the particle deposition is expected to be similar to some extent. Furthermore, to observe the effect of particle distribution at the inlet two different particle distributions are employed for this case.

It can be seen from table 7.4 and figure 7.9 that the deposition profiles between the present report and the reference paper (Zhang and Kleinstreuer, 2001) do not match well. In the first bifurcation the deposition shows agreement in the deposition efficiencies, this is further strengthened by the fact that a similar behaviour is observed

Table 7.4: Overview of the local deposition efficiency for St = 0.04 and St = 0.12 and for the two inlet distributions

Bifurcation	**Inlet Distribution**	**St = 0.04**		**St = 0.12**	
		Present	**Zhang and Kleinstreuer (2001)**	**Present**	**Zhang and Kleinstreuer (2001)**
First Bifurcation	Deterministic Parabolic	2.39	4.13	16.42	16.80
	Random Uniform	7.53	9.52	26.18	25.76
Second Bifurcation	Deterministic Parabolic	0.01	0.85	1.93	4.77
	Random Uniform	0.03	0.66	2.04	5.06
Upper Third Bifurcation	Deterministic Parabolic	0.90	1.25	6.96	5.41
	Random Uniform	0.89	1.44	8.42	5.73
Lower Third Bifurcation	Deterministic Parabolic	2.37	4.58	15.66	15.23
	Random Uniform	2.02	3.27	17.82	12.89

between a deterministic-parabolic and a random-uniform particle inlet distribution. The agreement in the first generation may be explained by the fact that the velocity profile just upstream of the bifurcation is the same between the present and reference case, but due to the difference in the bifurcation region the velocity profile downstream of the first bifurcation is different. The velocity profile in the first bifurcation is different, but due to a non-zero particle relaxation time the particles with St=0.12, for the most part, remain relatively unaffected by this change in velocity profile compared to the velocity profile just upstream.

It was not expected by the author to observe such a significant difference in the second generation. Another particle deposition study, albeit very short, was performed with a double bifurcation geometry which used a similar bifurcation geometry as used here (see chapter B for full details). In that particular geometry modelled after Longest and Vinchurkar (2007), the local deposition efficiency along a line normal to the inlet the agreement is much closer, see figure 7.10, suggesting that the bifurcation region may have a significant impact on the particle deposition.

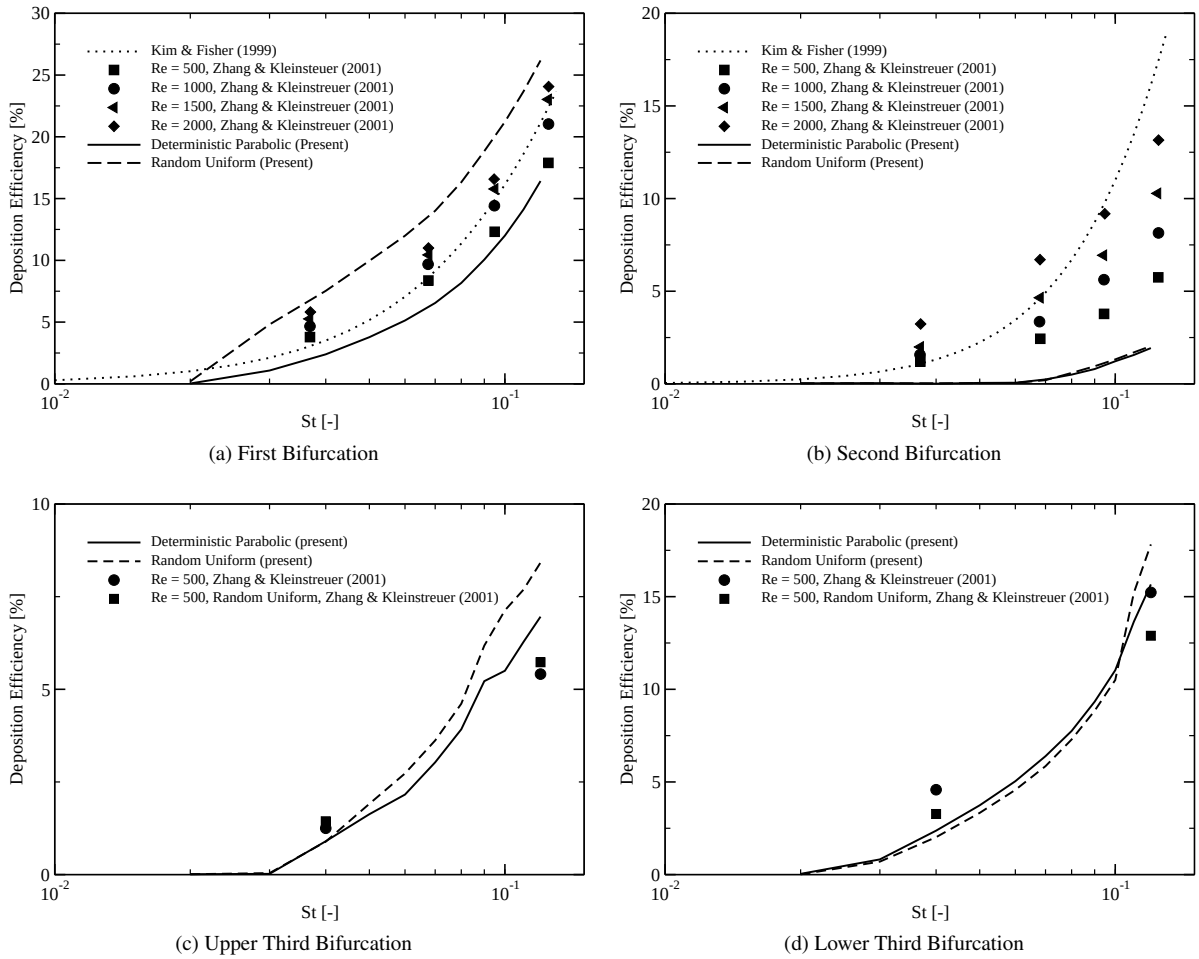

(a) First Bifurcation

(b) Second Bifurcation

(c) Upper Third Bifurcation

(d) Lower Third Bifurcation

Figure 7.9: Comparison of the particle depositions as a function of St in: (a) first bifurcation, (b) second bifurcation, (c) upper third bifurcation and (d) lower third bifurcation. Note that the data from Zhang and Kleinstreuer (2001) is based on a deterministic parabolic distribution unless specified otherwise.

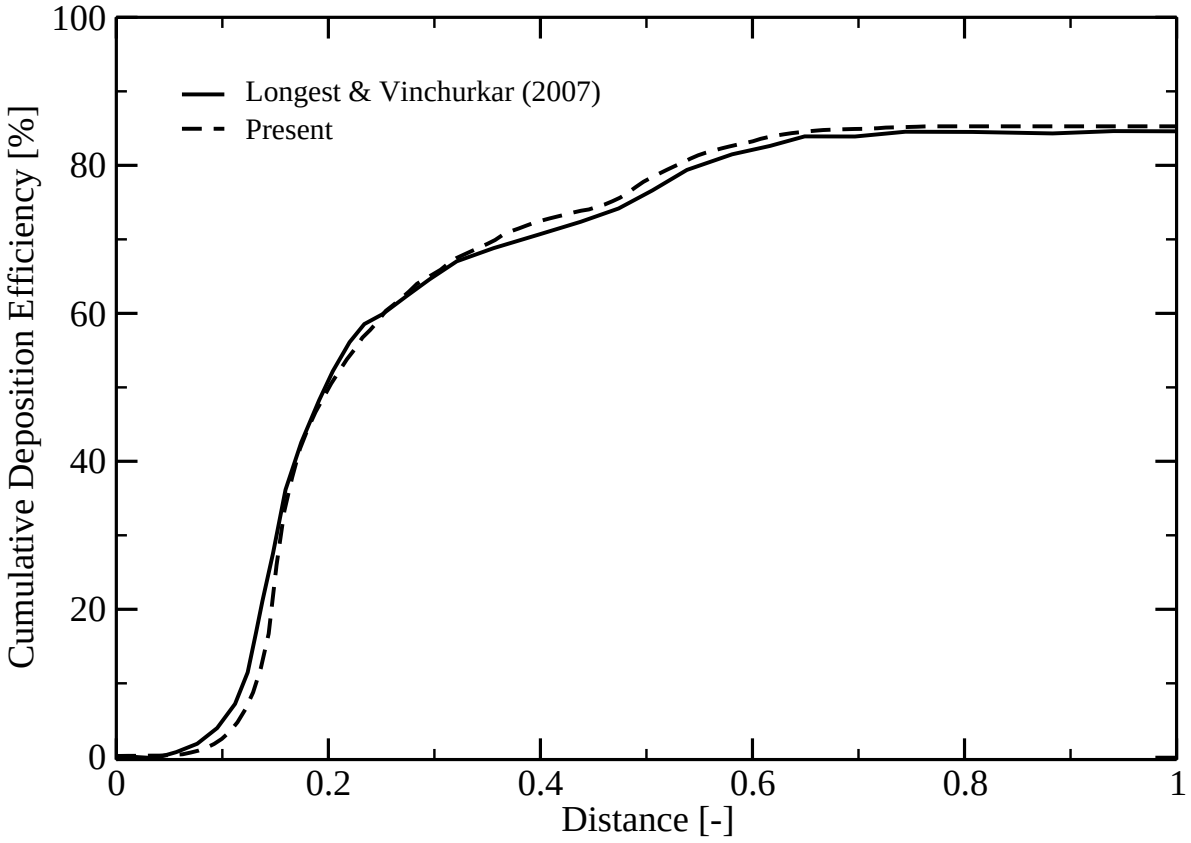

Figure 7.10: Comparison of cumulative particle deposition in a double bifurcation geometry between results found in chapter B and Longest and Vinchurkar (2007).

7.5 Magnetically Enhanced Particle Deposition

For the set of simulations with a magnetic force, the composition of the core-shell particles were set such that the total density is equal to the density of the previous section. The required diameter fraction of the magnetic core to total particle is $d^*_{mp} = 0.836$. The drug loading, as mentioned in section 4.11, is taken to be 30% by mass. In this set of simulations the magnetic field strength was varied to study the effect on the 'directability' of the bulk of the particles. The particle inlet distribution used in this section is deterministic parabolic and the wire position was kept constant; only the total particle diameter and the current were varied.

There are several methods to determine the steerability of the particles, one method is to only look the particles leaving the domain on the left or right side the second method is to also take into account the particles which already deposited in the left or right part. The ratio based on the first method is dubbed the penetration steering factor SF_{pen} (equation 7.2), the second is called the steering factor left SF_L (equation 7.3) after the location of the wire. Thus with the wire placed on the left side the SF_L is expected to become larger while this is not necessarily true for the SF_{pen} . It must be noted that the first bifurcation is not taken into consideration in the calculation of the SF_L .

$$SF_{pen} = \frac{Np_{left,escape}}{Np_{right,escape}} \tag{7.2}$$

$$SF_L = \frac{Np_{left,escape} + Np_{left,trapped}}{Np_{right,escape} + Np_{right,trapped}} \tag{7.3}$$

By using both the SF_{pen} and SF_L , it can be established in which manner the particle deposition behaves. If the $SF_{pen} = 0$ and $SF_L > 1$ then the particles are steered inside the domain itself but no particles remain available for deposition downstream of the geometry. And if both $SF_{pen} > 1$ and $SF_L > 1$ then the particles are steered and more particles leave the domain on the left side than on the right side. In the case of cancerous tissue only being present in the left side of the actual geometry then the preferred values are $SF_{pen} = 0$ and $SF_L > 1$, for establishing the best

method of steering the particles towards a location of the lung not present in the geometry then it is preferred to maximise the SF_{pen} and SF_L .

Under the presence of a magnetic field the deposition of the magnetic core-shell particles can be greatly increased (figure 7.11). In addition to the increased particle deposition a steering effect was observed: the particles are steered towards the wire location (left side) while also increasing the number of particles leaving the left side of the domain relative to the right side (figures 7.12 and 7.13). The SF_{pen} and SF_L series without magnetic force show that the particle distribution throughout the geometry is indeed symmetrical since the number of particles leaving the right and left side of the domain are practically identical. The fact that particles leave the domain indicates that the magnetic field gradient is large enough to steer the particles but not too large so that particles cannot escape the geometry. The downside of the magnetically enhanced drug delivery can be seen by looking at both the total deposition efficiency and SF_{pen} and/or SF_L : the increased steering comes at a cost of a significantly increased particle deposition. If the goal were to have particle penetrate primarily the left side of the geometry, a huge fraction of the particles would be filtered out. Clearly, for such purposes the present magnetic field is not optimal.

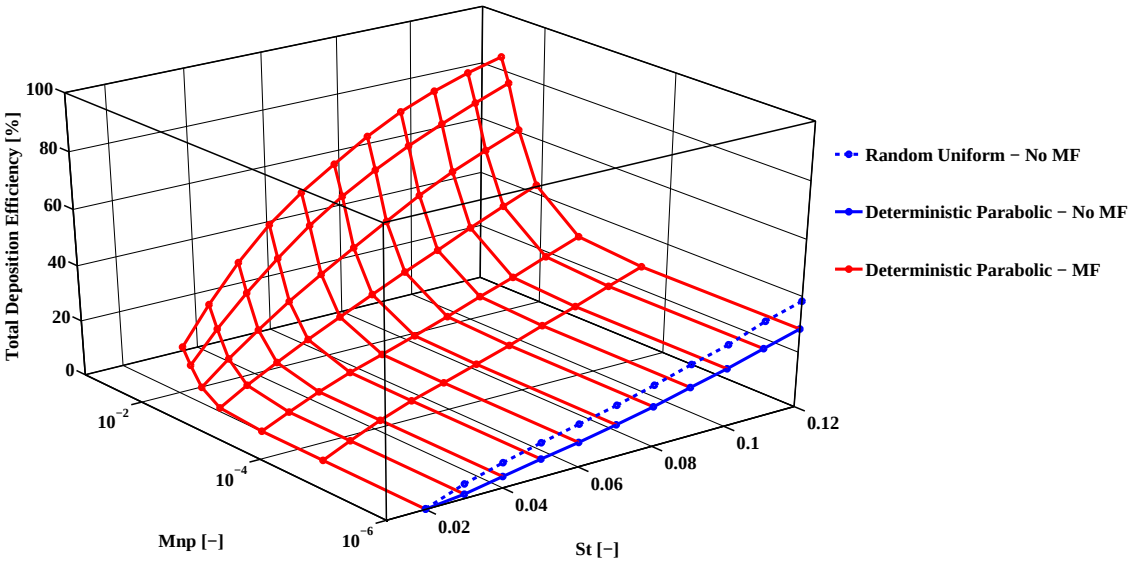

Figure 7.11: Total deposition efficiency, as a function of St and Mnp, in the triple bifurcation geometry for core-shell particles under the influence of a magnetic field.

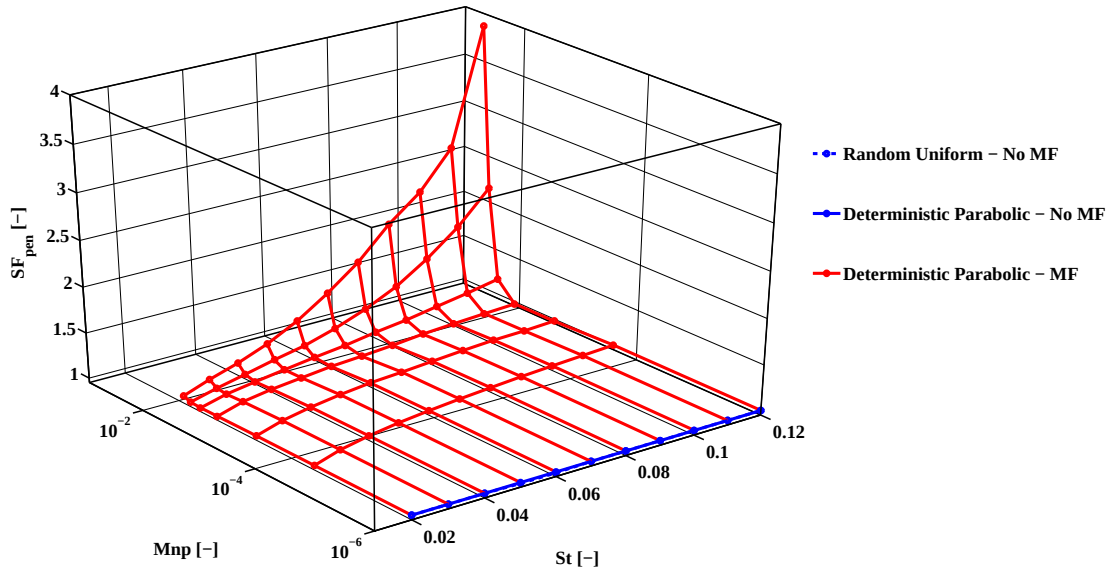

Figure 7.12: SF_{pen} as a function of both the St and Mnp.

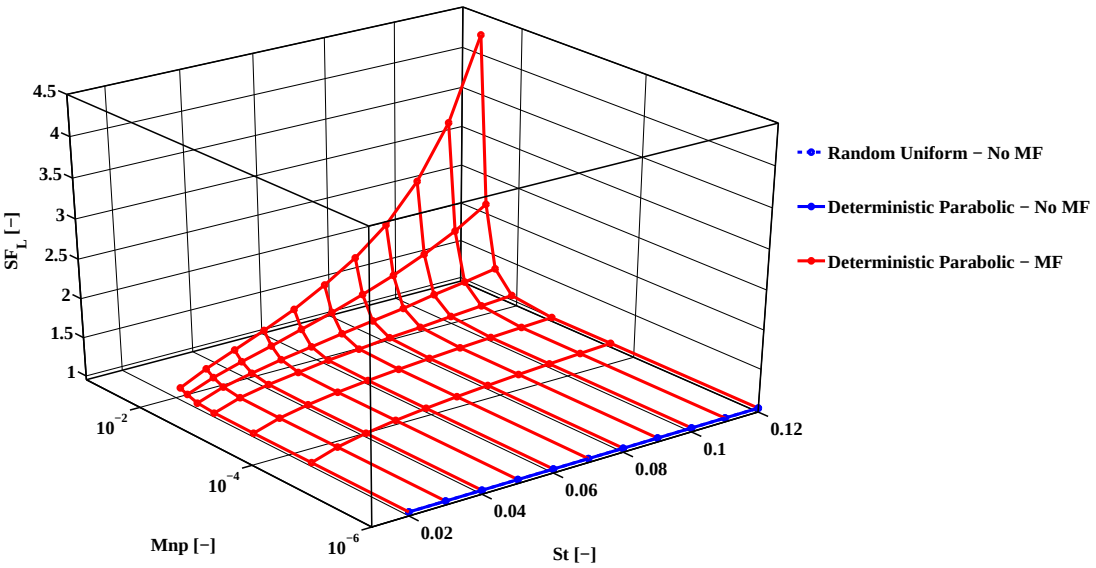

Figure 7.13: SF_L as a function of both the St and Mnp.

Chapter 8

Magnetic Drug Targeting in a Patient Specific Geometry

In light of the goal, patient specific drug delivery, a case study based on real patient geometry is performed here. First the meshing procedure is briefly described after which a short study on the grid and turbulence inlet properties is performed to establish the mesh and boundary conditions to be used in the final simulations. Then, experimental data is compared to solutions from multiple turbulence models to establish the model which captures the essences of the flow most accurately and which should be used in the particle deposition simulations. Finally, particle deposition simulations are performed for both with and without a presence of a magnetic field to see if the ratio of particles going to the left and right lung can be changed.

8.1 Mesh Generation

The geometry used is, apart from the inlet region, identical to that of Zhang et al. (2012) (Kleinstreuer et al. included the cigarette inlet), and has been obtained from Banko et al. (2014). The geometry file contained not only the airway geometry itself but also the structure necessary for the experimental set-up, see figure 8.1a. This excess geometry was removed in ICEM after which the airway geometry is revealed (figure 8.1b). Since the obtained geometry was the basis for the experimental set-up, the outlets were of course open (figure 8.1c) but for meshing purposes these have to be closed (figure 8.1d).

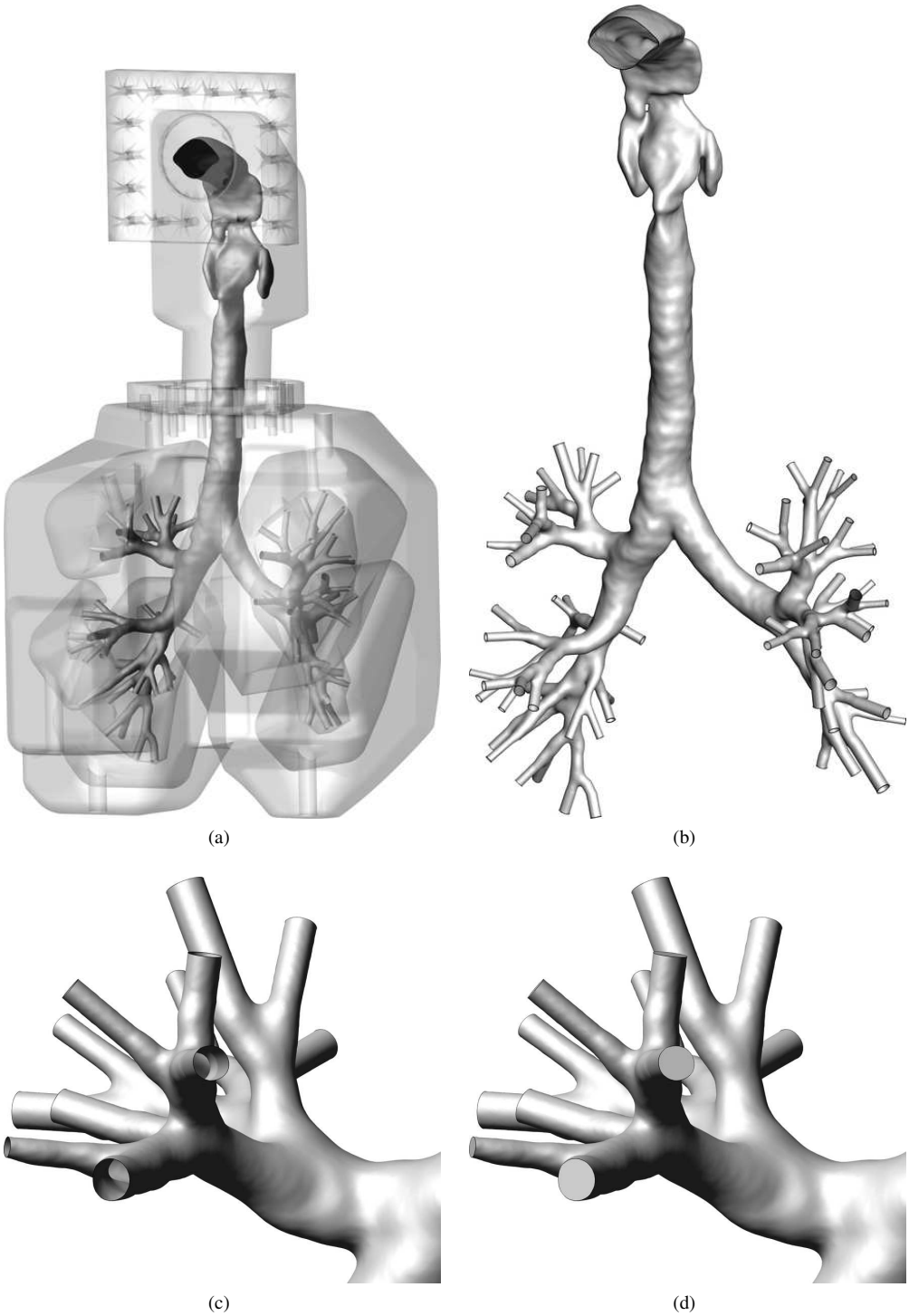

Figure 8.1: Overview of geometry preparation: (a) Geometry of the experimental set-up, (b) airway geometry, (c) close-up of the open outlets and (d) close-up of the closed outlets.

An Octree mesh was generated after closing the geometry after the preliminary mesh generation the volume elements were removed and the surface mesh was smoothed. Then, this surface mesh was extruded inwards by 5-10 layers (10 in the finest case) to create the prism boundary layer which are required to accurately model the phenomena in the boundary layers (such as flow separation). The remainder of the geometry was then filled using the Delauney meshing method. Three meshes were created, mesh A with 5 control volumes per boundary layer

(9×10^6 cells), mesh B with 10 control volumes per boundary layer (seen in figure 8.2b, 11×10^6 cells) and mesh C, which is not used in the present study, which features 10 boundary layers and a smoother transition between boundary layers and the rest of the volume with 15×10^6 cells. Mesh C was not used since ICEM crashed when checking the mesh, also an attempt was made to export an unchecked mesh (which may contain all sorts of errors) to Fluent but crashed multiple times (after a few hours).

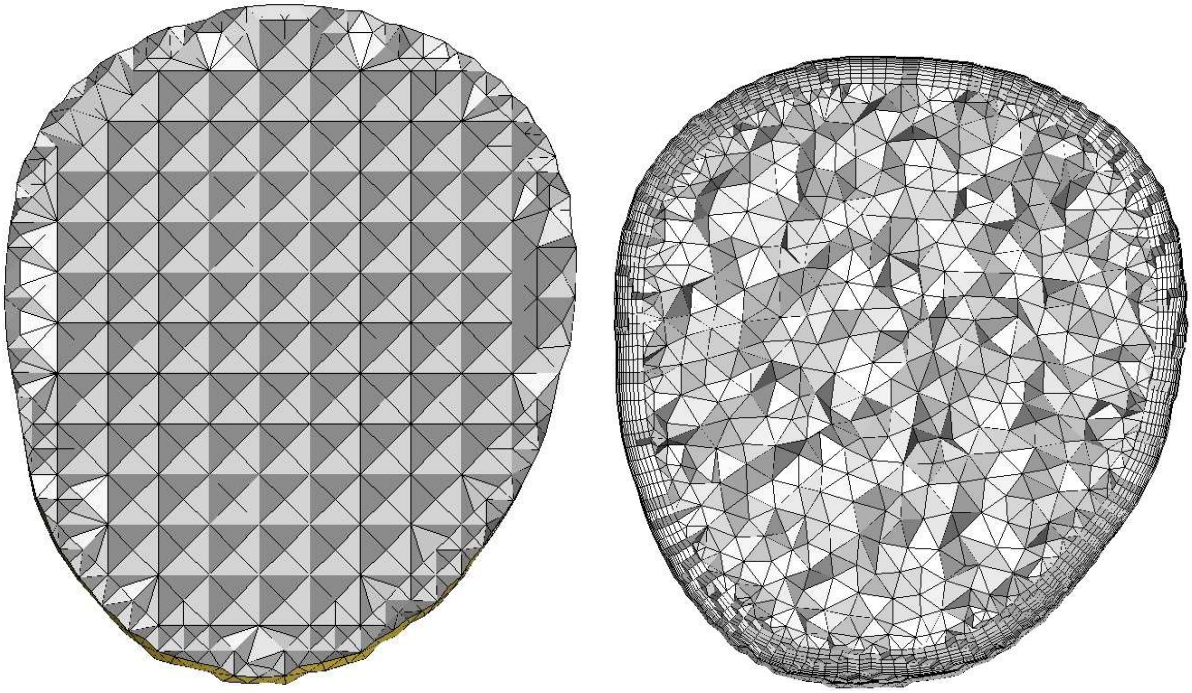

(a) (b)

Figure 8.2: Overview of the mesh throughout the meshing procedure in patient specific geometry: (a) cross section of Octree mesh, (b) cross section of final, Delauney, mesh.

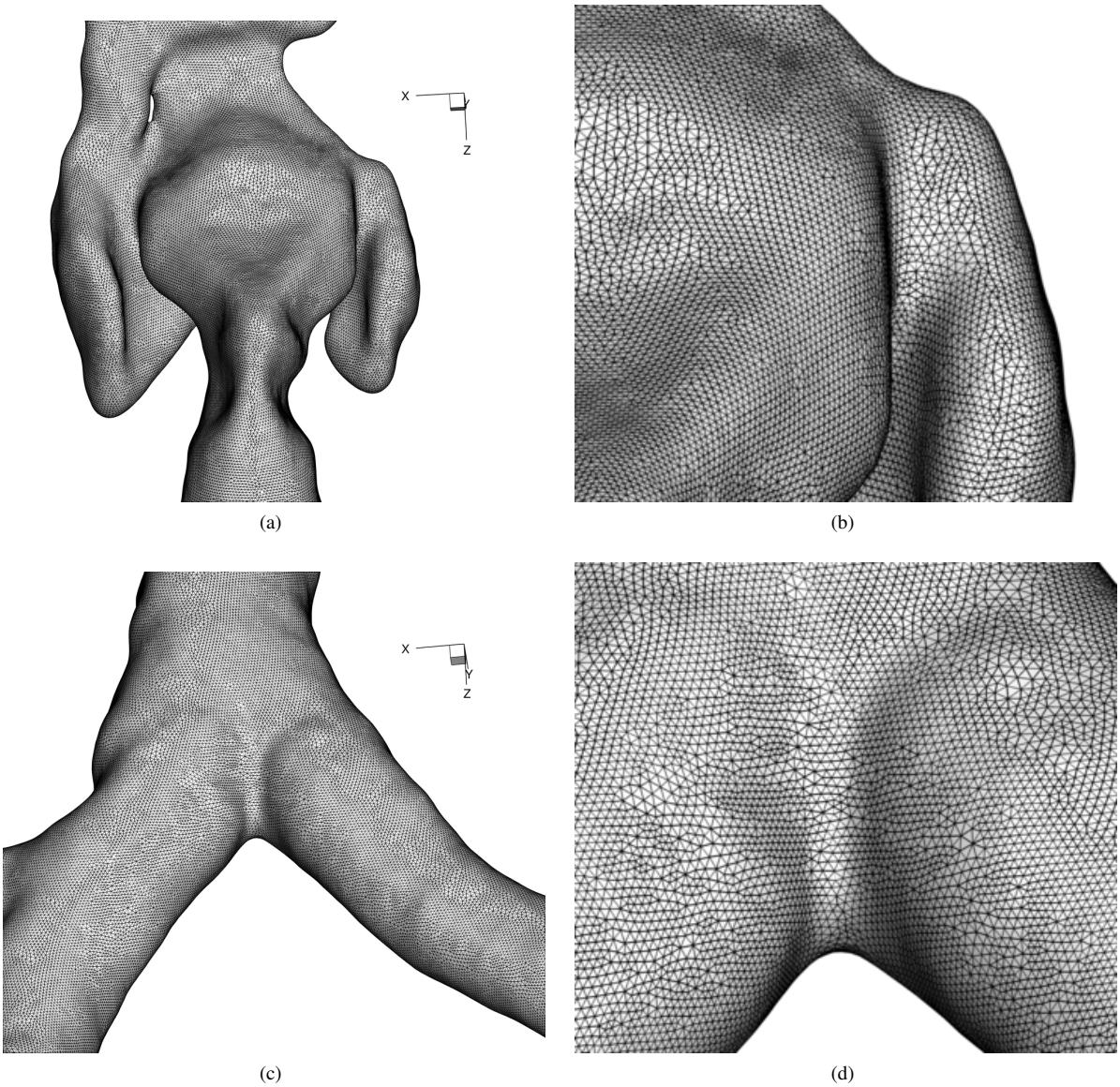

Figure 8.3: Surface mesh renderings of (a) the larynx, (b) a close-up of a section of the larynx, (c) the first bifurcation and (d) a close-up of the first bifurcation.

8.2 Flow Structures

In the following sections the simulations are compared to the experimental data obtained from Banko et al. (2014). First, a grid comparison study is performed. Then, a comparison for the inlet turbulence intensity and turbulent viscosity was performed. After the final mesh and inlet conditions were chosen several turbulence models were employed to investigate their performance compared to each other but also to the experimental data. Both the time averaged flow field (for RANS) and the turbulent kinetic energy profiles (RANS) are important to particle deposition; in the LES most of the scales are resolved and thus particle deposition can be performed by injecting them with the time-step and does not requires a separate model for turbulent dissipation.

The velocity profile used in the simulations is always a uniform profile, no-slip boundary condition is prescribed at the wall. Zero gauge pressure boundary conditions were applied to all 72 outlets, upon receiving the experimental data and the article from Banko et al. (2014) it was found that this is not consistent with the boundary condition from the experiment although the results up to the first bifurcation should be similar (based on the flow distribution among the left and right lung), see section 8.2.2.1 and table 8.4.

For the dimensionless numbers the same approach as Banko et al. (2014) is used: if the throat is simplified it can be seen as a cylinder with a diameter of 2 cm and the flow rate prescribed at the inlet is used to calculate the velocity through this circular plane.

Velocities and turbulent kinetic energy levels are compared for several locations in the geometry, an overview of the locations can be found in figure 8.4.

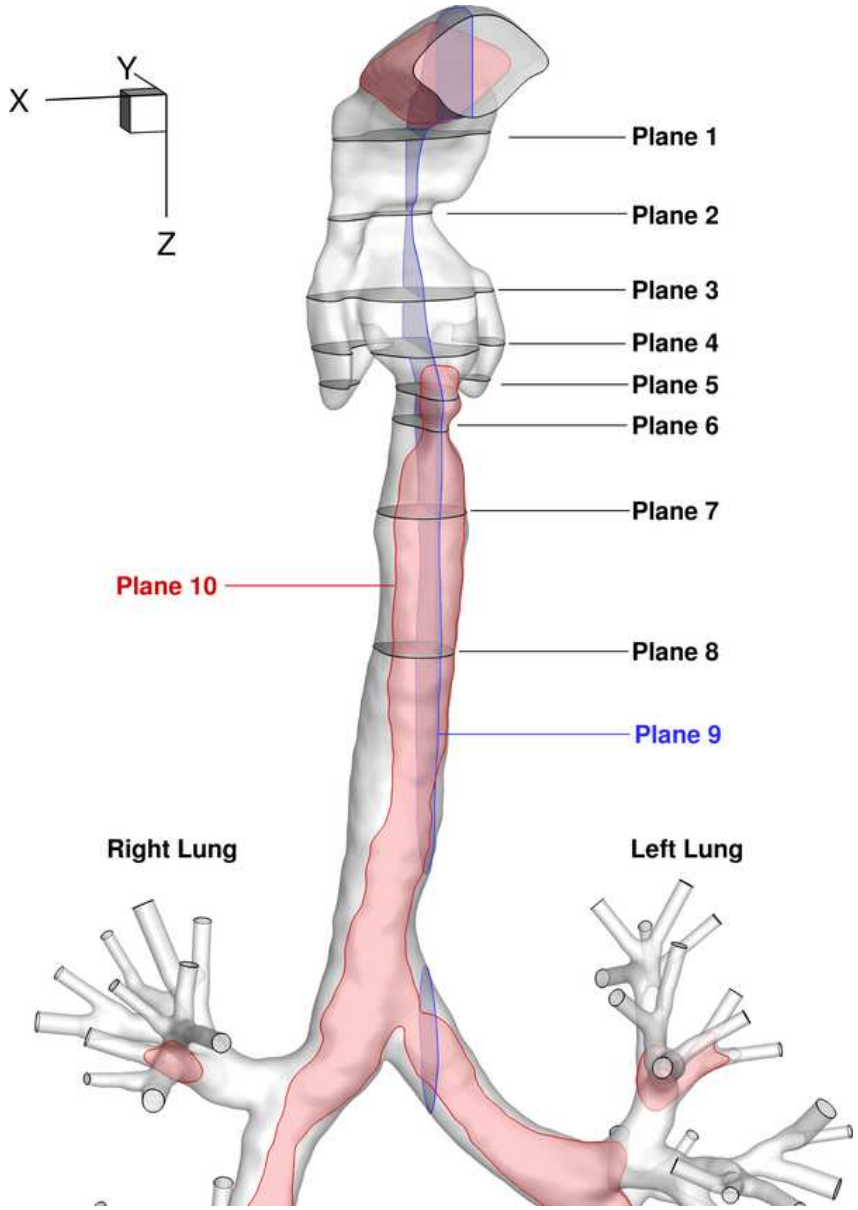

Figure 8.4: Overview of the location of the planes used to compare the experimental and simulation data. The z-coordinates of the slices 1-8 are: $z_1 = 0.1\ m$, $z_2 = 0.118\ m$, $z_3 = 0.135\ m$, $z_4 = 0.146\ m$, $z_5 = 0.154\ m$, $z_6 = 0.161\ m$, $z_7 = 0.18\ m$, $z_8 = 0.21\ m$. Plane 9 is located at $x = 0.255\ m$ and plane 10 is located at $y = 0.186\ m$.

8.2.1 Grid Comparison Study

The modelling of boundary layers and turbulence require certain mesh characteristics. To accurately model flow separation, which is likely to occur in a curved geometry such as the lungs, the viscous sublayer has to be resolved by increasing the mesh density near the wall. The dimensionless criterion for the viscous sublayer is the first cell height y^+ (equation 8.1), which should be on the order of 1, and is a function of the square root of the friction

velocity. Thus, the wall shear stress is required to determine the dimensionless first cell height. Because the wall shear stress is not known a priori several iterations of mesh generation may be required to achieve a properly resolved boundary layer mesh. First, two meshes are compared on their y^+ and velocity profiles and the effect of the turbulence prescribed at the inlet: turbulence intensity, which is the square root of the turbulent kinetic energy divided by the velocity magnitude $t_i = \sqrt{2k/3}U^{-1}$, and the turbulent viscosity, ν_t, non-dimensionalised by the molecular viscosity ν_m. Finally, the mesh best suited for this problem is used in a comparison of the turbulence models with three dimensional experimental data obtained with MRI.

The boundary condition employed at the inlet is a uniform velocity distribution where the prescribed flow rate is to 30 L/min or 60 L/min, the turbulent viscosity

Table 8.1: Boundary conditions at the inlet for cases A.1-A.3.

Case	**Mesh**	$\mathbf{t_i}$ **[%]**	ν_t/ν_m **[-]**	ϕ_V **[L/min]**	$\mathbf{Re_{ref}}$
A.1	1	5	10	30	2180
A.2	1	5	10	30	2180
A.3	2	5	10	60	4360

Before experimental data was obtained, two meshes were generated and simulations were performed with an air flow rate of 30 L/min, the resulting dimensionless first cell distance (y^+) is compared between the two cases and the resulting flow fields are compared. The dimensionless wall distance is defined as:

$$y^+ = \frac{v_\tau y}{\nu_f} \tag{8.1}$$

Where y is the cell distance, ν_f the kinematic viscosity of the fluid and v_τ the friction velocity defined as:

$$v_\tau = \sqrt{\frac{\tau_{wall}}{\rho_f}} \tag{8.2}$$

Where ρ_f is the fluid density and τ_{wall} the wall shear stress: $\tau_{wall} = \mu_f \left(\frac{\partial u}{\partial y}\right)_{y=0}$ with y the wall normal coordinate and u the velocity parallel to the wall.

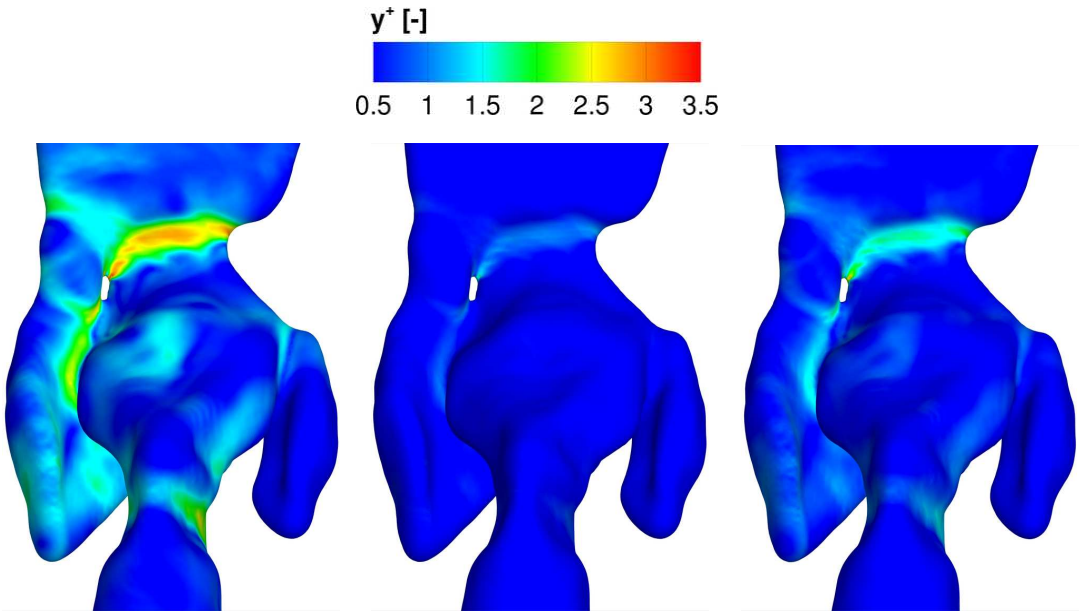

(a) Mesh 1: Re_{ref} = 2180 (b) Mesh 2: Re_{ref} = 2180 (c) Mesh 2: Re_{ref} = 4360

Figure 8.5: Contours of the dimensionless first cell height for: (a) mesh 1 with Re_{ref}=2180, (b) mesh 2 with Re_{ref}=2180 and (c) mesh 2 with Re_{ref}=4360.

The simulations show minor differences and the first cell distance is less than 5 for both meshes. However, the experiments were performed with an equivalent air flow rate of 60 L/min, or double that of the test simulations. Since the dimensionless wall distance is a function of the characteristic velocity, a doubling of the flow rate is expected to increase the dimensionless wall distance by approximately 40% (scales with the square root in the friction velocity) and thus it would mean that the coarser mesh would possibly not satisfy the $y^+ < 5$, $y^+ = O(1)$ criterion required to more accurately model the boundary layers. The results from the SST simulation was used to estimate whether or not the mesh would be suitable for LES. To do this the ratio between the grid length scale and the Kolmogorov length scale was calculated using the finest mesh with Re = 4360 by using the following definition:

$$l_{ratio} = \frac{V_{cell}^{1/3}}{\eta_k} \tag{8.3}$$

Where the η, the Kolmogorov length scale was calculated as:

$$\eta_k = \left(\frac{\nu_f^3}{\varepsilon}\right)^{1/4} \tag{8.4}$$

Where ν_f is the molecular kinematic viscosity and ε is the turbulent dissipation rate obtained from the SST-Transition simulation. The l_{ratio} from the region of the mouth until the bottom of the geometry has been plotted in figure 8.6 as a function of the z-coordinate. It can be seen that the mesh can be improved even further, especially in the region between the pharynx and larynx, but should be suitable for LES.

To touch quickly upon the refinement requirements to make the mesh better some estimations are provided. If the l_{ratio} needs to be reduced locally by a factor M_L then the total number of cells needs to be increased by a factor M_L^3 in that region since the length scale of the mesh is $V_{cell}^{1/3}$. Accompanying a local reduction in cell volume, the mesh near the modified zone may need to be reduced as well to avoid high transition ratios thereby further increasing the number of cells. If the entire mesh were to be refined by a factor two, the total cell count would approach 1×10^8 cells. For a better mesh it is suggested to locally decrease the mesh length scale by a factor of 2 or less to keep the model tractable. It must be noted that at lower flow rates the ratio of the integral scale to the Kolmogorov scale becomes smaller (scales with $Re^{3/4}$) and therefore decreases the length scale ratio when the same mesh is used.

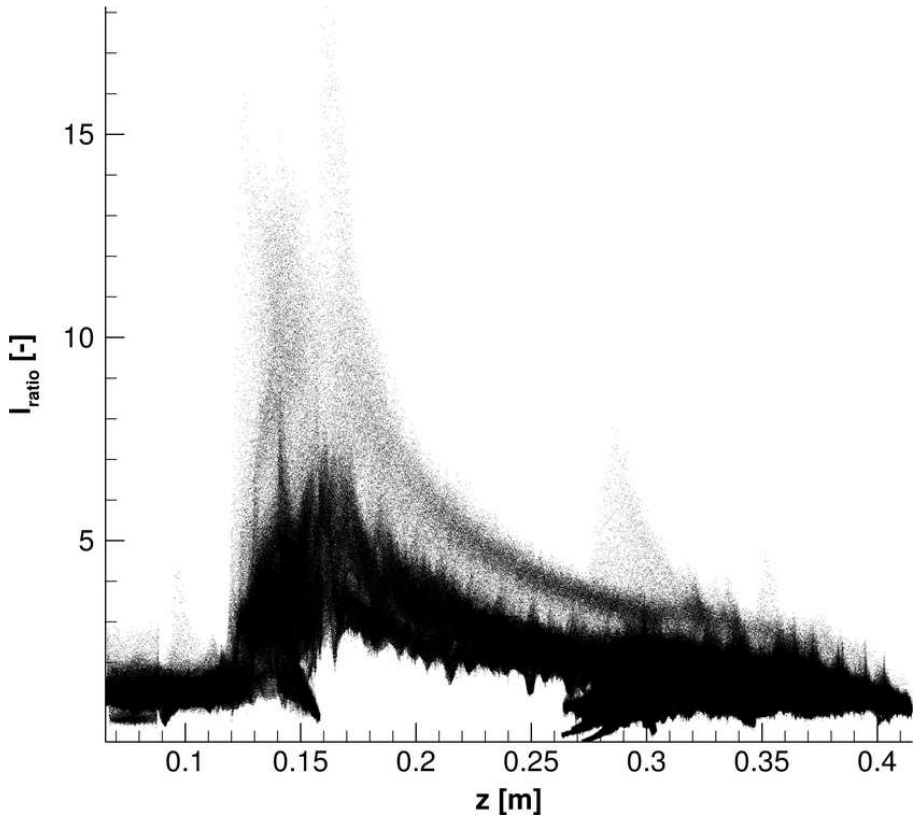

Figure 8.6: Scatter plot of the length scale ratio (equation 8.3) versus z-coordinate for all cells for a flow rate of 60 L/min.

8.2.1.1 Turbulence Inlet Parameters

Since no data regarding the turbulence at the inlet was available at the time of setting up the simulation an assumption had to be made regarding the turbulent intensity. A turbulent intensity of 5% and turbulent viscosity ratio of 10 is the Fluent default. After performing the first simulation it was noted that the turbulent viscosity ratio quickly dropped to < 2 and the turbulent intensity dropped to 2% after the inlet therefore an SST-Transition simulation was performed with these values prescribed at the inlet. The results are not exactly equal; the velocity magnitude contours are almost the same only the difference is the levels of TKE found in the region of the jet. Since no experimental data regarding the turbulent properties at the inlet is available and some RANS models require high levels of turbulence at the inlet the final inlet conditions chosen are a turbulent intensity of 5% and viscosity ratio of 10.

Table 8.2: Boundary conditions at the inlet for cases B.1-B.4.

Case	**Mesh**	$\mathbf{t_i}$ **[%]**	ν_t/ν_m **[-]**	ϕ_V **[L/min]**	$\mathbf{Re_{ref}}$
B.1	2	5	10	30	2180
B.2	2	5	2	30	2180
B.3	2	2	10	30	2180
B.4	2	2	2	30	2180

The velocity magnitude and turbulent kinetic energy in a cross-section of the upper airway is given for the two different meshes with the same turbulent inlet parameters is given in figures 8.7 and 8.9 or figures 8.8 and 8.10 a, b respectively. Only minor differences between the simulations are observed; the following comparisons will be made based on the results from the second mesh only.

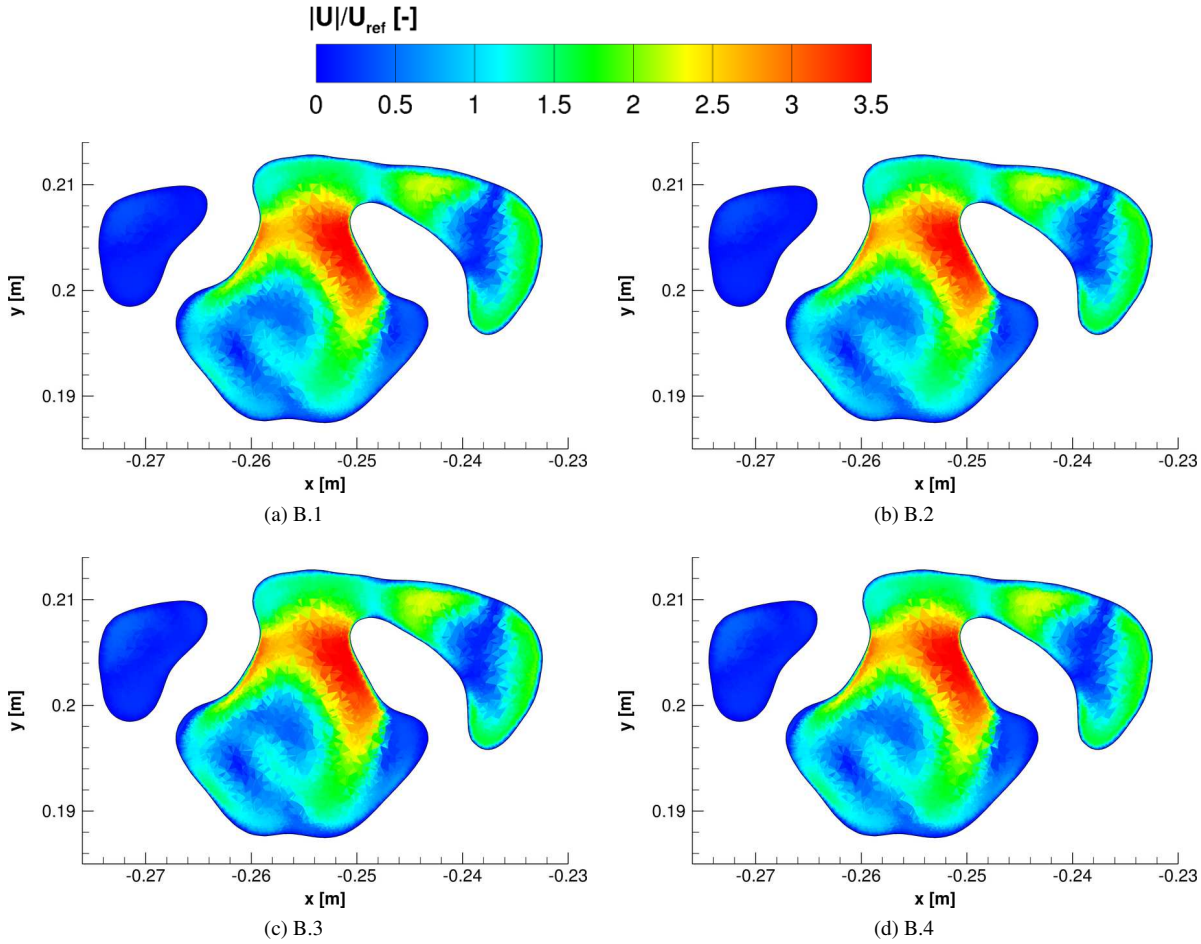

(a) B.1

(b) B.2

(c) B.3

(d) B.4

Figure 8.7: Contours of the scaled velocity magnitude in plane 4.

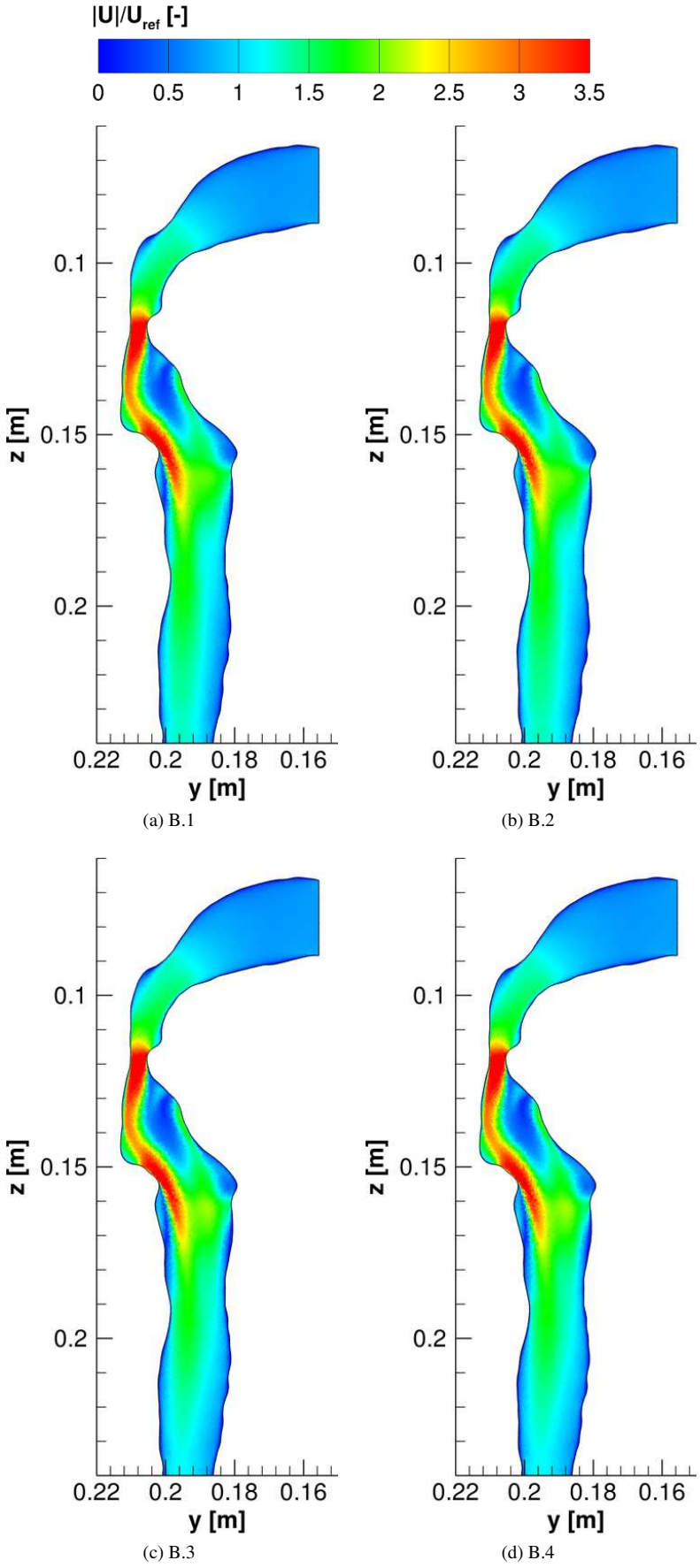

(a) B.1

(b) B.2

(c) B.3

(d) B.4

Figure 8.8: Contours of the scaled velocity magnitude in plane 9.

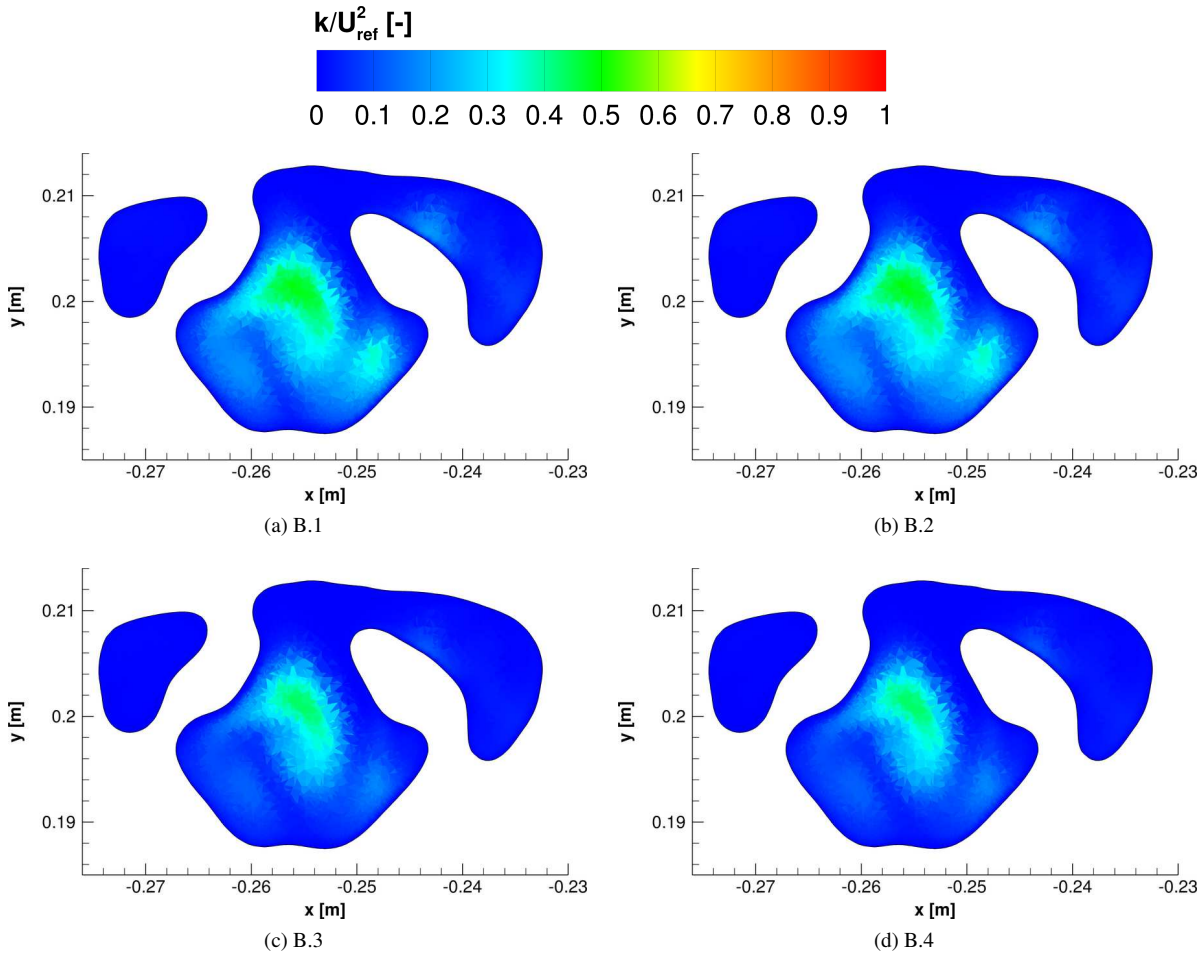

(a) B.1 (b) B.2

(c) B.3 (d) B.4

Figure 8.9: Contours of the scaled turbulent kinetic energy in plane 4.

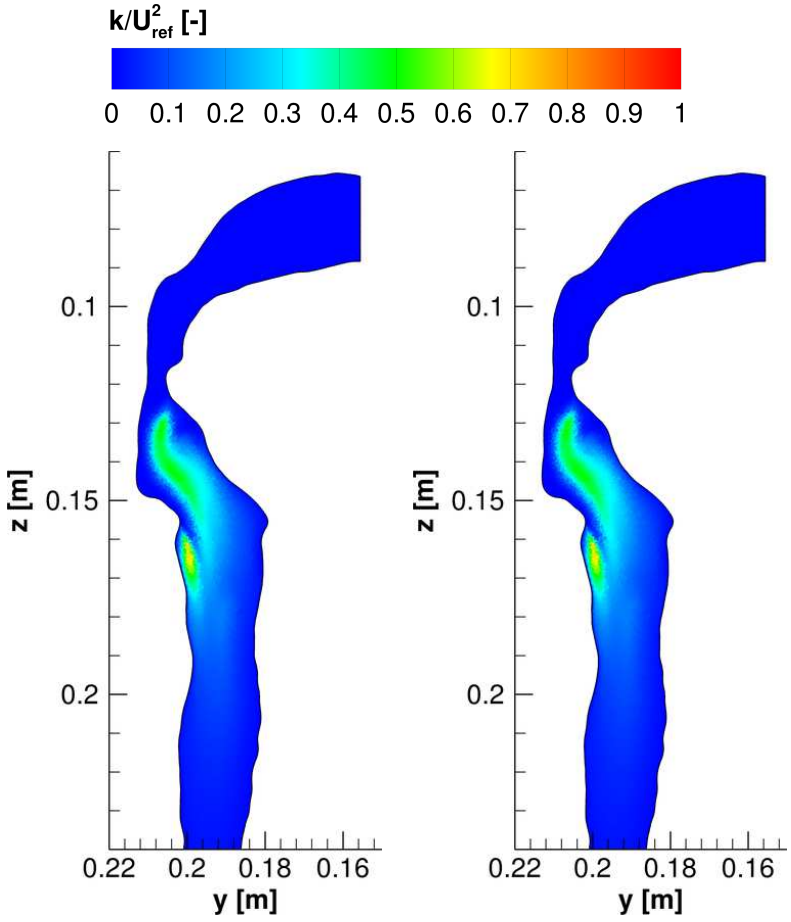

(a) B.1 (b) B.2

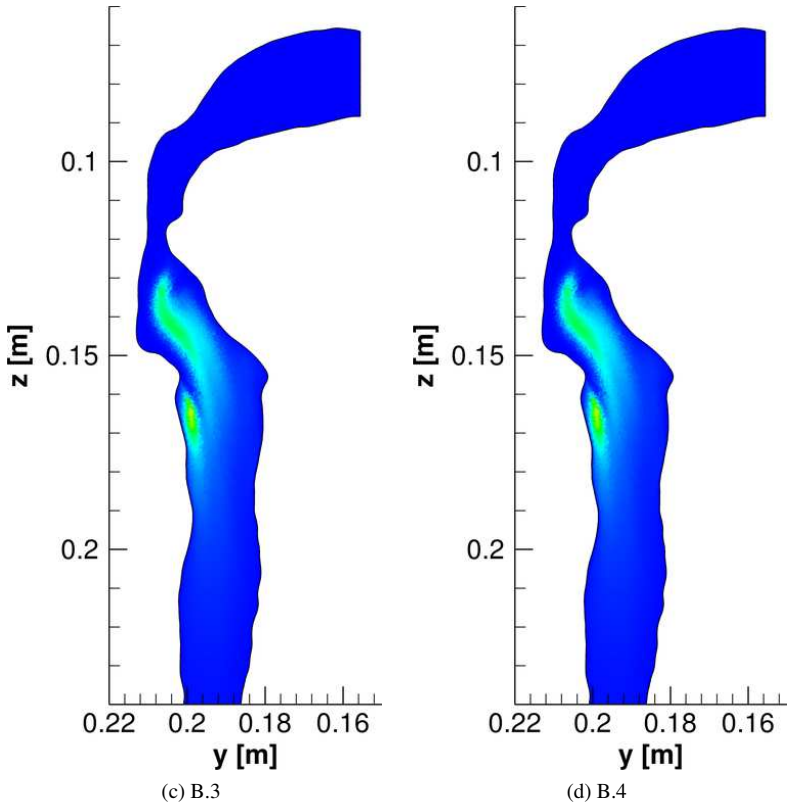

(c) B.3 (d) B.4

Figure 8.10: Contours of the scaled turbulent kinetic energy in plane 9.

8.2.2 Comparison with Experimental Data

Several turbulence models were employed to solve the flow and are compared on their ability to capture both velocity magnitude and secondary motions with respect to experimental data. Unfortunately, no experimental velocity fluctuation data is available and thus the turbulent kinetic energy was only compared between simulations.

8.2.2.1 Boundary Conditions

The boundary conditions can be found in table 8.3 below; the turbulent intensity and viscosity ratio were kept the same for all simulations. For the LES these turbulent properties were obtained by letting fluent generate two dimensional vortices. This method generates more turbulence-like-perturbations than fluctuations based on a random probability distribution. The time step used is $\Delta t = 1\times10^{-4}$ s, for a few cells in the geometry it is estimated that the value should be lowered by roughly a factor 5, however this would greatly increase the time necessary to obtain the first results (the first 0.2 s of the simulation took 3-4 weeks on 16 cores). A simulation which features a smaller time step has been submitted at the time of writing.

As mentioned previously, the outlet boundary conditions employed in the simulations are not equal to the those used in the experiment; in the experiment the flow rate for each of the lobes is equal; to achieve the same with the present mesh is not feasible as it requires part of the experimental set-up to be meshed (figure 8.1a) which would greatly increase the cell count. In table 8.4 the lobar ventilation ratios, which is the ratio of the flow rate through each lobe compared to the inlet, are given for each of the simulations, a simulation at a lower flow-rate by Zhang et al. (2012), the data from the MRI experiment (Banko et al., 2014) and measurements from Horsfield et al. (1971). The equal ventilation ratios for the five lobes in the experiment by Zhang et al. (2012) were by design (this information was not known at the time of starting the simulation but only until after the particle depositions were performed). From the table we can see that none of the simulations match the ventilation ratios in each specific lobe and therefore the velocity profiles are not expected to agree in these parts of the geometry. However, the flow rate ratio between the left and right lung agrees quite well and thus the velocity profiles is expected to show similarities in the region of the upper airway (and until the first bifurcation). Therefore, the focus in the comparison lies on the region between the inlet until slightly downstream the first bifurcation.

Table 8.3: Boundary conditions at the inlet for cases C.1-C.5.

Case	**Mesh**	**Turbulence Model**	$\mathbf{t_i}$ **[%]**	ν_t/ν_m **[-]**	ϕ_V **[L/min]**	$\mathbf{Re_{ref}}$
C.1	2	LES-Wale	5	10	60	4360
C.2	2	LES-Smagorinsky	5	10	60	4360
C.3	2	SST-Transition	5	10	60	4360
C.4	2	k-ε Realisable	5	10	60	4360
C.5	2	k-ω LRN	5	10	60	4360

Table 8.4: Lobar ventilation ratios (VR) for various simulations and experimental data.

	Horsfield et al. (1971)	**Zhang et al. (2012)**	**SST-Trans.**	**Banko et al. (2014)**	**LES-WALE**	**LES-Smagorinsky**	**SST-Trans.**	**k-ε Realisable**
Equiv. Air Flow rate [L/min]	30	30	30	60	60	60	60	60
VR Upper Left [-]	0.21	0.18	0.15	0.20	0.12	0.12	0.14	0.16
VR Lower Left [-]	0.25	0.26	0.29	0.20	0.27	0.27	0.32	0.26
VR Total Left [-]	0.45	0.44	0.44	0.40	0.38	0.40	0.46	0.42
VR Right Upper [-]	0.22	0.18	0.16	0.20	0.18	0.17	0.15	0.18
VR Right Middle [-]	0.10	0.10	0.11	0.20	0.12	0.11	0.11	0.10
VR Right Lower [-]	0.23	0.29	0.29	0.20	0.32	0.32	0.28	0.29
VR Total Right [-]	0.55	0.56	0.56	0.60	0.62	0.60	0.54	0.58

8.2.2.2 Velocities

Velocities were extracted from several slices (figure 8.4), the velocity magnitude and z-vorticity for a select number of planes are discussed while the remaining figures can be found in append C.3. In the experimental data provided by Zhang et al. (2012), geometry from the STL file was incorporated into the data-set and the wall of this geometry is plotted as a white line in the contour figures.

The LES was performed using second order implicit scheme in time however, the maximum Courant number observed based on the averaged filtered velocity magnitude is 2 in some places ($\Delta t = 1\times10^{-4}$ s); while Fluent is able to handle such time steps it might reduce the accuracy, therefore another simulation was submitted using a smaller time-step but is still running at the moment. Another cause of problems can be the relatively high growth ratio just outside of the boundary layer mesh, this was done to reduce the overall mesh size; a mesh with a smoother transition was also generated but featured roughly 15×10^6 cells and this would increase the computational cost even further due to an increased number of cells and a reduction of the time-step would be required if the Courant number were to be kept the same.

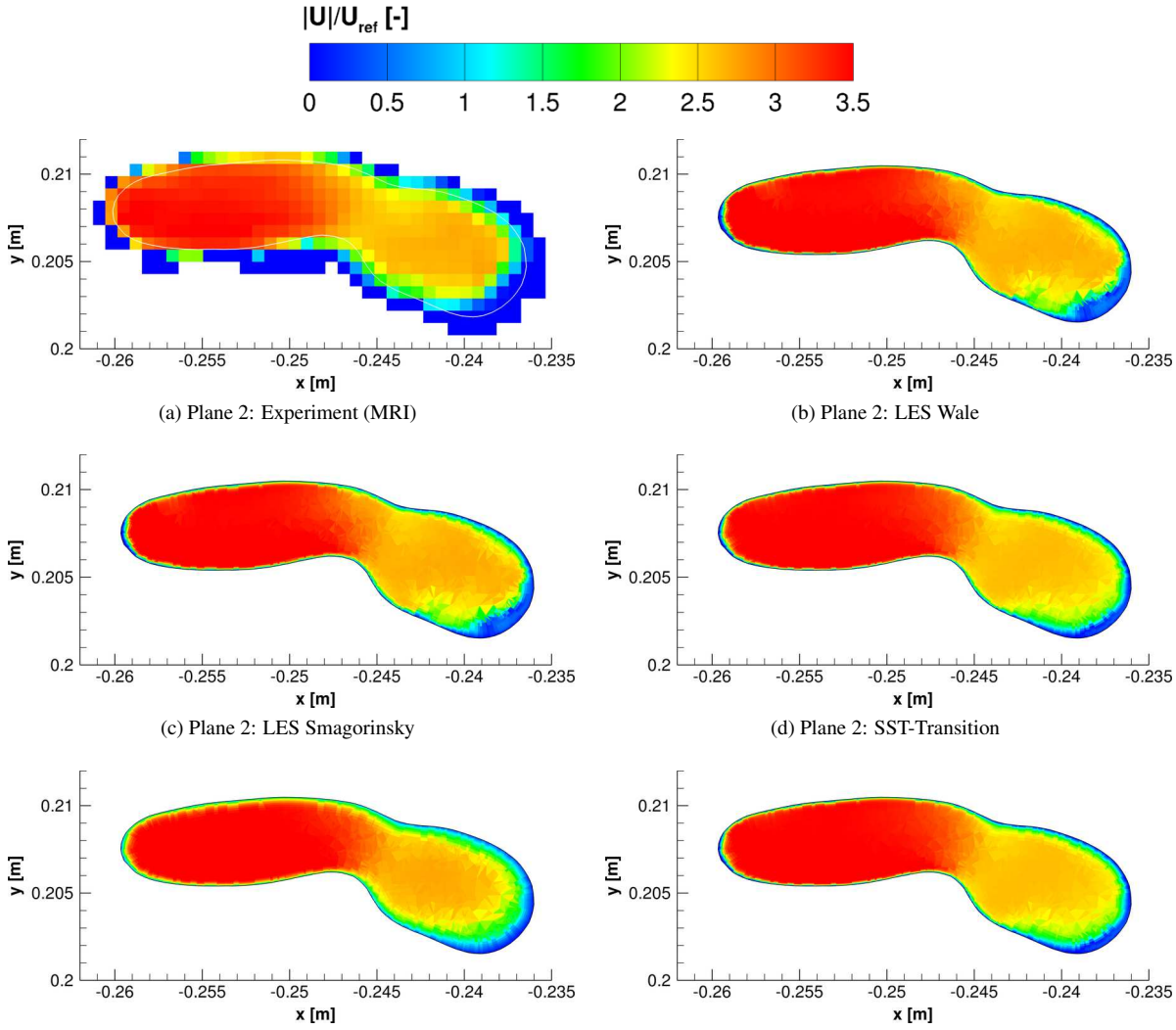

(a) Plane 2: Experiment (MRI)

(b) Plane 2: LES Wale

(c) Plane 2: LES Smagorinsky

(d) Plane 2: SST-Transition

(e) Plane 2: k-ε Realisable

(f) Plane 2: k-ω LRN

Figure 8.11: Contours of the scaled velocity magnitude in plane 2 for the experimental and simulation data.

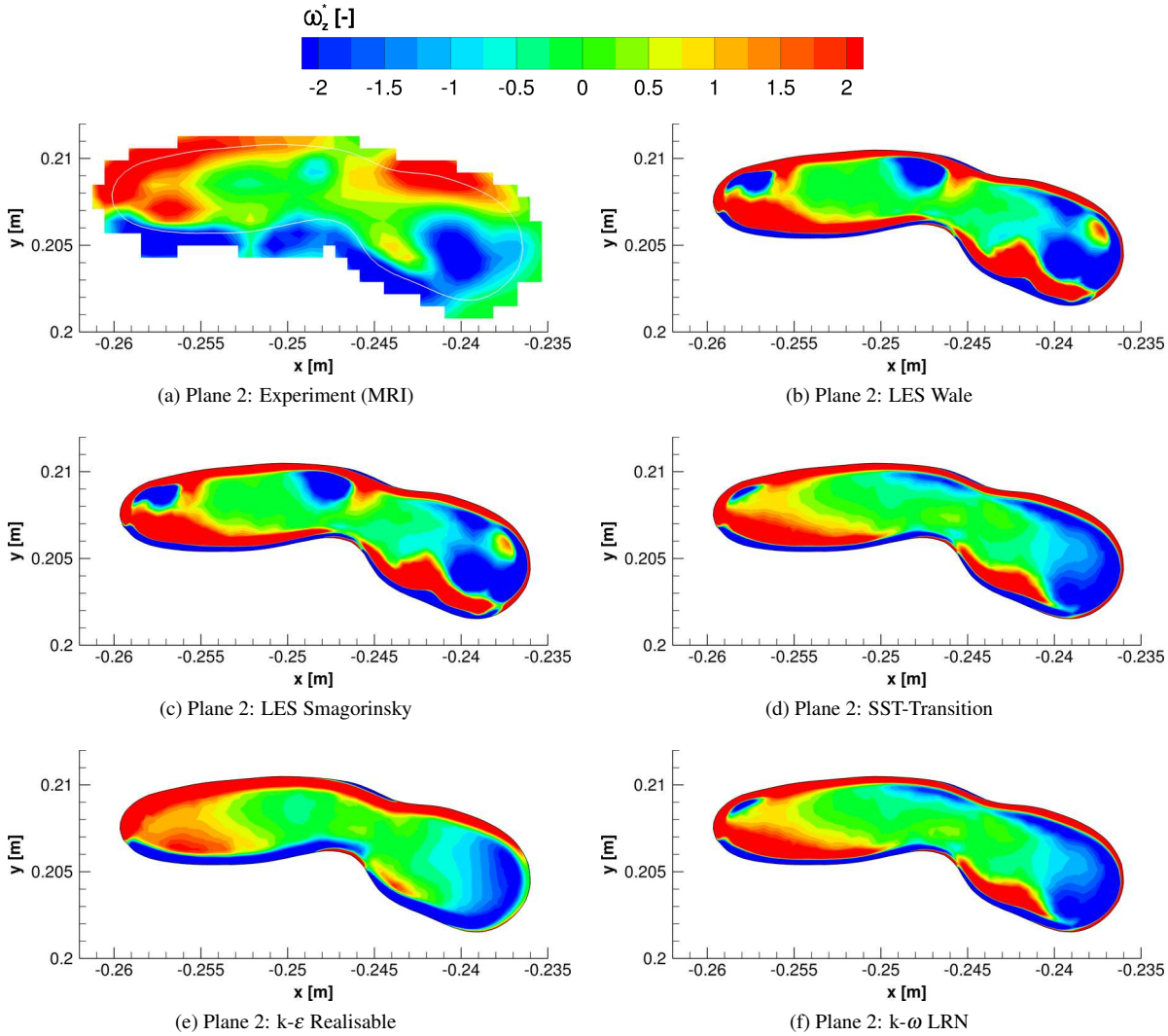

(a) Plane 2: Experiment (MRI)

(b) Plane 2: LES Wale

(c) Plane 2: LES Smagorinsky

(d) Plane 2: SST-Transition

(e) Plane 2: k-ε Realisable

(f) Plane 2: k-ω LRN

Figure 8.12: Contours of the scaled z-vorticity in plane 2 for the experimental and simulation data.

Plane 2 is located in the most narrow region of the upper airway (figure 8.12), the velocity magnitude here is the then the highest but the level of turbulence is very low; the turbulence starts to develop after the constriction (section 8.2.2.3). The velocity profiles obtained from each model all capture qualitatively the behaviour observed in the experiment and it must be noted that the inlet velocity profile used in the simulations is not the same as that from the experiment; the start of the jet (located on the left side in each figure) is captured in all models as well as the lower velocity zone located to the right followed by an almost stagnant zone located in the bottom right. The LES models predict a larger 'stagnant' zone than the other models (and thus must predict elsewhere in this plane higher velocities than in the RANS models) but it cannot be decided from the experimental data whether the LES or the RANS models are more accurate in the prediction of the size since the resolution of the experimental data is limited. The reason that the models all predict similar behaviour is due to the low level of turbulence and thus a practically laminar flow is solved.

The differences between the models can be better observed by looking at the z-vorticity, the LES simulations differ significantly from the RANS models and also from the experimental data. One of the explanations is that the inlet conditions are different between the simulation and experiment: the simulations used a uniform velocity profile for the RANS and for the LES a vortex synthesiser was used on top of the uniform inlet and since this plane is upstream of the turbulence, the vorticity and velocity magnitude were expected to differ. The k-ε Realisable most accurately captures the shapes of the positive vorticity region on the left side

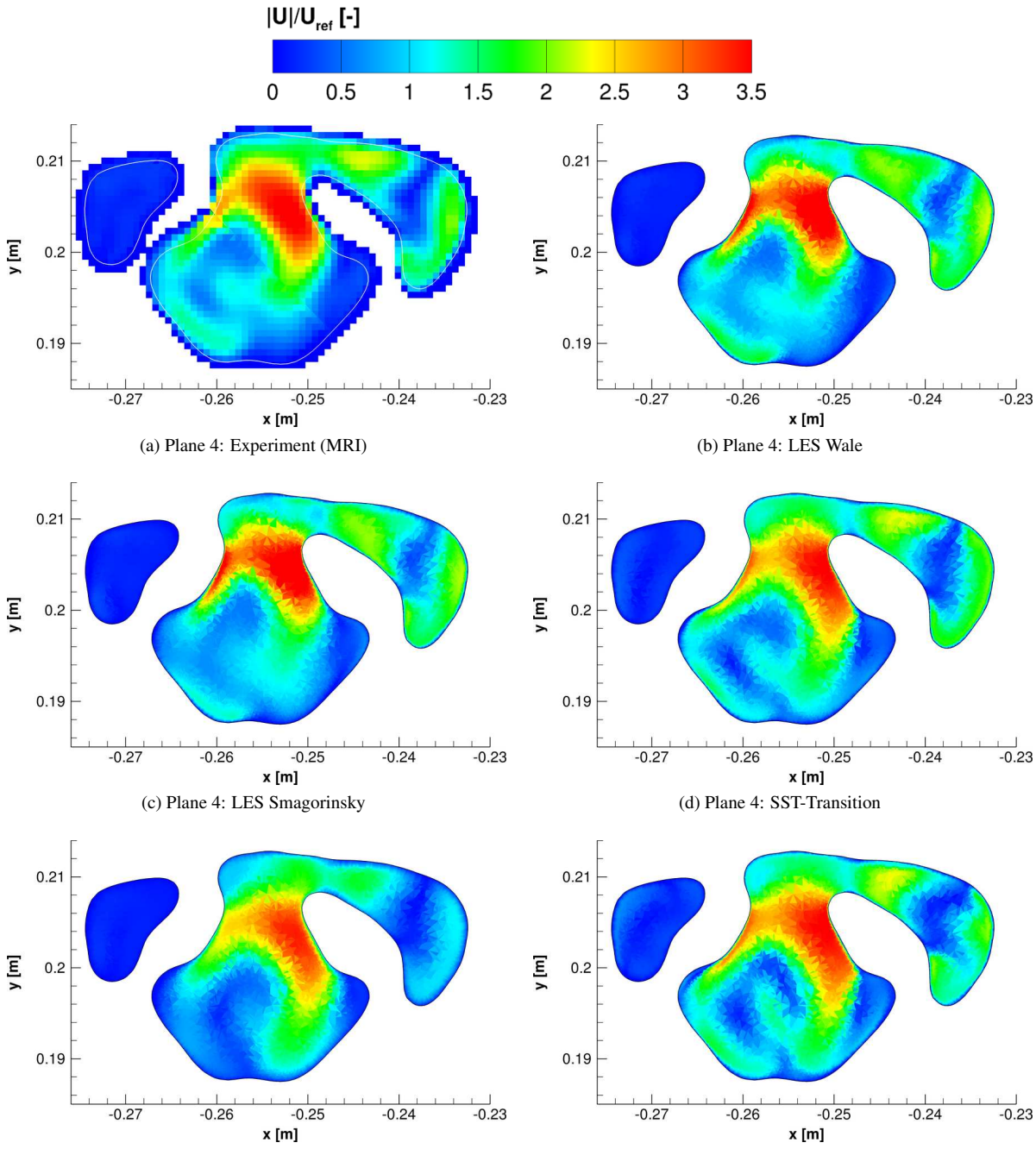

(a) Plane 4: Experiment (MRI)

(b) Plane 4: LES Wale

(c) Plane 4: LES Smagorinsky

(d) Plane 4: SST-Transition

(e) Plane 4: k-ε Realisable

(f) Plane 4: k-ω LRN

Figure 8.13: Contours of the scaled velocity magnitude in plane 4 for the experimental and simulation data.

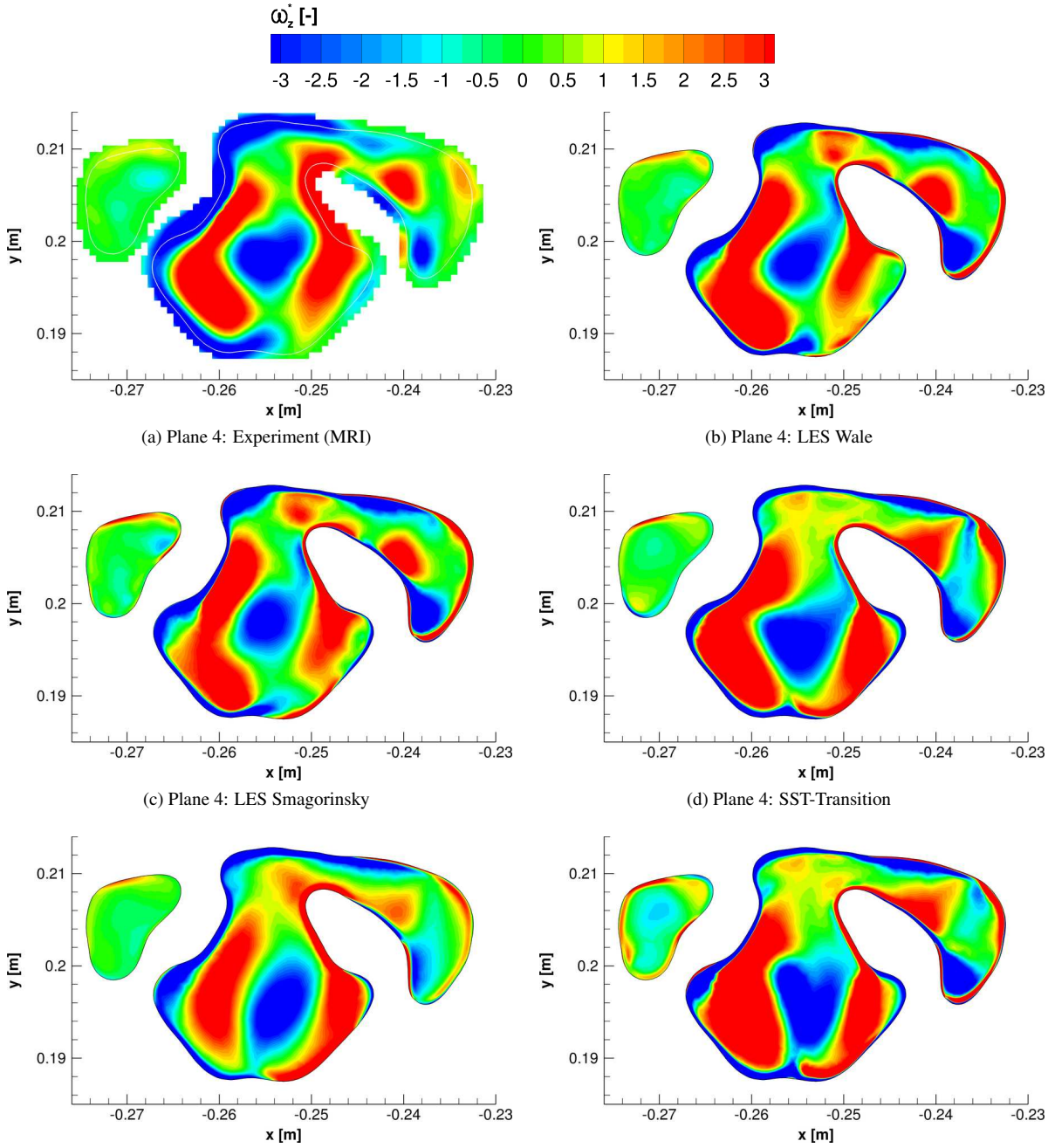

(a) Plane 4: Experiment (MRI)

(b) Plane 4: LES Wale

(c) Plane 4: LES Smagorinsky

(d) Plane 4: SST-Transition

(e) Plane 4: k-ε Realisable

(f) Plane 4: k-ω LRN

Figure 8.14: Contours of the scaled z-vorticity in plane 4 for the experimental and simulation data.

The fourth plane is located in the turbulent region of the flow, and as such the effect of different inlet velocity profile is expected to have less of an impact than was the case in the previous plane. Indeed, the LES and RANS approaches are all able to capture qualitatively the same structures (figures 8.13 and 8.14), the location of high velocity in the experiment is captured by all models however, the k-ε Realisable model is the only model which does not over predict the velocity magnitude in the region opposite of the highest velocity region, but rather under predicts it.

In the upper right corner of this plane there are two regions of twice the reference velocity magnitude separated by a region of low velocity magnitude. In this region are are some interesting differences between the models. The LES-WALE model seems to over predict the velocity magnitude in two additional regions as indicated by the two yellow spots in the rightmost green island. The k-ε Realisable model under predicts the velocity in the majority of the upper right corner.

The primary regions of negative and positive z-vorticity are predicted by all models although as was the case in the previous plane although there are some missing, or extra, regions present in simulation furthermore, the regions near the wall are much thicker in the experimental data which may be attributed to the uniform grid. Another interesting part of this plane is the right-pyriform sinus (or esophageal space) not connected to the main area of interest (when rendered as in these figures), where a positive z-vorticity is present in both the experimental data and simulations, but the simulations over predict the magnitude and the k-ω LRN over predicts the length of this region.

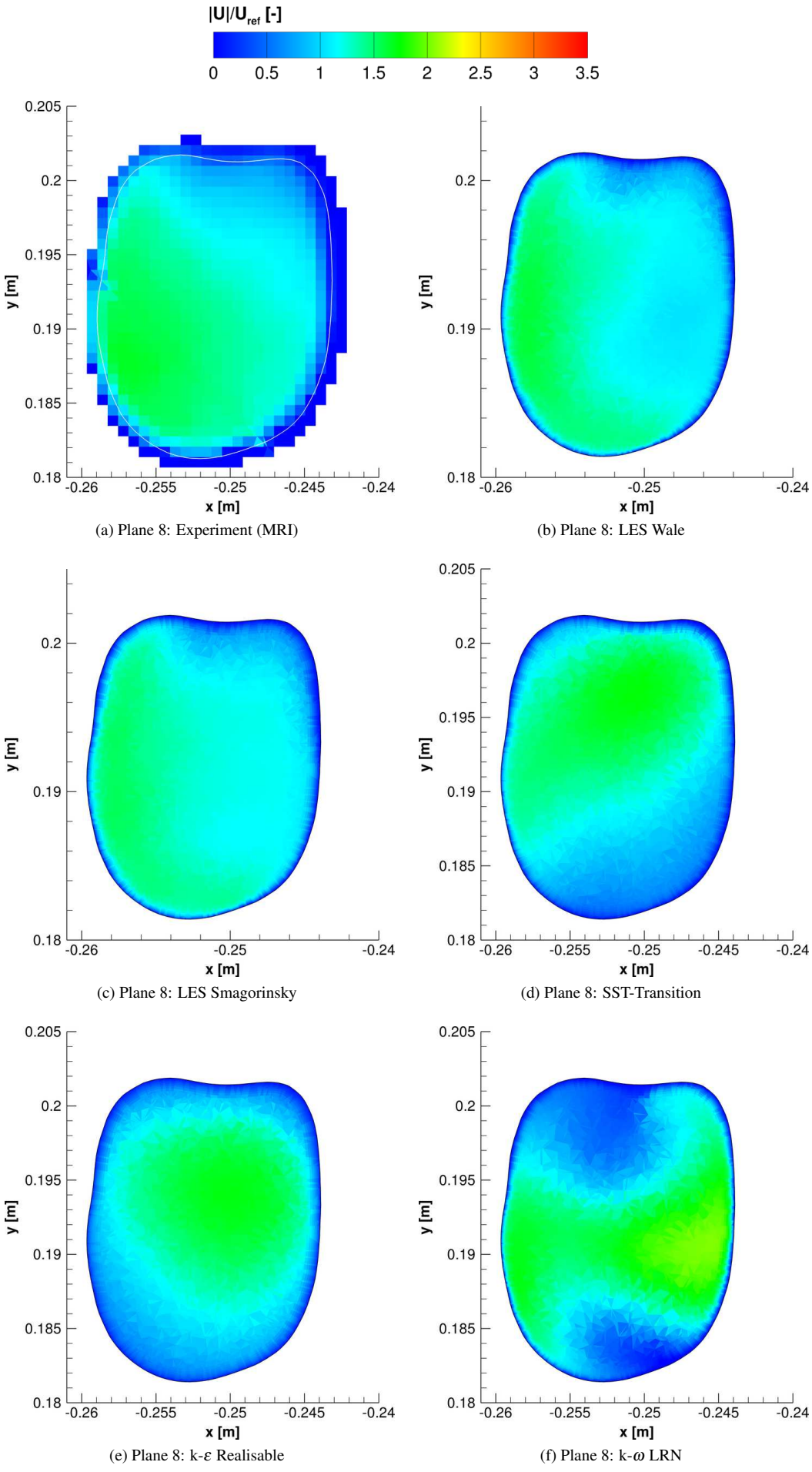

(a) Plane 8: Experiment (MRI)

(b) Plane 8: LES Wale

(c) Plane 8: LES Smagorinsky

(d) Plane 8: SST-Transition

(e) Plane 8: k-ε Realisable

(f) Plane 8: k-ω LRN

Figure 8.15: Contours of the scaled velocity magnitude in plane 8 for the experimental and simulation data.

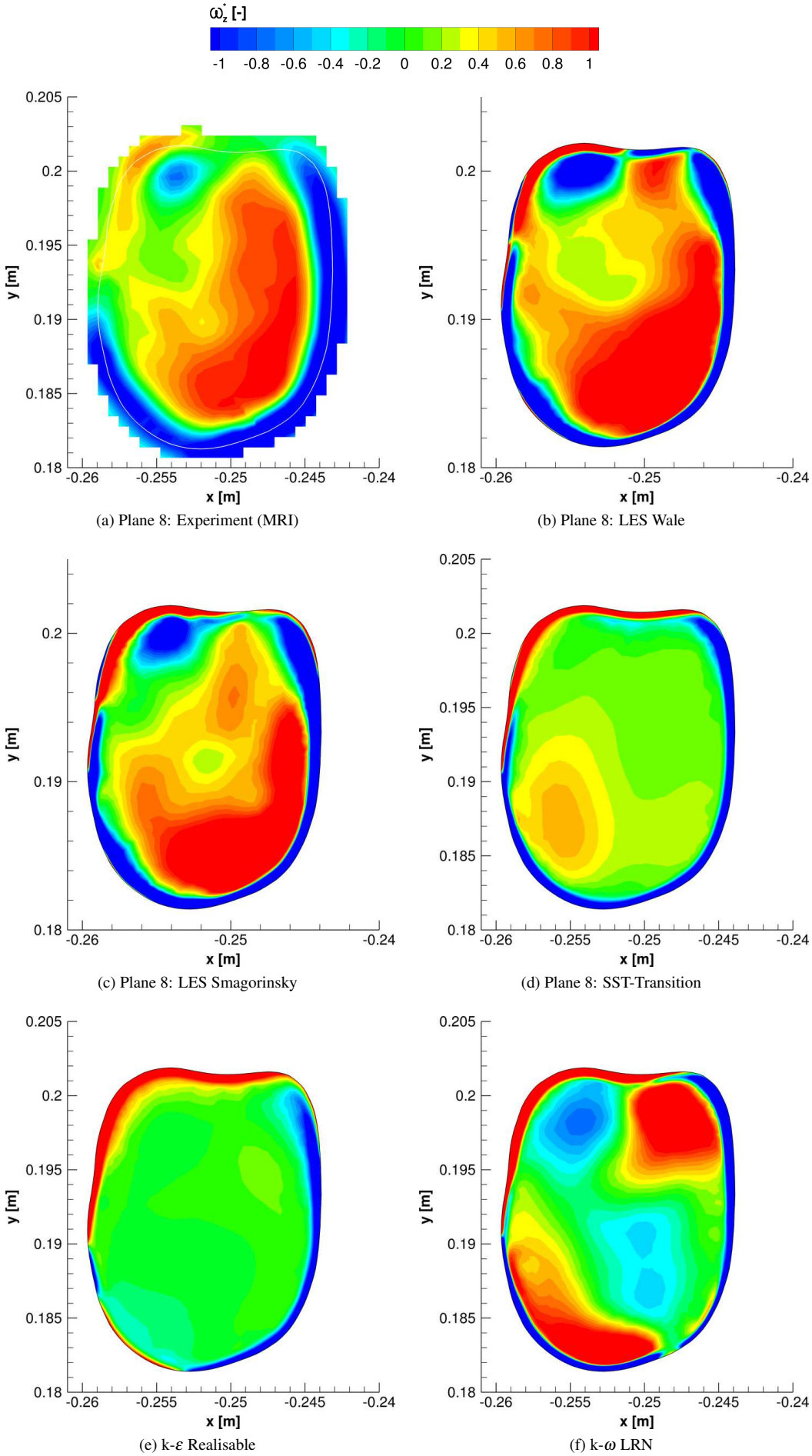

(a) Plane 8: Experiment (MRI)

(b) Plane 8: LES Wale

(c) Plane 8: LES Smagorinsky

(d) Plane 8: SST-Transition

(e) k-ε Realisable

(f) k-ω LRN

Figure 8.16: Contours of the scaled z-vorticity in plane 8 for the experimental and simulation data.

In the eighth plane, located downstream of the high turbulence region (although there is still turbulence present), there are major differences between the experimental data and RANS simulations, both the velocity magnitude and z-vorticity contours (figures 8.15 and 8.16 respectively) indicate that RANS models are not accurately describing the flow patterns observed in experiments. Though the large eddy simulations are also not fully capturing the phenomena in this plane, they are much closer to reality. Based on these velocity profiles, it is concluded that the particle motion will be more accurately described in LES than in RANS simulation however, it was opted to perform the simulations in the SST model due to time constraints.

The z-vorticity contours in the eighth plane, given in figure 8.16, show that between the models the LES capture the secondary motions most accurately; the RANS models fail to capture the secondary motions correctly in this plane.

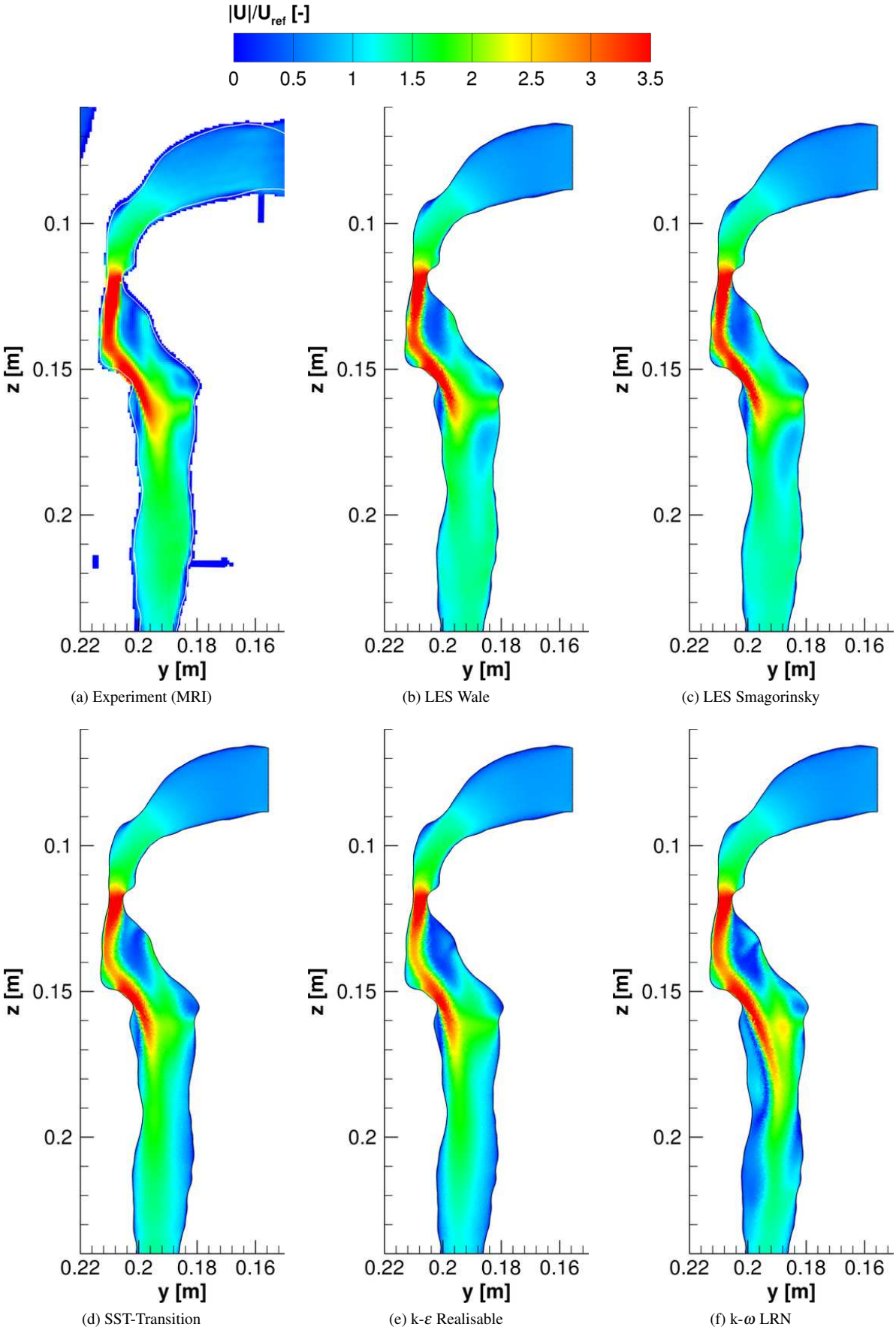

(a) Experiment (MRI)

(b) LES Wale

(c) LES Smagorinsky

(d) SST-Transition

(e) k-ε Realisable

(f) k-ω LRN

Figure 8.17: Contours of the scaled velocity magnitude in plane 9 for the experimental and simulation data.

A mid plane of the upper airway is given in figure 8.17, except for the k-omega LRN model, the turbulence models seem to be able to predict the qualitative behaviour found in the experiment quite well.

First, attention has to be drawn to the mouth region: the inlet conditions for the experiment and simulations are not the same. When the simulations were started experimental data was not yet available and therefore we opted for a uniform velocity inlet profile. It can be seen from this mid plane that this is not in agreement with the experiment. However, the turbulence occurring after the restriction/narrowing is expected to reduce the importance of the exact velocity profile; it must be noted that it is recommended for future endeavours to perform a simulation with an identical velocity inlet to provide a definitive answer regarding this issue. Indeed, it can be seen that although the inlet conditions are not identical a qualitative agreement is still obtained.

The velocity magnitude of the jet found by the LES agrees quite well with the experimental data however, the low velocity magnitude region just downstream and to the right of the jet (starts at approximately z = 0.17 m) is much larger in the LES than in the experimental data. The RANS turbulence models all seem to be incapable of capturing the flow field downstream the jet accurately. The k-ω LRN model however seems to deviate from the experiment the most. The jet is much longer, the over prediction of the velocity magnitude next to and just upstream the end of the jet is the most severe and the shape itself is also not captured accurately: it is directed to the front much earlier than in the other cases. Moreover, after the separation of the flow on the backside (y = 0.2 m, z = 0.155 m) the flow does not reattach until much more downstream which is in stark contrast to the experimental data, see figure 8.18 for the identification of this regime.

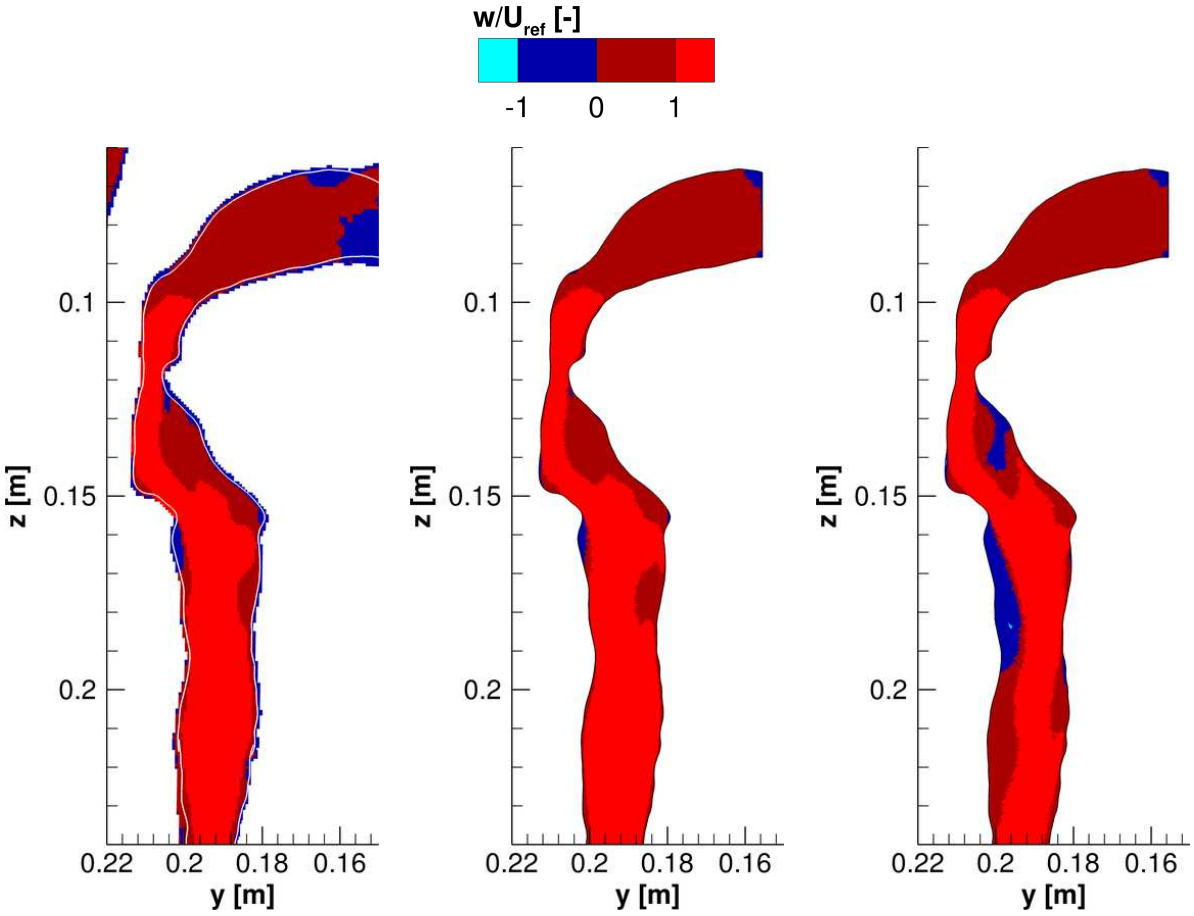

(a) Experiment (b) LES Wale (c) k-ω LRN

Figure 8.18: Contours of the scaled w velocity in plane 9 for the experimental and simulation data to highlight the regions where flow separation and reattachment occur, these figures for the other simulations can be found in figure C.21.

In figure 8.19 the z-velocity component is compared between the experiment and simulations, in this plane the velocity is visually distributed asymmetrically in both the experiments and, bar the SST, the simulations. In case of

the SST model, the high velocity 'jet' seems to be deflected towards the right side when approaching the bifurcation. The bifurcation on the left side (leading into the right lung) the velocity is over predicted for all models; the same is true for the other daughter tube. It must be noted that the plane is not perfectly matching the one from the experiments as can be seen from the white line defining fitted geometry: the constriction in the right daughter of the simulation-plane is slightly narrower than that of the experiment. The recirculating zone is captured by all models. In this region the models were expected to behave more alike then was the case in the previous cross sections (where the highly turbulent region is located) due to the decay of turbulence (see section 8.2.2.3). Overall, only a qualitative agreement is obtained and this will in turn reduce the accuracy of the particle simulations.

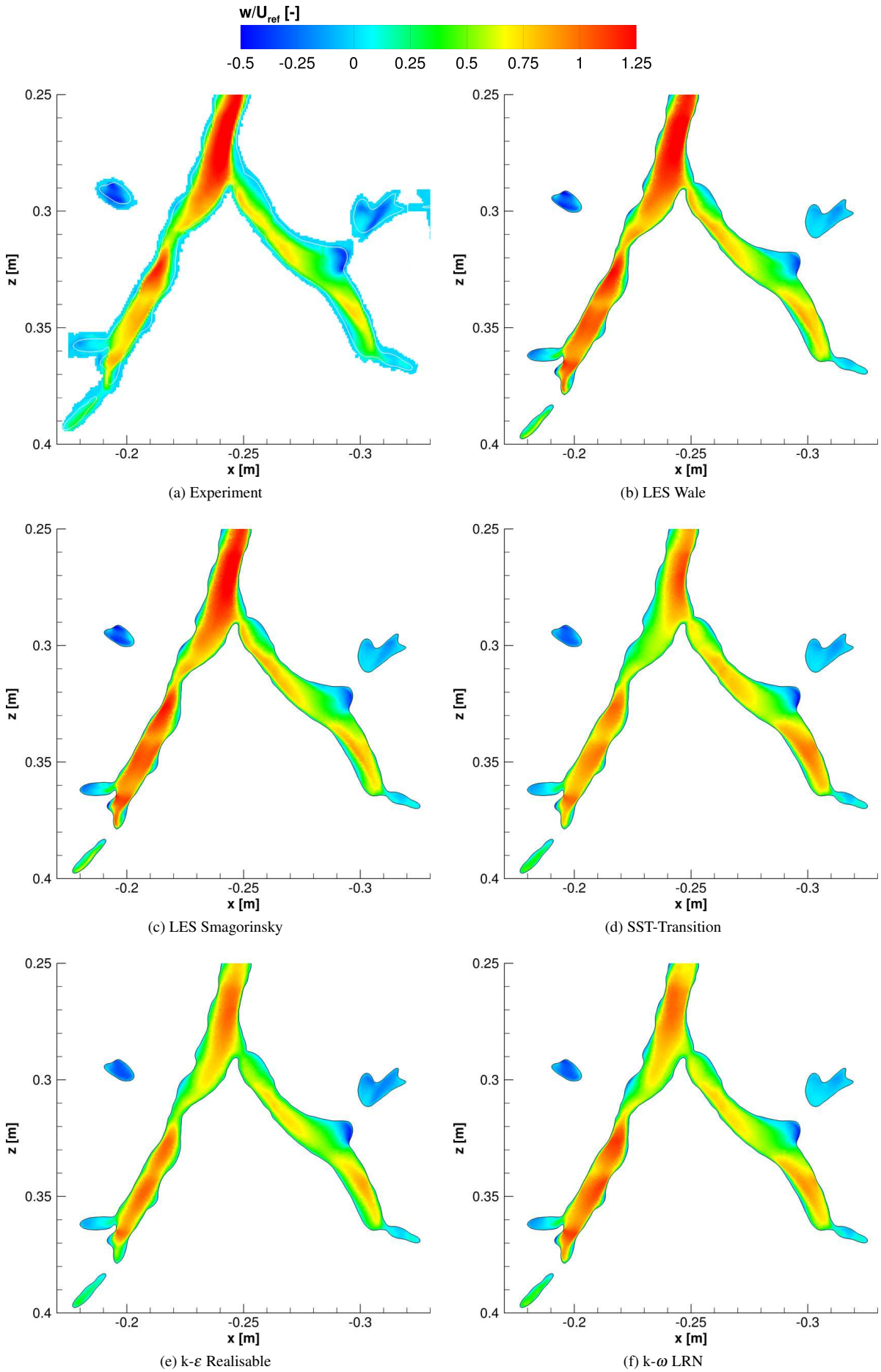

(a) Experiment

(b) LES Wale

(c) LES Smagorinsky

(d) SST-Transition

(e) k-ε Realisable

(f) k-ω LRN

Figure 8.19: Contours of the scaled w velocity in plane 10 for the experimental and simulation data.

To quantitatively compare the velocity fields, profiles are extracted from planes 1-8 (figures 8.20-8.27). Please note that the exact position of the profiles may be slightly different in the experiment due to alignment issues. The results of the simulations for profiles 1A-2B show relatively little differences; the major remark is that the velocity magnitude for the experimental data does not become zero until much further away. This may be due to both the misalignment of the data-set and the resolution of the MRI. In general, the LES show the best agreement with the experimental data although it should be noted that in plane 7 all models are off. Further differences between the experiment and simulation data, the LES included, are over- or underestimation of peaks. Figure 8.24b is a prime example of the former while figure 8.26b illustrates the latter.

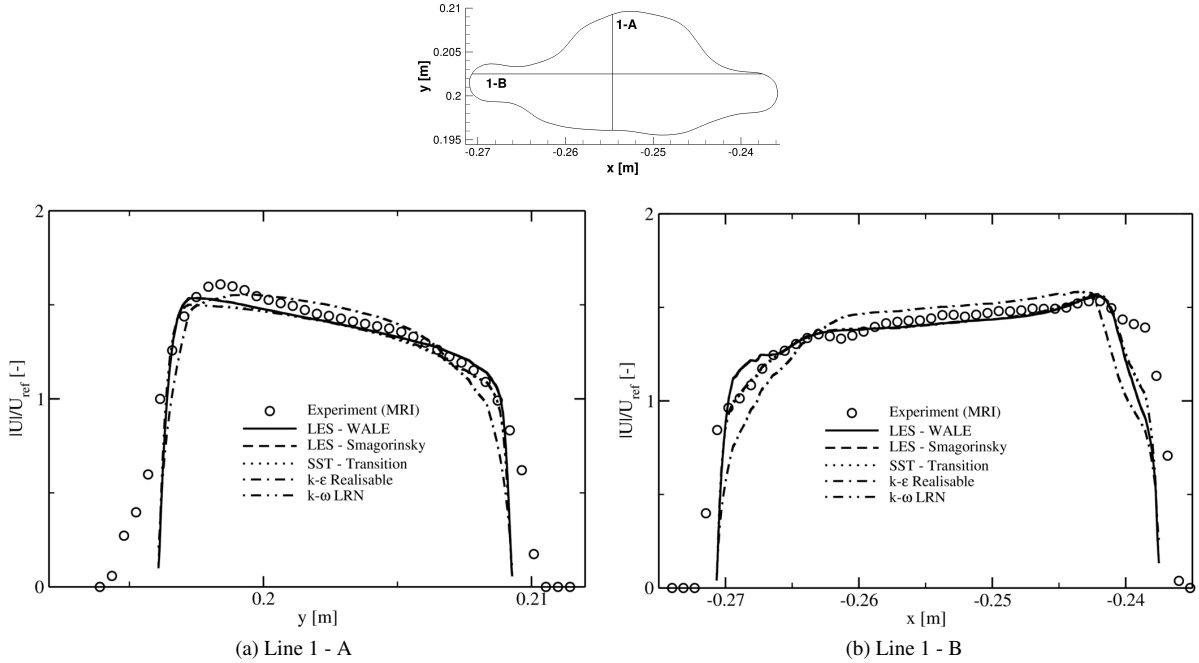

(a) Line 1 - A

(b) Line 1 - B

Figure 8.20: Scaled velocity magnitude profiles extracted in plane 1.

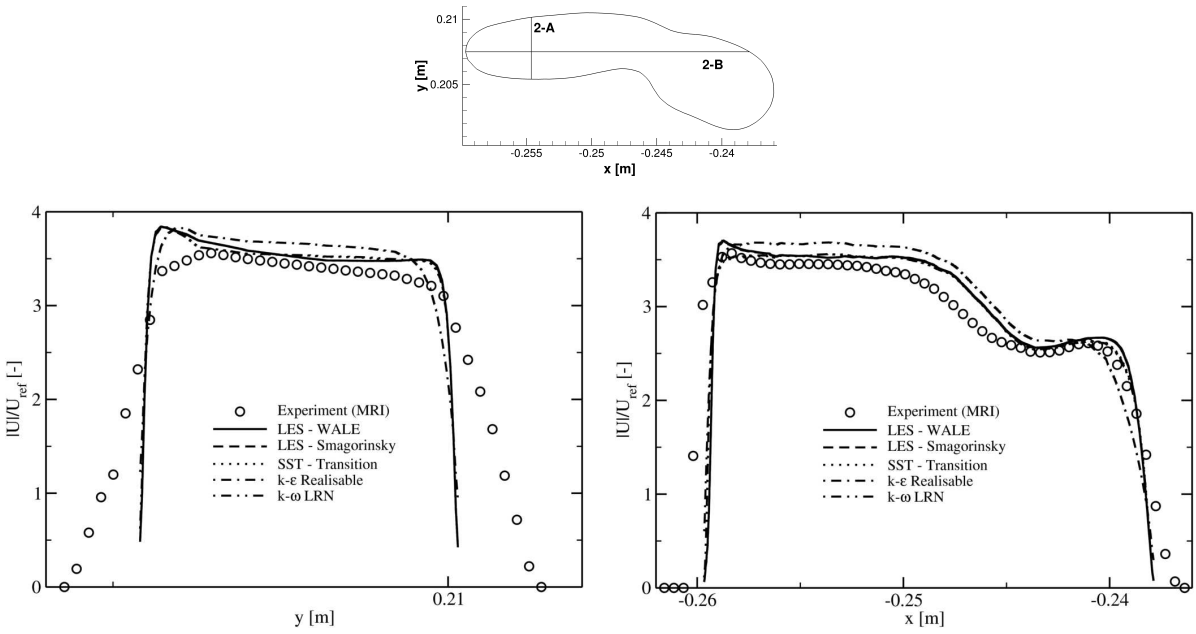

(a) Line 2 - A (b) Line 2 - B

Figure 8.21: Scaled velocity magnitude profiles extracted in plane 2.

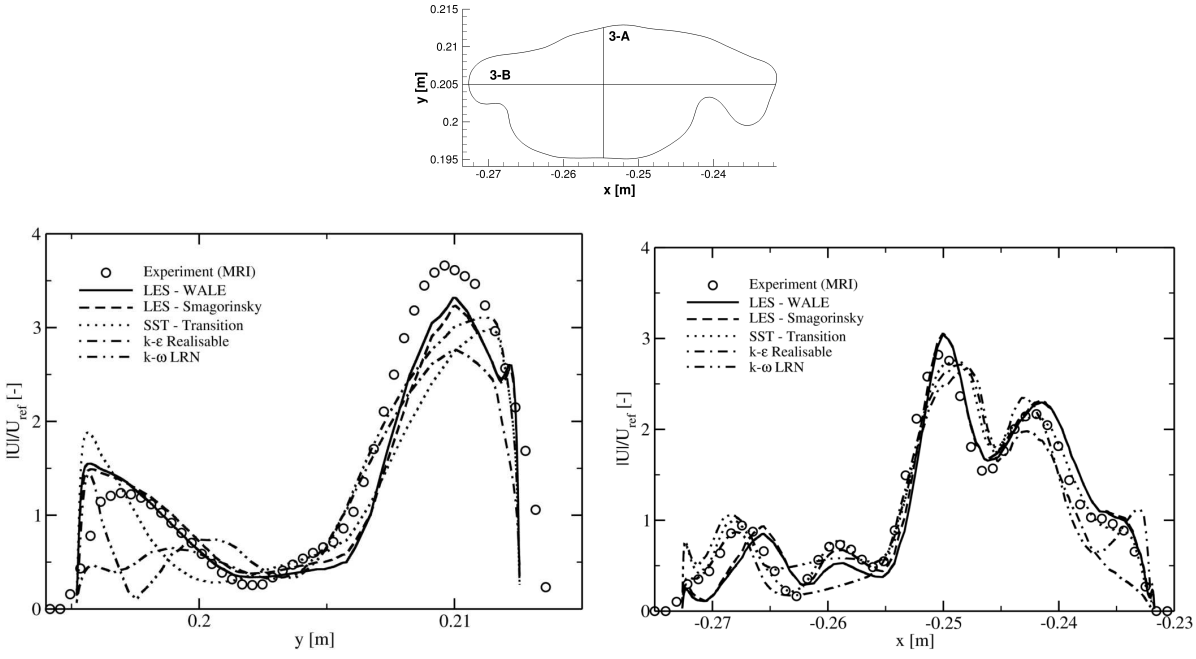

(a) Line 3 - A (b) Line 3 - B

Figure 8.22: Scaled velocity magnitude profiles extracted in plane 3.

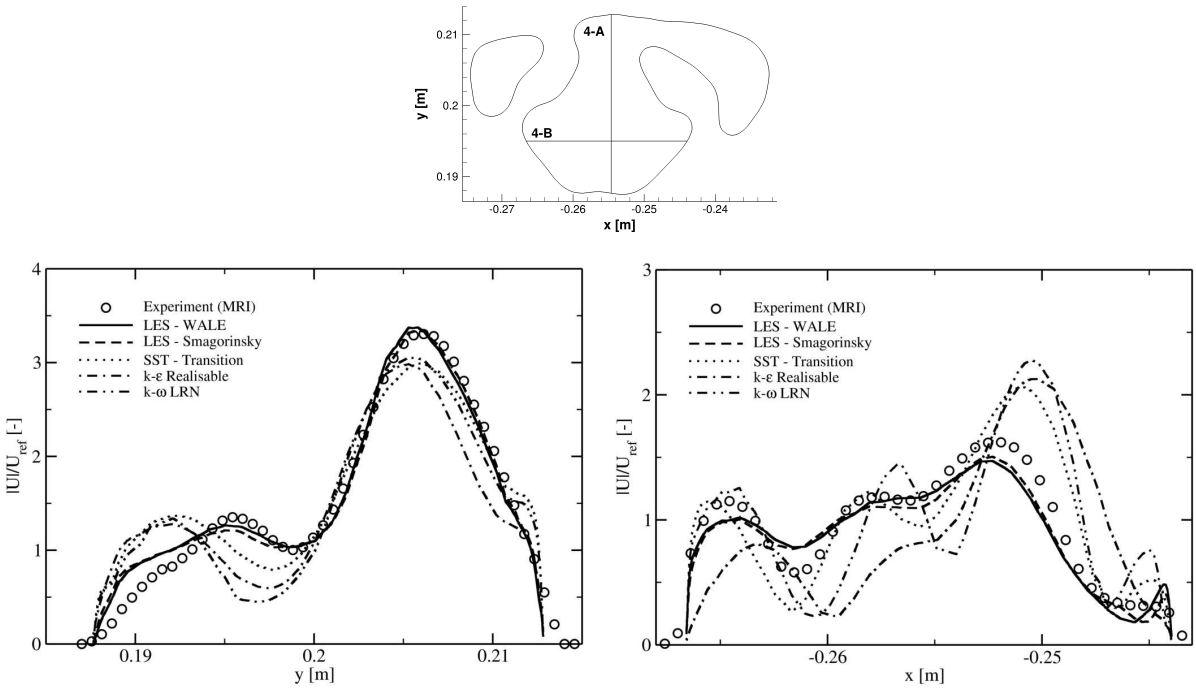

(a) Line 4 - A (b) Line 4 - B

Figure 8.23: Scaled velocity magnitude profiles extracted in plane 4.

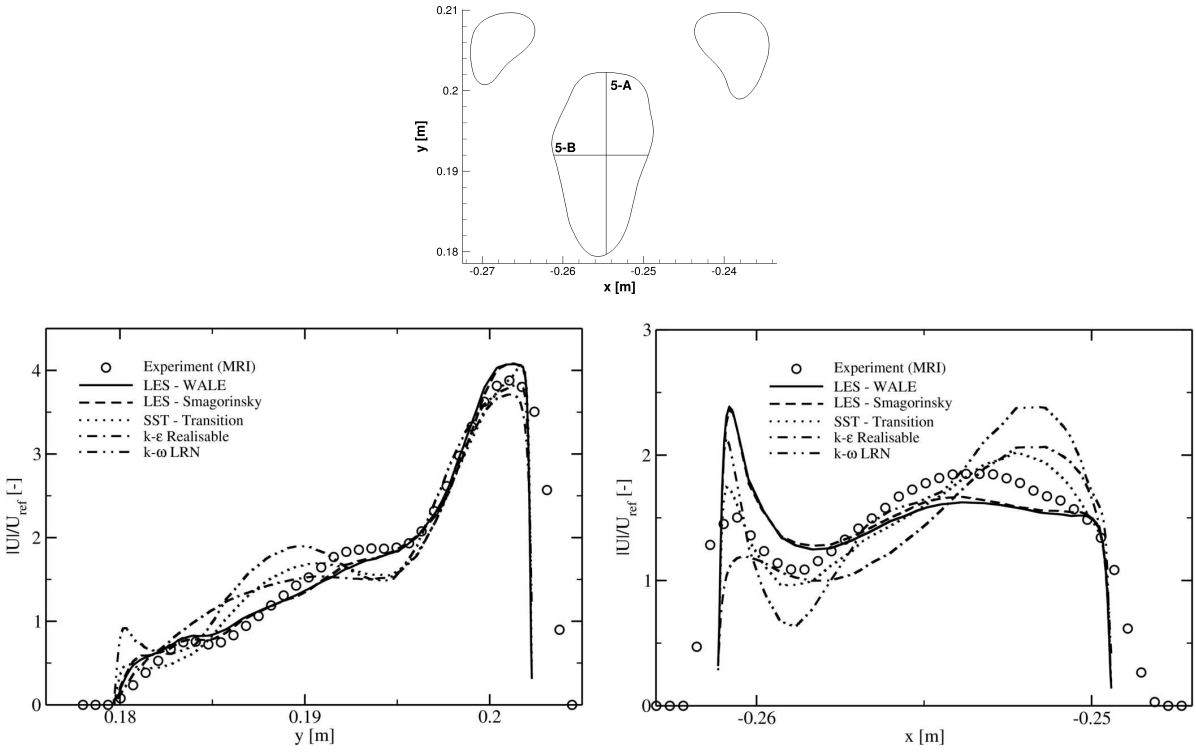

(a) Line 5 - A (b) Line 5 - B

Figure 8.24: Scaled velocity magnitude profiles extracted in plane 5.

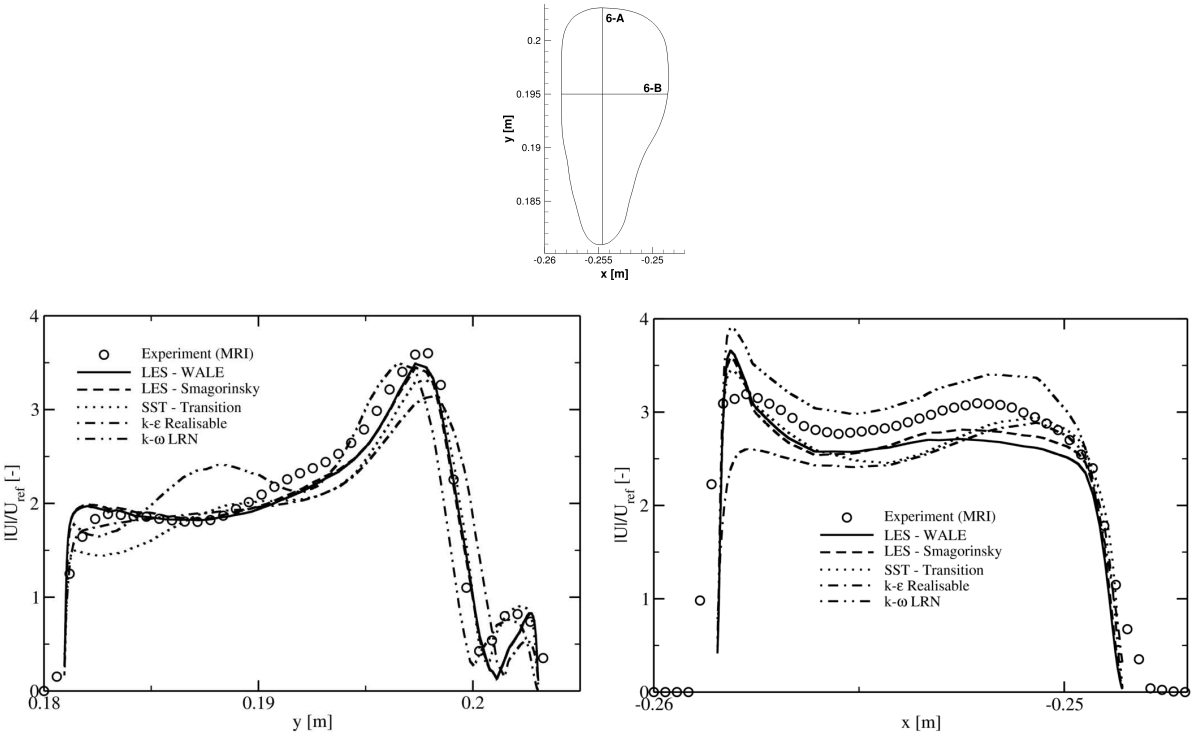

(a) Line 6 - A (b) Line 6 - B

Figure 8.25: Scaled velocity magnitude profiles extracted in plane 6.

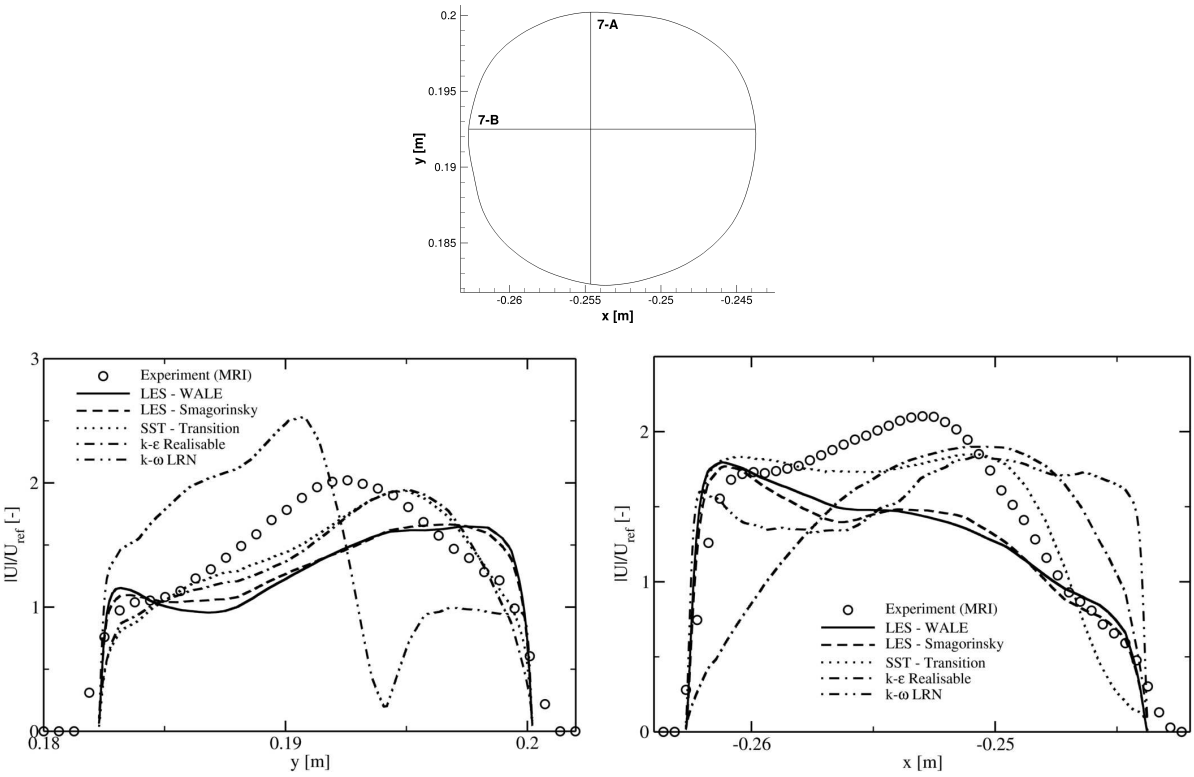

(a) Line 7 - A (b) Line 7 - B

Figure 8.26: Scaled velocity magnitude profiles extracted in plane 7.

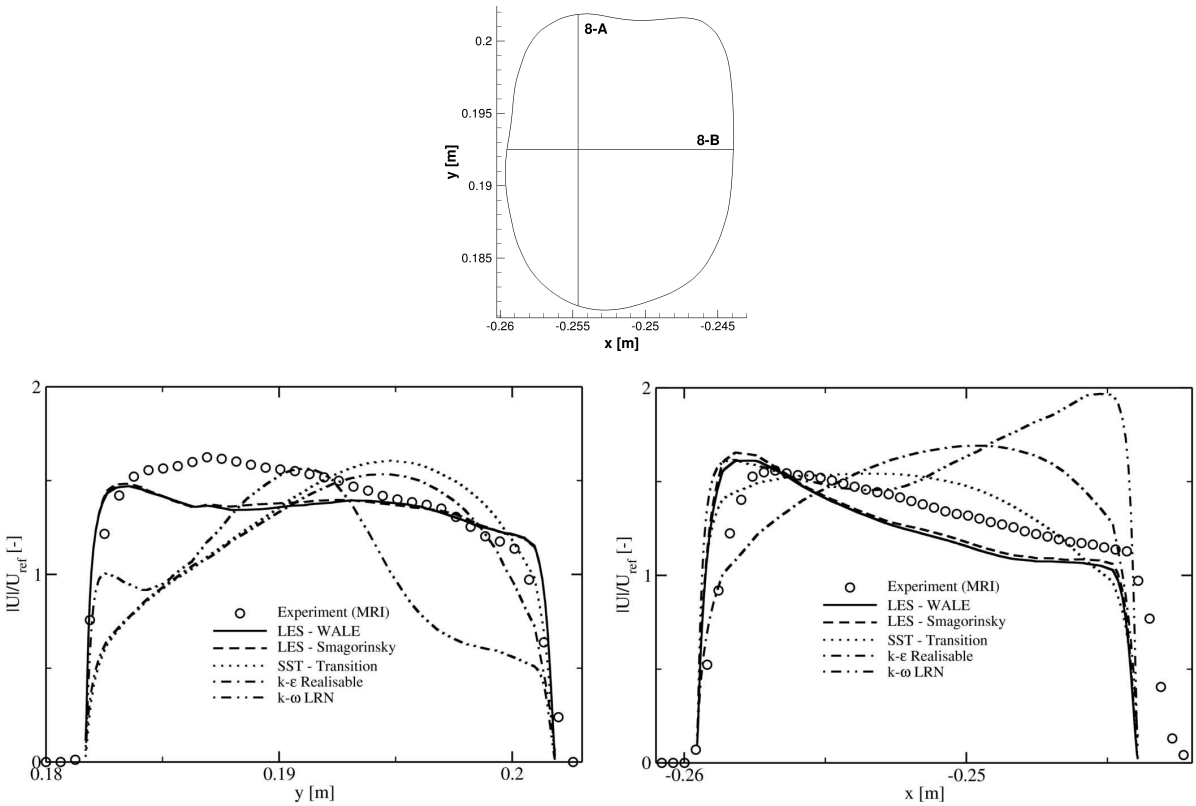

(a) Line 8 - A

(b) Line 8 - B

Figure 8.27: Scaled velocity magnitude profiles extracted in plane 8.

8.2.2.3 Turbulent Kinetic Energy

Due to a lack of experimental velocity fluctuation data the turbulent kinetic energy profiles obtained in the simulations cannot be compared to experimental data. What remains is to compare the different turbulence models to discuss their possible effect on particle deposition.

The turbulent kinetic energy in plane 4 and plane 9 are plotted in figure 8.28 and 8.29 respectively. The turbulence starts to occur after the oropharynx (the narrowing bend, in figure 8.29) which is similar to what other studies have found albeit in a simplified geometry (Zhang and Kleinstreuer, 2011). The turbulence is very localised and is significantly dampened ~10 cm downstream of its occurrence. The localised turbulence was also observed in the simplified geometry by Zhang and Kleinstreuer (2011).

The TKE observed in the large eddy simulations is much higher than in the RANS simulations and thus the turbulent dispersion observed in the LES will be higher than in the RANS simulations. It must be noted that for the RANS simulations a first order upwinding scheme was used due to oscillatory behaviour of the residuals (average of the pressure residual was 8×10^{-3}) which occurred when switching to second order upwinding; the use of the first order scheme can also be one of the explanations for the dampened levels of TKE but may not be the entire story; in some literature LES seem to predict larger peaks than RANS models, such as in the constricted tube by Zhang and Kleinstreuer (2011) where the LES predicts a TKE peak double the size of the SST (and also 50% larger than the experiments).

A suggestion would be to perform simulations in geometries consisting of just the mouth and throat and to increase the mesh density and maybe reduce the flow rate since it may be an issue related to the resolution of the grid (figure 8.6) and to find a correct procedure to tackle the oscillatory behaviour observed when second order discretisation was used.

Another peculiarity is that the flow reattachment point in most of the RANS models and the LES are approximately the same, even though the turbulent kinetic energy in the LES is larger in this region. If no velocity profiles were available one would expect the LES to reattach sooner due to the increased momentum transport (towards the wall) predicted by this model.

One of the advantages of LES compared to RANS models is that the root mean square (RMS) of the three velocity components is available, thus yielding information whether the large scale turbulence in this particular system is isotropic or not. The importance of this is that the particles feel the velocity field and its fluctuations and therefore an anisotropically fluctuating field will yield different deposition patterns than an isotropically fluctuating field. This is of importance for example in the region near the wall where for RANS models the fluctuations are still modelled isotropically; Dehbi (2008) showed that the fluctuations in the wall normal velocity component are over predicted when applying an isotropic model which will lead to an over-estimation of the particle deposition.

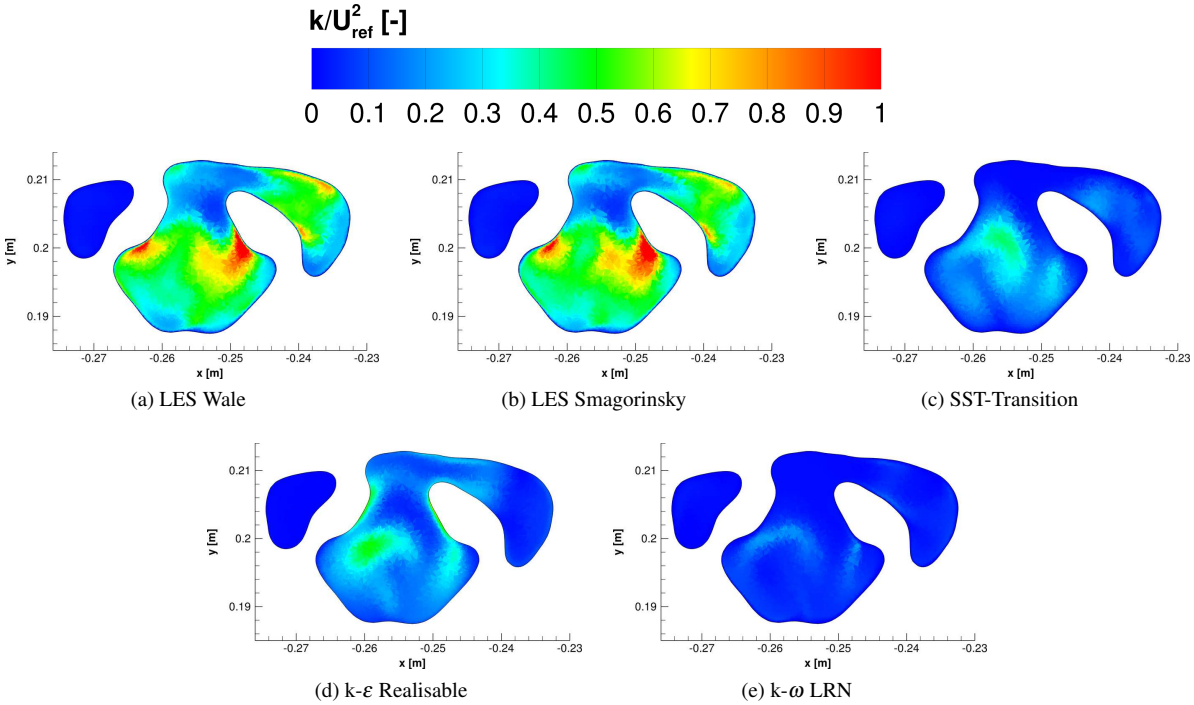

(a) LES Wale (b) LES Smagorinsky (c) SST-Transition

(d) k-ε Realisable (e) k-ω LRN

Figure 8.28: Contours of the scaled turbulent kinetic energy in plane 4.

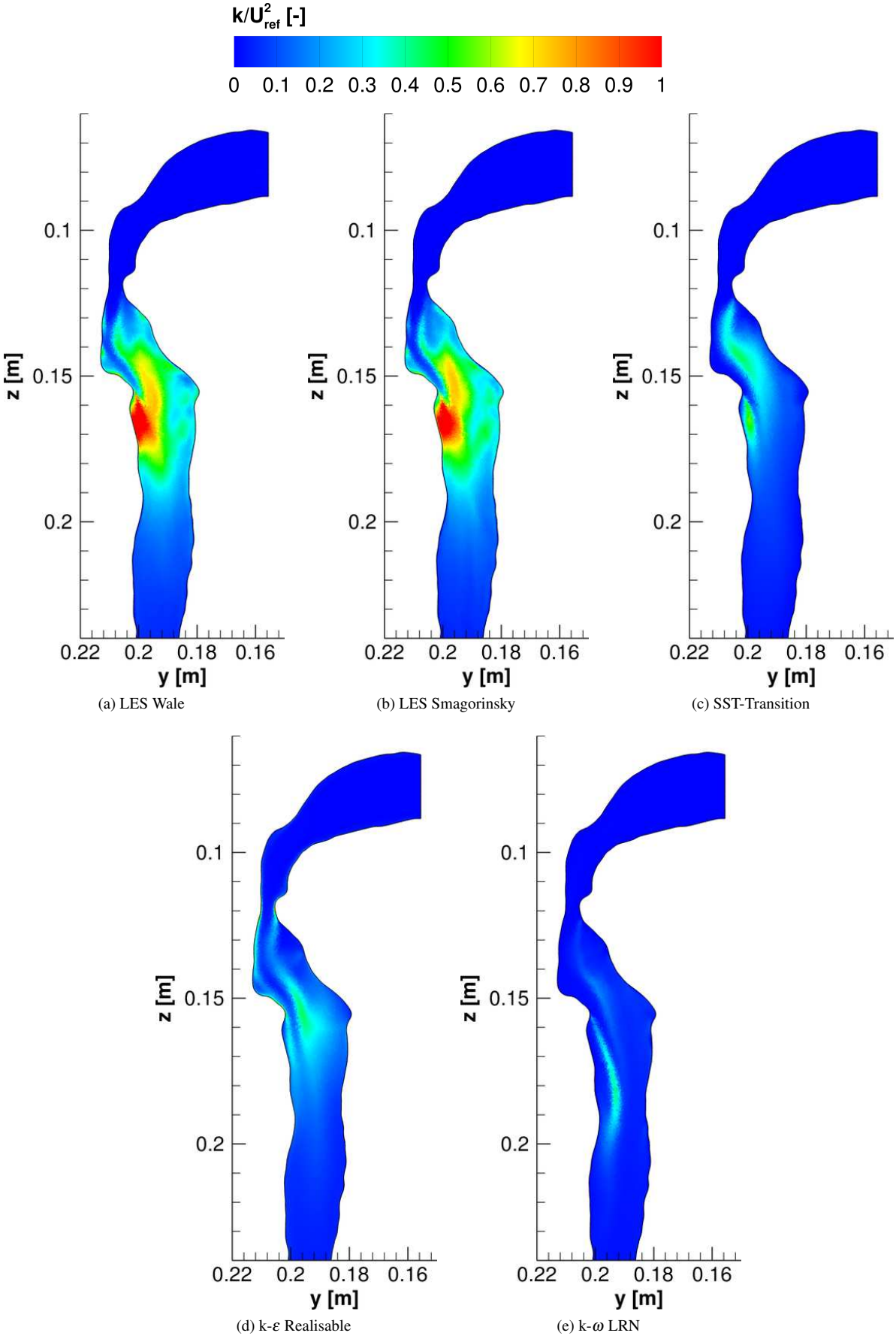

(a) LES Wale (b) LES Smagorinsky (c) SST-Transition

(d) k-ε Realisable (e) k-ω LRN

Figure 8.29: Contours of the scaled turbulent kinetic energy in plane 9.

8.3 Particle Deposition

In the comparison of the flow field it became clear that among the simulations the LES models show the most agreement with experimental data and thus the particle deposition should be performed using one of the two LES models however, due to time limitations the particle deposition is carried out with the SST-model instead. This means that the results presented in the present and the following section should only be compared to each other to investigate the effect of certain parameters which are likely to hold when a more accurate flow field is used, these parameters are the Stokes number (St_{ref}), inclusion of turbulent dispersion and the activation of a magnetic field. The latter will be discussed in section 8.4. It was estimated that the gravity does not significantly alter the deposition in the upper parts but may become important in the bottom part of the geometry slightly (see section 4.2) due to the decreasing velocities and smaller length scales. Therefore, the gravity was turned on (in the positive z-direction) in all but one simulation (to see if there was indeed a change to be observed in the bottom part of the geometry). An overview of the particle forces used can be found in table 8.5.

The choice of using the SST-Transition flow field for the basis of the particle deposition in conjunction with the isotropic turbulent dispersion will likely deviate from experimental observations (and also with respect to the LES) since the flow field downstream of the most turbulent region does not agree with the experimental observations. Additionally the isotropically modelled velocity fluctuations are also erroneous in proximity of the wall.

Table 8.5: Overview of the particle forces used in this chapter.

F_d	F_g and F_b	F_m	F_{Saffman}	$F_{\text{p.grad.}}$	Turbulent Dispersion
+	+	+	-	-	+

The local particle deposition efficiencies are given by the following formulae. These local deposition efficiencies allow for an injection other than the inlet and still obtain the correct efficiency for the bottom, left lung and right lung.

$$DE_{top} = 100\frac{N_{wall,z>z_{middle}}}{N_{inlet}} \tag{8.5}$$

$$DE_{bottom} = 100\frac{N_{wall,z<z_{middle}}}{N_{wall,z<z_{middle}} + N^{escape}_{left\,lung} + N^{escape}_{right\,lung}} \tag{8.6}$$

$$DE_{left\,lung} = 100\frac{N_{wall,z<z_{middle}\,\&\,x<x_{middle}}}{N^{escape}_{left\,lung} + N_{wall,z<z_{middle}\,\&\,x<x_{middle}}} \tag{8.7}$$

$$DE_{left\,lung} = 100\frac{N_{wall,z<z_{middle}\,\&\,x>x_{middle}}}{N^{escape}_{right\,lung} + N_{wall,z<z_{middle}\,\&\,x>x_{middle}}} \tag{8.8}$$

The definitions of z_{middle} and x_{middle} can be found in figure 8.30 below.

Some particles can be trapped in recirculation zones and their trajectory cannot be calculated within the prescribed number of iterations. Therefore an effective number of particles at the inlet is used for the calculations and is given by the following formula:

$$N_{in,effective} = N^{escape}_{right\,lung} + N^{escape}_{left\,lung} + N_{wall} \tag{8.9}$$

Additionally, to characterise the steerability of the particles a ratio of the total number of particles going to the left to the total number of particles going to the right has been defined as the Steering Factor (SF):

$$SF_L = \frac{N^{escape}_{left\,lung} + N_{wall,z<z_{middle}\,\&\,x<x_{middle}}}{N^{escape}_{right\,lung} + N_{wall,z<z_{middle}\,\&\,x>x_{middle}}} \tag{8.10}$$

If the particle distribution between the right and left lung is related to the flow distribution between the right and left lung (0.539:0.461 for the SST model) then the SF_L would tend to $SF_{L,FD}$ = 0.854 for very small St since they behave almost like tracers.

An additional parameter is the penetration steering factor SF_{pen} which is the relative amount of particles which escape the left side of the lung compared to the right side:

$$SF_{pen} = \frac{N_{left\ lung}^{escape}}{N_{right\ lung}^{escape}} \tag{8.11}$$

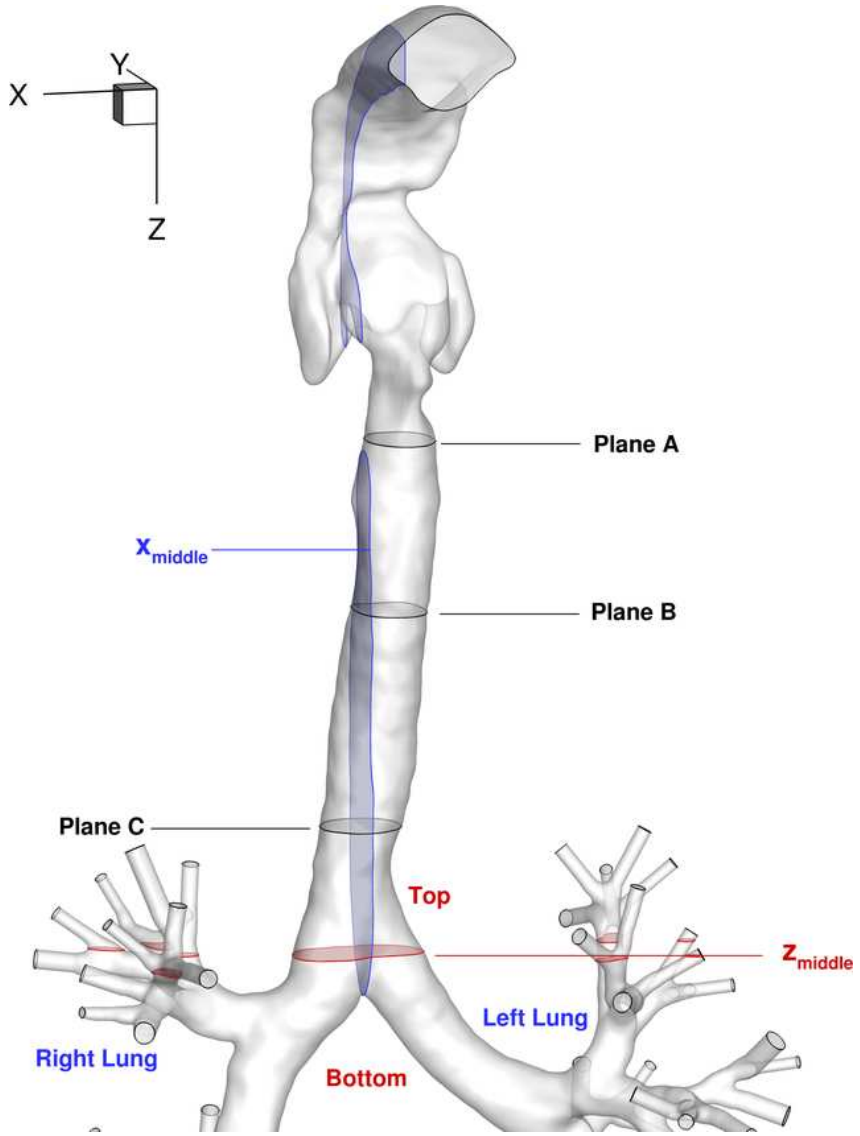

Figure 8.30: Schematic overview of the division of the geometry between top and bottom and left and right as well as several sampling planes. The coordinates are: z_{middle}=0.29 m, x_{middle}=-0.25 m, z_{planeA}=0.17 m, z_{planeB}=0.21 m, z_{planeC}=0.26 m.

8.3.1 Results of Passive Particle Deposition

The results for the passive particle deposition without turbulent dispersion are given in table 8.6. When particles are released at the inlet of the geometry, a fraction of the particles (depending on St, up to 77%) are captured in the mouth and upper part of the throat. Thus for studying the particle deposition in regions downstream of the throat, a significant number of particles have to be injected at the mouth for a statistically reliable number of particles to remain available for deposition. Therefore particles were injected in a plane downstream of the most turbulent region but upstream of the location of the magnetic wire (in the next section) this plane is referred to as plane A (z = 0.17 m). Particles are distributed on this plane using a random distribution which may describe the 'real' distribution at the height of plane A for particles released at the inlet. This allows for an increase in the total number

of injected particles without 'wasting' resources. The results of the particle injection at plane A are given in the same table (table 8.6).

The steering factor SF_L increases with increasing St when particles are injected at the mouth while it seems to be decreasing with increasing St when injected at plane A though the differences are very small. It seems that either the sample size for the inlet injection is too small or the random particle distribution (at plane A) assumption does not hold. To disprove the sample size the results with turbulent dispersion enabled, where the number of inject particles can be greatly increased, are given in table C.1. The same behaviour is observed: for the inlet injection the SF increases with increasing St however, for the injection at plane A it becomes clear that there is no clear cut relation between St and SF_L .

The penetration steering factor SF_{pen} for low deposition efficiencies is approximately equal to the SF_L which was expected due to the definitions of the two parameters. For the standard Fluent injections and the injection at plane A the SF_{pen} increases with increasing St.

This leaves us with the particle distributions, from the previous chapters we have seen that the particle distribution is not trivial. If the distribution of the particles at the height of the injection plane A for the inlet injection is plotted, see figure 8.31, a major difference can be seen for higher St. It must be noted that these distributions are from the case with the turbulent dispersion enabled. The reason why for lower St the distributions are more alike is that the particles follow the fluid motion more closely and the dispersion acts to 'randomise' the distribution, thus the assumption that the particle distribution at height A can be seen as a random distribution becomes less false when St decreases. Conversely, particles which deviate more and more from tracer behaviour are filtered upstream of plane A giving rise to the respective distribution shown in figure 8.31. This means that, for a more physiologically realistic study either particles should be injected from the inlet or the 'real' distribution at plane A should be used. Using the distribution from a previous simulation requires an equal St and that the magnetic field does not significantly alter the deposition behaviour in the mouth region; the resulting distribution can then be used to study for example different wire positions at a reduced computational cost.

Table 8.6: Particle deposition efficiencies and steering factor for two different injection planes with turbulent dispersion disabled. The number of particles injected for each injection are: 7×10^3 for the inlet injection, 26×10^3 for the injection at plane A.

St_{ref} [-]	Injection	DE_{top} [%]	DE_{bottom} [%]	DE_{LL} [%]	DE_{RL} [%]	SF_L [-]	SF_{pen} [-]
4.8×10^{-5}	Inlet	0.92	0.44	0.49	0.41	0.67	0.67
4.8×10^{-5}	Plane A	0.96	0.39	0.50	0.30	0.78	0.78
4.8×10^{-3}	Inlet	1.59	0.76	0.63	0.85	0.64	0.64
4.8×10^{-3}	Plane A	1.18	0.48	0.51	0.45	0.79	0.79
4.3×10^{-2}	Inlet	25.54	3.33	3.55	3.13	0.91	0.91
4.3×10^{-2}	Plane A	2.19	3.60	3.14	3.95	0.77	0.77
1.2×10^{-1}	Inlet	77.62	22.55	25.39	18.89	1.29	1.19
1.2×10^{-1}	Plane A	6.89	24.31	18.56	28.60	0.75	0.85

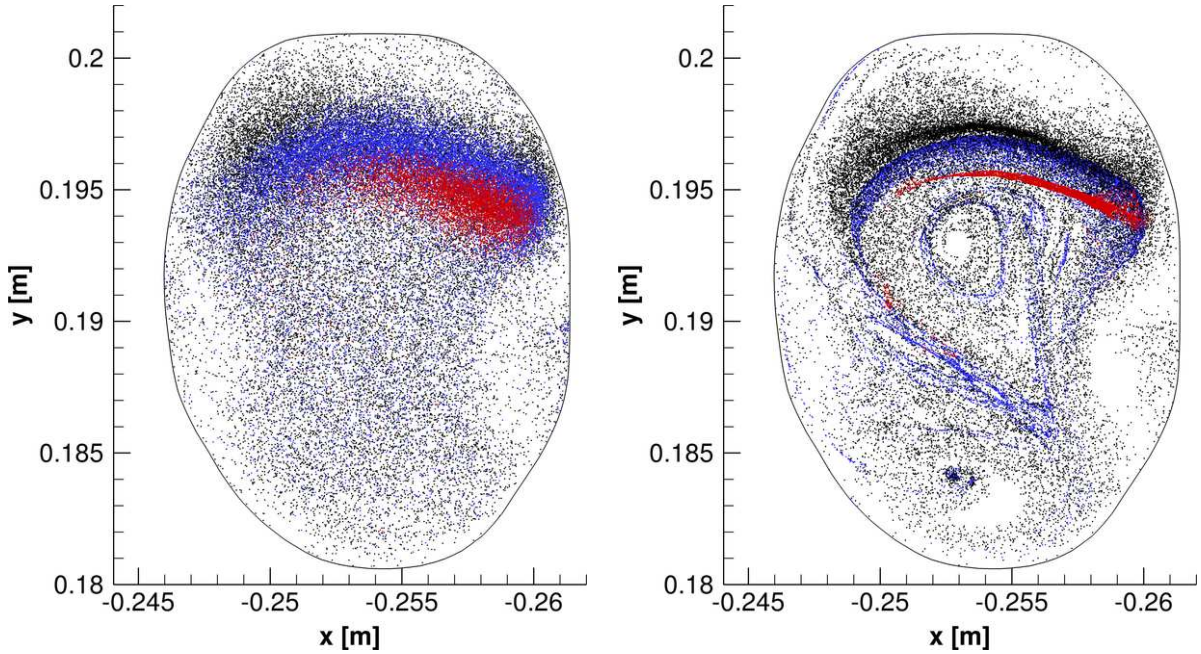

(a) With TD

(b) Without TD

Figure 8.31: Qualitative comparison of the particle distributions at plane A for injections at the inlet (random distribution) the left lung is located in the negative x-direction. Black: St = 4.8×10^{-5} , blue: St = 4.3×10^{-2} , red: St = 1.2×10^{-1}.

The standard Fluent injection used in tables 8.6 and C.1 is compared to a random particle distribution at the inlet (specified by generating a random distribution in a circle larger than the inlet and saving it as an injection file) with 2.8×10^5 particles. The motivation behind this is that Fluent releases a particle, or parcel, at the centre of the cell so the particles have a distribution equal to the cell centre distribution at the surface; since a boundary layer mesh is used a lot of particles are located very near to the wall. The results of this comparison are given in figures 8.32a and 8.32d. Note that an increased deposition efficiency in the top part of geometry will result in a significantly smaller sampling size for downstream statistics and thus the error becomes larger with increasing St number; some data points for the higher St were removed due to the low sampling size. For the total deposition the results obtained with a random inlet distribution always lie below the standard Fluent injection which is expected since relatively fewer particles are released near the wall. The SF_L is also significantly higher when a random distribution is used.

The inclusion of a turbulent dispersion model, which based on the turbulent kinetic energy adds velocity fluctuations to the flow field, has a significant effect on the particle deposition for particles ranging from St ranging from 4.8×10^{-5} - 1.2×10^{-1}. With the inclusion of turbulent dispersion, the deposition does not tend towards zero due to the velocity fluctuations near the wall. The deposition in each part of the geometry has increased (figures 8.32b and 8.32c). The SF_L shows quite interesting behaviour, when turbulent dispersion is activated it decreases when the particles are distributed randomly at the inlet while it increases when the Fluent surface injection is used. The SF_L also does not tend towards the previously mentioned $SF_{L,FD}$=0.854 for small St. When no turbulent dispersion is present, the steering factor remains practically constant until St = 3.3×10^{-2} there it starts to increase but when St = 1.2×10^{-1} it suddenly drops below the level of the SF_L at St $< 4.3\times10^{-2}$. It seems that when the particles behave more like a tracer the SF_L tends to SF_L =1.2 and the distribution at the height of the bifurcation is approximately constant. Increasing the St, and thus decreasing their tracer-like behaviour, to a critical level (St = 3.3×10^{-2}) changes the distribution at the height of the bifurcation such that the SF_L is increased. When St = $1.2\times10^{=1}$ this particle distribution pattern is modified such that there is an almost equal distribution of the particles at the height of the bifurcation. Unfortunately, the particles were not sampled in the bifurcation region itself but they were sampled 3 cm upstream of the bifurcation. A comparison between different St and the distribution at this plane can be found in figure C.43. When turbulent dispersion is enabled, the SF_L increases but does not show the drop like the simulations without turbulent dispersion do. Although not shown in this graph,

when core-shell particles are used the same behaviour is observed at around the same St numbers. This graph can be found in figure C.48.

The behaviour of the SF_{pen} is qualitatively similar to the SF_L though quantitative differences are observed at larger St due to the increased deposition and SF_L takes into account both the particles leaving the domain and those that deposit while SF_{pen} is purely based on the particles which leave the domain. Both the SF_L and SF_{pen} indicate that the majority of the particles released at the inlet when distributed randomly end up in the left lung when turbulent dispersion is not activated.

The local deposition efficiency in the left lung shows quite a remarkable behaviour, the efficiency at $St = 4.3\times10^{-2}$ is actually higher than that at $St = 7.7\times10^{-2}$ (6.6% vs 5.6%). The simulation has been performed multiple times (each of the times the inlet distribution was generated from scratch) and this behaviour was observed every time. Like the SF_L it seems to be related to the particle distributions which is a function of the St since for the core-shell particles the same behaviour was observed.

One small simulation, albeit with a relatively small sample size (3×10^4 particles), was performed with gravity turned off. The total deposition efficiencies do not differ significantly but the local deposition patterns differ in the more distal branches (figures C.52 and C.53). Notable however, is the discontinuity in the local deposition in the left lung; while the bump seems to be smaller when gravity is turned off, it is still present (figure C.50b). The particle distributions at z = 0.17 m, z = 0.21 m and z = 0.26 m, do not show any significant difference with gravity on or off (other than that the positions are slightly different because the particles at the inlet are distributed randomly every time, figure C.51). The steering factor shows the same behaviour as the simulations with gravity, further illustrating that in the upper part of the geometry the effect of gravity can be neglected (figure C.50c).

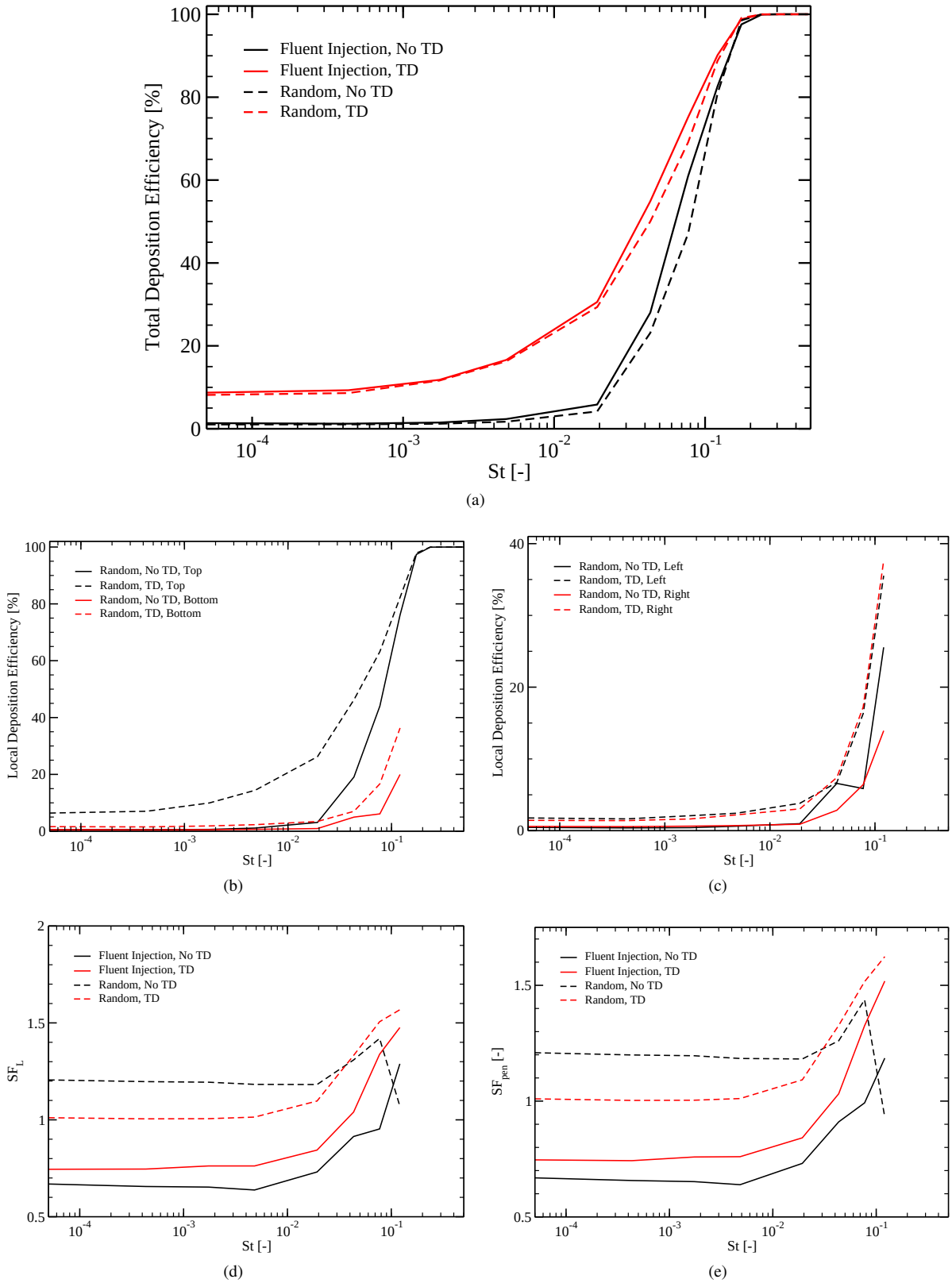

Figure 8.32: Results of the passive particle deposition in human specific geometry. (a) total deposition efficiency, (b) local deposition efficiency at the top and bottom part of the geometry, (c) local deposition efficiency in the left and right lung, (d) the steering factor and (e) the penetration steering factor. Note that all the particles were injected at the inlet and 2.8×10^5 particles were used in the random injection.

Since the data presented in the previous figures and tables is based on a rather crude segmentation of the geometry, the dimensionless surface concentration ζ is plotted for St = 1.2×10^{-1} for both with and without turbulent dispersion in figure 8.34. The surface concentration visually shows the effect of the turbulent dispersion and the filtering effect of the upper airway. The dimensionless surface concentration $\zeta_{1\text{ mm}}$, based on a 1 mm search radius, is defined as:

$$\zeta_{1\text{ mm}}(wall\,cell)\,[-] = \frac{x_{wall,centre} - N_{x_p \leq 1\,mm}}{N_{\text{in,effective}}} \tag{8.12}$$

From figures 8.34 and C.45-C.47 it can be seen that without the inclusion of turbulent dispersion, particles deposit at the back of the pharynx and the deposition increases with increasing St, bearing resemblance to the 90° bend studied in chapter 6.1. When turbulent dispersion is activated, the regions at which the particles previously deposited (without TD) remain present but the deposition efficiency is now increased and the area of deposition has greatly increased. Additionally, particles are now also deposited in an elongated clockwise (when entering the mouth and looking down the trachea) pattern downstream the larynx. This pattern can be explained by looking at the region where initially the particle distribution is the highest (for example plane A) and observing the particle distribution downstream of that place together with streamtraces (see figure C.44). The particles are deposited due to the wall normal velocity fluctuations; it should be noted again that the turbulent dispersion model in Fluent over predicts the wall normal velocity fluctuation due to isotropic assumption. Thus when turbulent dispersion is enabled, the deposition in the pharynx is a combination of the inertial impaction due to the deflection of the flow and turbulent dispersion and downstream of the larynx the turbulent dispersion plays the biggest role.

A comparison of the total deposition efficiency as a function of the impaction parameter ($IP = d_p^2\phi_V$) of the simulations compared to experimental data can be found in figure 8.33a. It must be noted that the impaction parameter is used in stead of the St due to the experimental data being reported as such; the IP does not take into account the density for example even though the deposition of massless particles or near massless particles is different from particles with a larger mass (smaller mass means smaller momentum). Therefore, for some of the data the total deposition efficiency as a function of the St is compared, see figure 8.33b. The limitation of the impaction parameter is illustrated in figure C.49. The simulations without turbulent dispersion falls within the range of simulations and experiments in a simplified geometry for St $< 1\times10^{-1}$ but in the present geometry full deposition is achieved for lower St than for the simplified geometries. With turbulent dispersion enabled however, the deposition is over predicted in the present simulations due to the isotropy of the velocity fluctuations; in the simulations performed by Zhang et al. (2005) (using the LRN k-ω model) a damping function was used to dampen the wall normal velocity fluctuation by a factor $f = 1 - e^{-0.02y^+} \approx 0.02y^+$ if $y^+ < 10$. This illustrates the need to alter the turbulent dispersion model or use a different model to solve the flow where the anisotropy may be resolved such as LES or a Reynolds Stress Transport model.

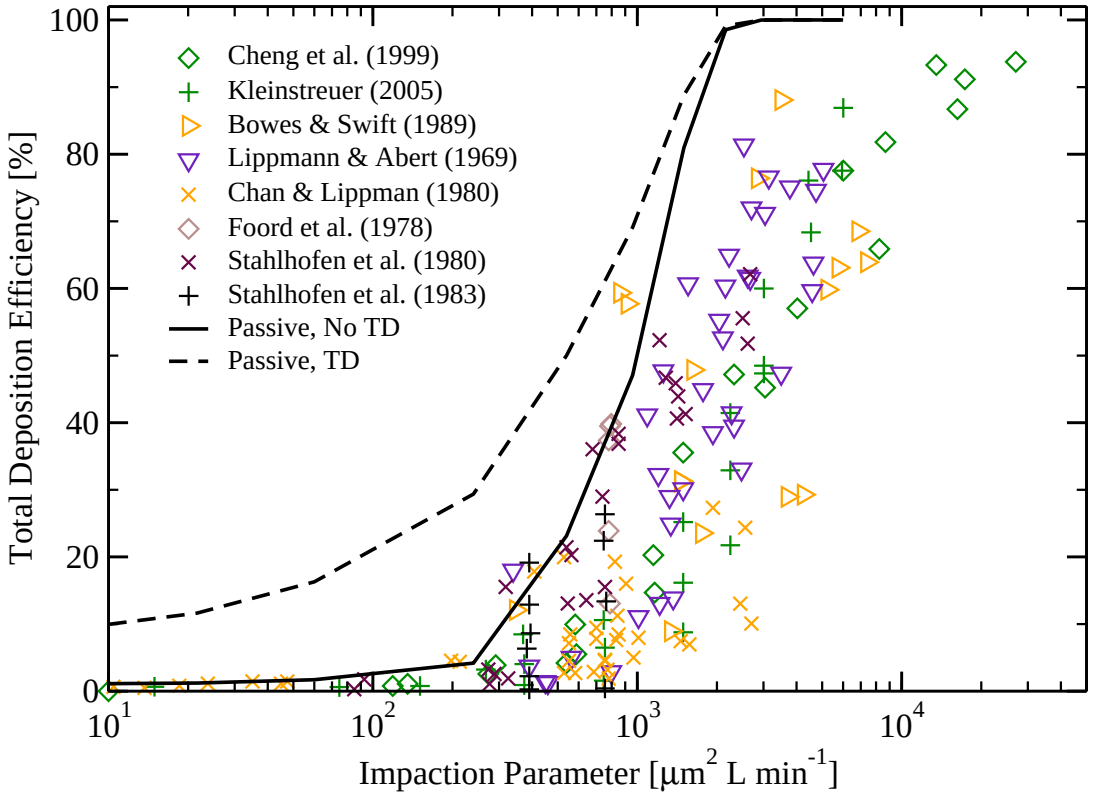

(a)

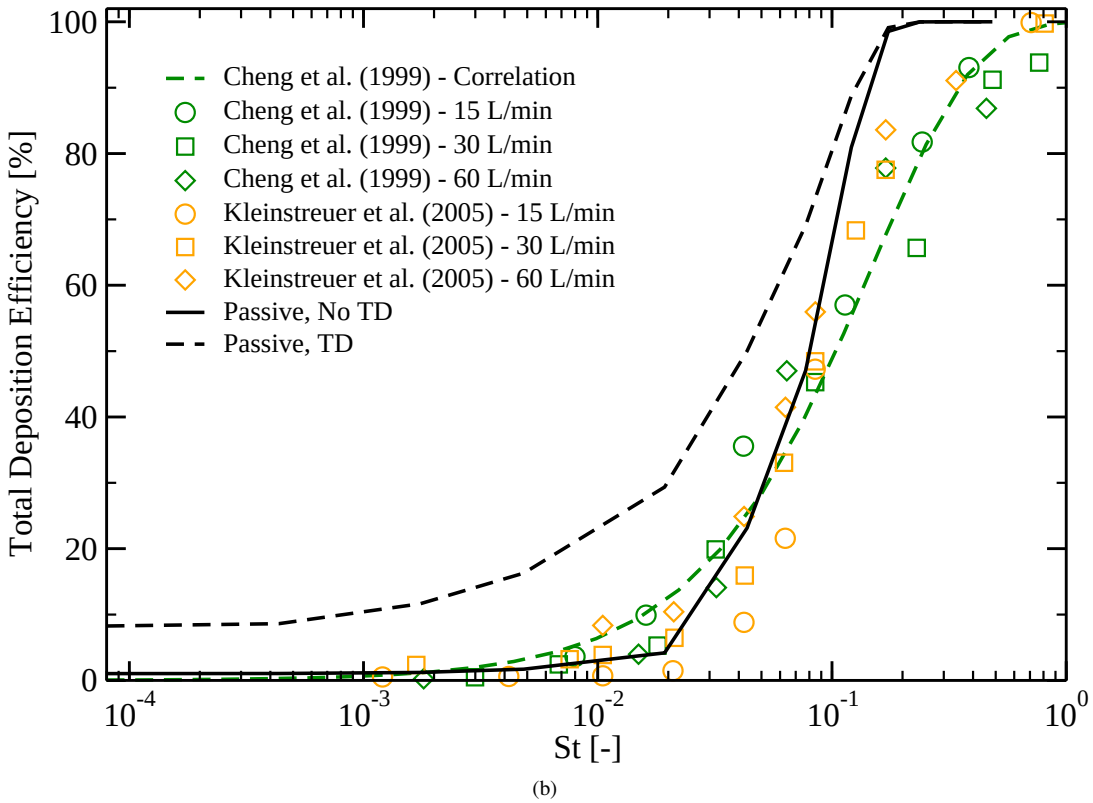

(b)

Figure 8.33: Comparison of total deposition efficiency as a function of (a) inertial impaction parameter ($IP = d_p^2 \phi_V$) and (b) St.

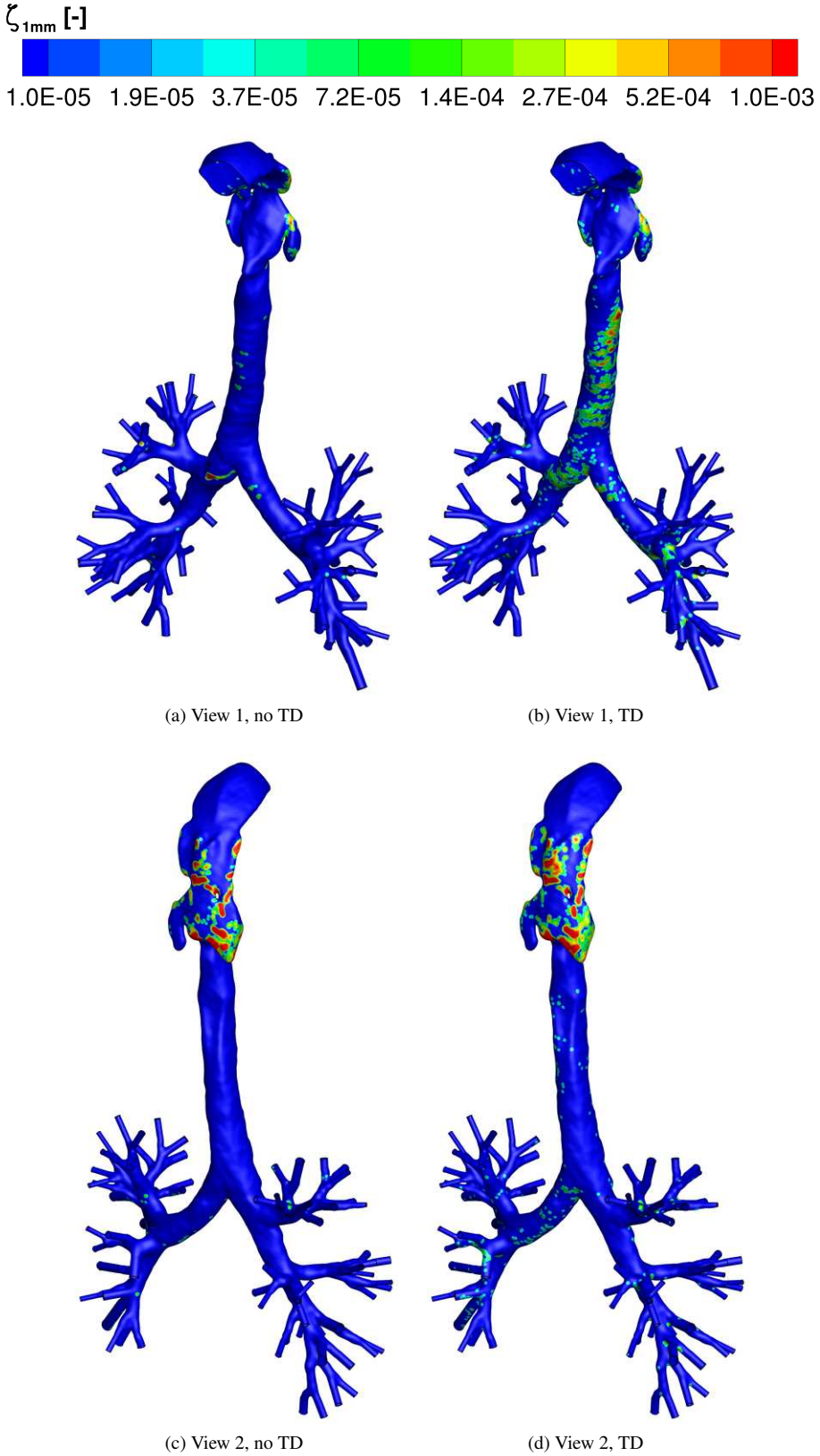

(a) View 1, no TD

(b) View 1, TD

(c) View 2, no TD

(d) View 2, TD

Figure 8.34: Contours of local deposition efficiency $\zeta_{1\text{ mm}}$ from particle deposition with turbulent dispersion disabled (a,c) and enabled (b,d) for St = 1.2×10^{-1}.

8.4 Magnetically Enhanced Particle Deposition

First core particles (d^*_{mp} = 1), which are the same particles as in the previous section, are used to demonstrate that particles can be steered under the influence of a magnetic field. Then core-shell particles, which feature a smaller magnetic volume than core particles (d^*_{mp} = 0.84), are used to see whether these more realistic particles can be used to steer administered drugs. The shell consists of carrier material (poly lactic acid, $\rho_{PLGA} = 1300\,kgm^{-3}$) and medicine (mass fraction of 30%, $\rho_{drug} = 1610\,kgm^{-3}$ after Righolt (2010)). The core is again maghemite with a density of 4860 kg/m^3.

Table 8.7: Overview of the particles used in the deposition study.

Particle	**d_{mp} [-]**	**Average density [kg/m^3]**
Core	1	4860
Core-shell A	0.84	3413

For the positioning of the current carrying wire, a point on the geometry-wall was arbitrarily selected, this point is called reference point A. Wire positions 1 and 2 correspond to a 1 cm and 10 cm displacement in the negative x-direction respectively. This means that the wire is positioned on the right side of the geometry (when facing the inlet) thus on the side of the left lung. Contours of the magnetic field strength B are given for a distance of 1 cm in figure 8.35a and 10 cm distance in figure 8.35b. The current through the wire in the figure is 10^5 A so that the magnetic field strength at the reference point on the geometry are 2T and 0.2T for a distance of 1 cm and 10 cm respectively. An overview of the positions can be found in table 8.8.

Table 8.8: Overview of the wire positions with the names, reference position, displacement from the reference position and the direction of displacement.

Wire	**Reference position x [m]**	**Reference position z [m]**	**Distance [cm]**	**Direction**
Position 1	-0.252	0.269	1	-x
Position 2	-0.252	0.269	10	-x

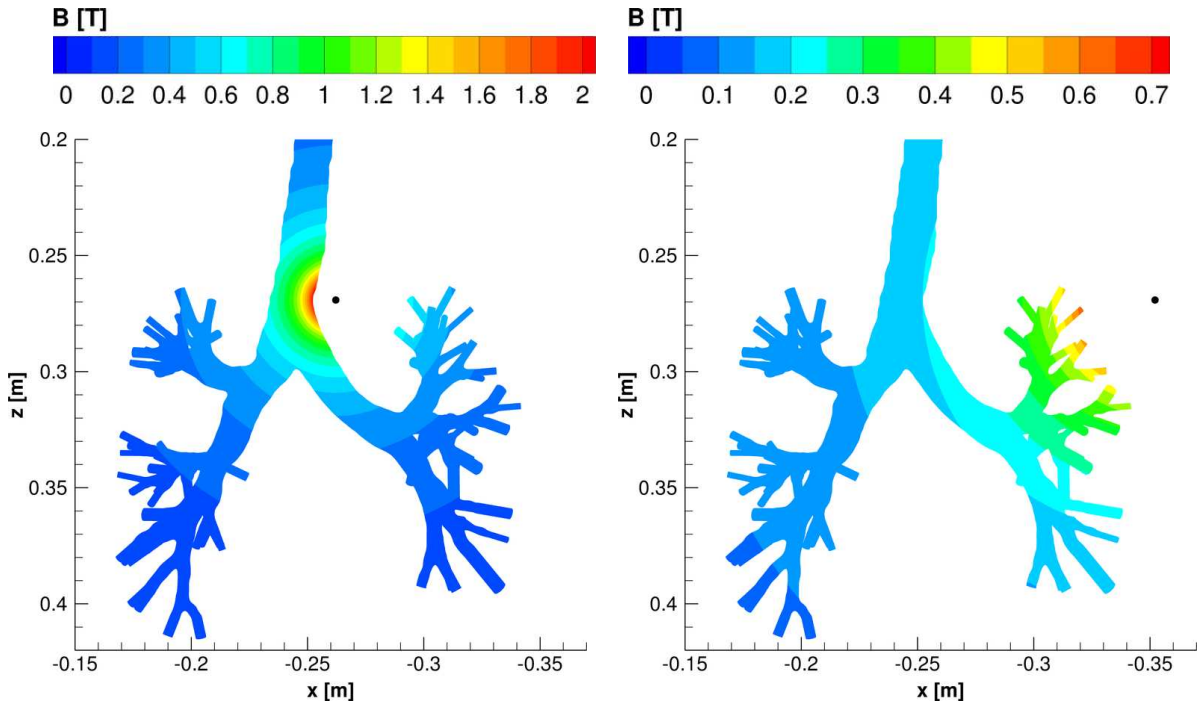

(a) Position 1: 1 cm distance

(b) Position 2: 1 cm distance

Figure 8.35: Contours of magnetic field strength (B) caused by an infinitely long current carrying wire perpendicular to the paper and placed (a) 1 cm away (in -x-direction) (b) 10 cm away from a reference point (x = -0.252 m and z = 0.269 m) on the trachea wall. The current through the wire in this figure is 1×10^5 A.

8.4.1 Results of Magnetic Particle Deposition

Before modelling more realistic magnetic particles surrounded by a layer of medicine, fully magnetic particles are studied. To start investigating the effect of the magnetic force, the simulation from the previous section is repeated but now with the presence of a magnetic field caused by the current flowing through the wire at positions 1 and 2, see figure 8.36 for a comparison of the total deposition efficiency. By changing the particle diameter, the St as well as the Mnp is changed, therefore additional simulations were performed to map the deposition efficiency as a function of both the St and the Mnp, see figure 8.37. From these figures it becomes clear that the deposition efficiency can be greatly enhanced by increasing the Mnp. It must be noted that the highest current used is 1×10^8 thus the resulting magnetic field strength at the reference point is then 2000 T (c.w. 2 T for an MRI machine) and thus is not feasible. The presence of the magnetic field definitely increases the deposition, provided the Mnp is large enough. The diagonal line (from Mnp = 1×10^{-4}, St = 1×10^{-4} to Mnp = 1×10^{-1}, St = 1×10^{-1}) belongs to a current of 1×10^5 A, with a corresponding magnetic field strength at the reference point of 2 T for wire position 1. Moving to the left from this line indicates the requirement of a magnetic field stronger than typically encountered in an MRI machine.

It is not just the Mnp and St which affect the deposition efficiency, the magnetic field distribution or rather its gradients, are crucial. When the distance between the target and the wire is increased, the magnetic field gradients decrease and the Mnp therefore also decreases ($Mnp \sim \Delta L^{-2}$ for saturated particles). The deposition efficiency for wire position 2 (figure 8.38) differs from that of wire position 1 (figure 8.37) in that for the same Mnp (for Mnp $> 1\times10^{-3}$) the deposition efficiency is higher for wire position 2. This is due to the different magnetic field distribution, in the case of wire position 1 large enough gradients are present only close to the wire while for position 2 the gradients are larger in a greater domain of the geometry. To achieve the same Mnp though, a much larger current or magnetic field strength is required so in practise it is more difficult to achieve a larger deposition for a more distal magnetic source for the particles.

From the SF_L and SF_{pen} plots in figures 8.39-8.42 it can be seen that particles can indeed be steered, though when looking at the St and Mnp combinations at which the steering is significantly increased and then looking up the total deposition it can be seen that a significant portion of the particles are filtered in the geometry. For the same reason that the deposition is increased for the same Mnp for wire position 2, the steering is also higher than the case

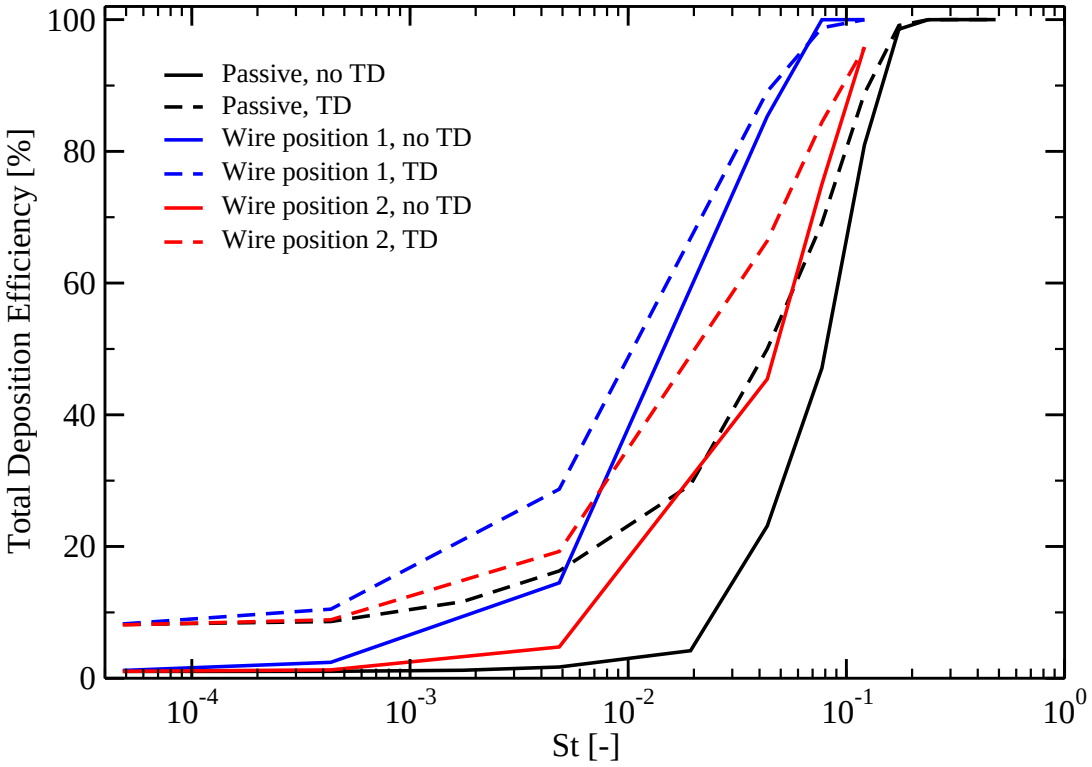

Figure 8.36: Comparison of passive and active particle deposition of fully magnetic particles (d^*_{mp}=1) for wire positions 1 and 2. The current is constant for all cases where the wire is present, I = 1×10^5 A.

of wire position 1. An interesting observation is that the SF_{pen} decreases with increasing Mnp for wire position 2 while the SF_L increases: the deposition efficiency in the left lung is increased thereby increasing the SF_L but decreasing the SF_{pen} .

A limitation of the current magnetic field configuration is the increased deposition efficiency in the upper part of the domain. This has the consequence that to get the same number of particles leaving the left side of the domain with a strong magnetic field, more particles need to be injected than for passive deposition. By comparing the surface concentrations for one St with and without the magnetic field the effect of the magnetic field can be more easily visualised, see figures 8.43 and 8.44. The majority of the particles are deposited close to the source of the magnetic field.

There may be several approaches to improve the magnetic targeting (although it should be noted that these conclusions and recommendations are based on a simplified simulation): the magnetic field configuration may be changed to optimise the deposition behaviour, another approach might be to use smaller particles of which very few will deposit and then locally apply a high gradient magnetic field to capture particles where necessary. The latter hinges upon that the small particles, unaffected by the magnetic field, are breathed out. Additional studies would be required to study how deep these particles can penetrate the domain and if they are actually breathed out.

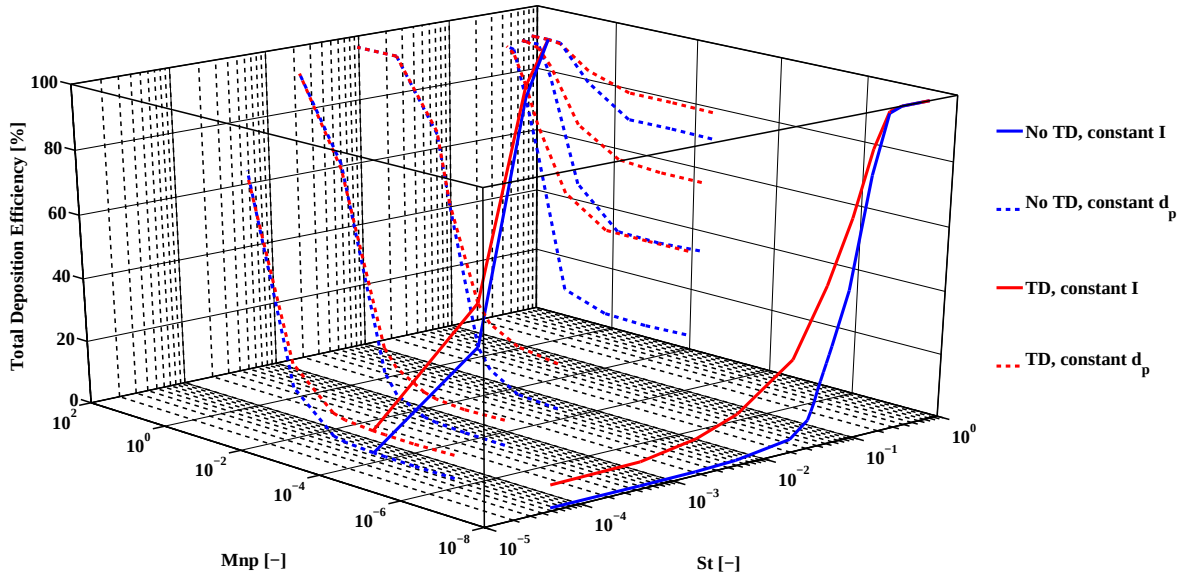

Figure 8.37: Total deposition efficiency of fully magnetic particles as a function of St and Mnp for wire position 1. Note that the simulation with Mnp = 1×10^{-8} is actually Mnp = 0, a small number was added to make the series visible.

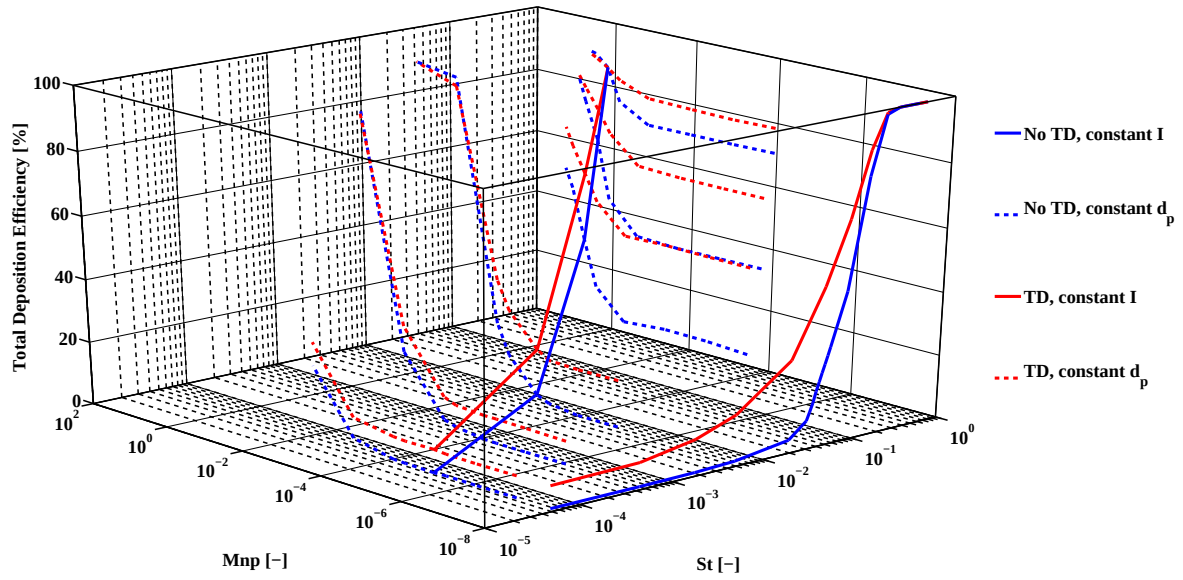

Figure 8.38: Total deposition efficiency of fully magnetic particles as a function of St and Mnp for wire position 2. Note that the simulation with Mnp = 1×10^{-8} is actually Mnp = 0, a small number was added to make the series visible.

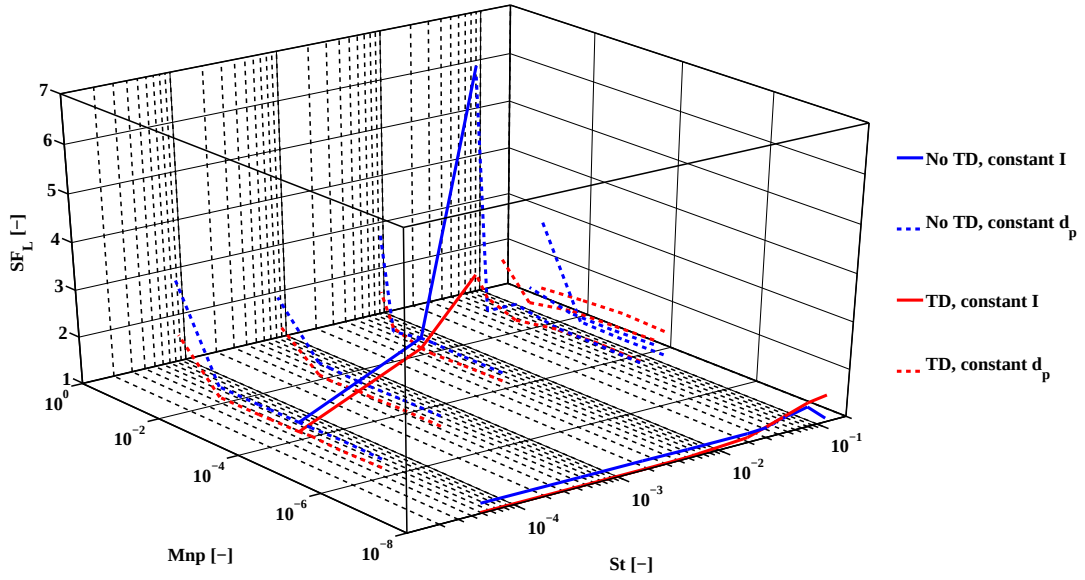

Figure 8.39: Steering factor SF_L of fully magnetic particles as a function of St and Mnp for wire position 1. Note that the simulation with Mnp = 1×10^{-8} is actually Mnp = 0, a small number was added to make the series visible.

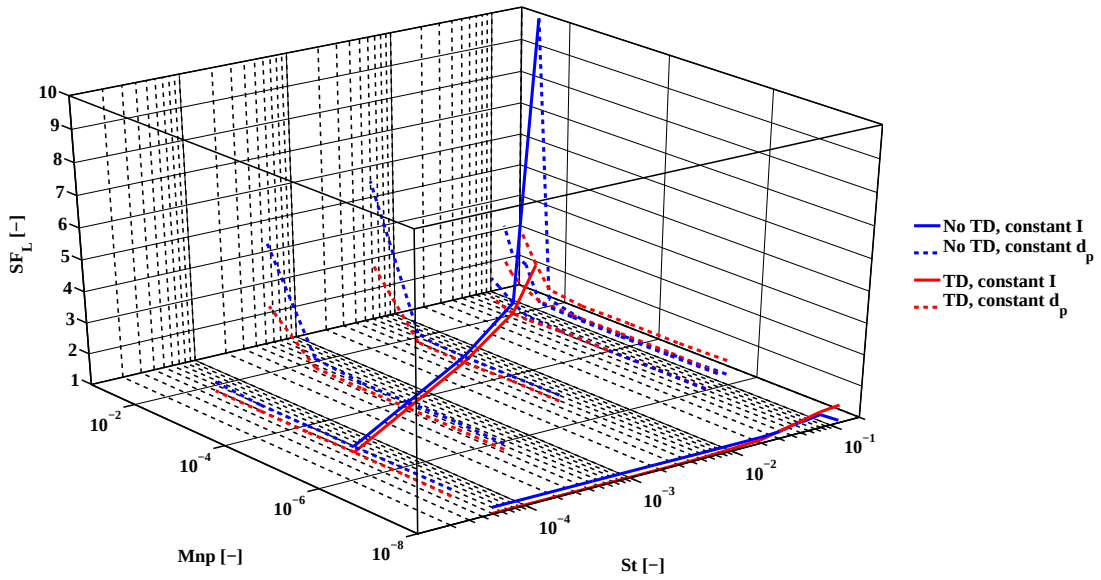

Figure 8.40: Steering factor SF_L of fully magnetic particles as a function of St and Mnp for wire position 2. Note that the simulation with Mnp = 1×10^{-8} is actually Mnp = 0, a small number was added to make the series visible.

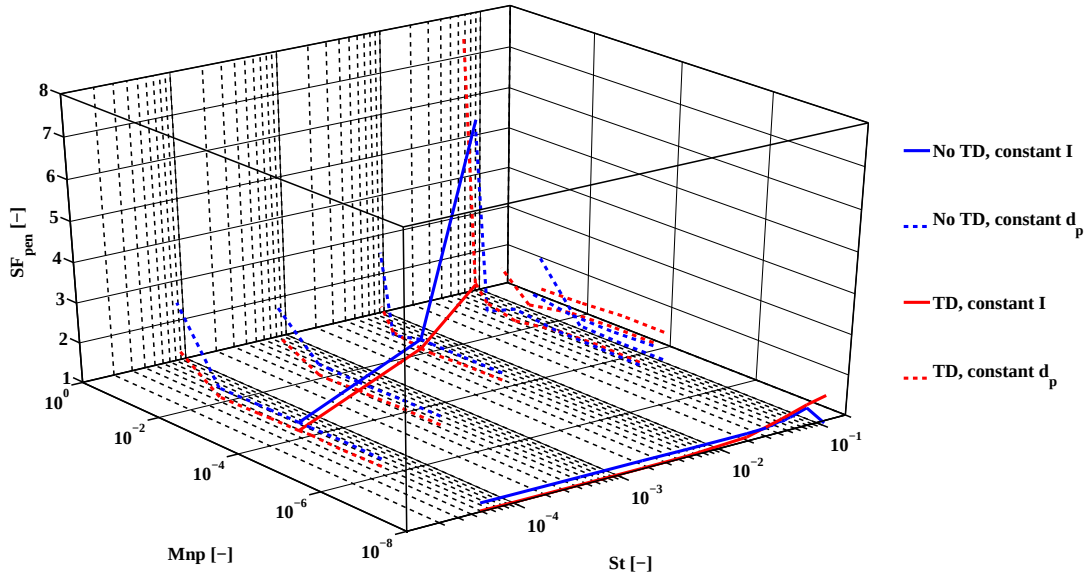

Figure 8.41: Penetration steering factor SF_{pen} of fully magnetic particles as a function of St and Mnp for wire position 1. Note that the simulation with Mnp = 1×10^{-8} is actually Mnp = 0, a small number was added to make the series visible.

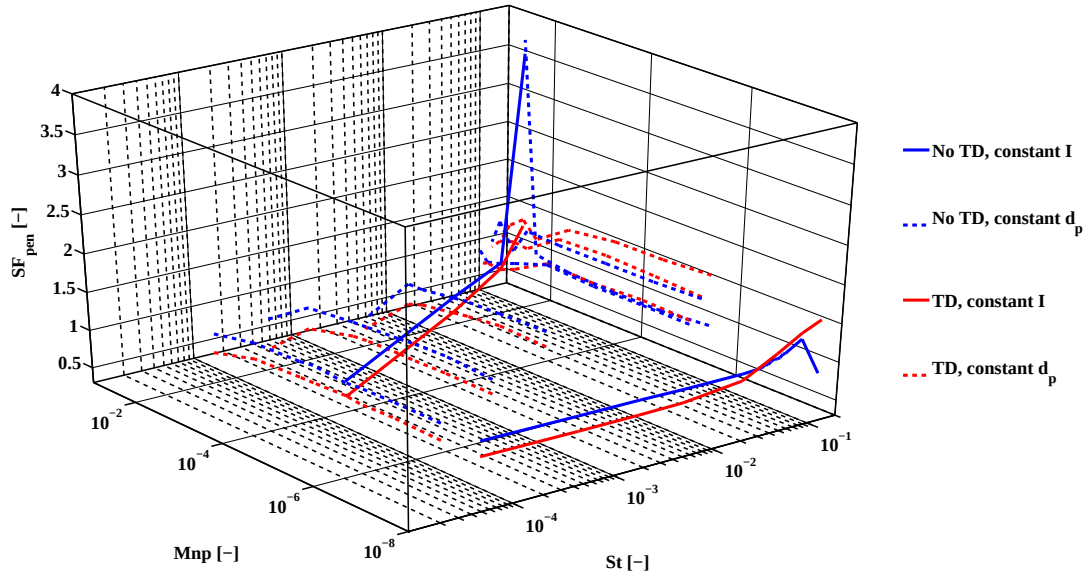

Figure 8.42: Penetration steering factor SF_{pen} of fully magnetic particles as a function of St and Mnp for wire position 2. Note that the simulation with Mnp = 1×10^{-8} is actually Mnp = 0, a small number was added to make the series visible.

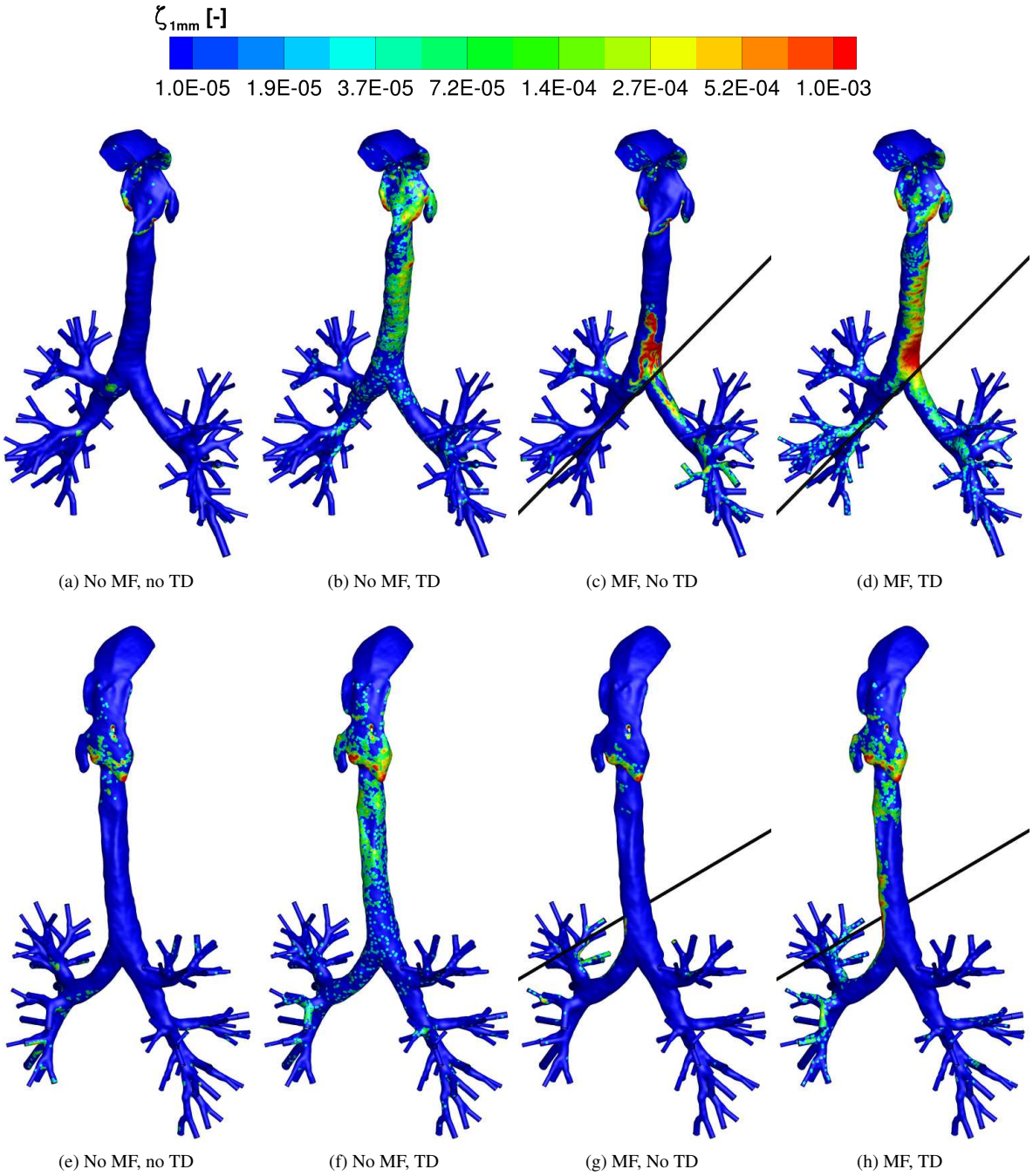

(a) No MF, no TD (b) No MF, TD (c) MF, No TD (d) MF, TD

(e) No MF, no TD (f) No MF, TD (g) MF, No TD (h) MF, TD

Figure 8.43: Contours of local deposition efficiency $\zeta_{1\text{ mm}}$ of core particles with St = 4.3×10^{-2} and Mnp = 1.7×10^{-1} for wire position 1.

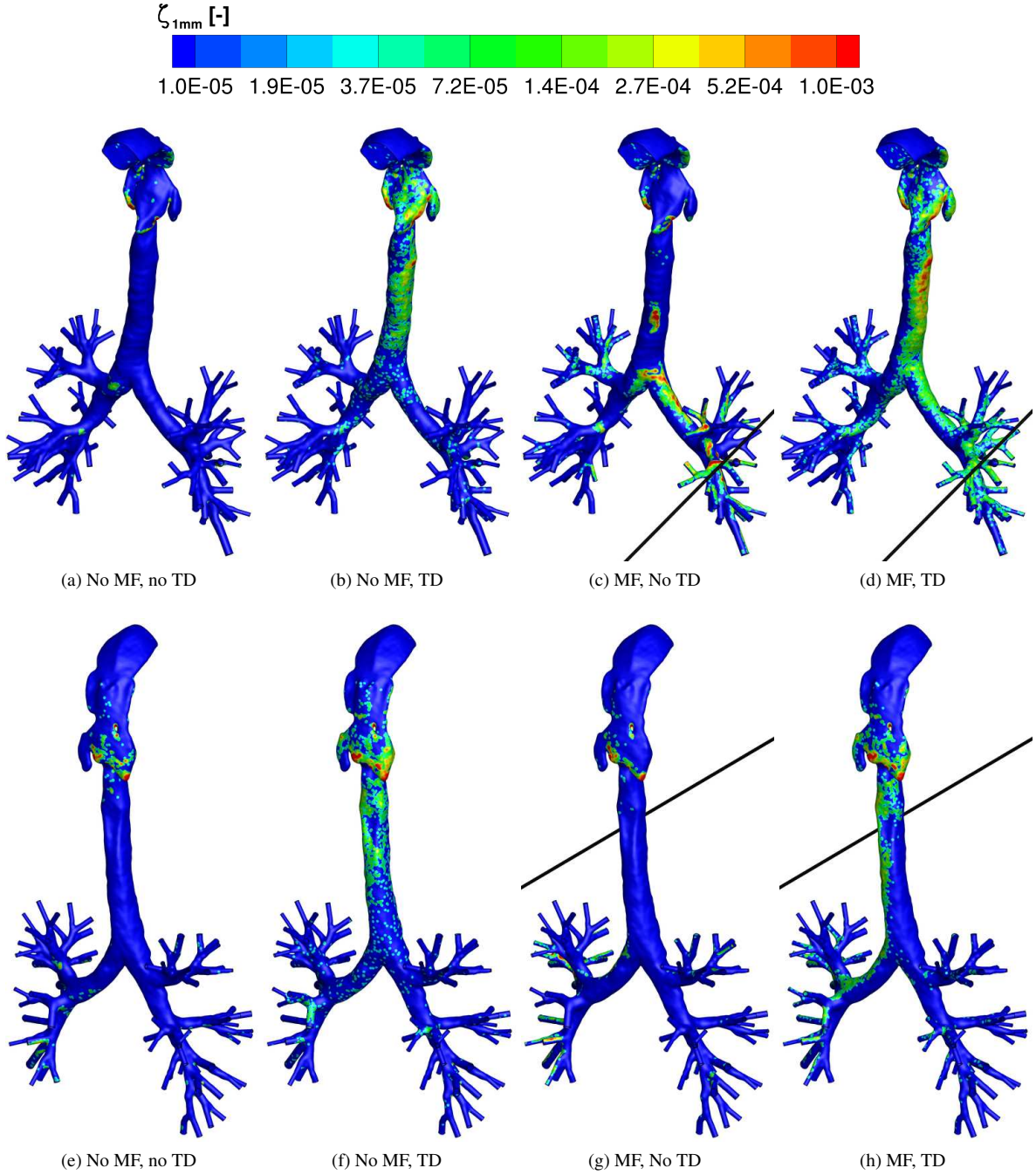

(a) No MF, no TD (b) No MF, TD (c) MF, No TD (d) MF, TD

(e) No MF, no TD (f) No MF, TD (g) MF, No TD (h) MF, TD

Figure 8.44: Contours of local deposition efficiency $\zeta_{1\text{ mm}}$ of core particles with St = 4.3×10^{-2} and Mnp = 5.6×10^{-3} for wire position 2.

8.4.1.1 Targeted Delivery of Core-Shell Particles

When a layer of drug-containing material is introduced around the magnetic particle the average density is changed and the d^*_{mp} is no longer 1. This means that for an equal total particle size the St is reduced ($\rho\downarrow$) and the Mnp is reduced ($d^*_{mp}\downarrow$). Additionally, because $F_g/F_D{\sim}\rho_p$ the gravitational effect becomes smaller: the lowest ratio is achieved if no magnetic core is present the F_g/F_D is then reduced by a factor 3 with respect to fully magnetic particles. Thus with $d^*_{mp} = 0.84$ for core-shell A particles, the density (table 8.7) is 3412 kg/m^3 and the F_g/F_D is 70% of the F_g/F_D for fully magnetic particles. So while it does have some impact (roughly equal to the effect of going up one generation velocity wise, $F_g/F_D{\sim}U^{-1}_{char}$), the results are still described very well by just the St and Mnp as evidenced by figures 8.46-8.49 and figure C.65. Additionally, the total deposition efficiency of the magnetically

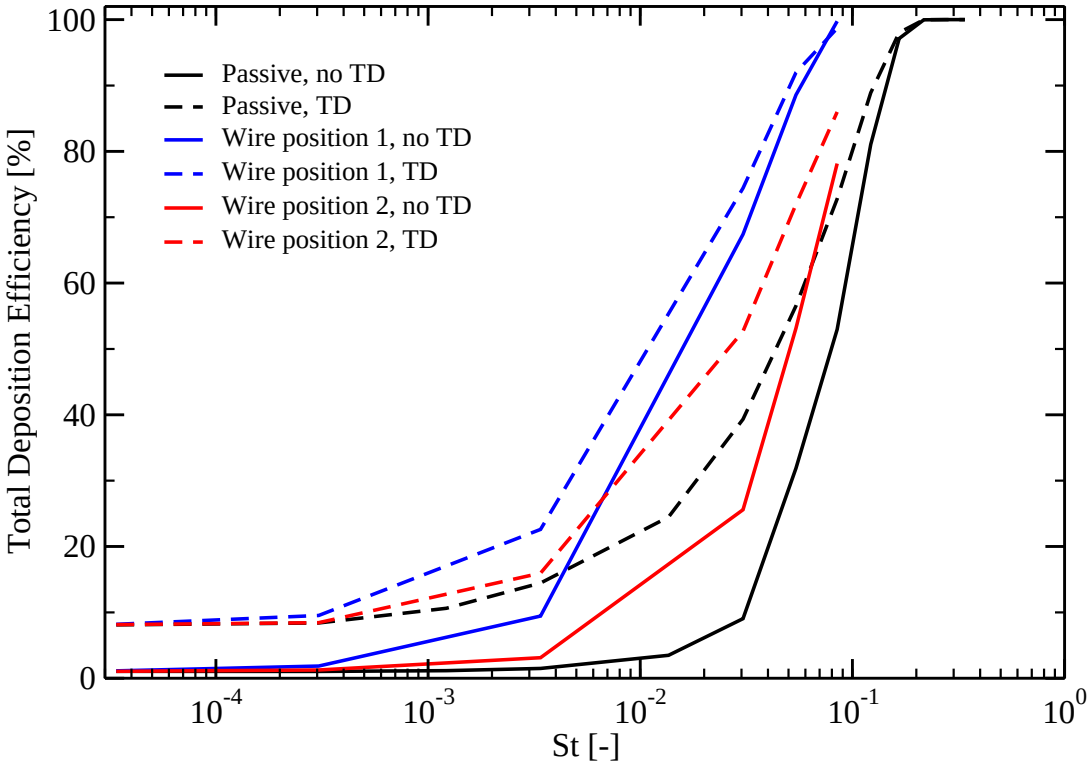

Figure 8.45: Comparison of passive and active particle deposition of core-shell particles (d^*_{mp}=0.84) for wire positions 1 and 2. The current is constant for all cases where the wire is present, I = 1×10^5 A.

enhanced particle deposition (corresponding to a magnetic field strength at the wall of 2T for wire position 1) is compared against passive deposition as a function of St in figure 8.45 to show that the presence of a magnetic force increases the deposition. The reason why the total deposition efficiency and steering factor are well described by just the St and Mnp is that the gravity only has an affect for larger particles and for distal generations, since a lot of the particles are filtered in the throat and thus only a small percentage of the particles is affected by gravity.

The SF_L and SF_{pen} do not compare very well in figures 8.50-8.57, but this might be due to a lack of points since the SF_L and SF_{pen} rise very rapidly for Mnp > 0.2. What can be seen from the figures is that both fully magnetic particles as well as core-shell particles can be steered and they are subject to the same disadvantage of the increased filtering effect observed when the St and Mnp are increased.

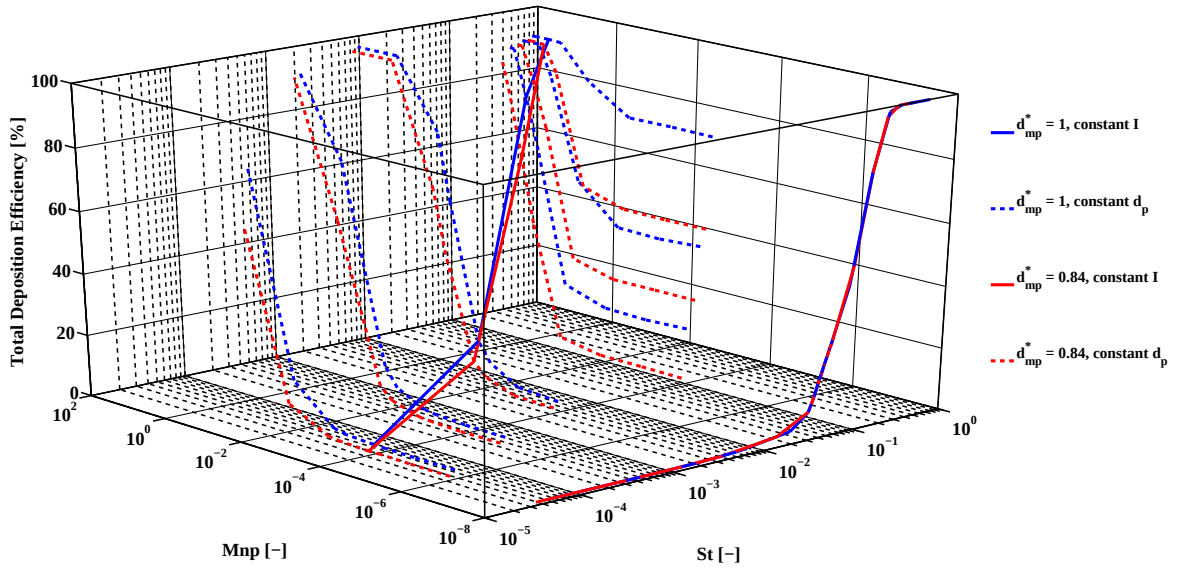

Figure 8.46: Comparison of the total deposition efficiency between fully magnetic particles ($d^*_{mp} = 1$) and core-shell A particles ($d^*_{mp} = 0.84$) for wire position 1 without turbulent dispersion. Note that the simulation with Mnp = 1×10^{-8} is actually Mnp = 0, a small number was added to make the series visible.

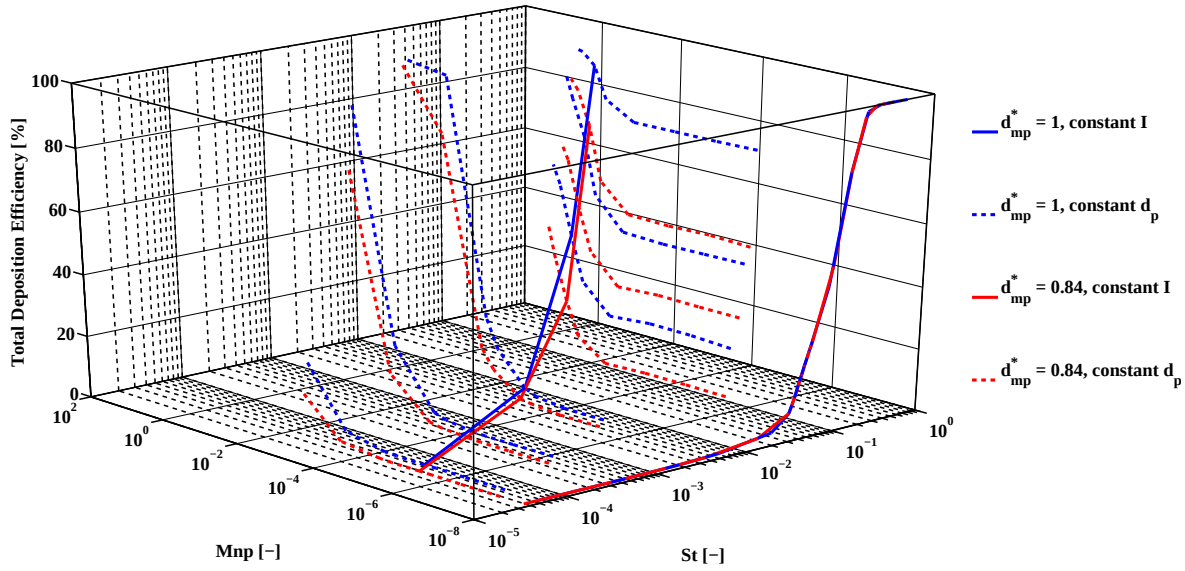

Figure 8.47: Comparison of the total deposition efficiency between fully magnetic particles ($d^*_{mp} = 1$) and core-shell A particles ($d^*_{mp} = 0.84$) for wire position 2 without turbulent dispersion. Note that the simulation with Mnp = 1×10^{-8} is actually Mnp = 0, a small number was added to make the series visible.

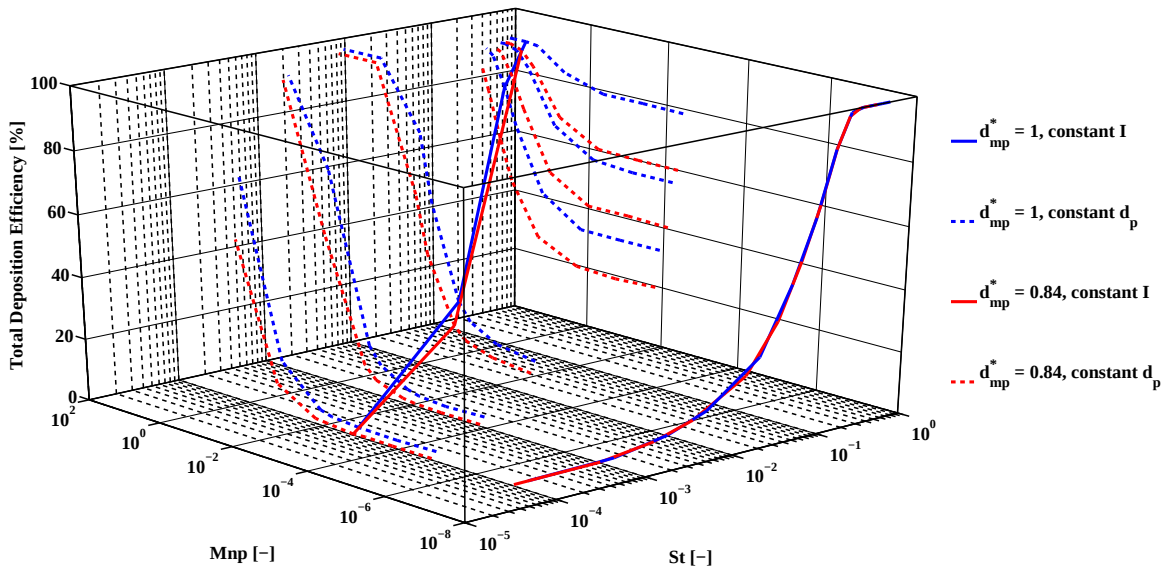

Figure 8.48: Comparison of the total deposition efficiency between fully magnetic particles ($d^*_{mp} = 1$) and core-shell A particles ($d^*_{mp} = 0.84$) for wire position 1 with turbulent dispersion. Note that the simulation with Mnp = 1×10^{-8} is actually Mnp = 0, a small number was added to make the series visible.

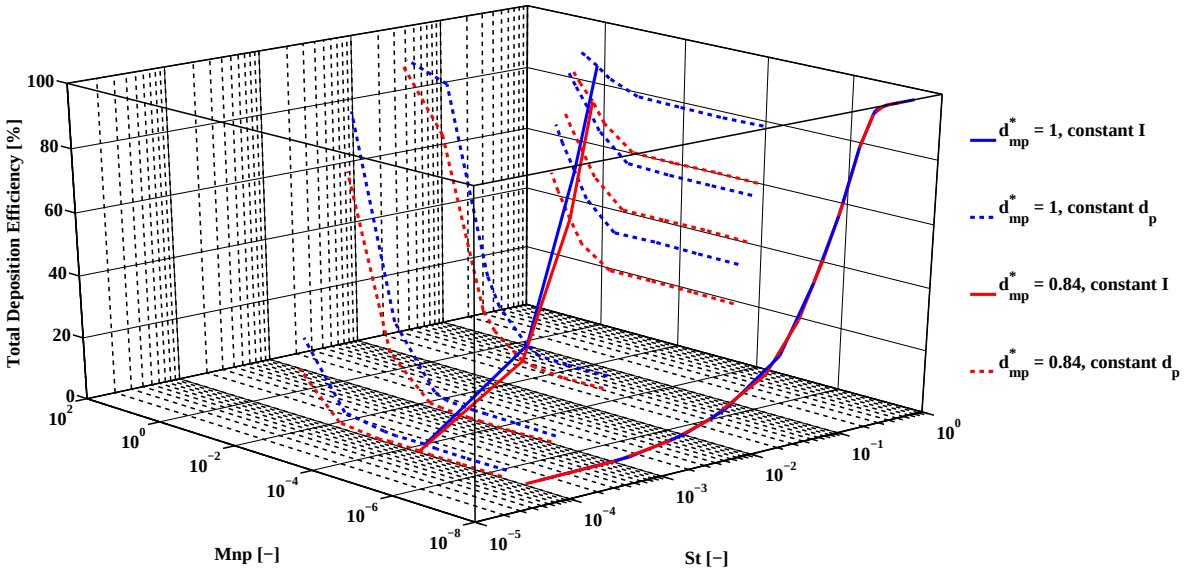

Figure 8.49: Comparison of the total deposition efficiency between fully magnetic particles ($d^*_{mp} = 1$) and core-shell A particles ($d^*_{mp} = 0.84$) for wire position 2 with turbulent dispersion. Note that the simulation with Mnp = 1×10^{-8} is actually Mnp = 0, a small number was added to make the series visible.

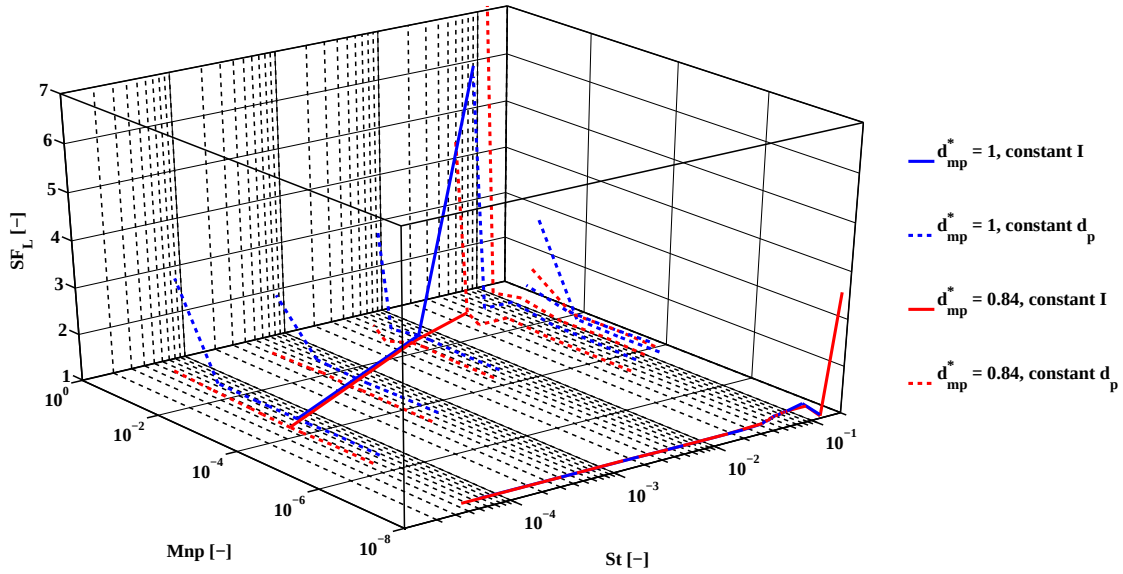

Figure 8.50: Comparison of SF_L between fully magnetic particles ($d^*_{mp} = 1$) and core-shell A particles ($d^*_{mp} = 0.84$) for wire position 1 without turbulent dispersion. Note that the simulation with Mnp = 1×10^{-8} is actually Mnp = 0, a small number was added to make the series visible.

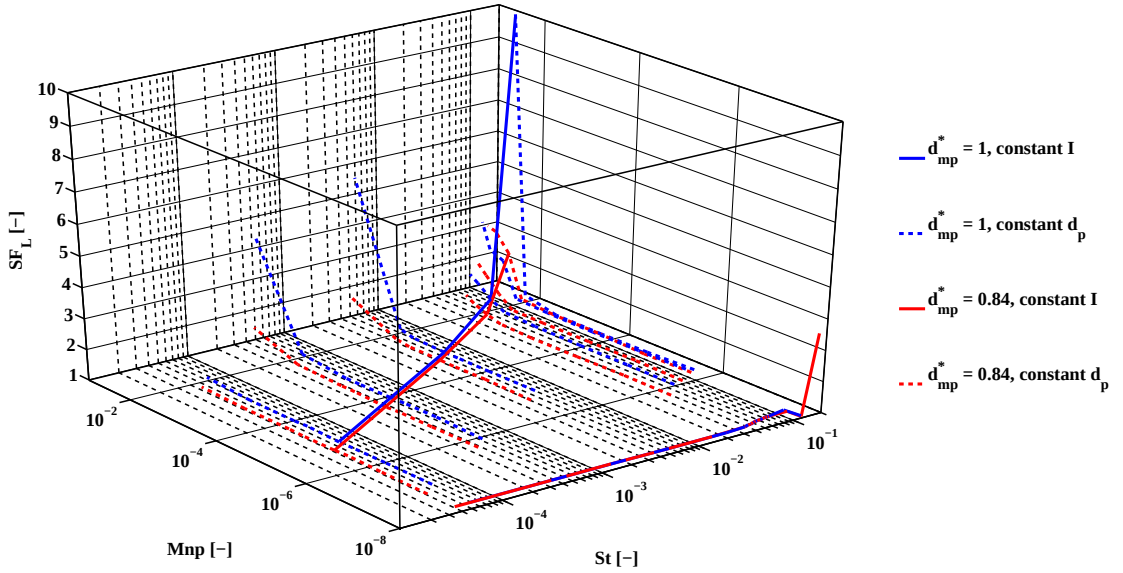

Figure 8.51: Comparison of SF_L between fully magnetic particles ($d^*_{mp} = 1$) and core-shell A particles ($d^*_{mp} = 0.84$) for wire position 2 without turbulent dispersion. Note that the simulation with Mnp = 1×10^{-8} is actually Mnp = 0, a small number was added to make the series visible.

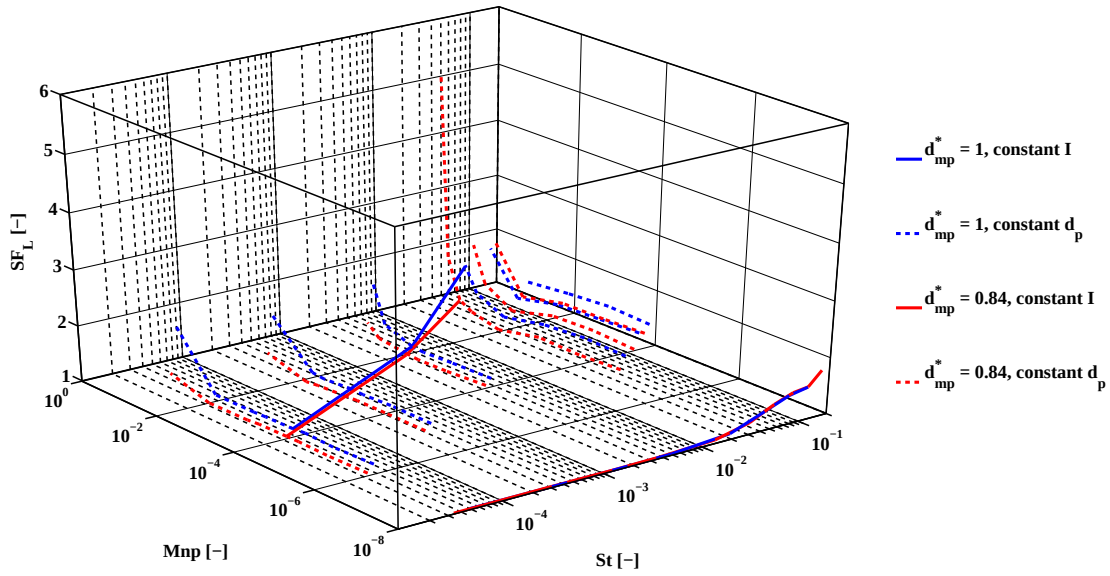

Figure 8.52: Comparison of SF_L between fully magnetic particles ($d^*_{mp} = 1$) and core-shell A particles ($d^*_{mp} = 0.84$) for wire position 1 with turbulent dispersion. Note that the simulation with Mnp = 1×10^{-8} is actually Mnp = 0, a small number was added to make the series visible.

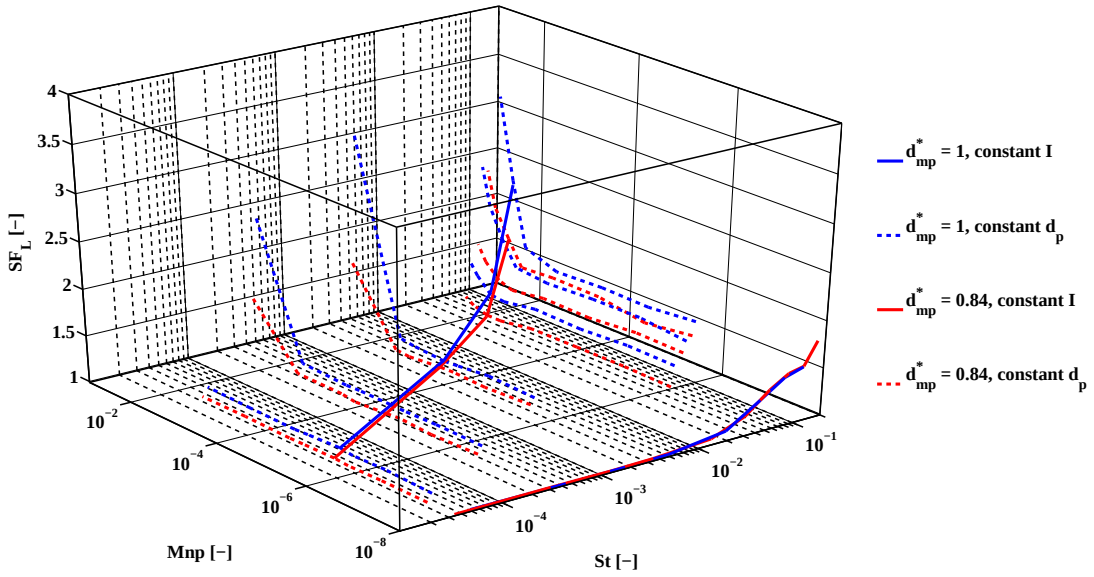

Figure 8.53: Comparison of SF_L between fully magnetic particles ($d^*_{mp} = 1$) and core-shell A particles ($d^*_{mp} = 0.84$) for wire position 2 with turbulent dispersion. Note that the simulation with Mnp = 1×10^{-8} is actually Mnp = 0, a small number was added to make the series visible.

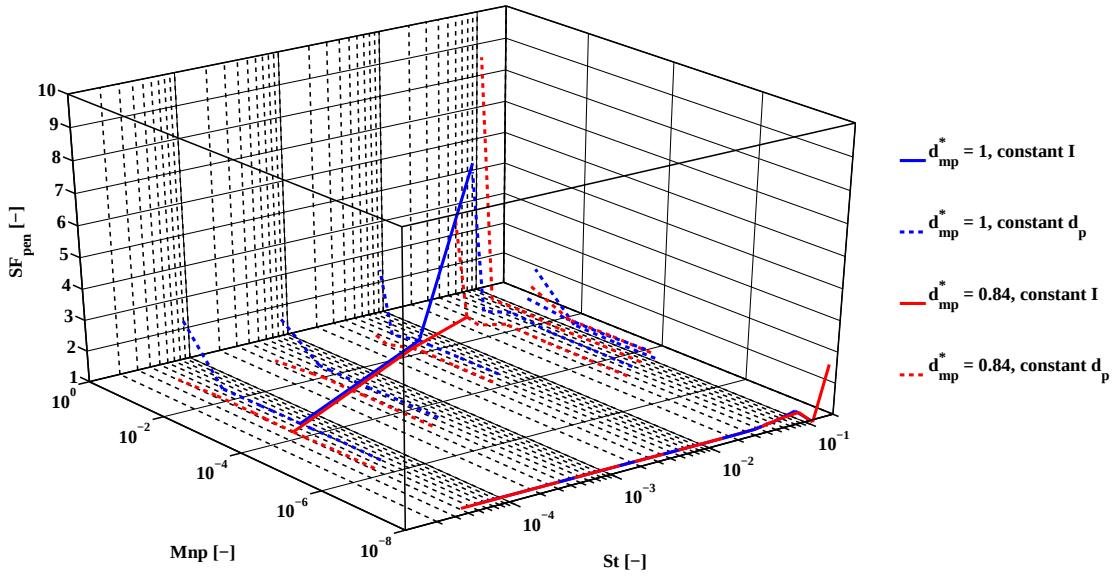

Figure 8.54: Comparison of SF_{pen} between fully magnetic particles ($d^*_{mp} = 1$) and core-shell A particles ($d^*_{mp} = 0.84$) for wire position 1 without turbulent dispersion. Note that the simulation with Mnp = 1×10^{-8} is actually Mnp = 0, a small number was added to make the series visible.

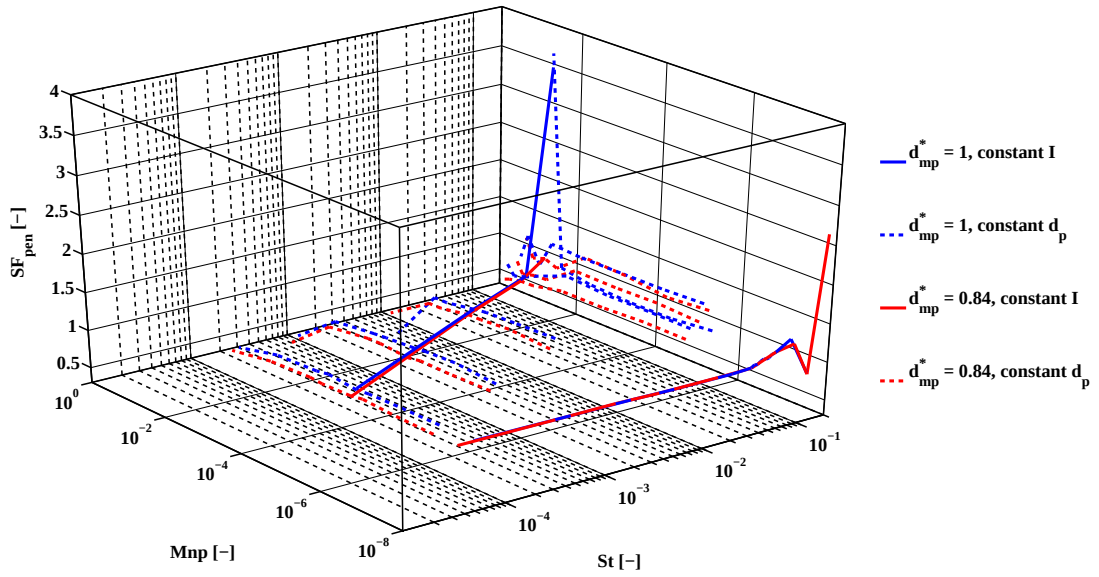

Figure 8.55: Comparison of SF_{pen} between fully magnetic particles ($d^*_{mp} = 1$) and core-shell A particles ($d^*_{mp} = 0.84$) for wire position 2 without turbulent dispersion. Note that the simulation with Mnp = 1×10^{-8} is actually Mnp = 0, a small number was added to make the series visible.

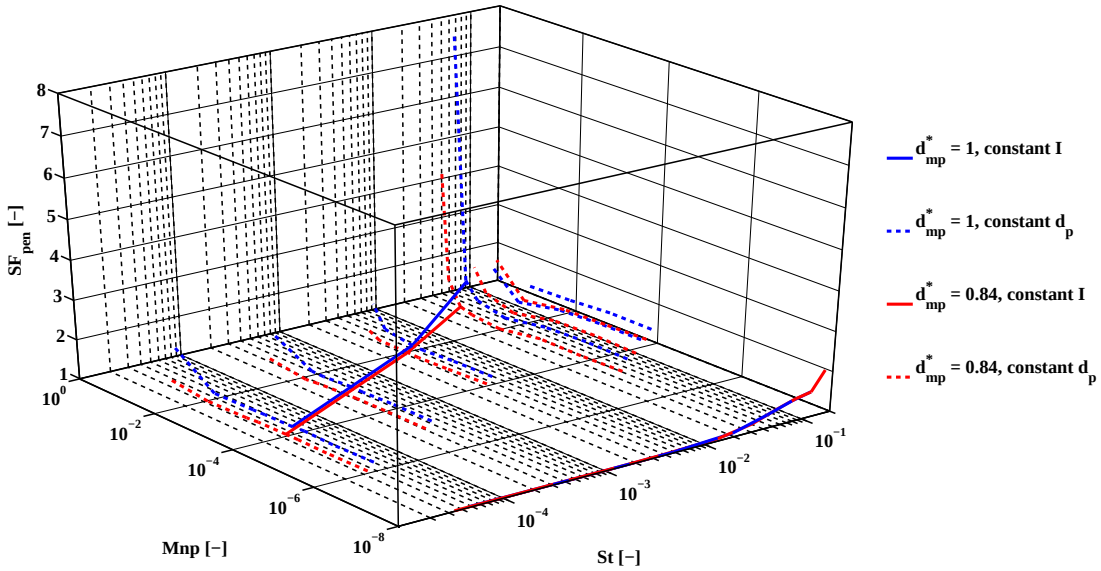

Figure 8.56: Comparison of SF_{pen} between fully magnetic particles ($d^*_{mp} = 1$) and core-shell A particles ($d^*_{mp} = 0.84$) for wire position 1 with turbulent dispersion. Note that the simulation with Mnp = 1×10^{-8} is actually Mnp = 0, a small number was added to make the series visible.

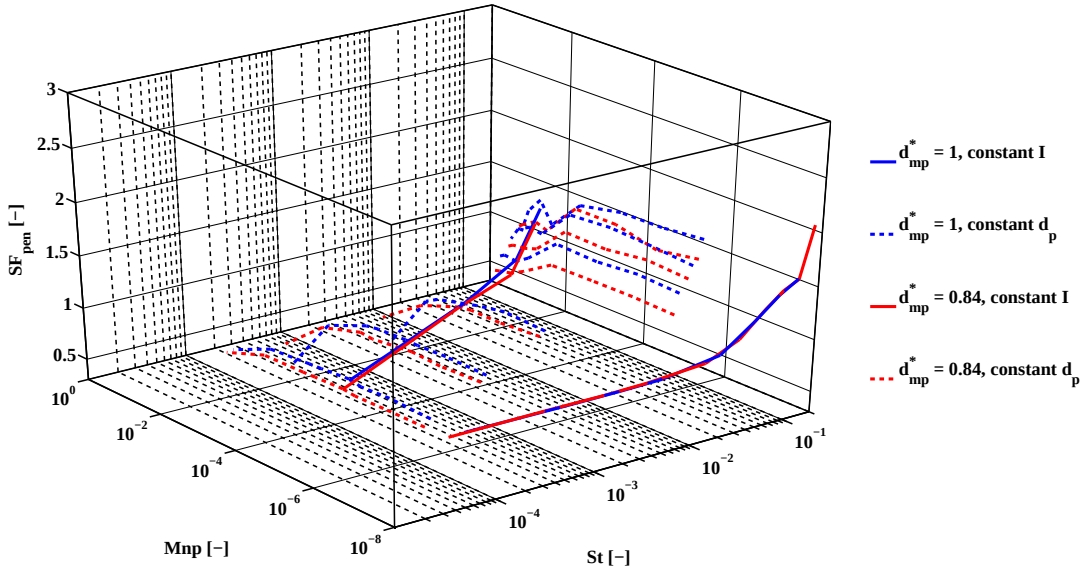

Figure 8.57: Comparison of SF_{pen} between fully magnetic particles ($d^*_{mp} = 1$) and core-shell A particles ($d^*_{mp} = 0.84$) for wire position 2 with turbulent dispersion. Note that the simulation with Mnp = 1×10^{-8} is actually Mnp = 0, a small number was added to make the series visible.

Chapter 9

Conclusions

9.1 90 Degree Bend - Passive Deposition

The results of the 90° bend without magnetic force, modelled after Breuer et al. (2006); Cohen Stuart (2009) match the reference papers. A qualitative agreement was established by comparing the stream traces from the present study with Cohen Stuart (2009). Velocity profiles sampled at 0° , 45° and 90° deflection planes showed a good agreement with Cohen Stuart (2009). Particle deposition was performed using two particle inlet distributions: (1) a random uniform distribution and (2) a deterministic uniform distribution. The results of the random uniform distribution in the present case showed the best agreement with Breuer et al. (2006) while the deterministic uniform distribution results showed the best agreement with Cohen Stuart (2009). Therefore, it is likely that the two reference papers used different particle inlet distributions.

9.2 90 Degree Bend - Magnetically Enhanced Deposition

The 90° bend with magnetic force was modelled after Haverkort (2008); Cohen Stuart (2009) and features a different geometry from the case study in the 90° bend without magnetic force. The diameter and the lengths of inlet and outlet tubes are different, the curvature ratio is the same. The Reynolds number, and thus the Dean number, are lower in this case study.

The velocity profiles show good agreement with profiles found by Haverkort (2008); Cohen Stuart (2009). When particles are added to this geometry, without the presence of a magnetic field, a small error is observed in both the present study and the reference case. This is expected to be caused by numerical errors and the relatively coarse mesh. When the magnetic force is added to the simulation, the total and cumulative deposition for position 1 and 4 show good agreement with the reference cases and thus the magnetic force implementation of the present study has been validated against previous studies.

9.3 Triple Bifurcation Geometry

The geometry for the triple bifurcation in the bifurcation areas in the present study does not match the reference paper, since a different geometry was used a grid independence study was performed by comparing the one dimensional deposition in a mesh with 3 million cells to a mesh with 6 million cells. The difference in deposition between the two meshes is minimal.

The different bifurcation area is reflected in both the velocity profiles and the particle depositions; the velocity profiles at the various stations, while showing some agreement, do not match well. Some of the areas show significant deviation which is caused by the different cross sectional area change between the two geometries. Due to the level of agreement with the double bifurcation the differences in the triple bifurcation geometry may be explained due to the geometrical difference in the bifurcation regions.

From the penetration steering factor SF_{pen} and total steering factor SF_L it was shown that particles can be steered effectively towards one side of the geometry by the use of a magnetic field.

9.4 Human Specific Geometry

Since the lobar ventilation ratios do not match between the simulations and experimental data the velocity profiles will not be close to the experimental data if the entire domain is considered. However, since the flow distribution of left lung to right lung is approximately equal to the experiments, the flow up until the first bifurcation was compared. Upstream of the second bifurcation the LES simulations qualitatively agreed with the experimental data throughout the entirety of the chosen planes. The RANS models agreed qualitatively only up to the region of the highest turbulence, further downstream (plane 8) the correct secondary motions are not captured by the RANS models. Out of the RANS models, the SST-Transition and k-ε Realisable model perform the best.

Based on the agreement with the experimental data it can be concluded that a LES model is needed to describe the flow accurately and RANS models are thus not sufficient. The difference between the Smagorinsky and WALE subgrid models is very small. However, a simulation which uses the exact boundary conditions such that the flow distribution matches those of the experiments is required to provide a definitive answer.

The turbulent kinetic energy profiles between the LES and RANS models did not agree with one another; the LES predict a much higher intensity. The higher level of TKE may be explained by the first order discretisation used for the RANS models and by differences observed between the models in general: Zhang and Kleinstreuer (2011) showed that LES predict a higher peak in a stenosed tube. Because only time-averaged velocity profiles were available for the experimental data, the turbulent kinetic energy was compared only among the models and thus no conclusion can be made as to the validity of the results.

Despite the better agreement of the LES, it was decided to perform the particle deposition studies from this report using RANS models based on the time needed to perform these simulations. The SST-Transition data was the RANS model of choice since it showed the best agreement with the experimental data. A limitation related to the use of a RANS model is the turbulent dispersion model which adds isotropic velocity fluctuations based on the turbulent kinetic energy. The wall normal component of the fluctuations is greatly over-estimated (Dehbi, 2008).

For passive particles the deposition is described by the St and the activation of turbulent dispersion, the inclusion of gravity does not have a significant impact on the particle deposition but is expected to become significant if more generations of branches are considered.

The steering of magnetic particles was displayed by adding a magnetic field, the deposition in the target side is increased as evidenced by the increase in SF_L for an increase in Mnp (for both distances). Both the SF_L and SF_{pen} depend on the wire position or magnetic field gradients in the geometry. For a wire placed at 1 cm away from the reference point the SF_{pen} increases with increasing Mnp but decreases for a wire displaced 10 cm with increasing Mnp number.

A downside to the magnetic field used in the present study is that at St and Mnp where considerable steering is observed the deposition efficiency becomes very large and therefore significantly reduces the total number of particles which penetrate the geometry.

The activation of turbulent dispersion increases the total deposition efficiency while reducing the SF_L and SF_{pen} for cases both with and without magnetic force. Magnetically enhanced deposition in a patient specific geometry from the mouth until roughly 6 generations of the conductive airways is described by the St, Mnp, inclusion of turbulent dispersion and wire configuration.

9.5 Research Questions

Is it possible to steer magnetic particles in the human airways by using a magnetic field?

Yes, in chapters 7 and 8 it was demonstrated that particles can be steered by using a current carrying wire in both simplified conductive airway bifurcations as well as a patient specific geometry. The parameters which quantify the steering are the steering factors SF_L and SF_{pen}, in both the simplified bifurcation geometry and the patient specific geometry an increase of the steering factors were observed for increasing Mnp for a given St. The targeting effect was also observed in the surface concentration plots.

The downside observed in the present study was the increase in total particle deposition meaning that the total number of particles which penetrate the geometry may be significantly reduced when a considerable steering effect is present.

Due to the throat geometry, the flow can transition from laminar to turbulent. Do the turbulence models predict this behaviour and is a Reynolds Averaged Navier-Stokes model good enough?

Yes, the models employed in the present study can predict the transition from laminar to turbulent and vice

versa but whether the RANS model is good enough requires additional studies; all the turbulence models employed in the present study were able to predict a local highly turbulent region but the amplitude of the fluctuations does not agree among the models. The LES predict much higher turbulent kinetic energy while the RANS models under predict the values. This may be due to the first order upwinding used in the RANS simulations and a model difference; in Zhang and Kleinstreuer (2011) both the k-ω LRN and SST-Transition under predict the TKE compared to their LES while the regular k-ω practically predicts the same values as the LES. To answer whether a RANS model is good enough requires simulations performed with second order discretisation, or rather a revised solving strategy since second order discretisations were tested but did not converge (pressure residuals oscillated at O(10^{-2})) and to validate the results and provide a definitive answer experimental data is most definitely required.

Do the simulations agree with the flow structures and/or particle deposition behaviour observed in experiments

Depending on the case, yes. The passive particle deposition in the 90 degree bend qualitatively agree with experimental observations and the same is the case for the passive particle deposition in the first bifurcation of the bifurcating geometry. However, in the second bifurcation the results are totally off. The flow structures in the patient specific geometry qualitatively agrees with experimental observations up until the first bifurcation; a different set of simulations with the boundary conditions from the experiments is required not only to provide a better comparison but also to make it easier to validate against future particle deposition experiments.

Chapter 10

Recommendations

10.1 Regarding Limitations of the Present Work

- Since Fluent does not have a very realistic deposition rule, and although its effect is not significant for an idealised throat geometry (chapter 6.1), a more advanced deposition rule should be implemented to study its significance for patient specific geometries. Such a deposition rule should take into account the nonzero volume of the particle.
- The mesh used in the patient specific simulations featured a rather sharp transition from boundary layer mesh to 'free stream' mesh, another mesh was generated which featured a smoother transition at the cost of a roughly 4 million grid cell increase. A simulation can be performed with the smoother mesh to see if it provides any benefits, although it must be noted that this smoothed mesh gave problems on the workstation due to memory issues.
- If deemed necessary for accuracy the inlet piece of geometry can also be meshed and used to generate a more accurate inlet velocity profile at the cost of increased computational power. Additionally, the velocity profile from the experiments can be used to provide a cheaper method of prescribing a more correct inlet velocity field.
- The implementation of the correct boundaries conditions from the experiments into the simulation should be one of the next steps, the easiest of methods is to calculate the flow rate through each of the 72 outlets from the experimental results and prescribe the same outflow in the simulations otherwise the entire outlet region has to be taken into account which will significantly increase the mesh size. Additionally, it is recommended that more experiments are performed, of primary interest (to the author) are turbulent kinetic energy profiles and deposition patterns.
- A particle deposition study using a LES is strongly recommended and the usage of the SST-Transition model is a major limitation of the present study. However, LES are computationally intense even for passive particles if they are injected every fluid flow time step. This becomes even more extreme when magnetic targeting is used. Also an implicit bounded time differencing scheme was used for the LES and thus a higher Courant number is allowed, it may be worth wile to submit an extra job with a much smaller time-step to see if the accuracy improves significantly.
- A straight, infinitely long, current carrying wire does not provide a very good magnetic field distribution if the goal is to increase the amount of particles which penetrate one side of the lung. Alternate, and more realistic, magnetic field configurations should be studied.
- A real patient undergoing treatment is unlikely to provide a constant inhalation flow rate much less achieve the 60 L/min flow rate used in the simulations; a (patient specific) breathing pattern will provide a more realistic basis for drug delivery. Additionally, some literature claims that the majority of small particles are exhaled ($d_p < 0.5\ \mu m$), a simulation featuring a realistic breathing pattern may provide additional insight to the optimum particle size and targeting strategy. To build up to the patient specific geometry, a straight cylinder or the 90° bend and bifurcation geometries should be studied first.

10.2 Future Studies

- Since both magnetically enhanced particle deposition in the upper airway and conducting airway has been studied, it may be interesting to study the effect of the magnetic force on particle deposition in alveolar sacs where the amount of deposition will then be a function of gravitational settling and the magnetic force, depending on the strength of the field. Even more interesting would be to study this in combination with expanding alveolar sacs. This may provide an alternative to the steering strategy employed in the present study; if small particles are breathed out then applying a highly localised high gradient magnetic field could deposit particles where necessary without affecting the majority of other particles which are subsequently breathed out.
- There are many aspects of the human airway system which can still be studied, some of less importance than others. Some of these topics are: isometric expansion, non-isometric expansion, disease induced narrowing, more generations and thick layers of mucus (of varying viscosities) up to the point of clogging. For a controlled method of studying geometrical defects caused by diseases in idealised geometry, the study of Kleinstreuer and Zhang (2003b) can be reproduced, or another well defined defect can be added to the geometry of chapter 7.

Bibliography

Ansys 2011. *ANSYS FLUENT Theory Guide*, volume 15317.

Anthony, J. W., Bideaux, R. A., Bladh, K. W., and Nichols, M. C., editors 2001. *Handbook of Mineralogy*. Mineralogical Society of America, Chantilly, VA 20151-1110, USA.

Banko, A. J., Coletti, F., Schiavazzi, D., Elkins, C., and Eaton, J. K. 2014. Three-dimensional inspiratory flow in subject-specific airways from mouth to eighth bronchial generation. *Submitted to Journal of Fluid Mechanics*, Unknown(Unknown):1–26.

Bellary, S. and Barnett, a. H. 2006. Review: Inhaled insulin: overcoming barriers to insulin therapy? *The British Journal of Diabetes & Vascular Disease*, 6(3):103–108.

Breuer, M., Baytekin, H., and Matida, E. 2006. Prediction of aerosol deposition in bends using LES and an efficient Lagrangian tracking method. *Journal of Aerosol Science*, 37(11):1407–1428.

Cohen Stuart, D. 2009. *The Development of a Discrete Particle Model for 3D Unstructured Grids : Application to Magnetic Drug Targeting*. PhD thesis, Delft University of Technology.

Comer, J. K., Kleinstreuer, C., and Zhang, Z. 2001. Flow structures and particle deposition patterns in double-bifurcation airway models. Part 1. Air flow fields. *Journal of Fluid Mechanics*, 435(2001):25–41.

Cullity, B. and Graham, C. 2011. *Introduction to Magnetic Materials*. John Wiley & Sons, 2nd editio edition.

Dames, P., Gleich, B., Flemmer, A., Hajek, K., Seidl, N., Wiekhorst, F., Eberbeck, D., Bittmann, I., Bergemann, C., Weyh, T., Trahms, L., Rosenecker, J., and Rudolph, C. 2007. Targeted delivery of magnetic aerosol droplets to the lung. *Nature nanotechnology*, 2(8):495–499.

Dehbi, A. 2008. A CFD model for particle dispersion in turbulent boundary layer flows. *Nuclear Engineering and Design*, 238(3):707–715.

Haverkort, J. 2008. *Analytical and Computational Analysis of Magnetic Drug Targeting in Simplified and Realistic Arterial Geometries*. PhD thesis, Delft University of Technology.

Horsfield, K., Dart, G., Olson, D. E., Filley, G. F., and Cumming, G. 1971. Models of the Human Bronchial Tree. *Journal of applied physiology*, 31(2):207–217.

Kleinstreuer, C. and Zhang, Z. 2003a. Laminar-to-turbulent fluid-particle flows in a human airway model. *International Journal of Multiphase Flow*, 29(2):271–289.

Kleinstreuer, C. and Zhang, Z. 2003b. Targeted Drug Aeroso Deposition Analysis for a Four-Generation Lung Airway Model With Hemispherical Tumors. *Journal of Biomechanical Engineering*, 125(2):197–206.

Kleinstreuer, C., Zhang, Z., and Donohue, J. F. 2008. Targeted drug-aerosol delivery in the human respiratory system. *Annual review of biomedical engineering*, 10:195–220.

Laube, B. 2005. The expanding role of aerosols in systemic drug delivery, gene therapy, and vaccination. *Respiratory care*, 50(9):1161–76.

Longest, P. W. and Vinchurkar, S. 2007. Effects of mesh style and grid convergence on particle deposition in bifurcating airway models with comparisons to experimental data. *Medical engineering & physics*, 29(3):350–66.

Longest, W. P. and Vinchurkar, S. 2007. Validating CFD predictions of respiratory aerosol deposition: effects of upstream transition and turbulence. *Journal of biomechanics*, 40(2):305–316.

Menter, F. R., Langtry, R., and Völker, S. 2006. Transition Modelling for General Purpose CFD Codes. *Flow, Turbulence and Combustion*, 77(1-4):277–303.

Morsi, S. a. and Alexander, a. J. 1972. An investigation of particle trajectories in two-phase flow systems. *Journal of Fluid Mechanics*, 55(02):193–208.

Moskowitz, B. M. 1991. Hitchhiker's Guide to Magnetism.

Pandey, R. and Khuller, G. K. 2005. Antitubercular inhaled therapy: opportunities, progress and challenges. *The Journal of antimicrobial chemotherapy*, 55(4):430–5.

Pedley, T. 1977. Pulmonary Fluid Dynamics. *Annual Review of Fluid Mechanics*, 9:229–274.

Polysciences, I. 2013. PLGA (Poly Lactic co-Glycolic Acid) Uniform Dry Microspheres.

Pui, D. Y. H., Romay-novas, F., and Liu, B. Y. H. 1987. Experimental Study of Particle Deposition in Bends of Circular Cross Section. *Aerosol Science and Technology*, 7(3):301–315.

Righolt, B. 2010. Numerical Simulations of Magnetic Drug Targeting in Realistic Arterial Bifurcations Delft University of Technology.

Sanjar, S. and Matthews, J. 2001. Treating Systemic Diseases via the Lung. *Journal of Aerosol Medicine*, 14(S1):51–58.

Zhang, Z. and Kleinstreuer, C. 2001. Effect of Particle Inlet Distributions on Deposition in a Triple Bifurcation Lung Airway Model. *Journal of Aerosol Medicine*, 14(1):13–29.

Zhang, Z. and Kleinstreuer, C. 2011. Laminar-to-turbulent fluid – nanoparticle dynamics simulations : Model comparisons and nanoparticle-deposition applications. *International Journal for Numerical Methods in Biomedical Engineering*, 27:1930–1950.

Zhang, Z., Kleinstreuer, C., Donohue, J., and Kim, C. 2005. Comparison of micro- and nano-size particle depositions in a human upper airway model. *Journal of Aerosol Science*, 36(2):211–233.

Zhang, Z., Kleinstreuer, C., and Feng, Y. 2012. Vapor deposition during cigarette smoke inhalation in a subject-specific human airway model. *Journal of Aerosol Science*, 53:40–60.

Zhang, Z., Kleinstreuer, C., and Kim, C. S. 2001. Flow Structure and Particle Transport in a Triple Bifurcation Airway Model. *Journal of Fluids Engineering*, 123(2):320.

Appendix A

Theory Supplements

A.1 SIMPLE method

The SIMPLE method is a pressure-velocity coupling method. The mass flux through a face is corrected by adding the following term to the original flux (Ansys, 2011):

$$J'_f \;=\; d_f \left(p'_{cell,1} - p'_{cell,2}\right) \tag{A.1}$$

where d_f is a function of the Rhie-Chow algorithm coefficients a_p of the neighbouring cells. The new flux is then substituted into the continuity equation which yields the following expression:

$$a_p p' \;=\; \sum_{Nb}^{N_{neighbours}} a_{Nb} p'_{Nb} + S \tag{A.2}$$

where a_p and a_{Nb} are coefficients and the source term S is:

$$S \;=\; \sum_{f}^{N_{faces}} J_f^n * A_f \tag{A.3}$$

once the pressure correction is calculated the pressure field and face fluxes can be updated by adding the new values to the old ones:

$$p^{n+1} \;=\; p^n + \alpha_p p' \tag{A.4}$$

$$J_f^{n+1} \;=\; J_f^n + d_f \left(p'_{cell,1} - p'_{cell,2}\right) \tag{A.5}$$

the continuity balance is now satisfied with flux corrections.

A.2 K-Epsilon Realisable

A.2.1 K-epsilon limitation

$$-\rho\overline{u_i\prime u_j\prime} = \mu_t \left(\frac{\partial \overline{u}_i}{\partial x_j} + \frac{\overline{u}_j}{\partial x_i}\right) - \frac{2}{3}\delta_{ij}\left(\rho k + \mu_t \frac{\overline{u}_k}{\partial x_k}\right) \tag{A.6}$$

Dividing by ρ and assuming incompressible flow we get for the normal components (i=j):

$$\overline{u_i\prime u_i\prime} = -\nu_t 2\frac{\partial \overline{u}_i}{\partial x_i} + \frac{2}{3}k\delta_{ii} \tag{A.7}$$

A.2.2 Modified turbulent viscosity

The modified turbulent viscosity in the k-ε Realisable model is defined as:

$$\mu_t = \rho \left(A_0 + A_s \frac{k}{\varepsilon} U^* \right)^{-1} \frac{k^2}{\varepsilon} \tag{A.8}$$

with, $A_0 = 4.04$ and

$$U^* = \sqrt{S_{ij} S_{ij} + \tilde{\Omega}_{ij} \tilde{\Omega}_{ij}} \tag{A.9}$$

where $S_{ij} = \frac{1}{2} \left(\frac{\partial U_i}{\partial x_j} + \frac{\partial U_j}{\partial x_i} \right)$ and

$$\tilde{\Omega}_{ij} = \overline{\Omega_{ij}} - 3\varepsilon_{ijk}\omega_k \tag{A.10}$$

where ω_k is the angular velocity of the rotating reference frame and Ω_{ij}, the mean rate of rotation tensor, is defined as $\Omega_{ij} = \frac{1}{2} \left(\frac{\partial U_i}{\partial x_j} - \frac{\partial U_j}{\partial x_i} \right)$. Regarding the remaining variables in the model, A_s in equation 3.11 is defined as $A_s = \sqrt{6} cos(\phi)$, with

$$\phi = \frac{1}{3} cos^{-1}(\sqrt{6} W) \tag{A.11}$$

where W is defined as:

$$W = \frac{S_{ij} S_{jk} S_{ki}}{\sqrt{S_{ij} S_{ij}}^3} \tag{A.12}$$

A.3 SST

Only a few definitions are given in this section, for a full description of the SST-Transition model the reader is referred to Menter et al. (2006).

$$Re_{\theta t} = f(Ti, \lambda_\theta) \tag{A.13}$$

where $Ti = 100 \frac{\sqrt{2k/3}}{U}$ is the turbulence intensity and $\lambda_\theta = \frac{\rho \theta^2}{\mu} \frac{dU}{ds}$ is the Thwaites' pressure gradient coefficient.

$$F_{length} = f(\overline{Re}_{\theta t}) \tag{A.14}$$

$$Re_{\theta c} = f(\overline{Re}_{\theta t}) \tag{A.15}$$

$$P_{\theta t} = c_{\theta t} \frac{U^2}{500\mu} \left(Re_{\theta t} - \overline{Re}_{\theta t} \right) (1 - F_{\theta t}) \tag{A.16}$$

$$\gamma_{eff} = max(\gamma, \gamma_{sep}) \tag{A.17}$$

the definition of γ_{sep} can be found in the paper of Menter et al. (2006)

A.4 Particle Motion

A.4.1 Morsi and Alexander Drag Law

Below you can find the drag laws from Morsi and Alexander (1972).

$$f = 1 \text{ if } Re_p \leq 1 \times 10^{-1} \tag{A.18a}$$

$$f = \frac{Re_p}{24}\left(3.69 + \frac{22.73}{Re_p} + \frac{0.0903}{Re_p^2}\right) \quad \text{if } 1\times10^{-1} < Re_p < 1\times10^{0} \tag{A.18b}$$

$$f = \frac{Re_p}{24}\left(1.222 + \frac{29.1667}{Re_p} - \frac{3.8889}{Re_p^2}\right) \quad \text{if } 1\times10^{0} < Re_p < 1\times10^{1} \tag{A.18c}$$

$$f = \frac{Re_p}{24}\left(0.6167 + \frac{46.5}{Re_p} - \frac{116.67}{Re_p^2}\right) \quad \text{if } 1\times10^{1} < Re_p < 1\times10^{2} \tag{A.18d}$$

$$f = \frac{Re_p}{24}\left(0.3644 + \frac{98.33}{Re_p} - \frac{2778}{Re_p^2}\right) \quad \text{if } 1\times10^{2} < Re_p < 1\times10^{3} \tag{A.18e}$$

$$f = \frac{Re_p}{24}\left(0.357 + \frac{148.62}{Re_p} - \frac{4.75\times10^{4}}{Re_p^2}\right) \quad \text{if } 1\times10^{3} < Re_p < 5\times10^{3} \tag{A.18f}$$

$$f = \frac{Re_p}{24}\left(0.46 - \frac{490.546}{Re_p} + \frac{57.87\times10^{4}}{Re_p^2}\right) \quad \text{if } 5\times10^{3} < Re_p < 1\times10^{4} \tag{A.18g}$$

$$f = \frac{Re_p}{24}\left(0.5191 - \frac{1662.5}{Re_p} + \frac{5.4167\times10^{6}}{Re_p^2}\right) \quad \text{if } 1\times10^{4} < Re_p < 5\times10^{4} \tag{A.18h}$$

A.4.2 Bifurcation Estimations

The cross sectional area of the two daughter tubes is assumed to be a factor $G_{f,a}$ larger than the parent tube. Also a symmetric split, $A_{daughter,1} + A_{daughter,2} = 2A_{daughter}$, is assumed so that:

$$2A_{daughter} = A_{parent} G_{f,a} \tag{A.19}$$

The area is defined as $A_i = \frac{\pi}{4} D_i^2$, where D_i is the diameter of the tube. Substituting this into the equation above gives:

$$2D_{daughter}^2 = D_{parent}^2 G_{f,a} \tag{A.20}$$

So:

$$D_{daughter} = D_{parent}\sqrt{\frac{G_{f,a}}{2}} \tag{A.21}$$

Also for the mass flow rate we have that

$$\phi_{m,daughter1} + \phi_{m,daughter2} = \phi_{m,parent} \tag{A.22}$$

where I assumed that the density does not change from bifurcation to bifurcation so that:

$$Q_{daughter,1} + Q_{daughter,2} = Q_{parent} \tag{A.23}$$

where Q denotes volumetric flow rates and $Q_{daughter,1} + Q_{daughter,2} = 2Q_{daughter}$. The flow rate in a tube is given by $Q_i = A_i U_i$ where U_i is the average velocity (the one we also scale with in the St, Re etc). Substituting this into the equation above yields:

$$2A_{daughter} U_{daughter} = A_{parent} U_{parent} \tag{A.24}$$

so

$$U_{daughter} = U_{parent}\frac{A_{parent}}{2A_{daughter}} \tag{A.25}$$

where we can see that it can be rewritten by using the relation given in equation A.19 to give:

$$U_{daughter} = U_{parent} \frac{1}{G_{f,a}} \tag{A.26}$$

For subsequent bifurcations you just plug in the daughter velocity or diameter as the parent diameter N times, so that you can obtain a relation for the diameter and velocity for the Nth bifurcation in terms of the reference diameter D_0 and velocity U_0 for example (where 0 was used here to indicate that it is based on the trachea):

$$D_N = D_0 \left(\sqrt{\frac{G_{f,a}}{2}} \right)^N \tag{A.27}$$

$$U_N = U_0 \left(\frac{1}{G_{f,a}} \right)^N \tag{A.28}$$

Appendix B

Extra Case Study: Double Bifurcation

The case study presented here, was used by the author to practise with the Ansys Meshing and generating the smoothed carina; at the time the flow field was solved to quickly compare against literature results. Particle deposition was added at a later stage to investigate the deposition efficiency in the second bifurcation. The double bifurcation geometry represents the third until the fifth generation of the conducting airways. The model parameters are different from those in chapter 7 and are obtained from Longest and Vinchurkar (2007).

B.1 Case Study Overview

The parameters used to construct the geometry are given in table B.1. The most notable differences from the triple bifurcation geometry are the angles and bend radii. The mesh employed in the present chapter is a tetrahedral mesh consisting of 7×10^5 cells.

A fully developed parabolic inlet velocity profiles is used together with a deterministic parabolic particle distribution to match Longest and Vinchurkar (2007). The inlet Reynolds number used by Longest and Vinchurkar (2007) is $Re = 1788$ and the aerosol $St = 0.25$, the inlet diameter $D_1 = 0.56\,cm$. To match the Re and St the mean velocity has been set to $U_{mean} = 5.1\,m \cdot s^{-1}$, the fluid density $\rho_f = 1.34\,kg \cdot m^{-3}$, the dynamic viscosity $\mu_f = 2.15 \cdot 10^{-5} Pa \cdot s$, the particle density $\rho_p = 1060\,kg \cdot m^{-3}$ and particle diameter $d_p = 10\,\mu m$. An overview of the case is given in tables B.1 and B.2

Table B.1: Overview of the geometrical parameters used to construct the geometry. All dimensions are in cm unless stated otherwise.

Bifurcation	**First**		**Second**	
Parent tube diameter	D_1	0.56	D_2	0.45
Daughter tube diameter	D_2	0.45	D_3	0.36
Tube lengths	L_1	1.09	L_3	0.77
	L_2	0.92		
Carinal ridge radius of curvature	$R_{c,1}$	$0.2D_2$	$R_{c,2}$	$0.2D_3$
Bifurcation bend radius	$R_{b,1}$	$2.5D_2$	$R_{b,2}$	$2.5D_3$
Bifurcation half angle	θ	35 degrees		

Table B.2: Overview of the parameters used in the 90° bent tube simulation.

Boundary Conditions	
Inlet	Fully developed velocity profile, $Re_D = 1780$
Wall	No-slip condition for fluid, trap condition for particles
Outlet	Zero gauge pressure
Particle distribution	Deterministic Parabolic
Fluid Properties	
Density	$1.34\,kg \cdot m^{-3}$
Dynamic viscosity	$2.15 \cdot 10^{-5} Pa \cdot s$
Particle Properties	
Density	$1060\,kg \cdot m^{-3}$
Diameter	$10\,\mu m$
St	0.25

B.2 Flow Field

Contours of the velocity magnitude in the mid plane are given in figure B.1 and for the individual planes stream traces and velocity magnitude contours are given in figure B.2. Please note that the exact position was not given and thus the slices made in the present study may not be exactly the same as from the reference paper. The results agree qualitatively. Longest and Vinchurkar (2007) did not only use a tetrahedral mesh but also different styles, to show that a difference in meshing style does make a difference in the flow field these figures, copied from the original article, are given in figure B.3. The results from the present study show slightly more agreement with their hexahedral mesh than their tetrahedral mesh.

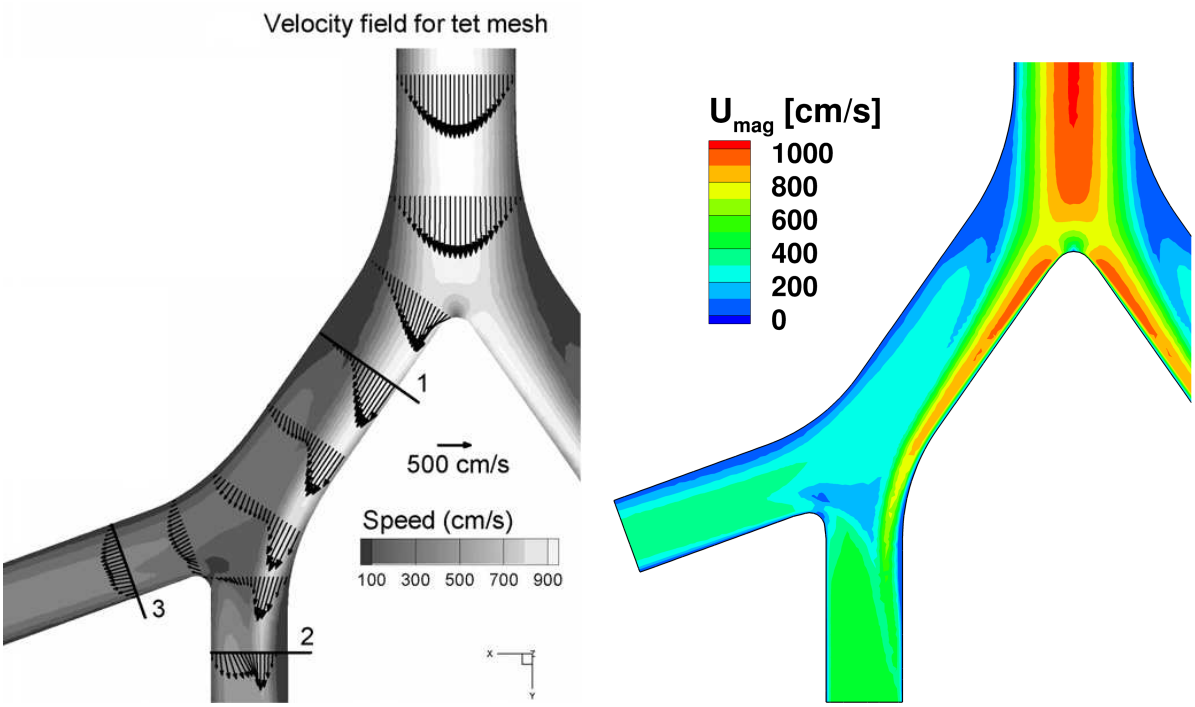

(a) Longest and Vinchurkar (2007): Tetrahedral Mesh

(b) Present: Hybrid Hexahedral-Tetrahedral Mesh

Figure B.1: Comparison of the velocity magnitude in the mid plane of the double bifurcation geometry between (a) results from Longest and Vinchurkar (2007), (b) present study.

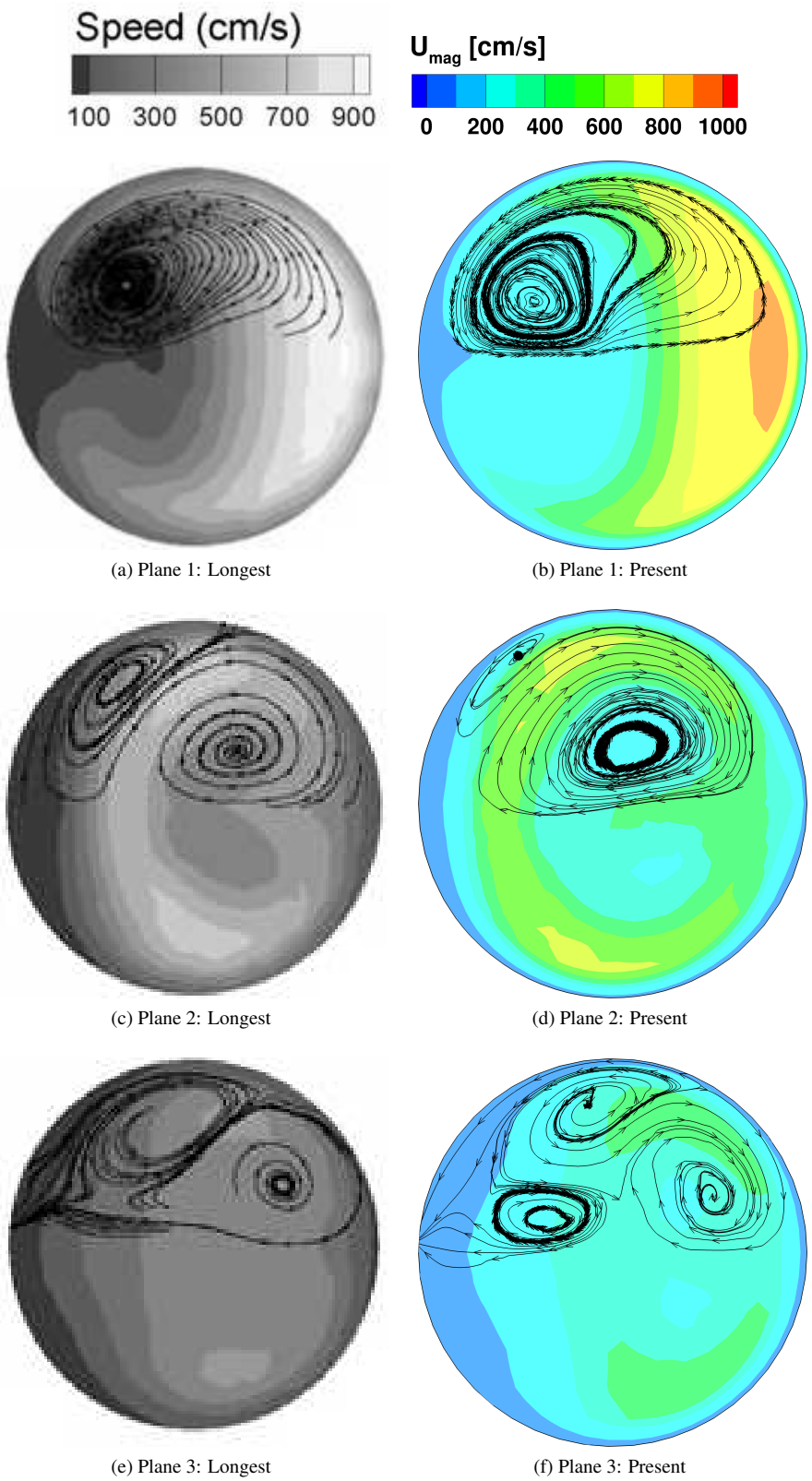

(a) Plane 1: Longest

(b) Plane 1: Present

(c) Plane 2: Longest

(d) Plane 2: Present

(e) Plane 3: Longest

(f) Plane 3: Present

Figure B.2: Velocity magnitude contours and streamtraces with data from Longest and Vinchurkar (2007) and results from the present study.

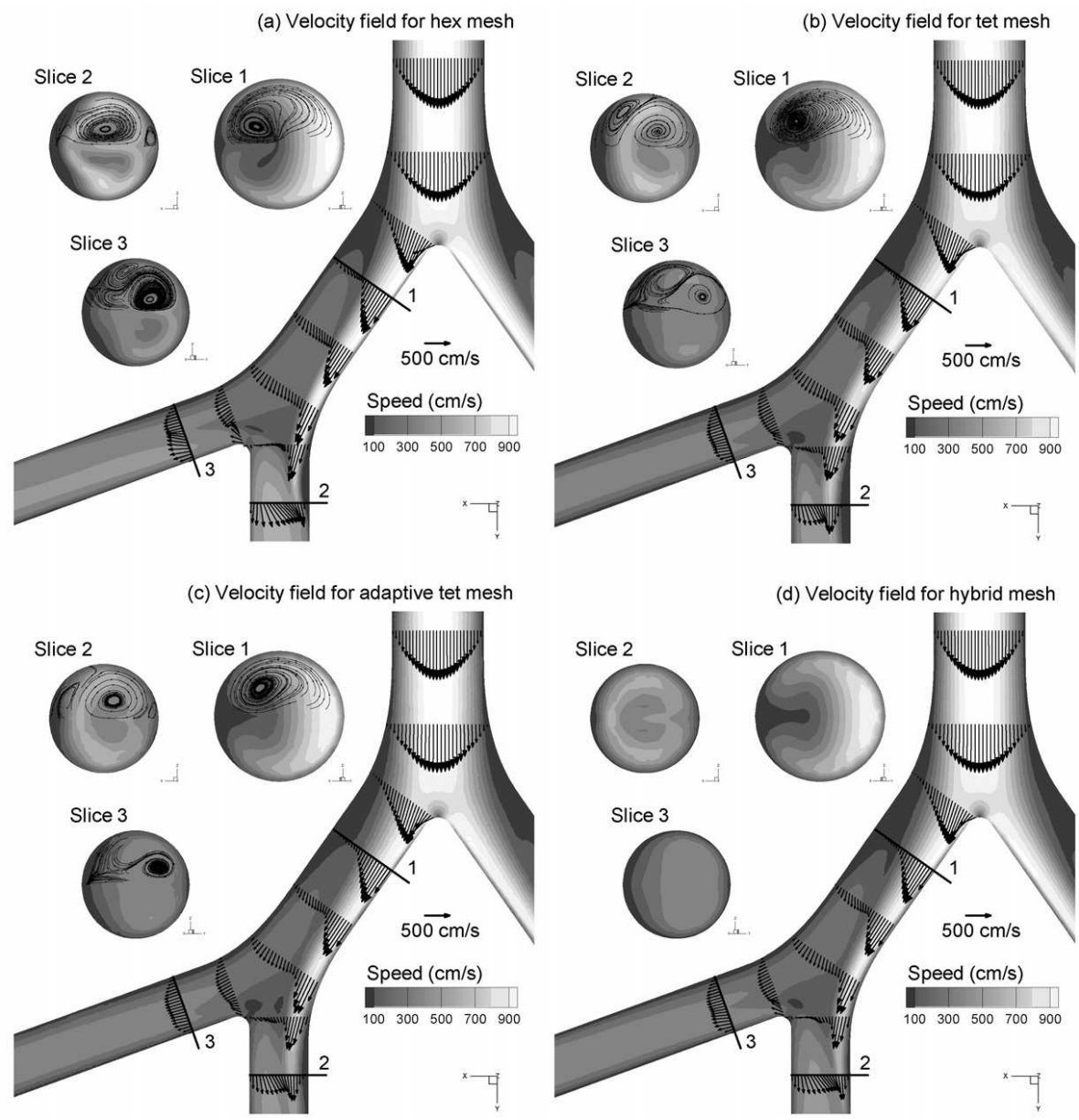

Figure B.3: Simulation results from Longest and Vinchurkar (2007) (figure copied directly from their paper).

B.3 Particle Deposition

Longest and Vinchurkar (2007) carried out the particle deposition with only one St number, therefore the same St number is used here. The particle deposition is compared by using the one dimensional deposition along a line originating from the inlet. The deposition matches quite well, especially compared to the poor results from chapter 7.

The drag model used is the model from Morsi and Alexander (1972). Minor discrepancies are expected since Longest and Vinchurkar (2007) used a modified lift model while the standard Fluent Saffman lift model was employed in the present study. The pressure gradient force was also included by Longest and Vinchurkar (2007) and therefore also included here. Gravity is acting perpendicular to the direction of the inlet flow. An overview of the forces acting on the particle can be found in table B.3.

Table B.3: Overview of the particle forces used in this chapter.

F_d	F_g and F_b	F_m	F_{Saffman}	$F_{\text{p.grad.}}$	Turbulent Dispersion
+	+	-	+	+	-

The deposition along the z-direction is given in figure B.4 below for a deterministic parabolic inlet distribution and a fully developed velocity profile together with the results from Longest and Vinchurkar (2007) and shows good agreement.

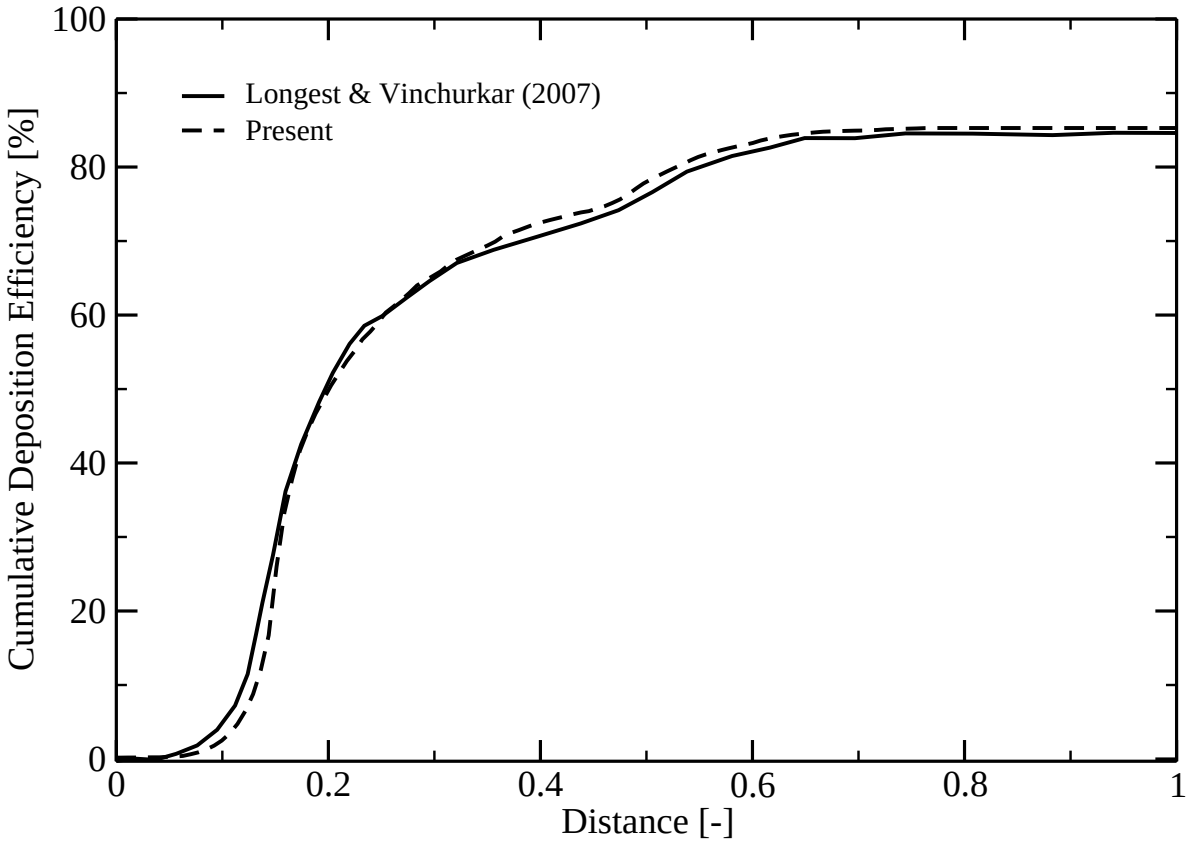

Figure B.4: Comparison of cumulative particle deposition in a double bifurcation geometry between results found in chapter B and Longest and Vinchurkar (2007).

Appendix C

Patient Specific Geometry Supplements

C.1 Mesh Estimation

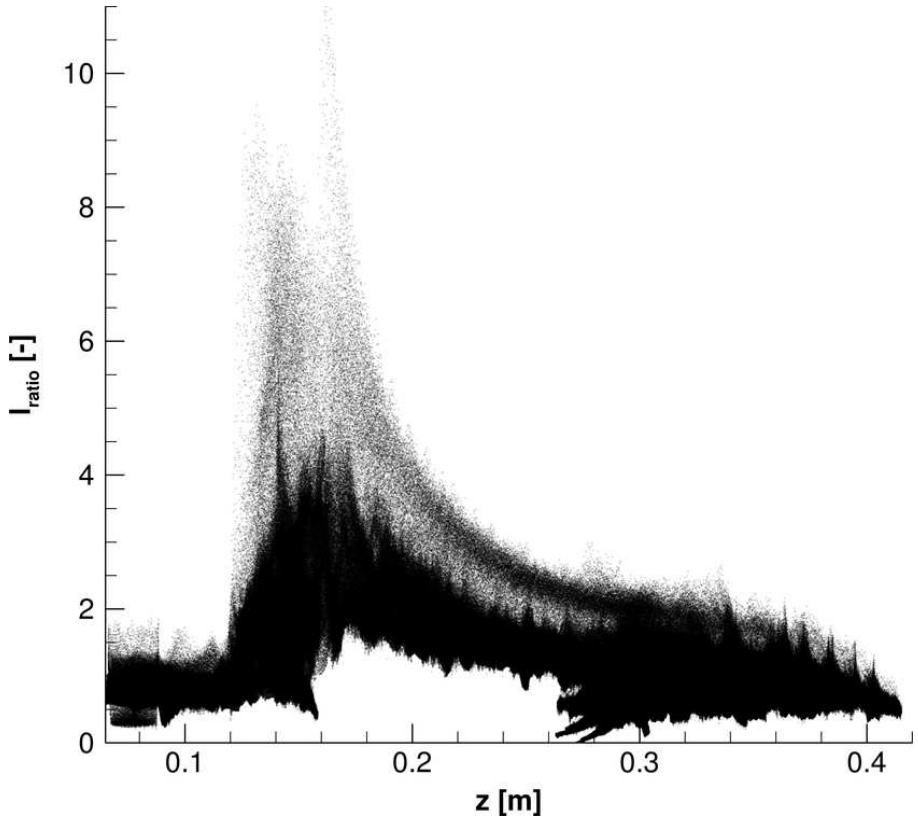

Figure C.1: Scatter plot of the length scale ratio (equation 8.3) versus z-coordinate for all cells for a flow rate of 30 L/min.

C.2 Turbulence Inlet Parameters: Additional Figures

C.2.1 Velocity Magnitude

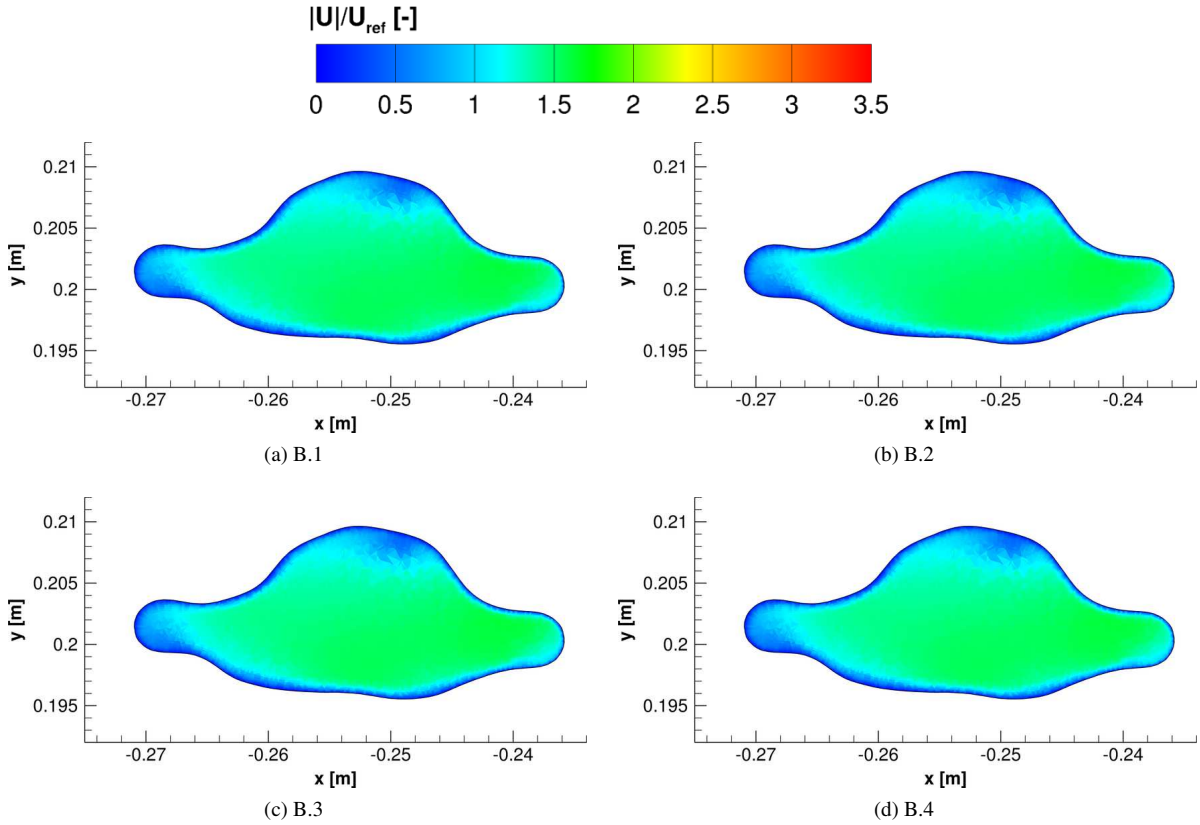

(a) B.1 (b) B.2

(c) B.3 (d) B.4

Figure C.2: Contours of the scaled velocity magnitude in plane 1.

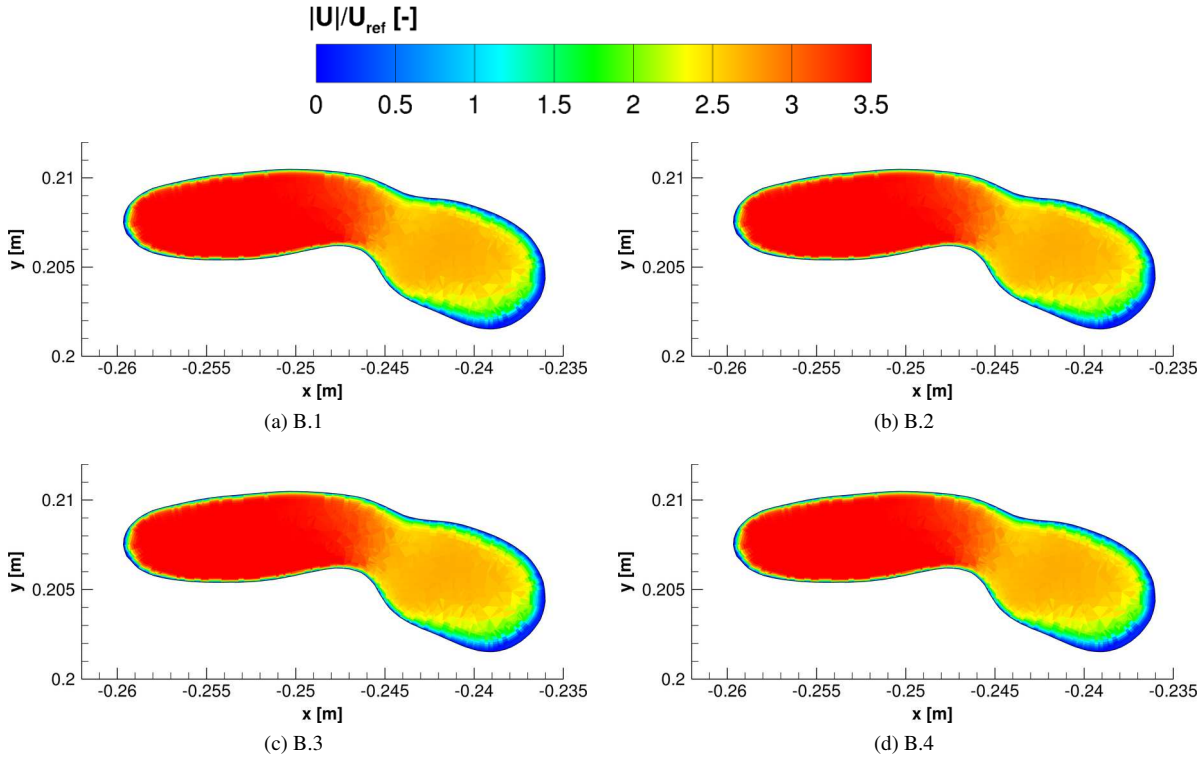

(a) B.1 (b) B.2

(c) B.3 (d) B.4

Figure C.3: Contours of the scaled velocity magnitude in plane 2.

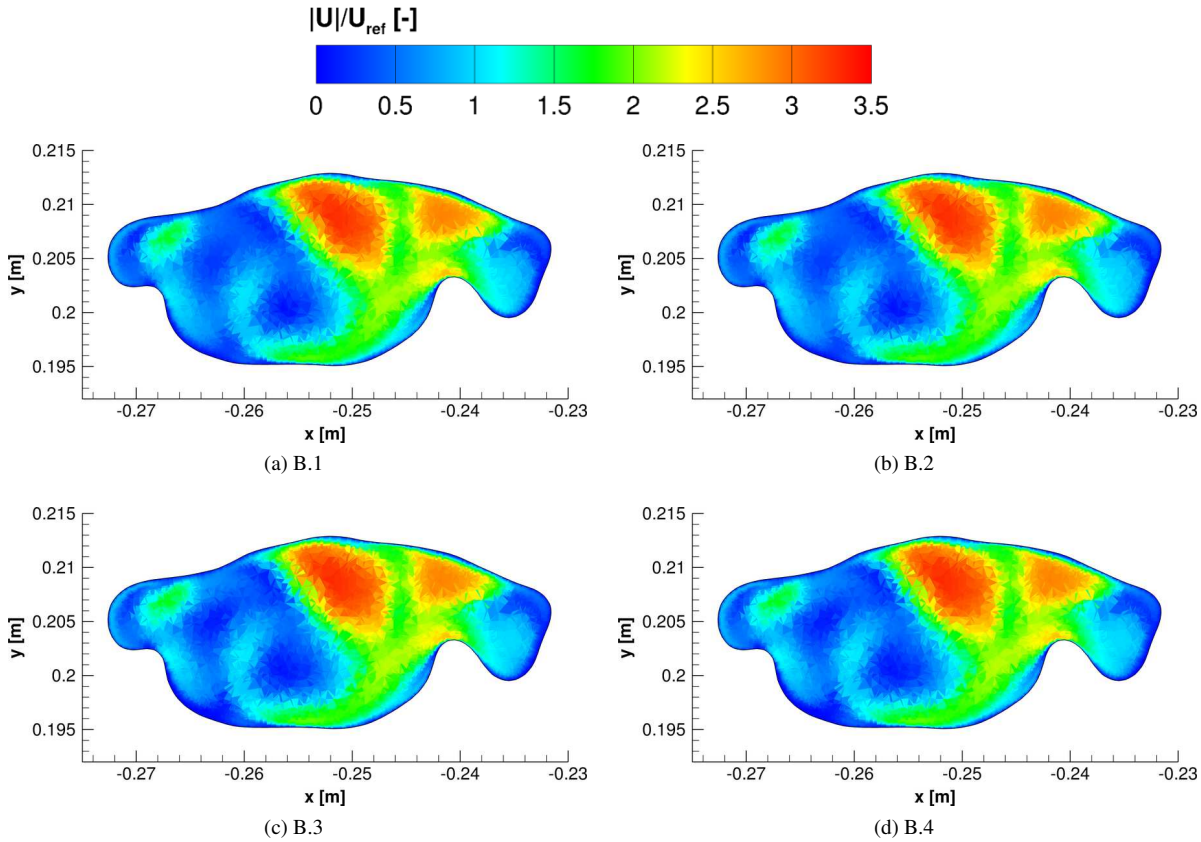

(a) B.1 (b) B.2

(c) B.3 (d) B.4

Figure C.4: Contours of the scaled velocity magnitude in plane 3.

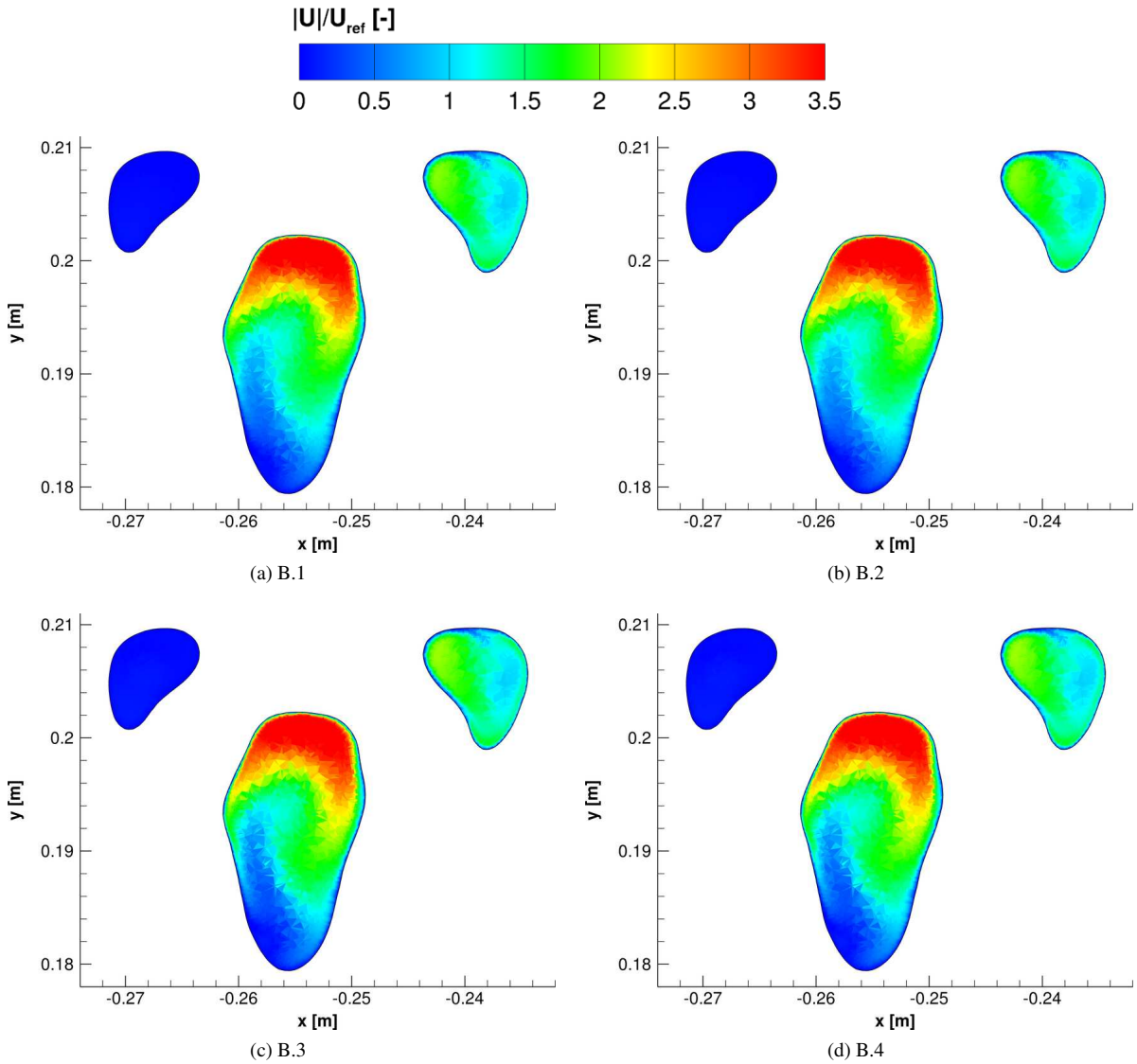

(a) B.1

(b) B.2

(c) B.3

(d) B.4

Figure C.5: Contours of the scaled velocity magnitude in plane 5.

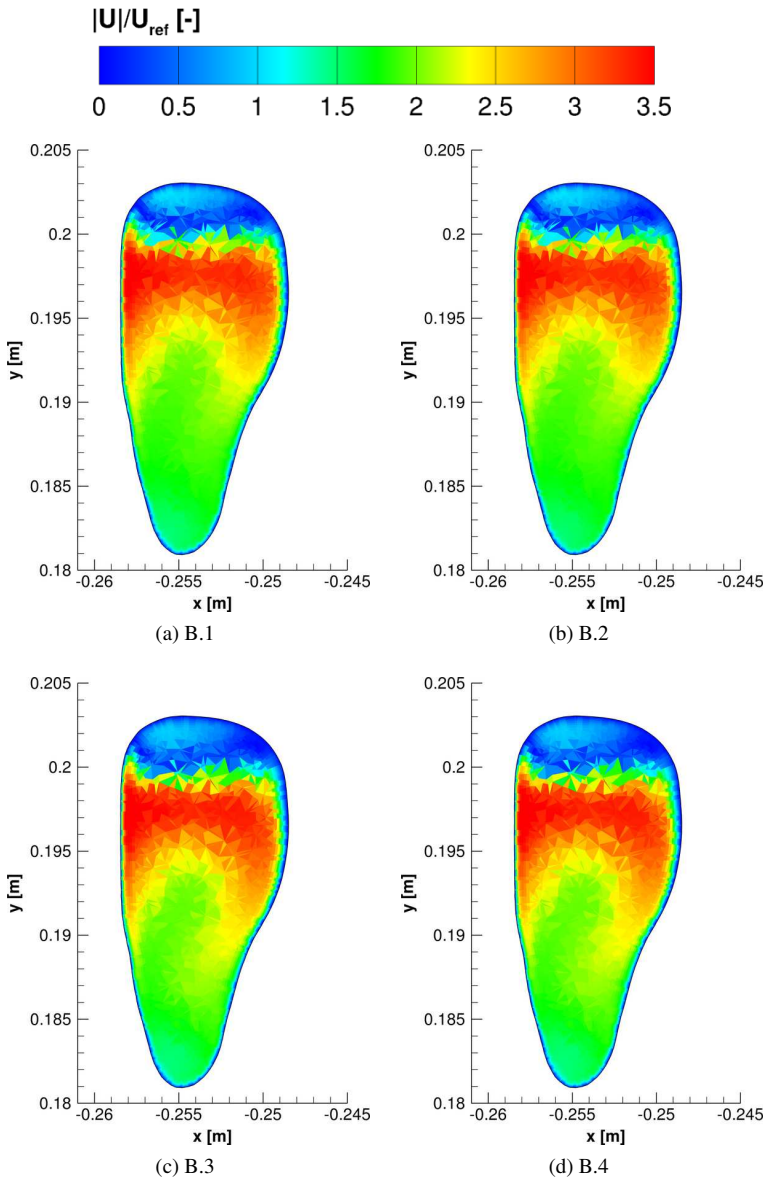

(a) B.1 (b) B.2

(c) B.3 (d) B.4

Figure C.6: Contours of the scaled velocity magnitude in plane 6.

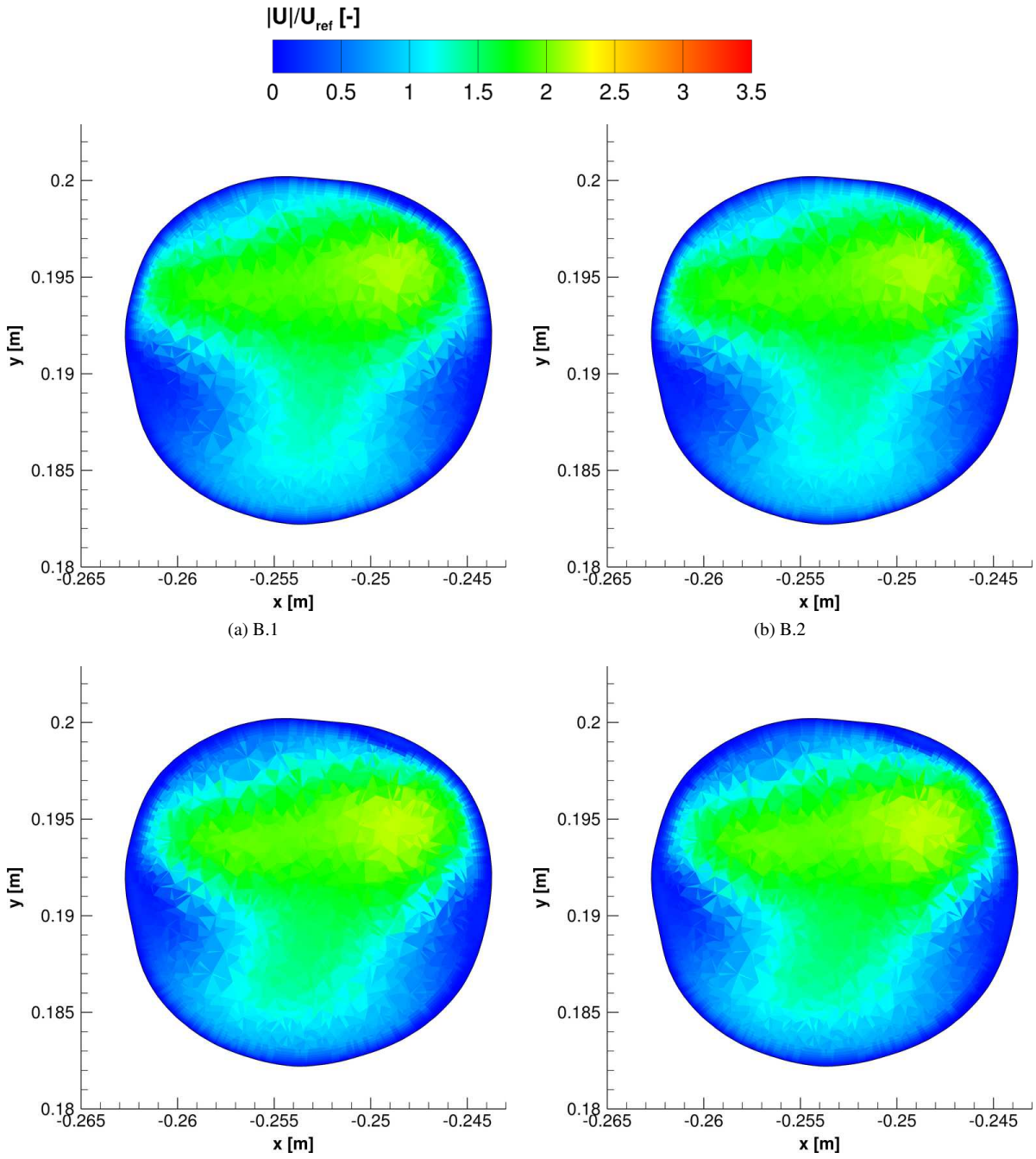

(a) B.1 (b) B.2

(c) B.3 (d) B.4

Figure C.7: Contours of the scaled velocity magnitude in plane 7.

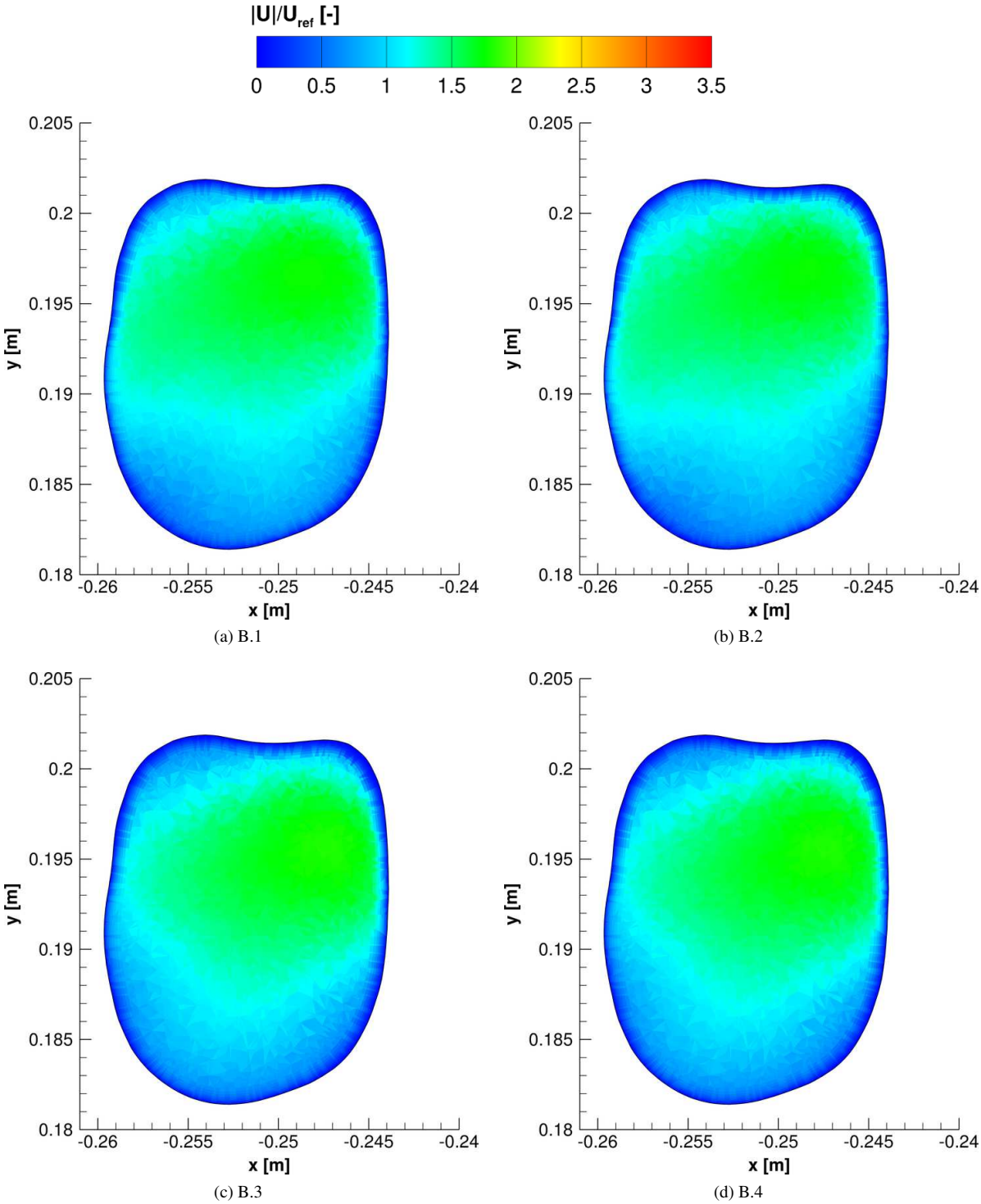

(a) B.1

(b) B.2

(c) B.3

(d) B.4

Figure C.8: Contours of the scaled velocity magnitude in plane 8.

C.2.2 Turbulent Kinetic Energy

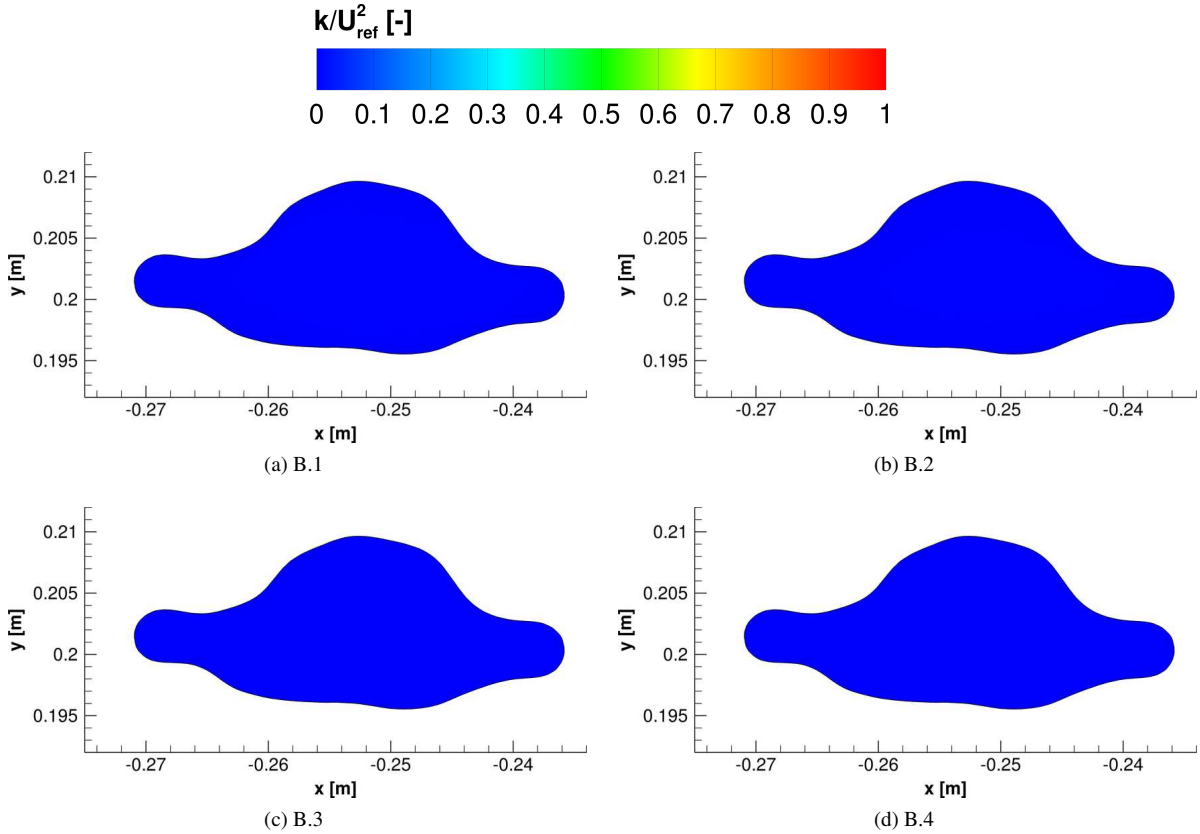

(a) B.1 (b) B.2

(c) B.3 (d) B.4

Figure C.9: Contours of the scaled turbulent kinetic energy in plane 1.

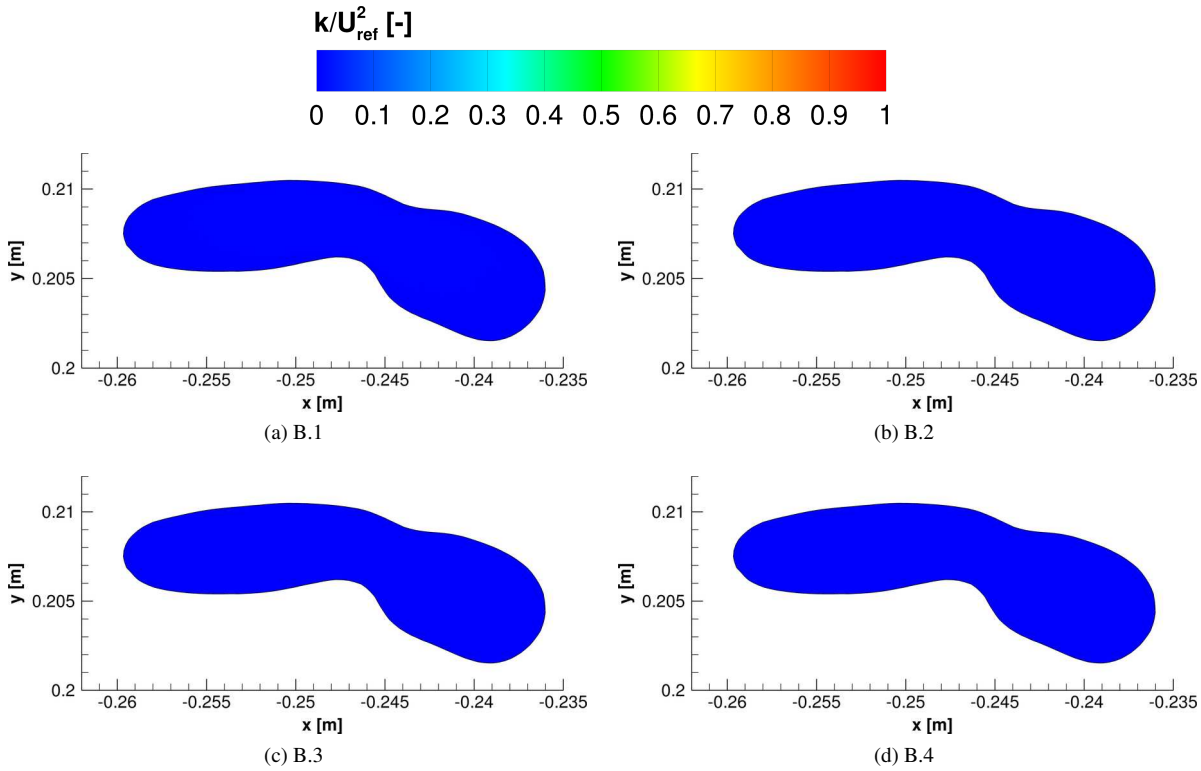

(a) B.1 (b) B.2

(c) B.3 (d) B.4

Figure C.10: Contours of the scaled turbulent kinetic energy in plane 2.

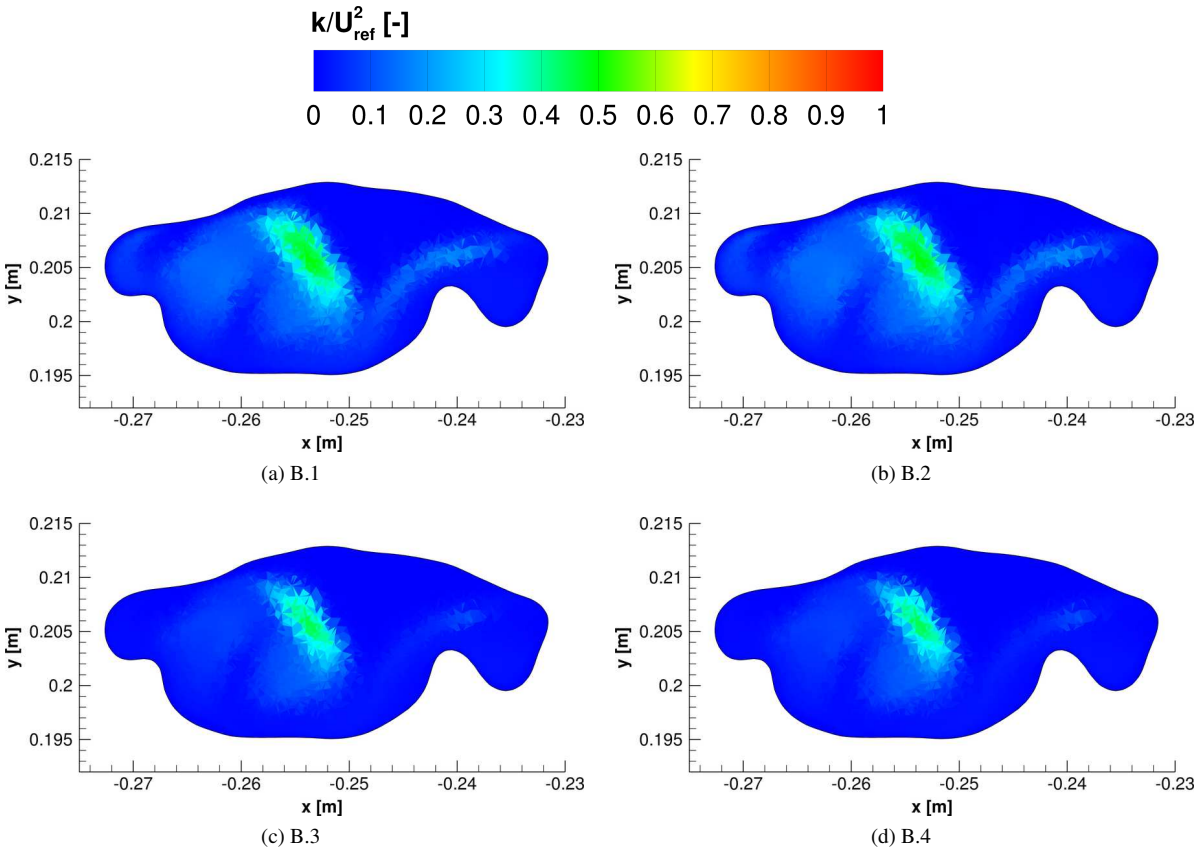

(a) B.1 (b) B.2

(c) B.3 (d) B.4

Figure C.11: Contours of the scaled turbulent kinetic energy in plane 3.

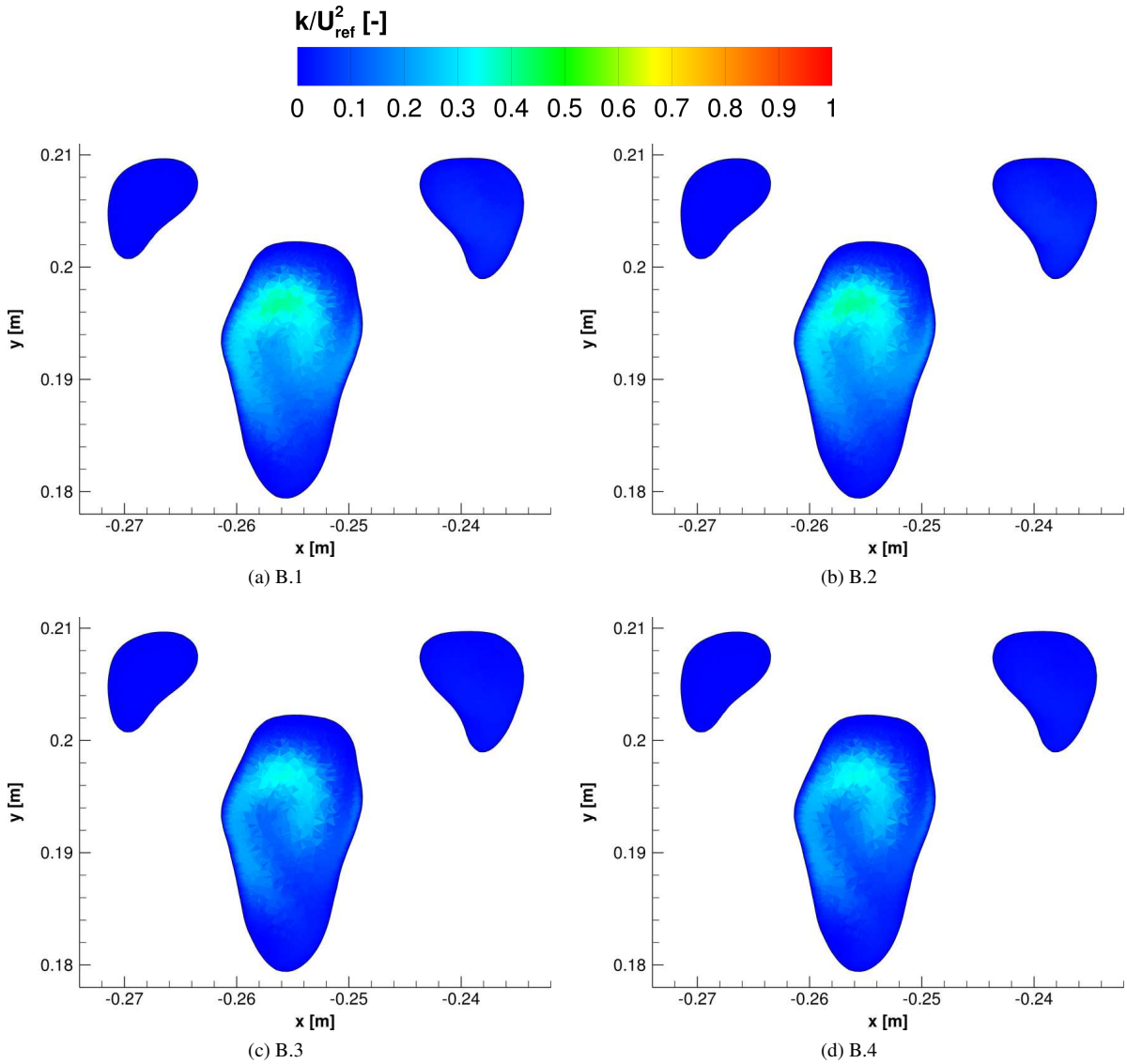

(a) B.1

(b) B.2

(c) B.3

(d) B.4

Figure C.12: Contours of the scaled turbulent kinetic energy in plane 5.

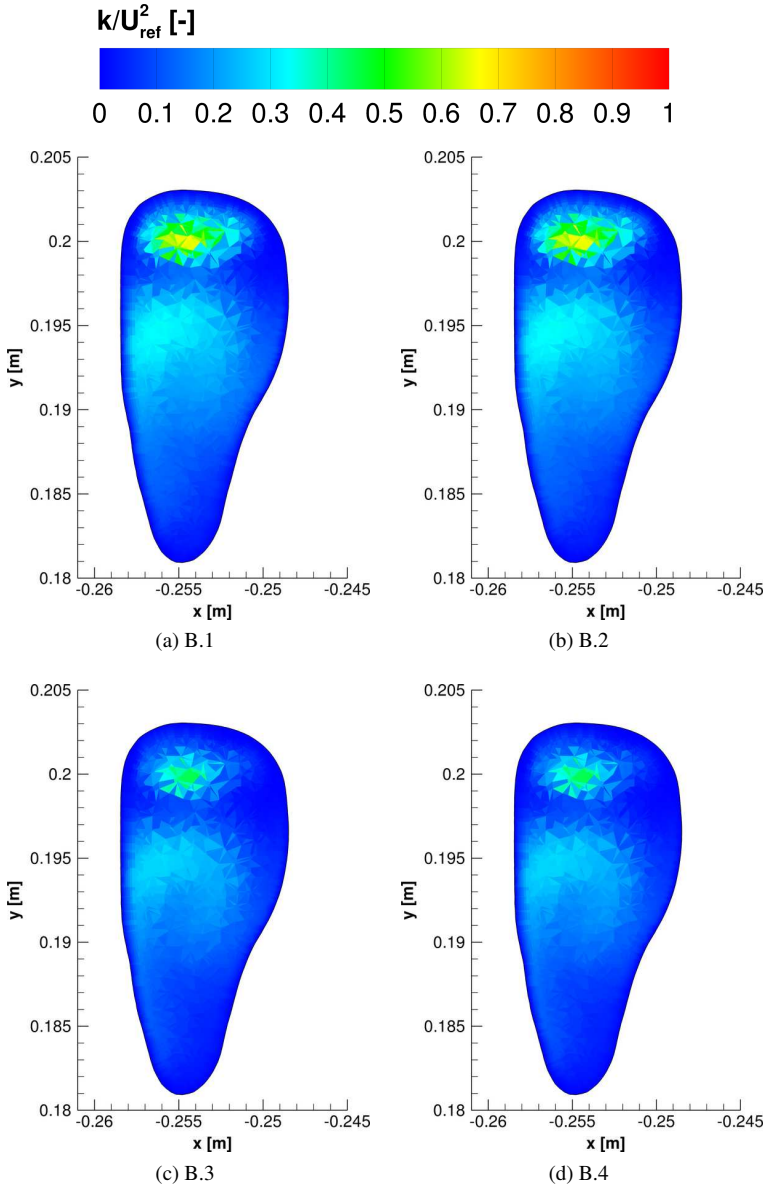

(a) B.1 (b) B.2

(c) B.3 (d) B.4

Figure C.13: Contours of the scaled turbulent kinetic energy in plane 6.

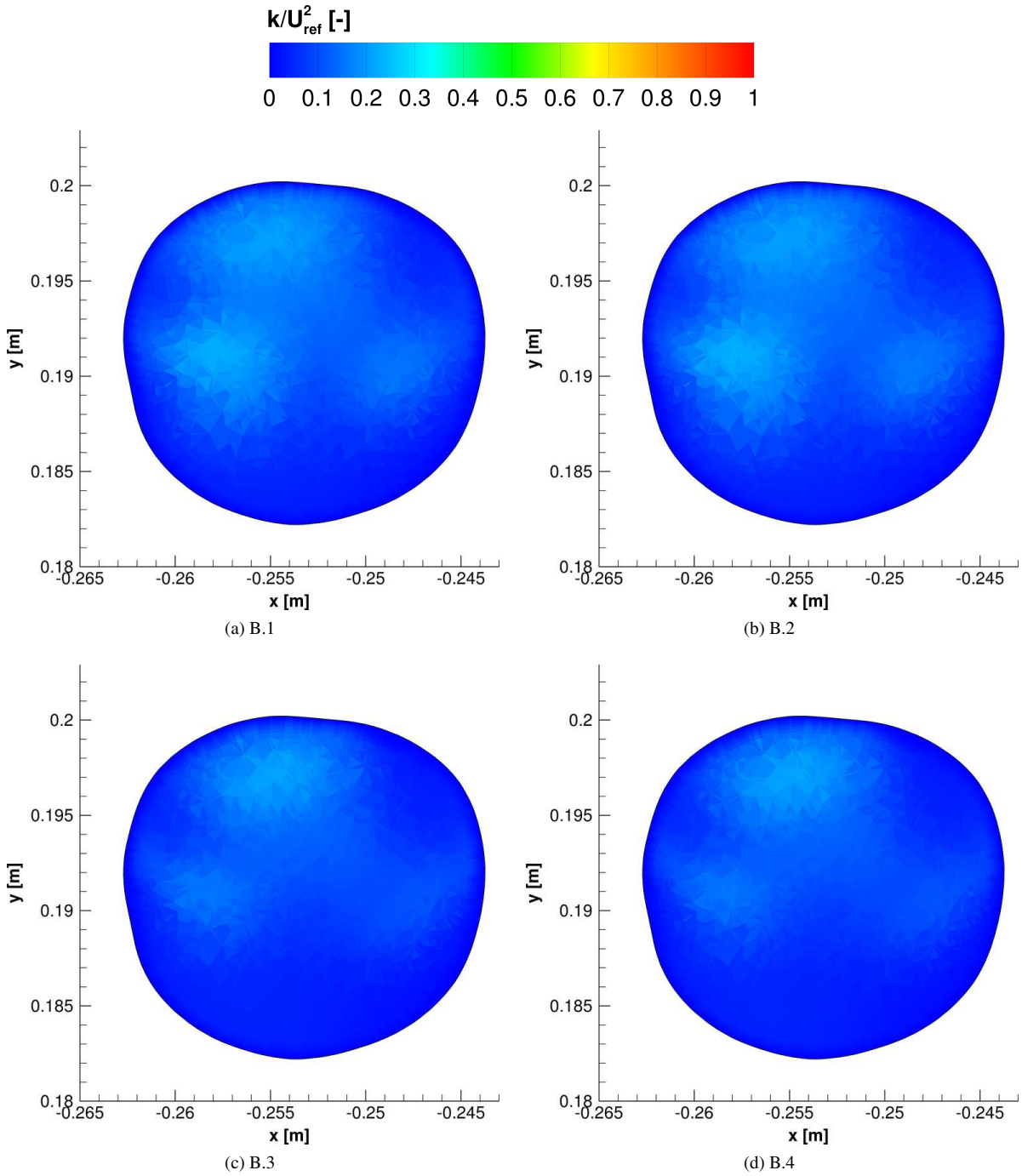

(a) B.1 (b) B.2

(c) B.3 (d) B.4

Figure C.14: Contours of the scaled turbulent kinetic energy in plane 7.

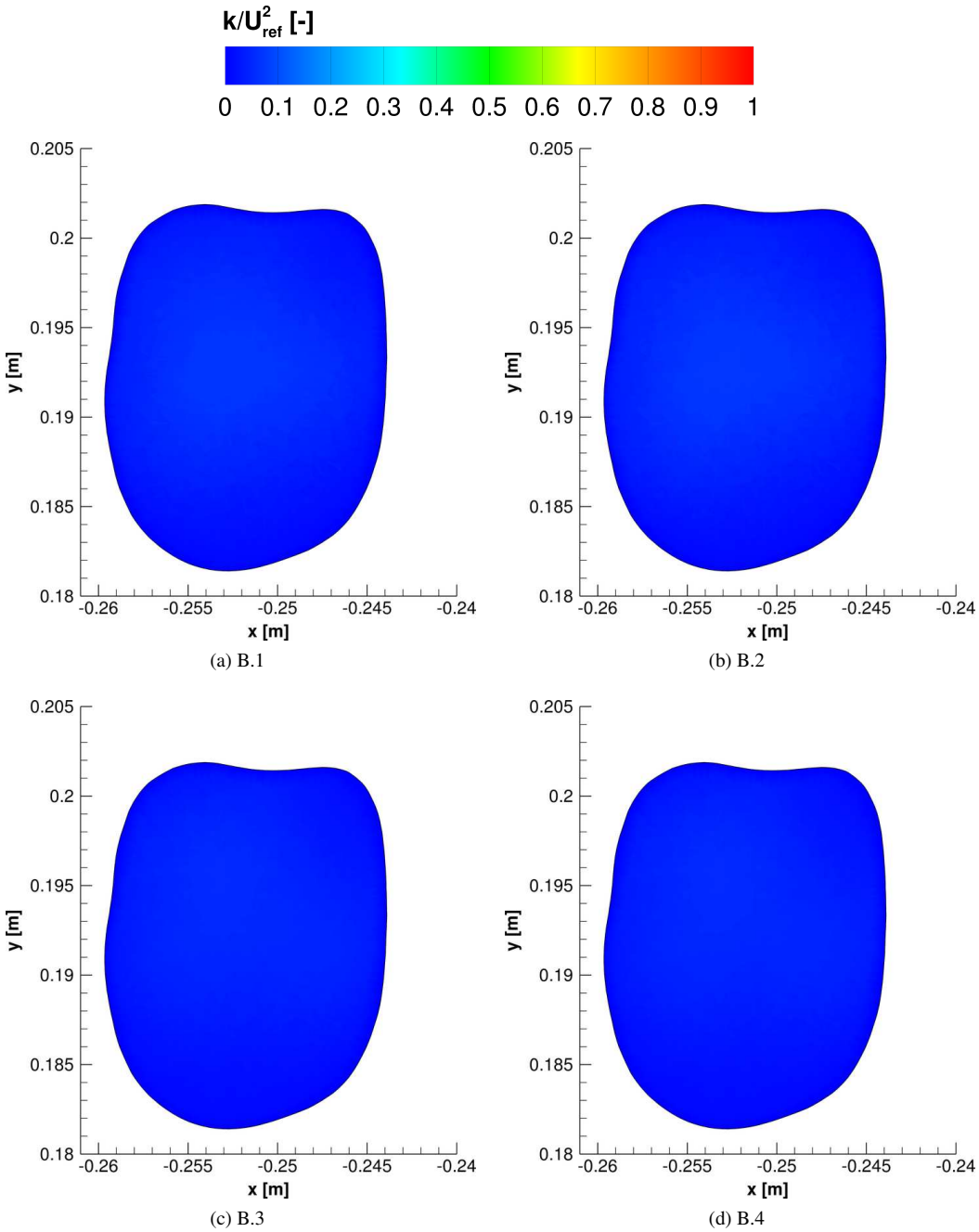

(a) B.1 (b) B.2

(c) B.3 (d) B.4

Figure C.15: Contours of the scaled turbulent kinetic energy in plane 8.

C.3 Flow Structures Comparison

C.3.1 Velocity Magnitude

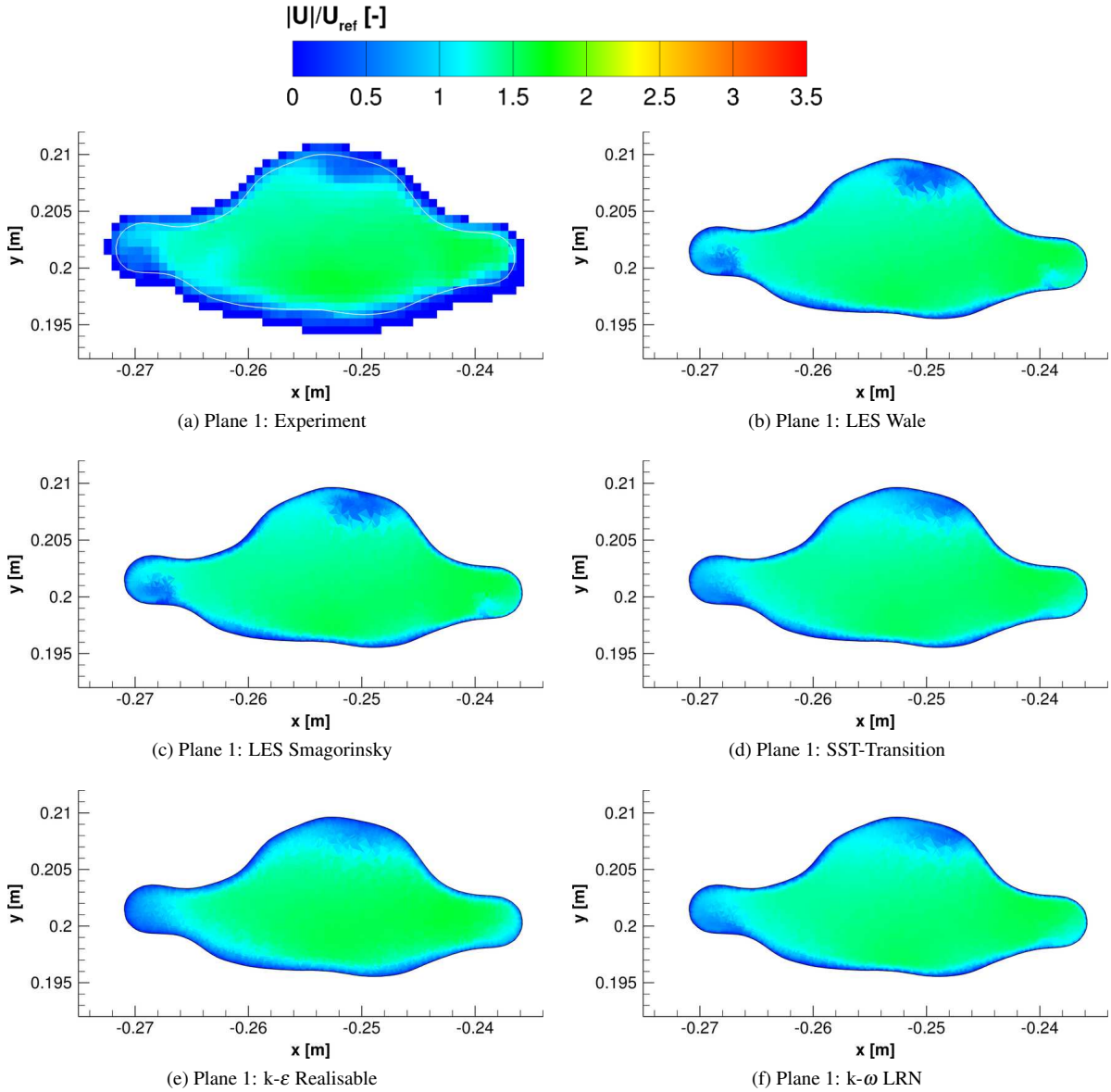

(a) Plane 1: Experiment

(b) Plane 1: LES Wale

(c) Plane 1: LES Smagorinsky

(d) Plane 1: SST-Transition

(e) Plane 1: k-ε Realisable

(f) Plane 1: k-ω LRN

Figure C.16: Contours of the scaled velocity magnitude in Plane 1 for the experimental and simulation data.

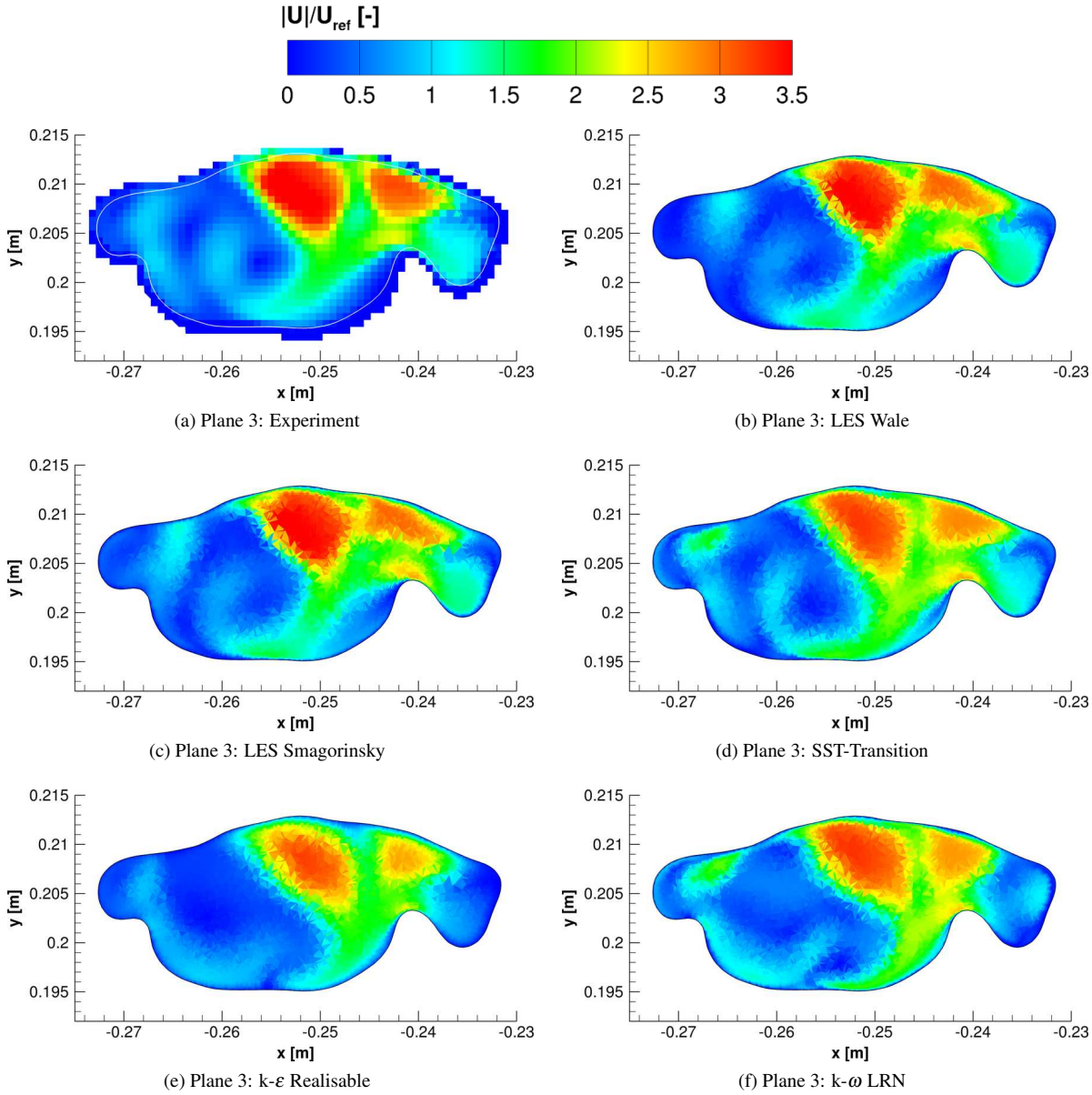

(a) Plane 3: Experiment

(b) Plane 3: LES Wale

(c) Plane 3: LES Smagorinsky

(d) Plane 3: SST-Transition

(e) Plane 3: k-ε Realisable

(f) Plane 3: k-ω LRN

Figure C.17: Contours of the scaled velocity magnitude in Plane 3 for the experimental and simulation data.

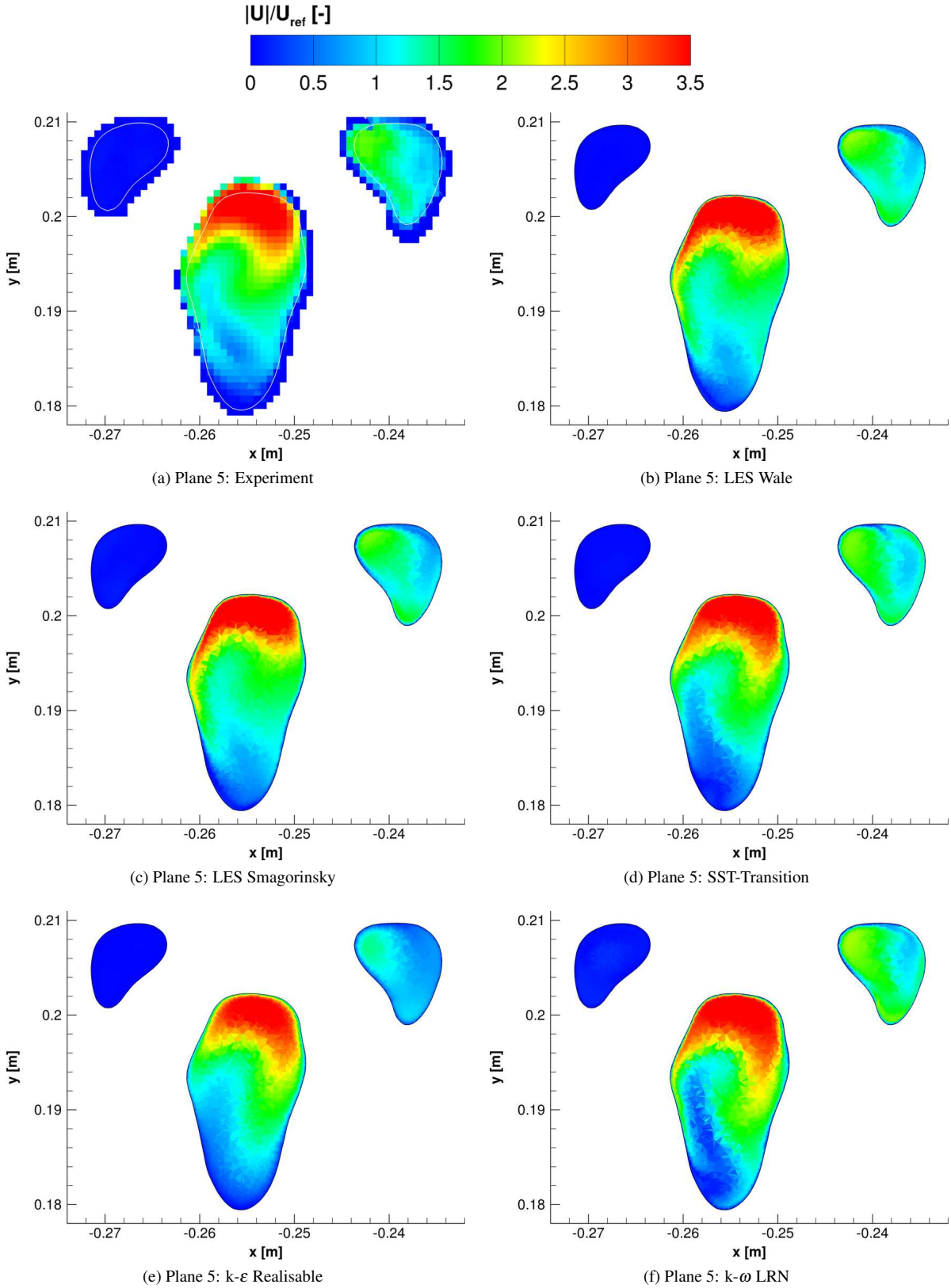

(a) Plane 5: Experiment

(b) Plane 5: LES Wale

(c) Plane 5: LES Smagorinsky

(d) Plane 5: SST-Transition

(e) Plane 5: k-ε Realisable

(f) Plane 5: k-ω LRN

Figure C.18: Contours of the scaled velocity magnitude in Plane 5 for the experimental and simulation data.

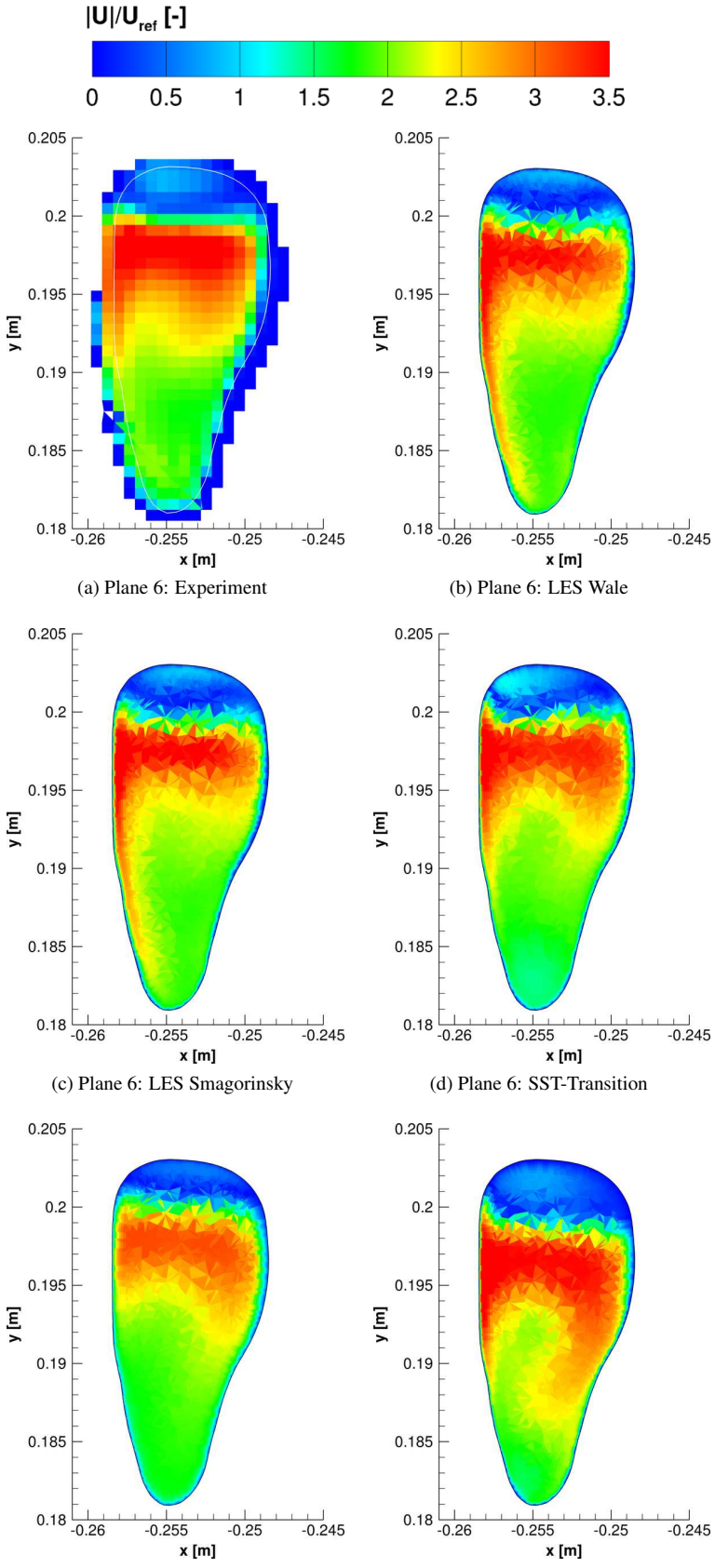

(a) Plane 6: Experiment

(b) Plane 6: LES Wale

(c) Plane 6: LES Smagorinsky

(d) Plane 6: SST-Transition

(e) Plane 6: k-ε Realisable

(f) Plane 6: k-ω LRN

Figure C.19: Contours of the scaled velocity magnitude in Plane 6 for the experimental and simulation data.

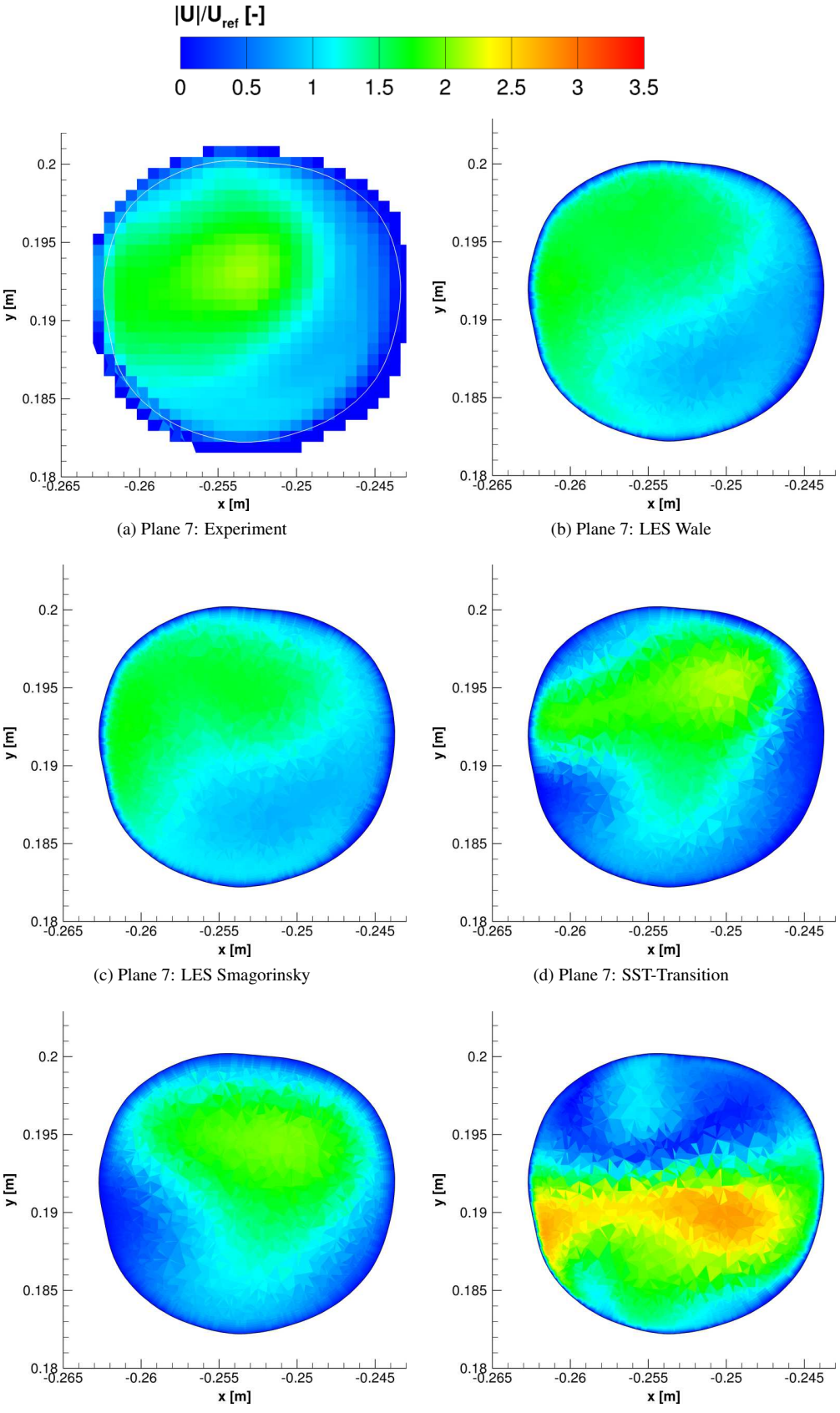

(a) Plane 7: Experiment

(b) Plane 7: LES Wale

(c) Plane 7: LES Smagorinsky

(d) Plane 7: SST-Transition

(e) Plane 7: k-ε Realisable

(f) Plane 7: k-ω LRN

Figure C.20: Contours of the scaled velocity magnitude in Plane 7 for the experimental and simulation data.

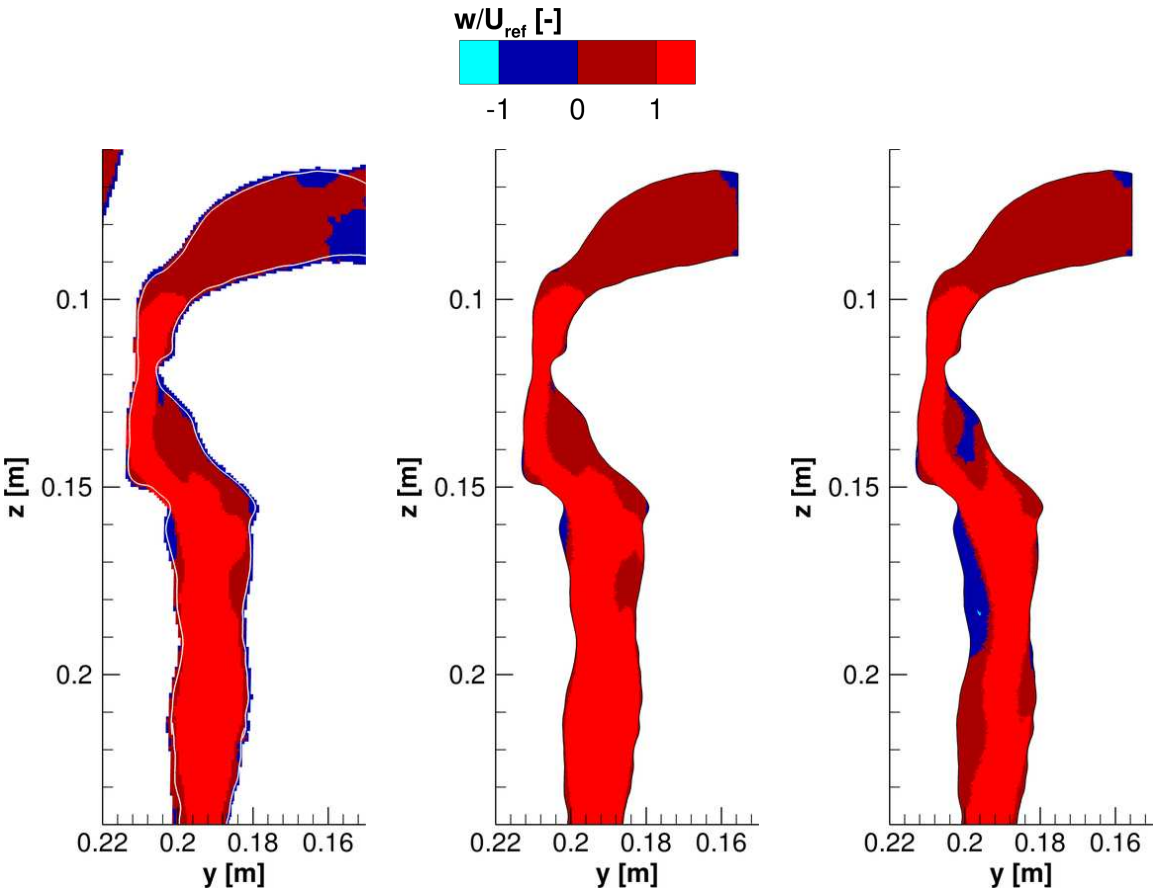

(a) Experiment (b) LES Wale (c) k-ω LRN

(d) SST-Transition (e) k-ε Realisable (f) LES Smagorinsky

Figure C.21: Contours of the scaled w velocity in a cross section for the experimental and simulation data to highlight the regions where flow separation and reattachment occur.

C.3.2 Z Vorticity

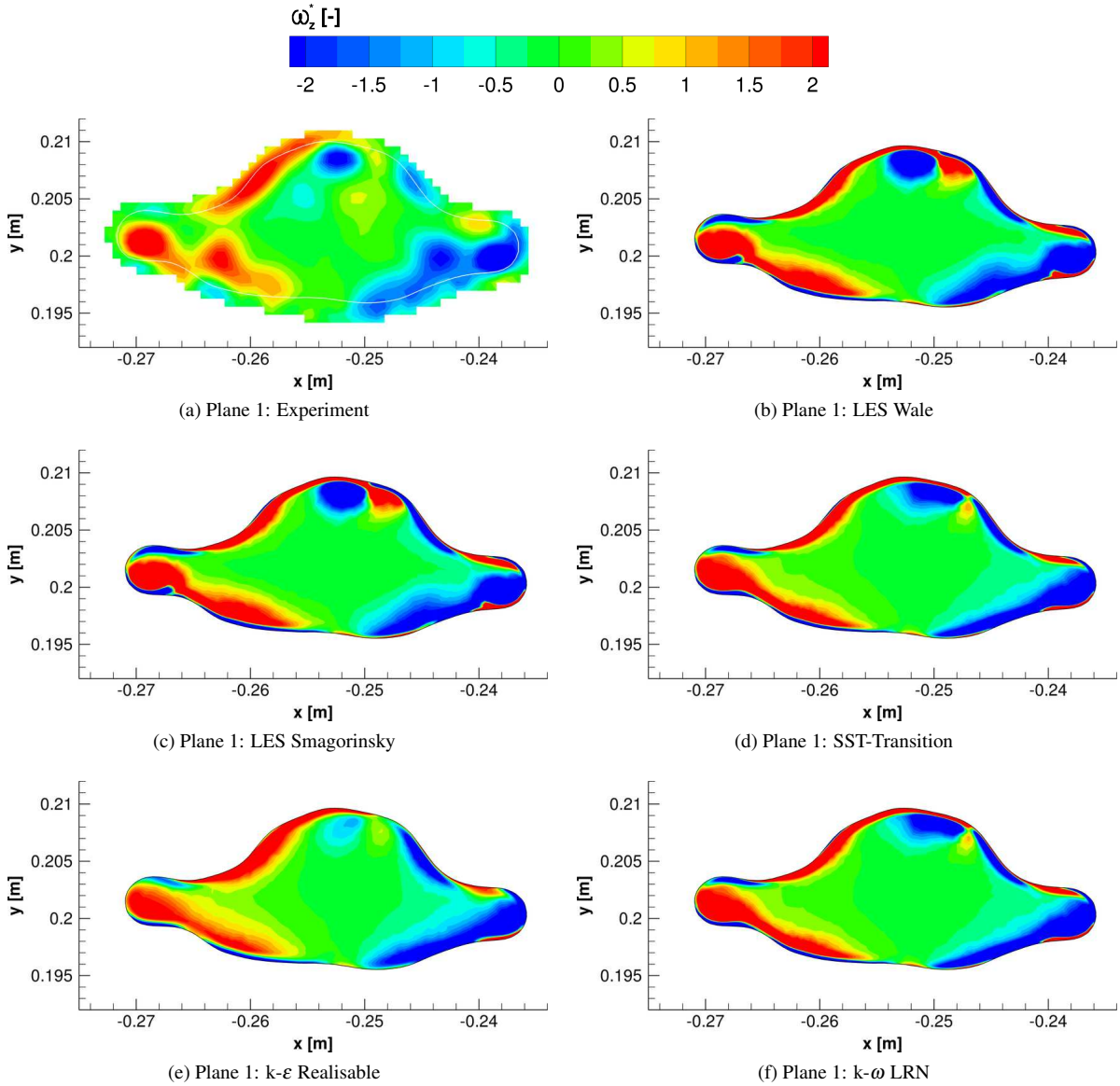

(a) Plane 1: Experiment

(b) Plane 1: LES Wale

(c) Plane 1: LES Smagorinsky

(d) Plane 1: SST-Transition

(e) Plane 1: k-ε Realisable

(f) Plane 1: k-ω LRN

Figure C.22: Contours of the scaled z-vorticity in Plane 1 for the experimental and simulation data.

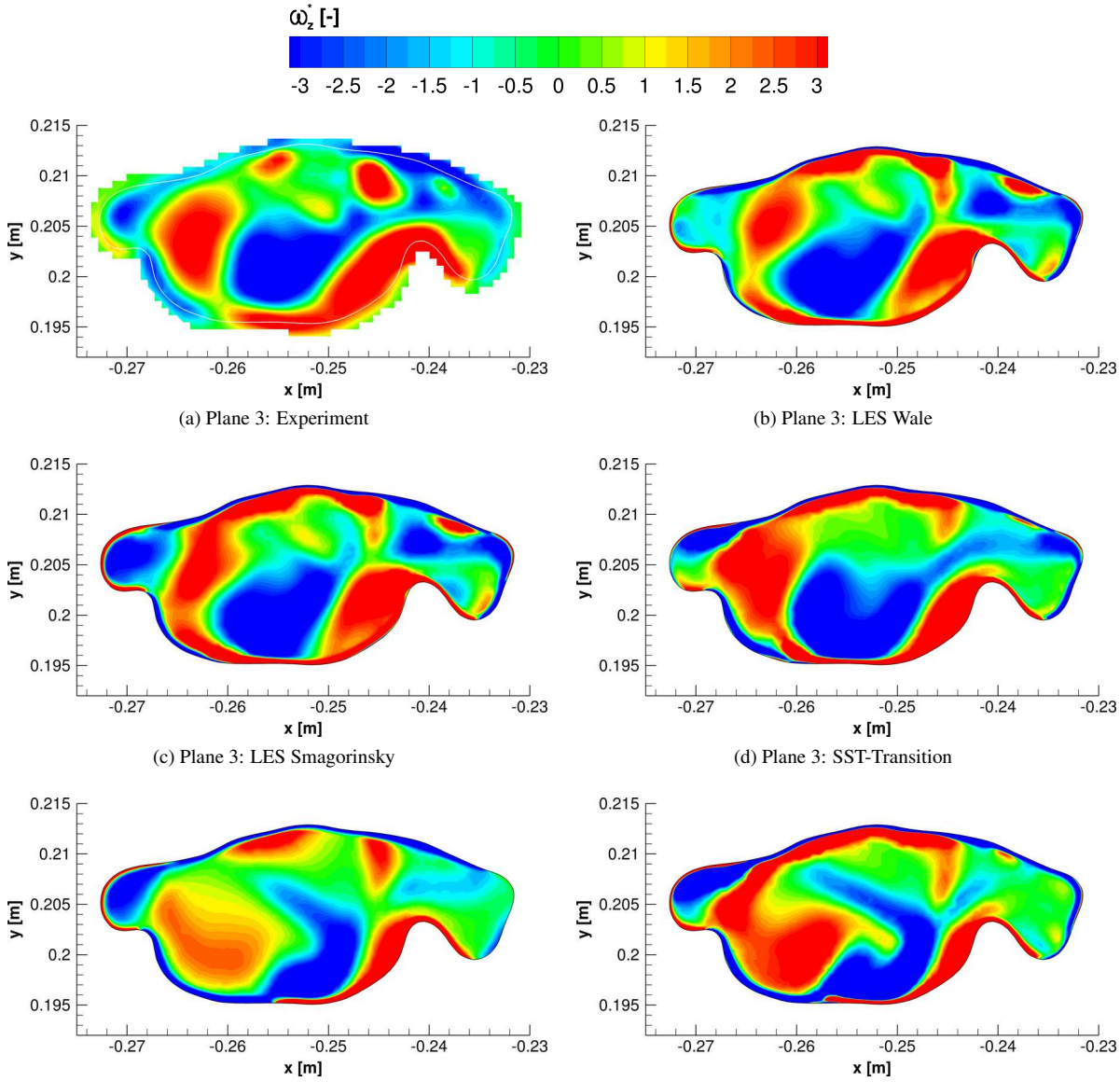

(a) Plane 3: Experiment

(b) Plane 3: LES Wale

(c) Plane 3: LES Smagorinsky

(d) Plane 3: SST-Transition

(e) Plane 3: k-ε Realisable

(f) Plane 3: k-ω LRN

Figure C.23: Contours of the scaled z-vorticity in Plane 3 for the experimental and simulation data.

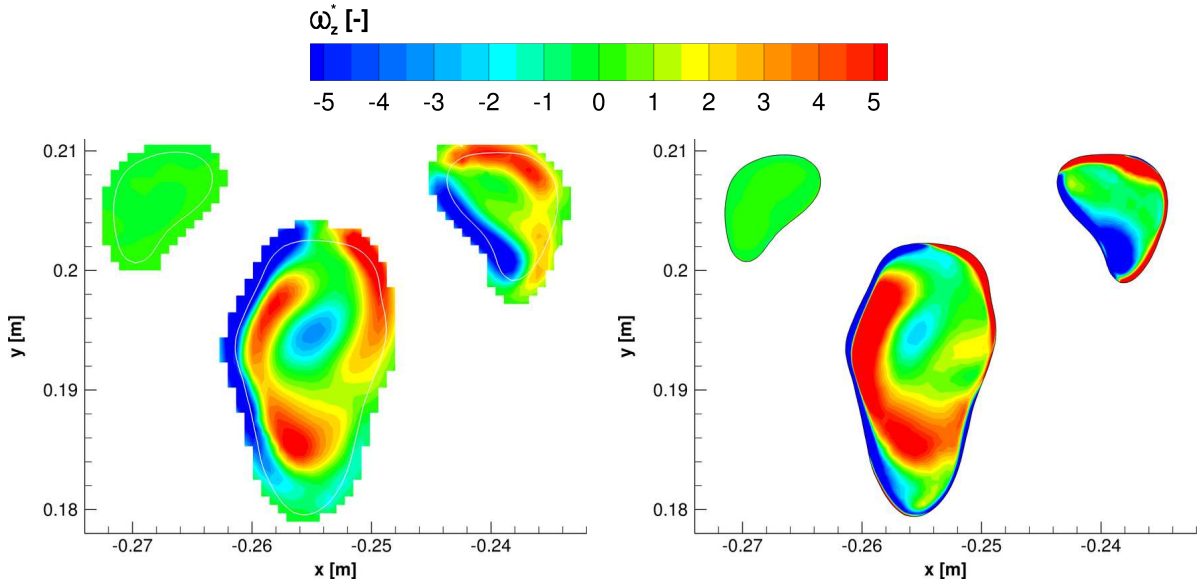

(a) Plane 5: Experiment

(b) Plane 5: LES Wale

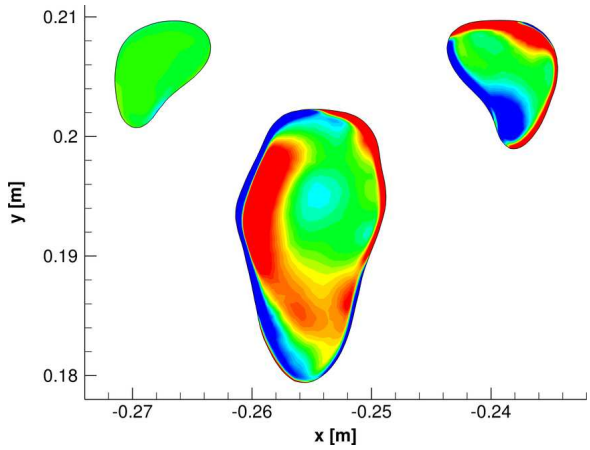

(c) Plane 5: LES Smagorinsky

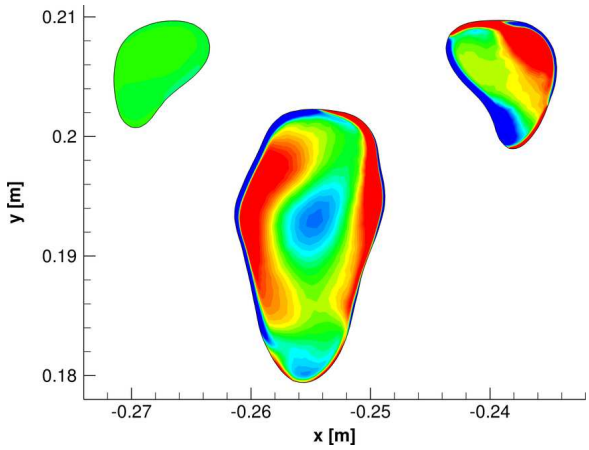

(d) Plane 5: SST-Transition

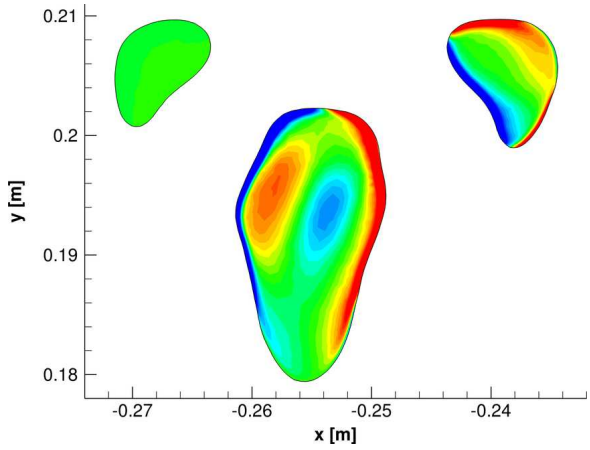

(e) Plane 5: k-ε Realisable

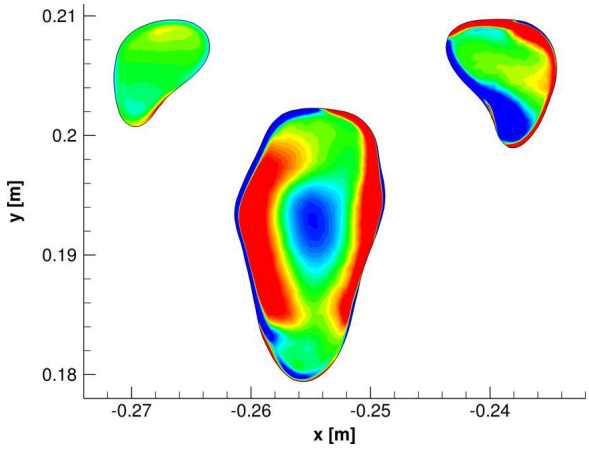

(f) Plane 5: k-ω LRN

Figure C.24: Contours of the scaled z-vorticity in Plane 5 for the experimental and simulation data.

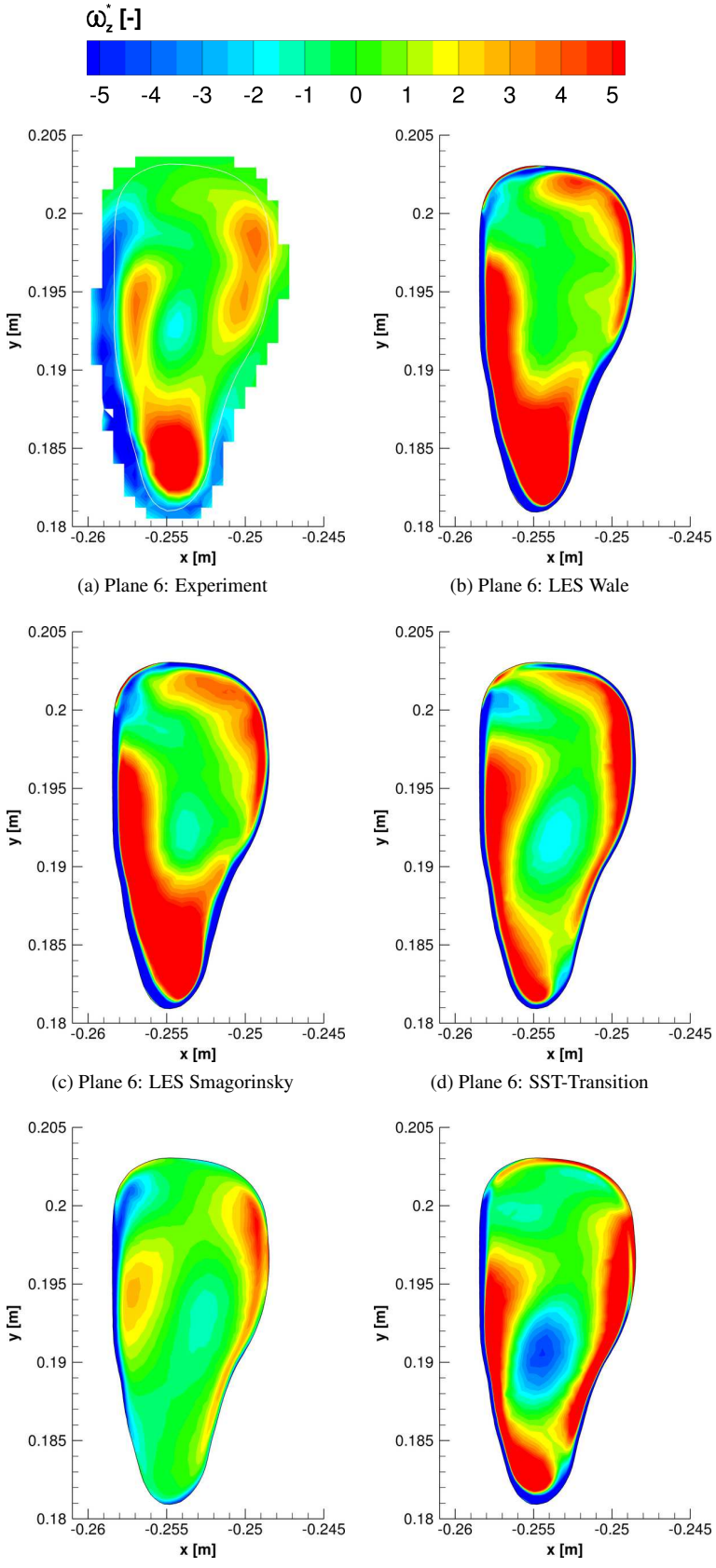

(a) Plane 6: Experiment

(b) Plane 6: LES Wale

(c) Plane 6: LES Smagorinsky

(d) Plane 6: SST-Transition

(e) Plane 6: k-ε Realisable

(f) Plane 6: k-ω LRN

Figure C.25: Contours of the scaled z-vorticity in Plane 6 for the experimental and simulation data.

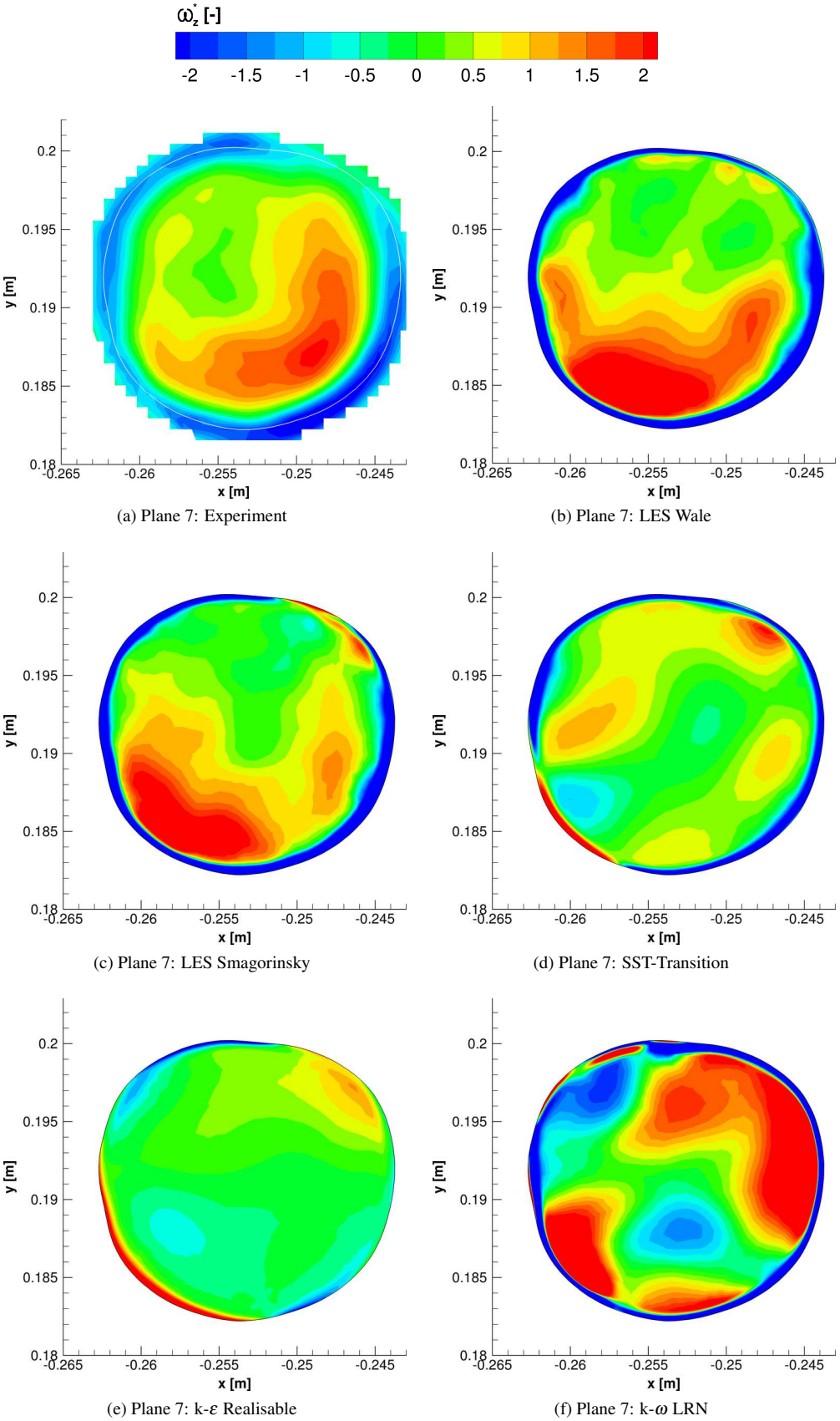

(a) Plane 7: Experiment

(b) Plane 7: LES Wale

(c) Plane 7: LES Smagorinsky

(d) Plane 7: SST-Transition

(e) Plane 7: k-ε Realisable

(f) Plane 7: k-ω LRN

Figure C.26: Contours of the scaled z-vorticity in Plane 7 for the experimental and simulation data.

C.3.3 Magnitude of Secondary Velocities

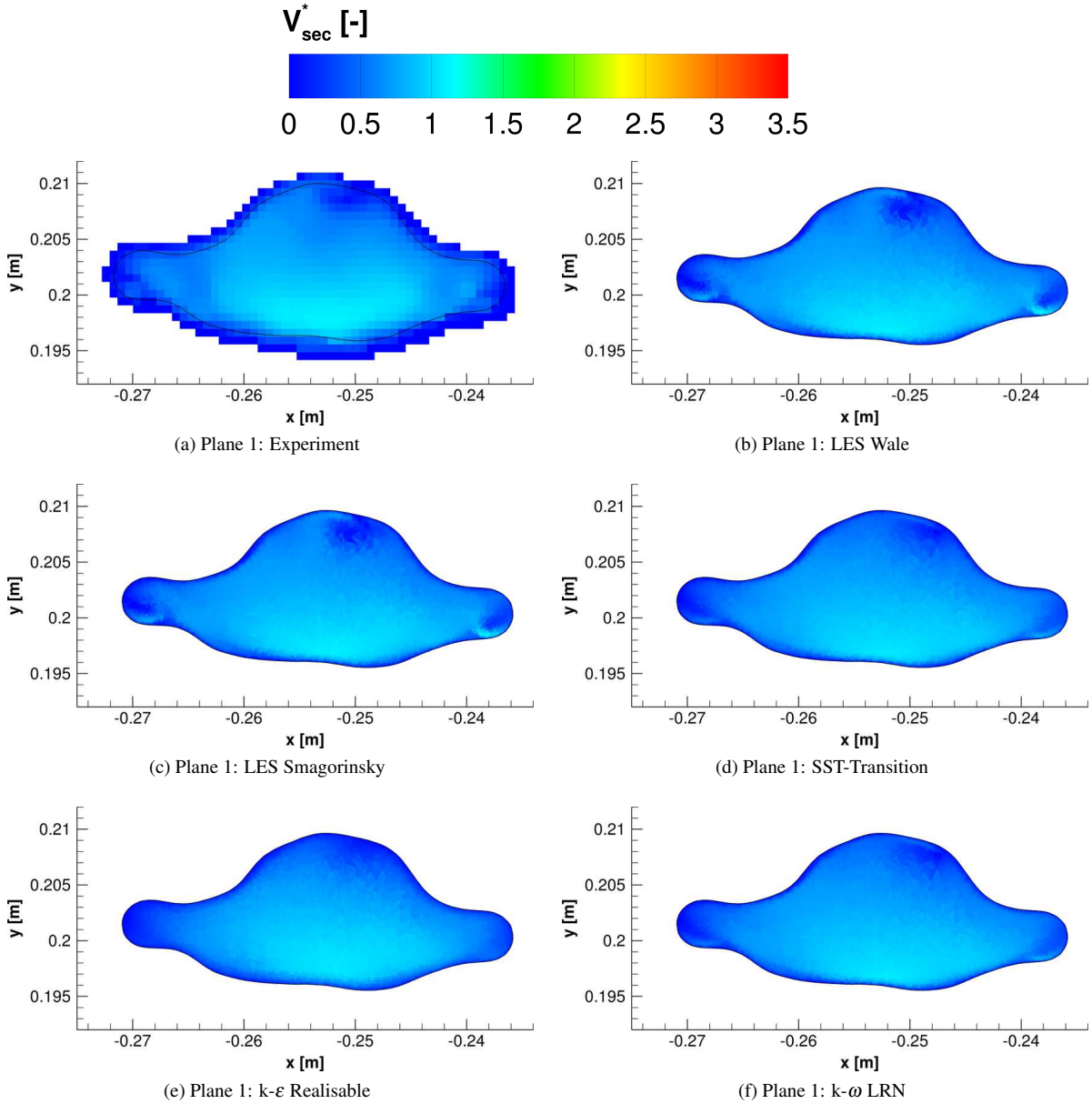

(a) Plane 1: Experiment

(b) Plane 1: LES Wale

(c) Plane 1: LES Smagorinsky

(d) Plane 1: SST-Transition

(e) Plane 1: k-ε Realisable

(f) Plane 1: k-ω LRN

Figure C.27: Contours of the scaled secondary motion magnitude in Plane 1 for the experimental and simulation data.

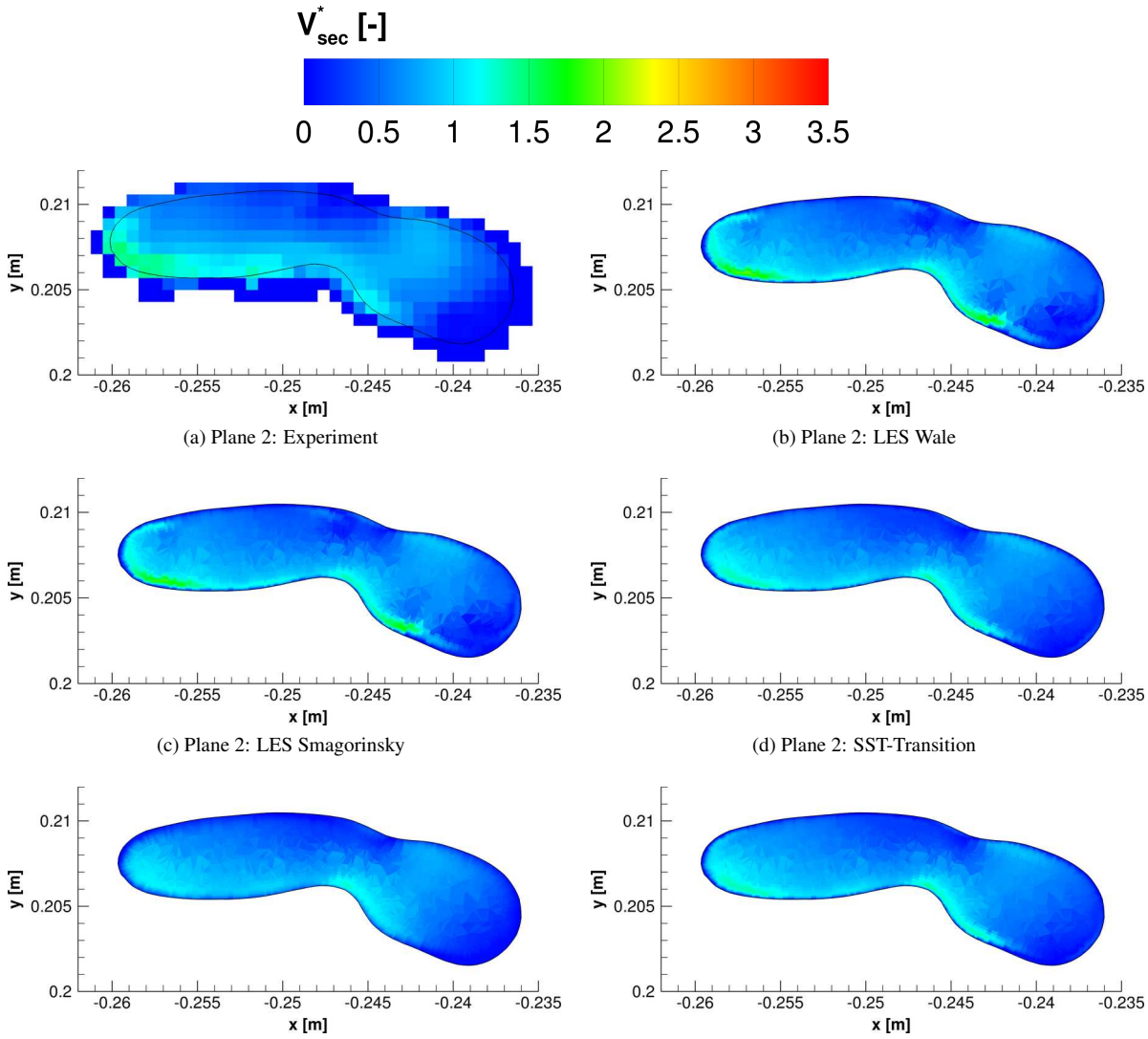

(a) Plane 2: Experiment

(b) Plane 2: LES Wale

(c) Plane 2: LES Smagorinsky

(d) Plane 2: SST-Transition

(e) Plane 2: k-ε Realisable

(f) Plane 2: k-ω LRN

Figure C.28: Contours of the scaled secondary motion magnitude in plane 2 for the experimental and simulation data.

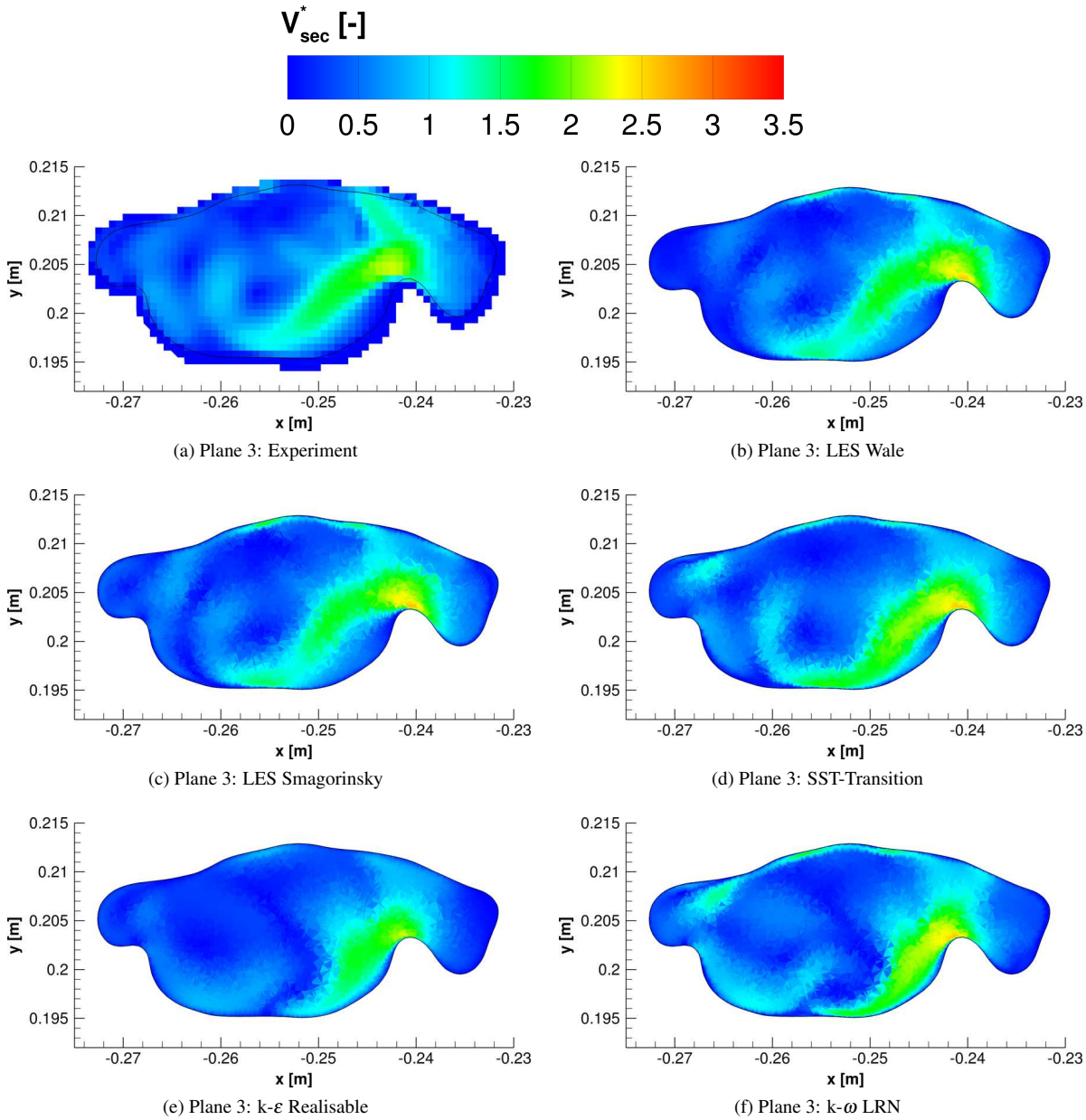

(a) Plane 3: Experiment

(b) Plane 3: LES Wale

(c) Plane 3: LES Smagorinsky

(d) Plane 3: SST-Transition

(e) Plane 3: k-ε Realisable

(f) Plane 3: k-ω LRN

Figure C.29: Contours of the scaled secondary motion magnitude in Plane 3 for the experimental and simulation data.

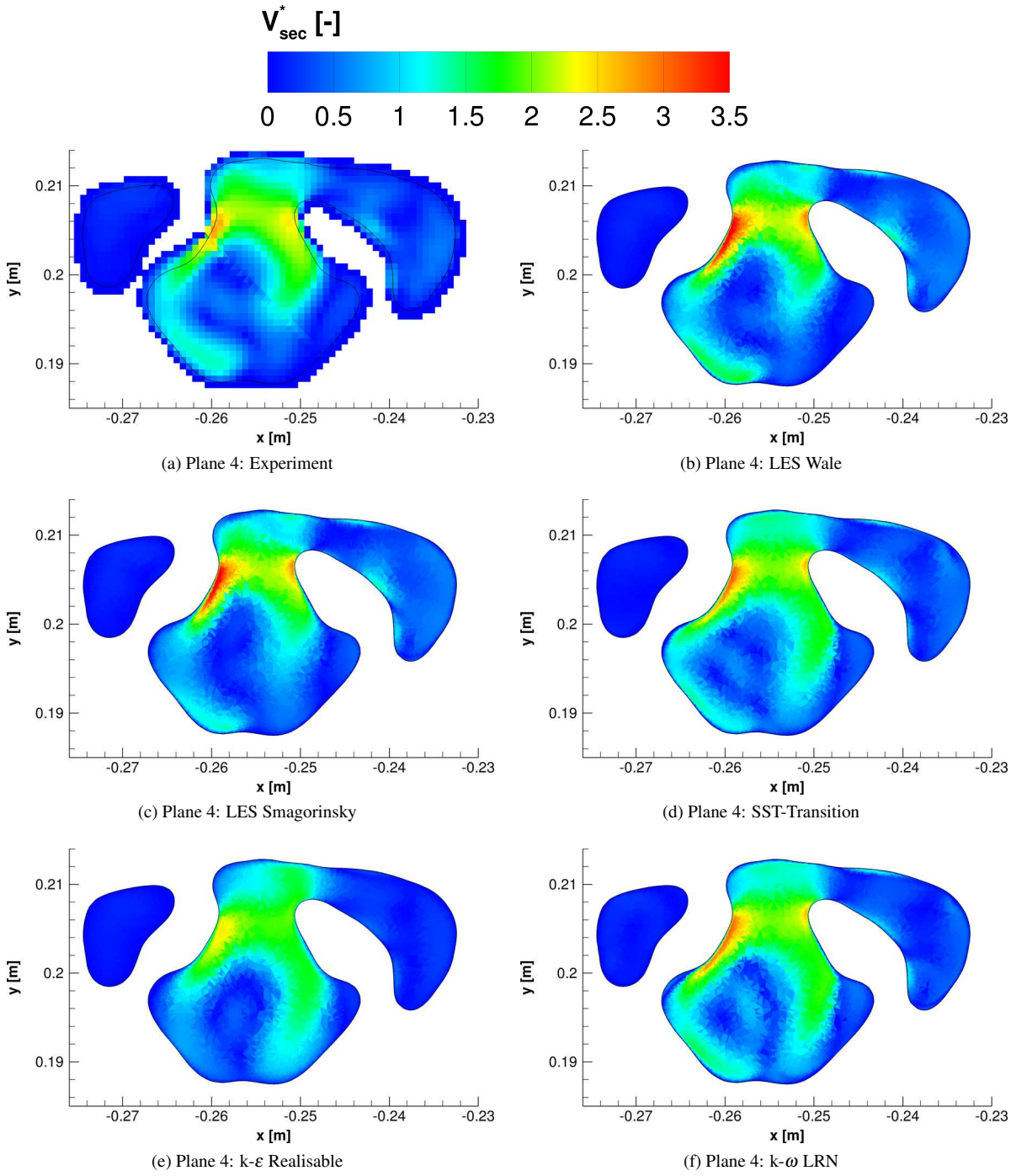

(a) Plane 4: Experiment

(b) Plane 4: LES Wale

(c) Plane 4: LES Smagorinsky

(d) Plane 4: SST-Transition

(e) Plane 4: k-ε Realisable

(f) Plane 4: k-ω LRN

Figure C.30: Contours of the scaled secondary motion magnitude in plane 4 for the experimental and simulation data.

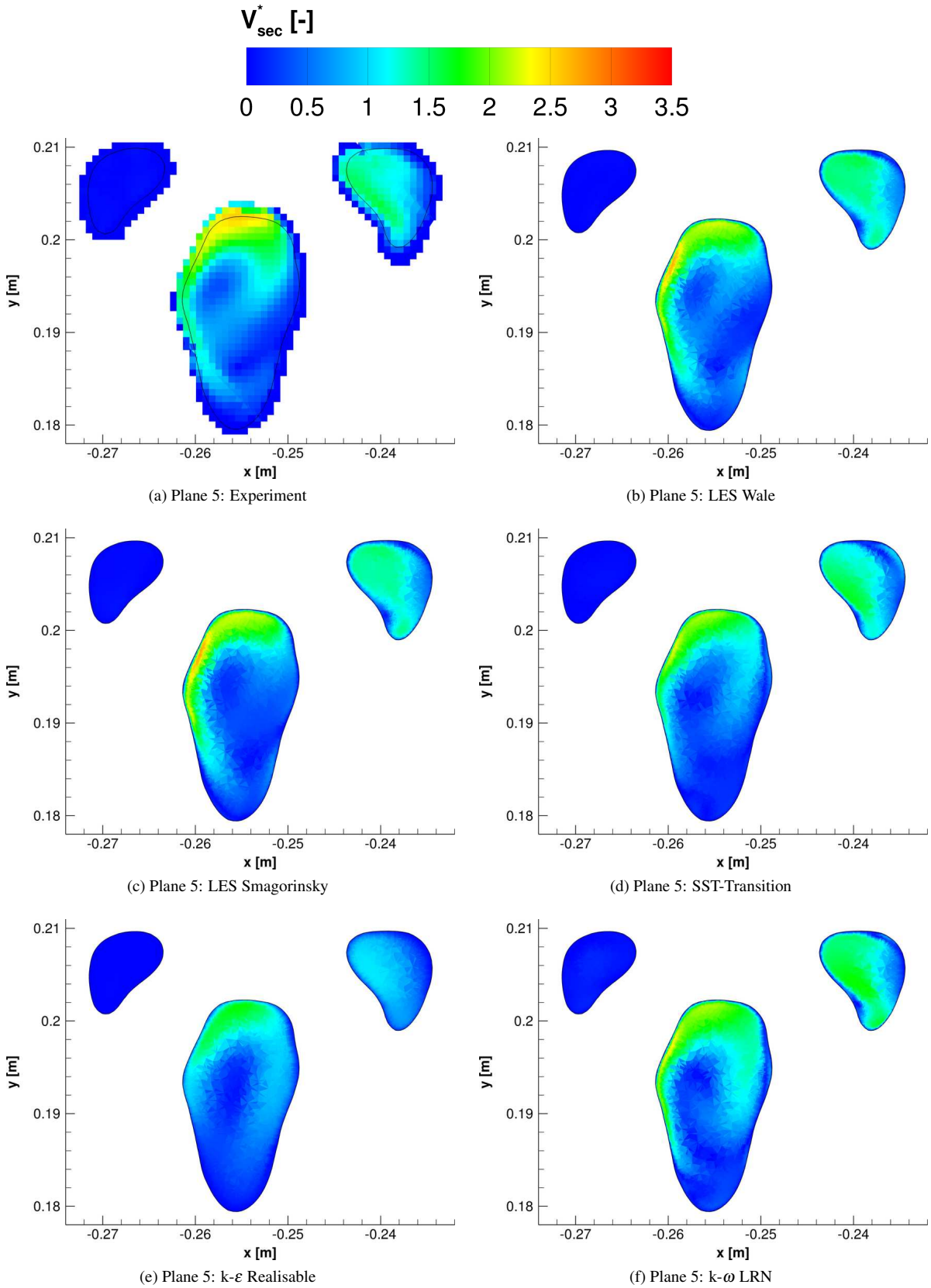

(a) Plane 5: Experiment

(b) Plane 5: LES Wale

(c) Plane 5: LES Smagorinsky

(d) Plane 5: SST-Transition

(e) Plane 5: k-ε Realisable

(f) Plane 5: k-ω LRN

Figure C.31: Contours of the scaled secondary motion magnitude in Plane 5 for the experimental and simulation data.

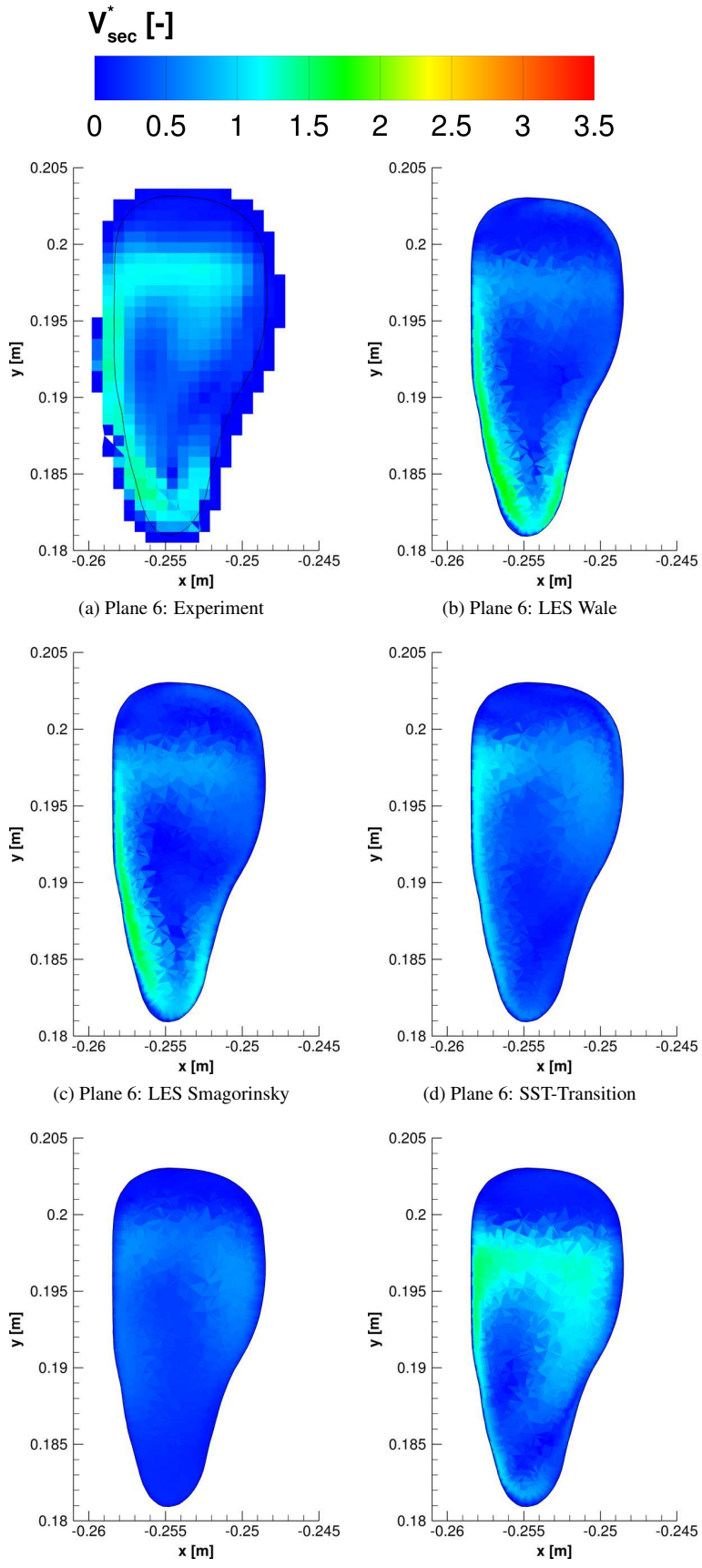

(a) Plane 6: Experiment

(b) Plane 6: LES Wale

(c) Plane 6: LES Smagorinsky

(d) Plane 6: SST-Transition

(e) Plane 6: k-ε Realisable

(f) Plane 6: k-ω LRN

Figure C.32: Contours of the scaled secondary motion magnitude in Plane 6 for the experimental and simulation data.

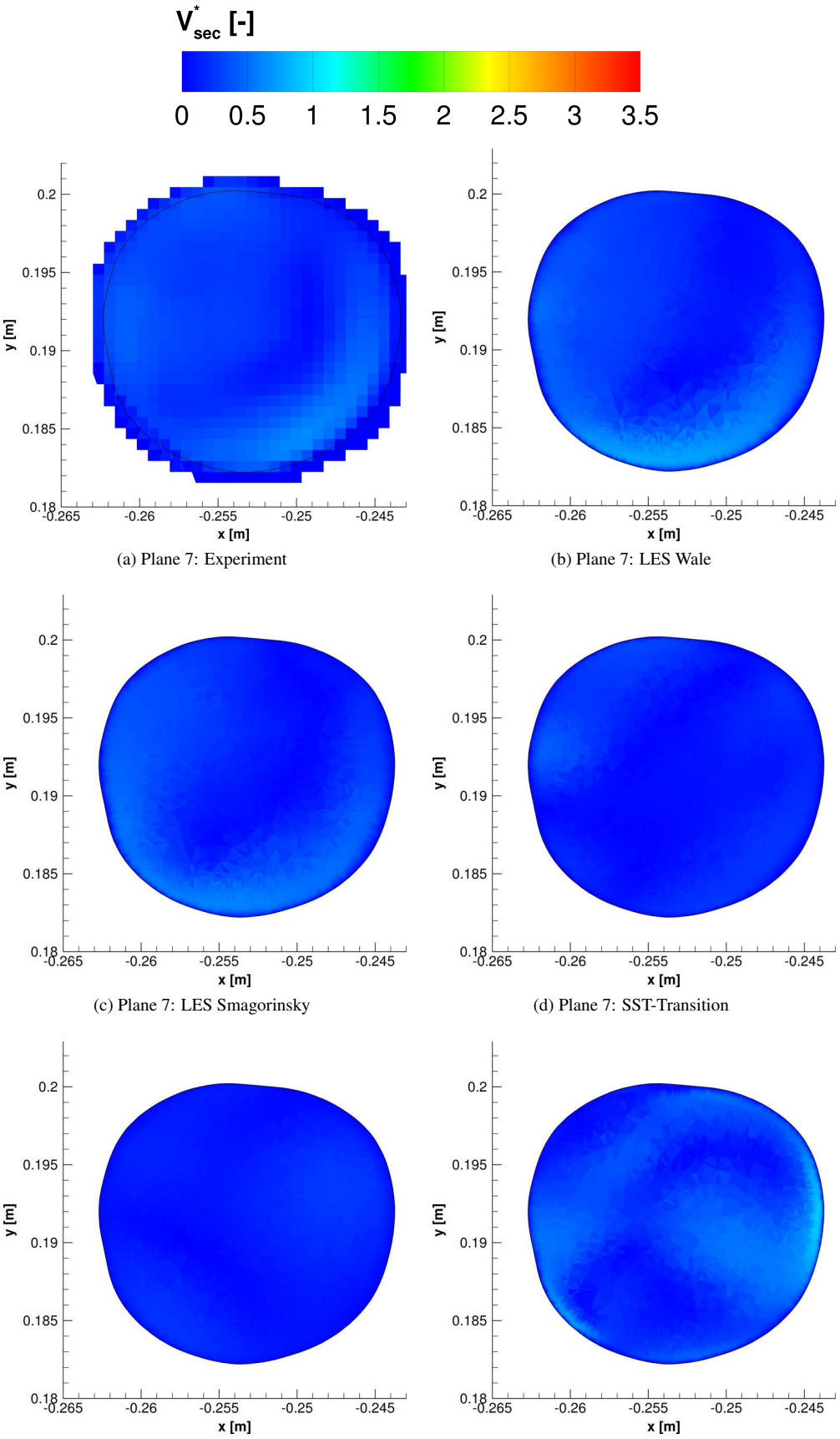

(a) Plane 7: Experiment

(b) Plane 7: LES Wale

(c) Plane 7: LES Smagorinsky

(d) Plane 7: SST-Transition

(e) Plane 7: k-ε Realisable

(f) Plane 7: k-ω LRN

Figure C.33: Contours of the scaled secondary motion magnitude in Plane 7 for the experimental and simulation data.

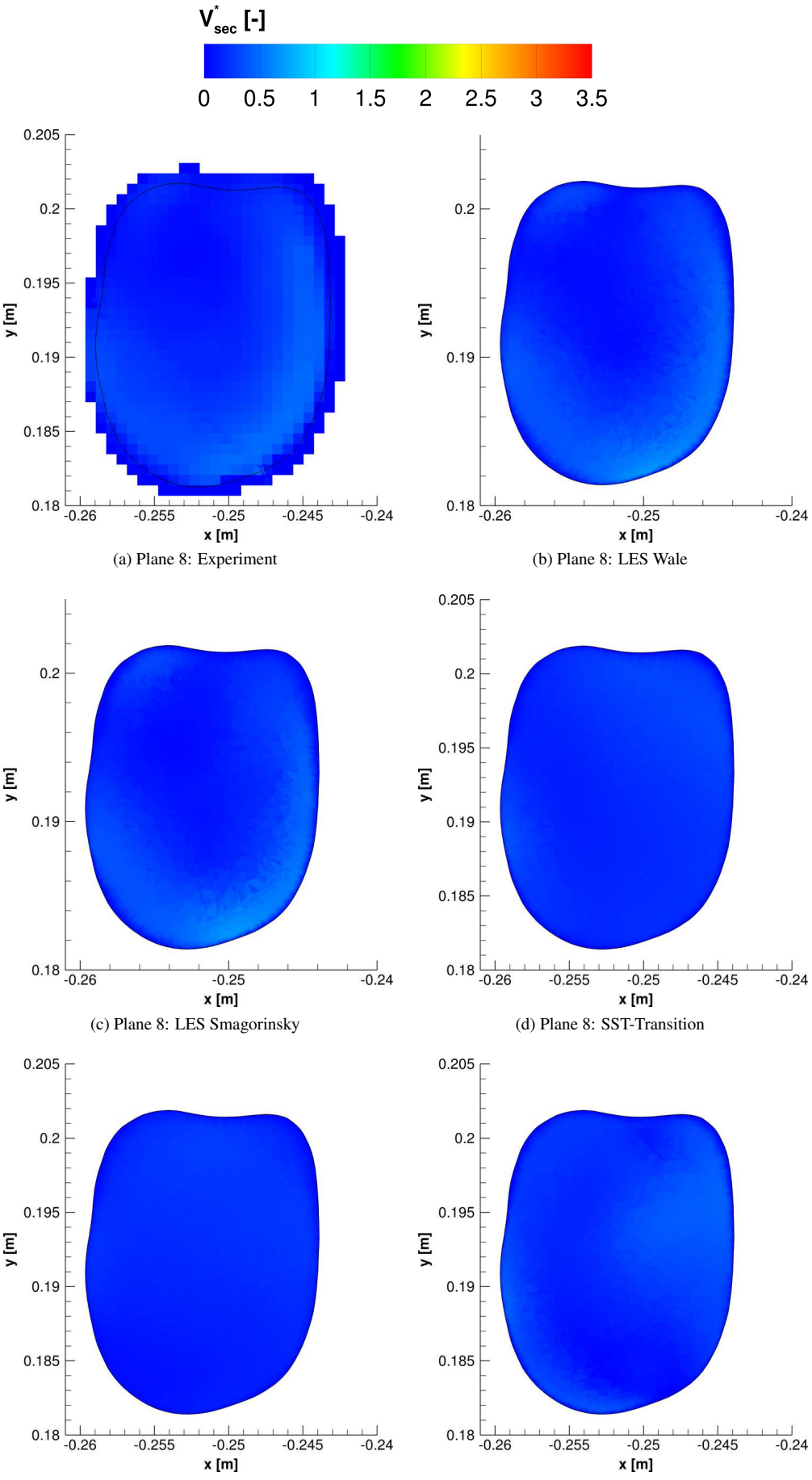

(a) Plane 8: Experiment

(b) Plane 8: LES Wale

(c) Plane 8: LES Smagorinsky

(d) Plane 8: SST-Transition

(e) Plane 8: k-ε Realisable

(f) Plane 8: k-ω LRN

Figure C.34: Contours of the scaled secondary motion magnitude in plane 8 for the experimental and simulation data.

C.3.4 Turbulent Kinetic Energy

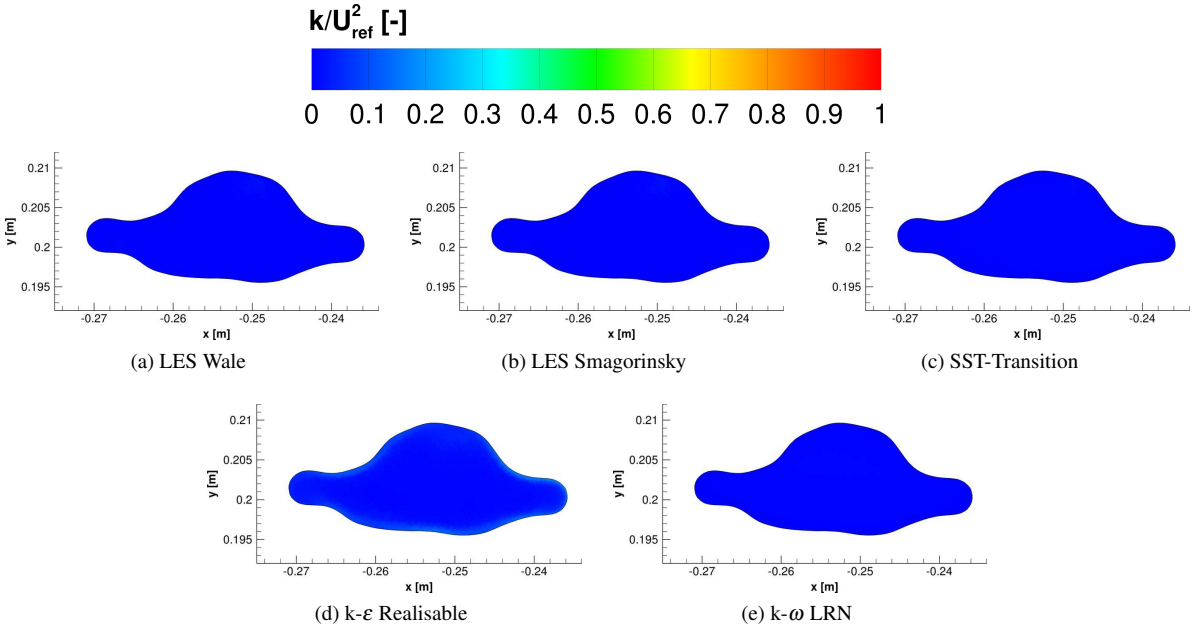

(a) LES Wale (b) LES Smagorinsky (c) SST-Transition

(d) k-ε Realisable (e) k-ω LRN

Figure C.35: Contours of the scaled turbulent kinetic energy in plane 1.

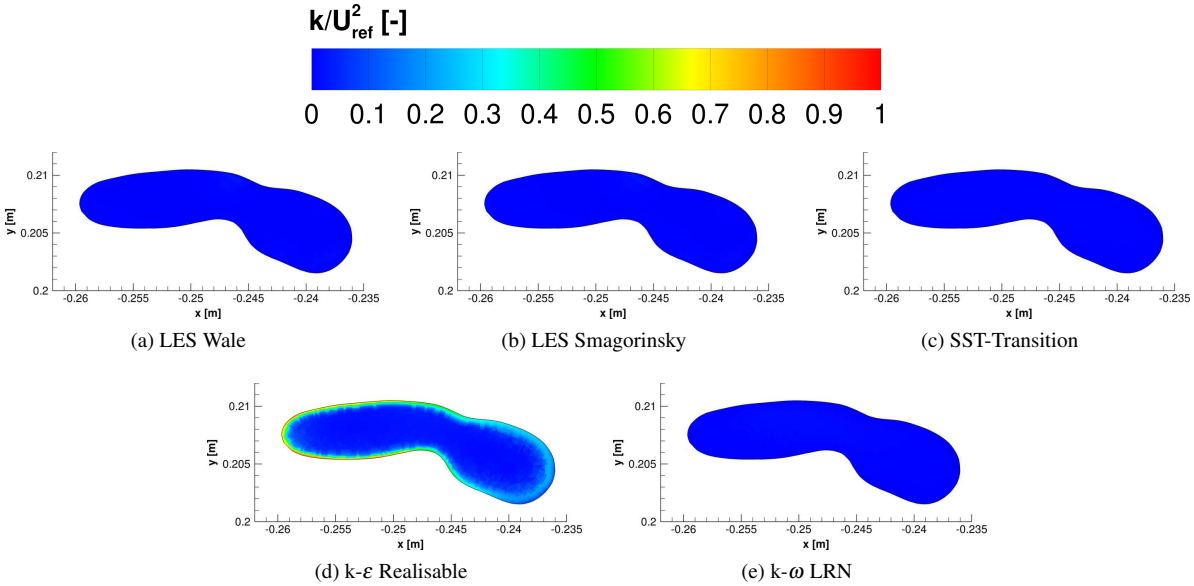

(a) LES Wale (b) LES Smagorinsky (c) SST-Transition

(d) k-ε Realisable (e) k-ω LRN

Figure C.36: Contours of the scaled turbulent kinetic energy in plane 2.

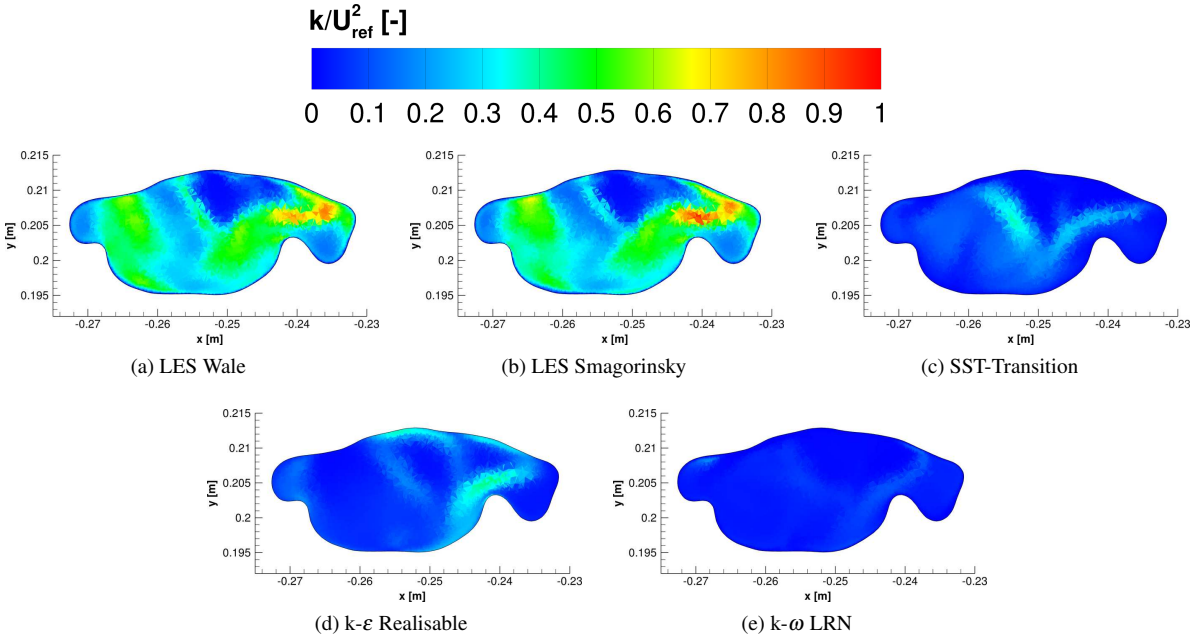

(a) LES Wale (b) LES Smagorinsky (c) SST-Transition

(d) k-ε Realisable (e) k-ω LRN

Figure C.37: Contours of the scaled turbulent kinetic energy in plane 3.

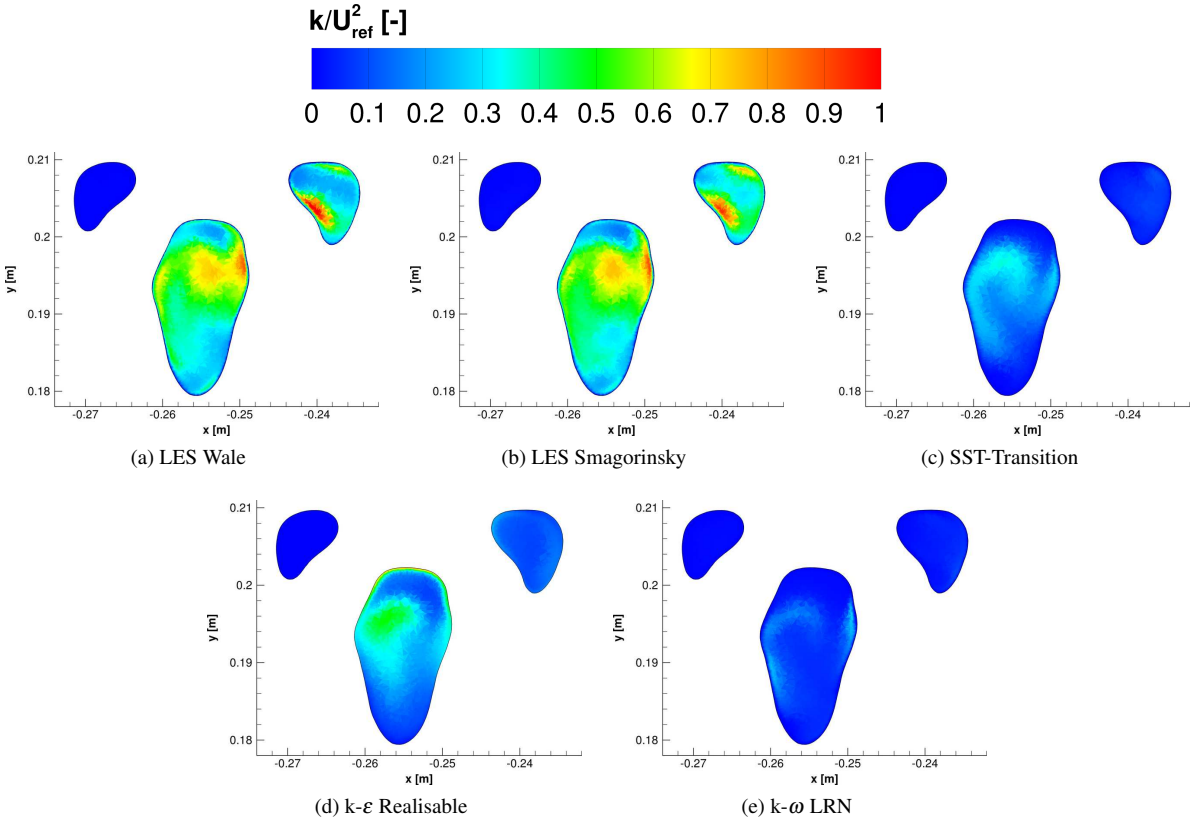

(a) LES Wale (b) LES Smagorinsky (c) SST-Transition

(d) k-ε Realisable (e) k-ω LRN

Figure C.38: Contours of the scaled turbulent kinetic energy in plane 5.

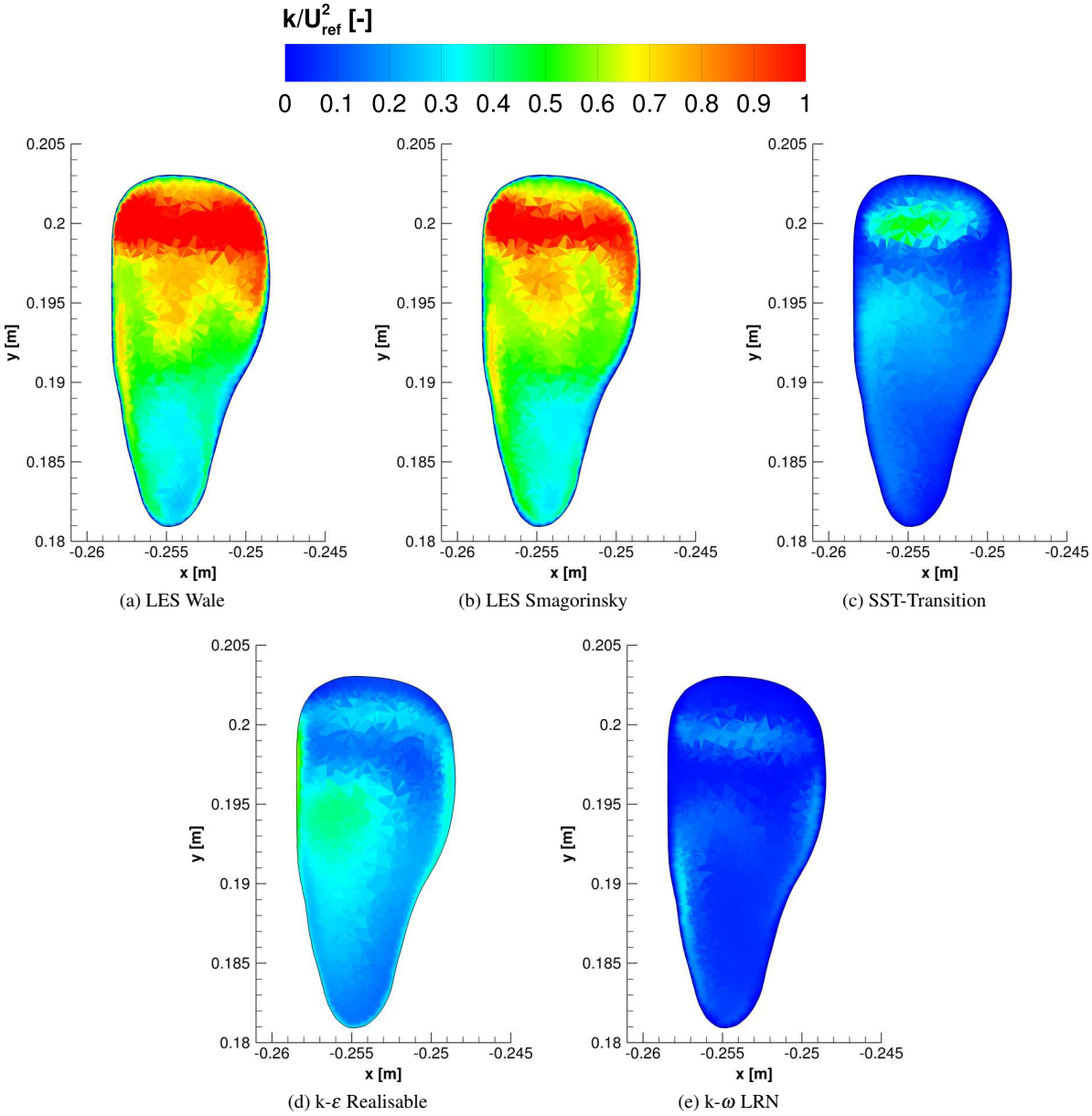

(a) LES Wale (b) LES Smagorinsky (c) SST-Transition

(d) k-ε Realisable (e) k-ω LRN

Figure C.39: Contours of the scaled turbulent kinetic energy in plane 6.

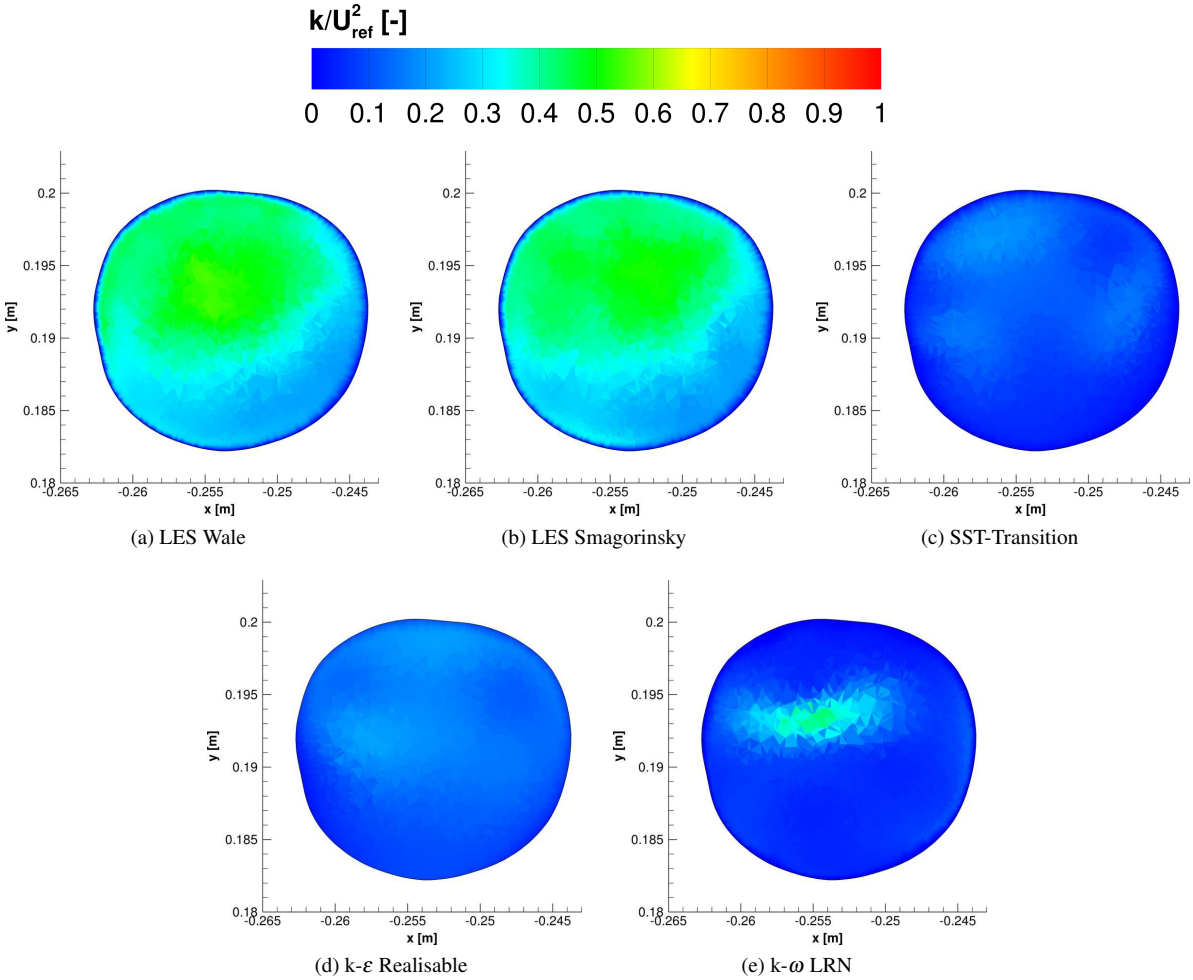

(a) LES Wale (b) LES Smagorinsky (c) SST-Transition

(d) k-ε Realisable (e) k-ω LRN

Figure C.40: Contours of the scaled turbulent kinetic energy in plane 7.

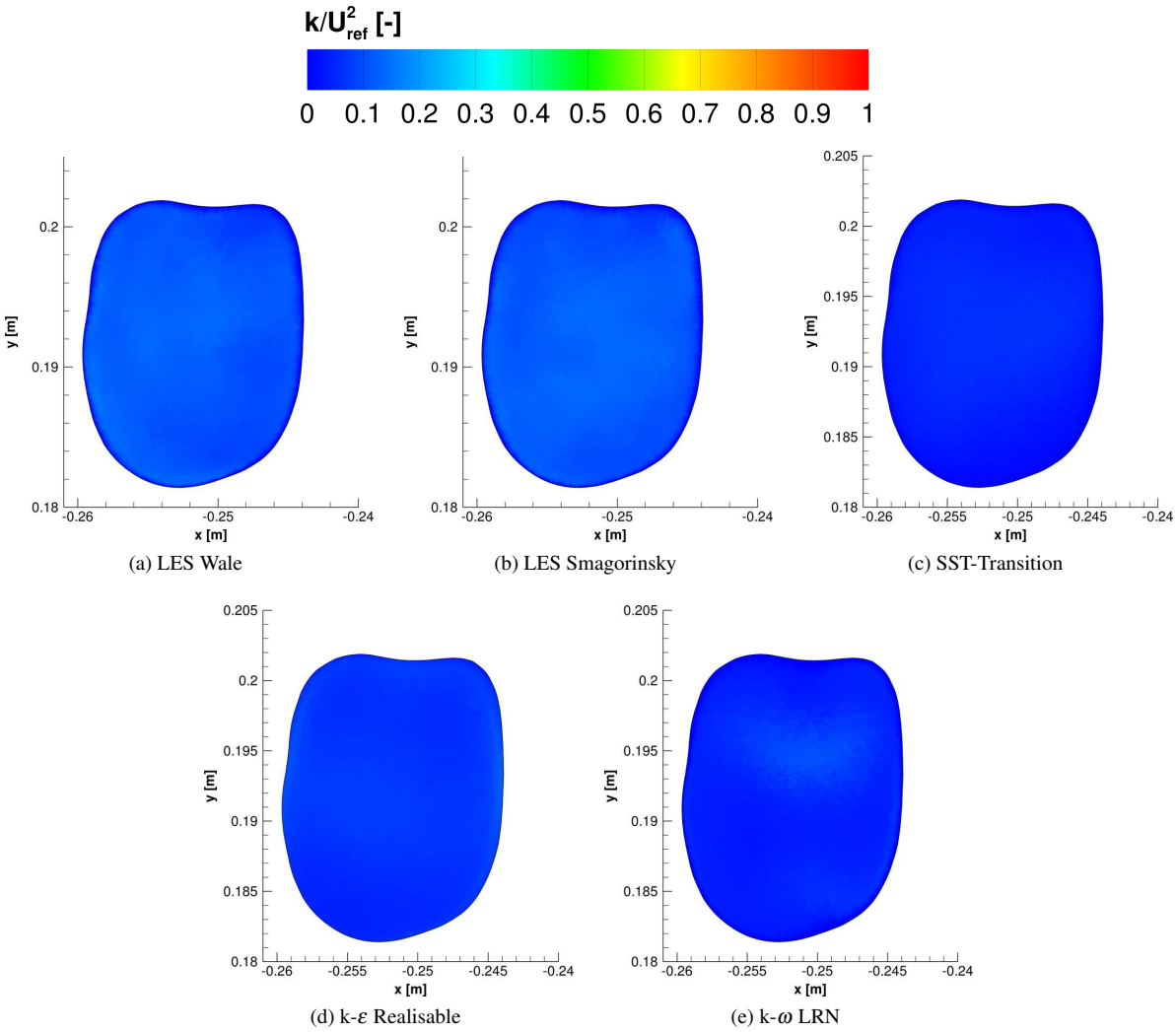

(a) LES Wale (b) LES Smagorinsky (c) SST-Transition

(d) k-ε Realisable (e) k-ω LRN

Figure C.41: Contours of the scaled turbulent kinetic energy in plane 8.

C.4 Passive Particle Deposition

Table C.1: Particle deposition efficiencies and steering factor for two different injection planes with turbulent dispersion enabled. The number of particles injected for each injection are: 20×10^3 for the inlet injection, 26×10^3 for the injection at plane A.

St_{ref} [-]	Injection	DE_{top} [%]	DE_{bottom} [%]	DE_{LL} [%]	DE_{RL} [%]	SF_L [-]	SF_{pen} [-]
4.8×10^{-5}	Inlet	7.18	1.65	1.55	1.71	0.745	0.75
4.8×10^{-5}	Plane A	5.24	1.43	1.62	1.30	0.710	0.71
4.8×10^{-3}	Inlet	14.80	2.12	2.29	2.00	0.762	0.76
4.8×10^{-3}	Plane A	10.03	2.19	2.66	1.85	0.717	0.71
4.3×10^{-2}	Inlet	51.60	6.82	7.19	6.42	1.040	1.03
4.3×10^{-2}	Plane A	19.25	6.47	6.92	6.16	0.685	0.68
1.2×10^{-1}	Inlet	84.19	37.77	37.08	38.81	1.476	1.52
1.2×10^{-1}	Plane A	25.67	39.39	38.49	40.01	0.692	0.71

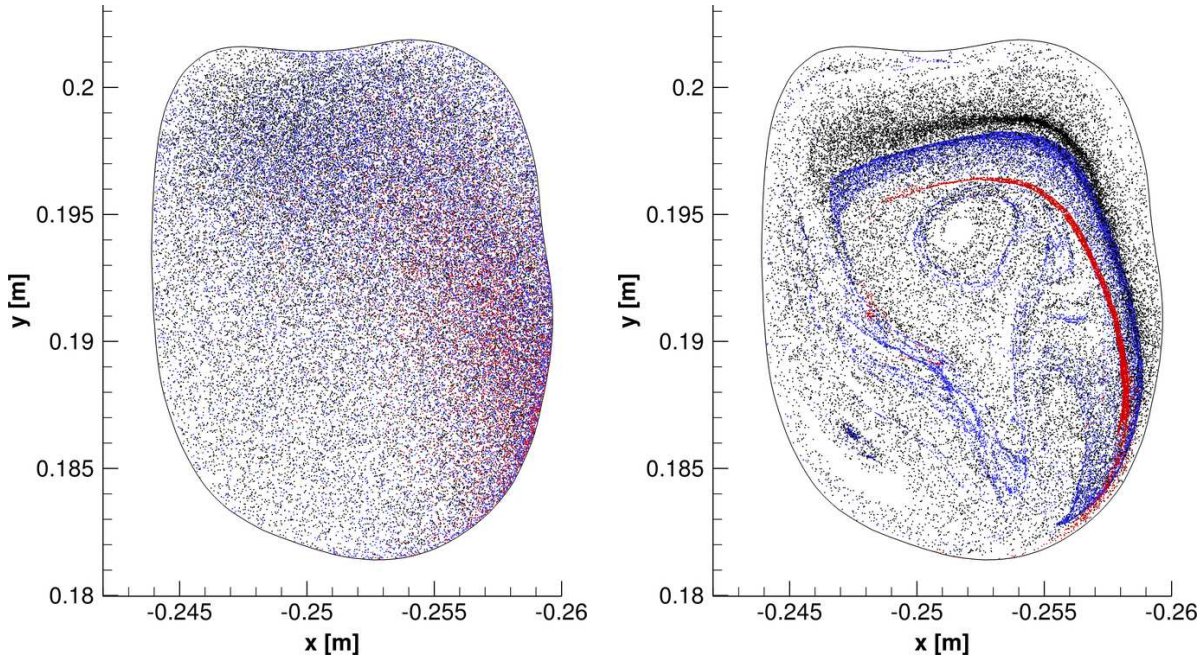

(a) Without

(b) Without

Figure C.42: Qualitative comparison of the particle distributions in a plane at z = 0.21 m for injections at the inlet (random distribution) the left lung is located in the negative x-direction. Black: St = 4.8×10^{-5} , blue: St = 4.3×10^{-2} , red: St = 1.2×10^{-1}.

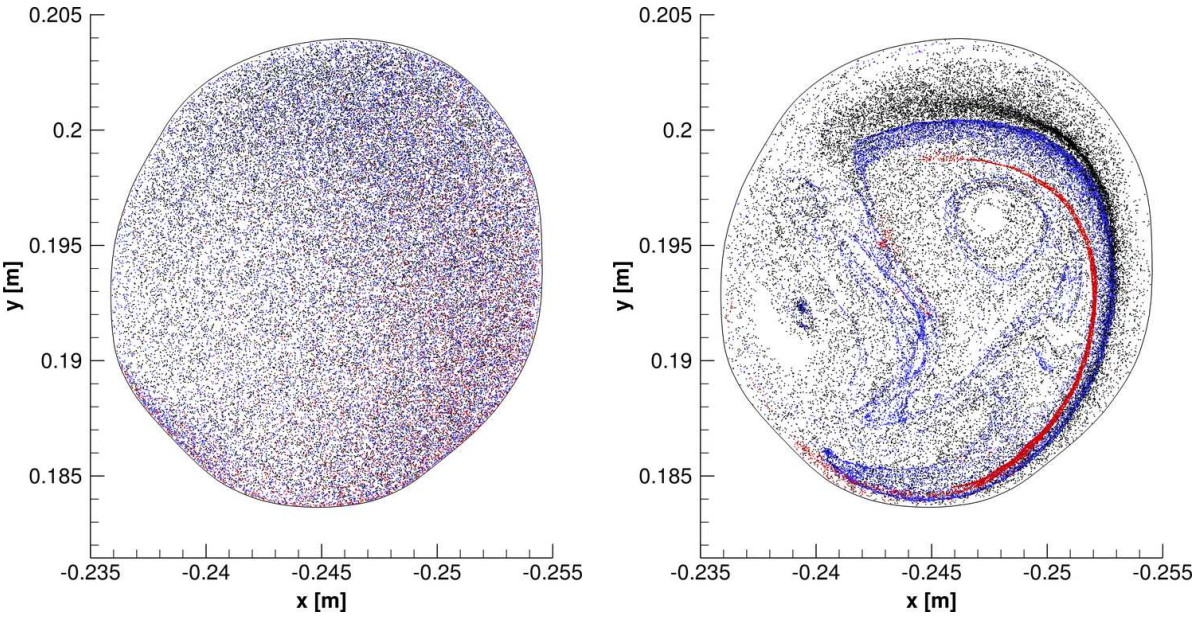

(a) With TD

(b) Without TD

Figure C.43: Qualitative comparison of the particle distributions in a plane at z = 0.26 m for injections at the inlet (random distribution) the left lung is located in the negative x-direction. Black: St = 4.8×10^{-5} , blue: St = 4.3×10^{-2} , red: St = 1.2×10^{-1}.

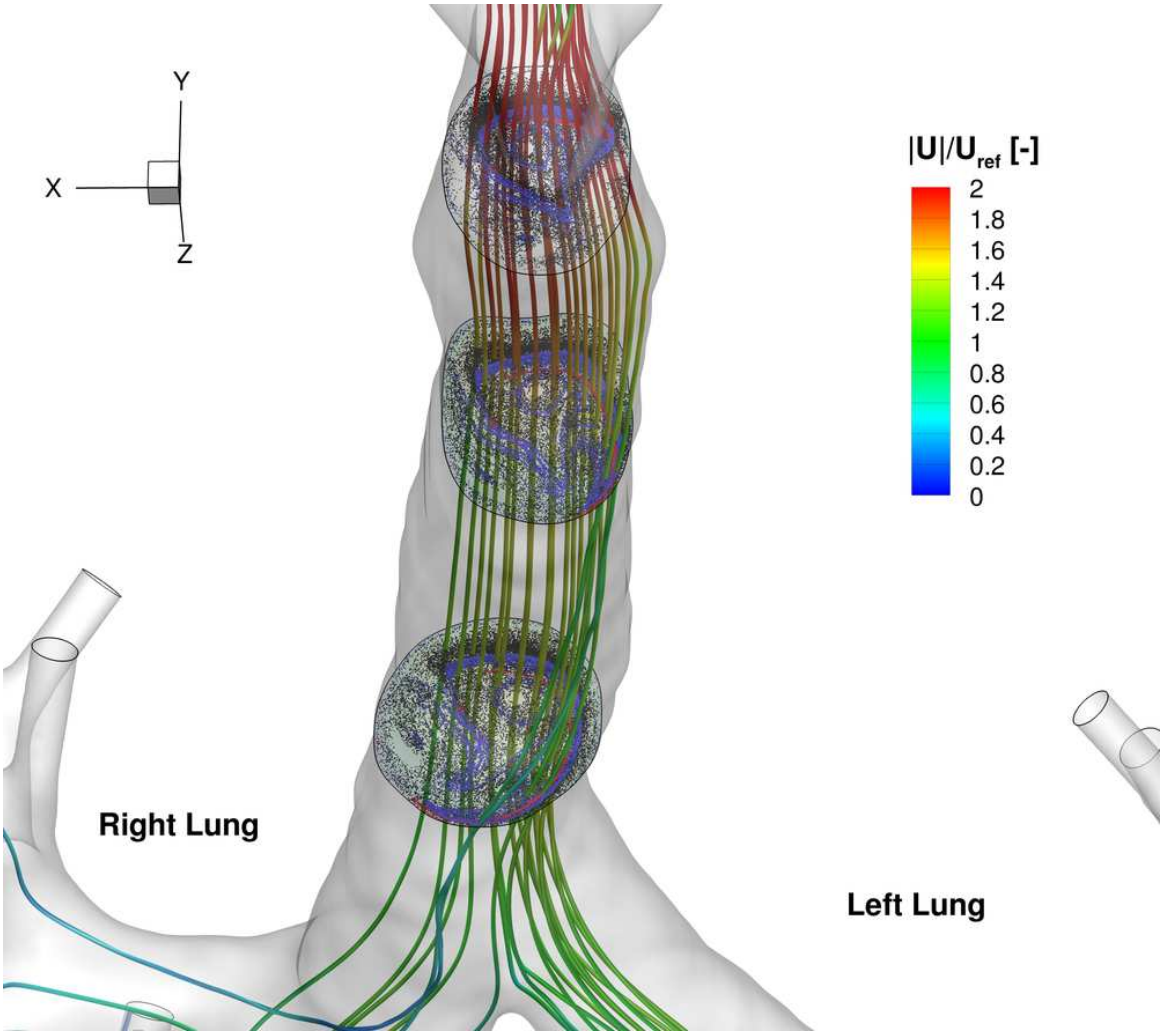

Figure C.44: Particle distributions of simulations without turbulent dispersion at the planes in figures 8.31, C.42 and C.43 together with stream traces coloured by the scaled velocity magnitude. The streamtraces were calculated from rakes at regions of high velocity magnitude (and high particle concentration) in a plane with z = 0.17 m.

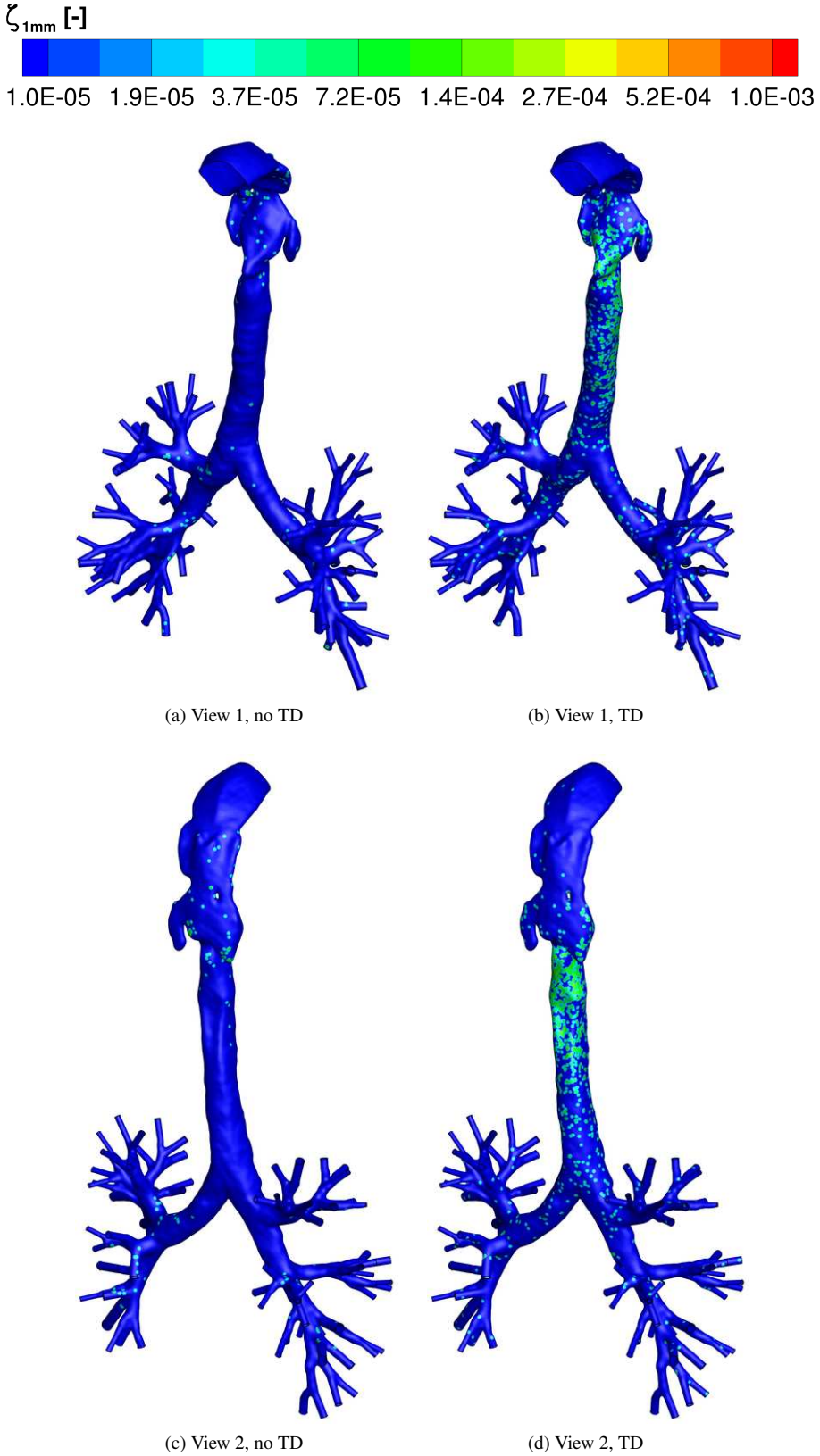

(a) View 1, no TD

(b) View 1, TD

(c) View 2, no TD

(d) View 2, TD

Figure C.45: Contours of local deposition efficiency $\zeta_{1\text{ mm}}$ from particle deposition with turbulent dispersion disabled (a,c) and enabled (b,d) for St = 4.8×10^{-5}.

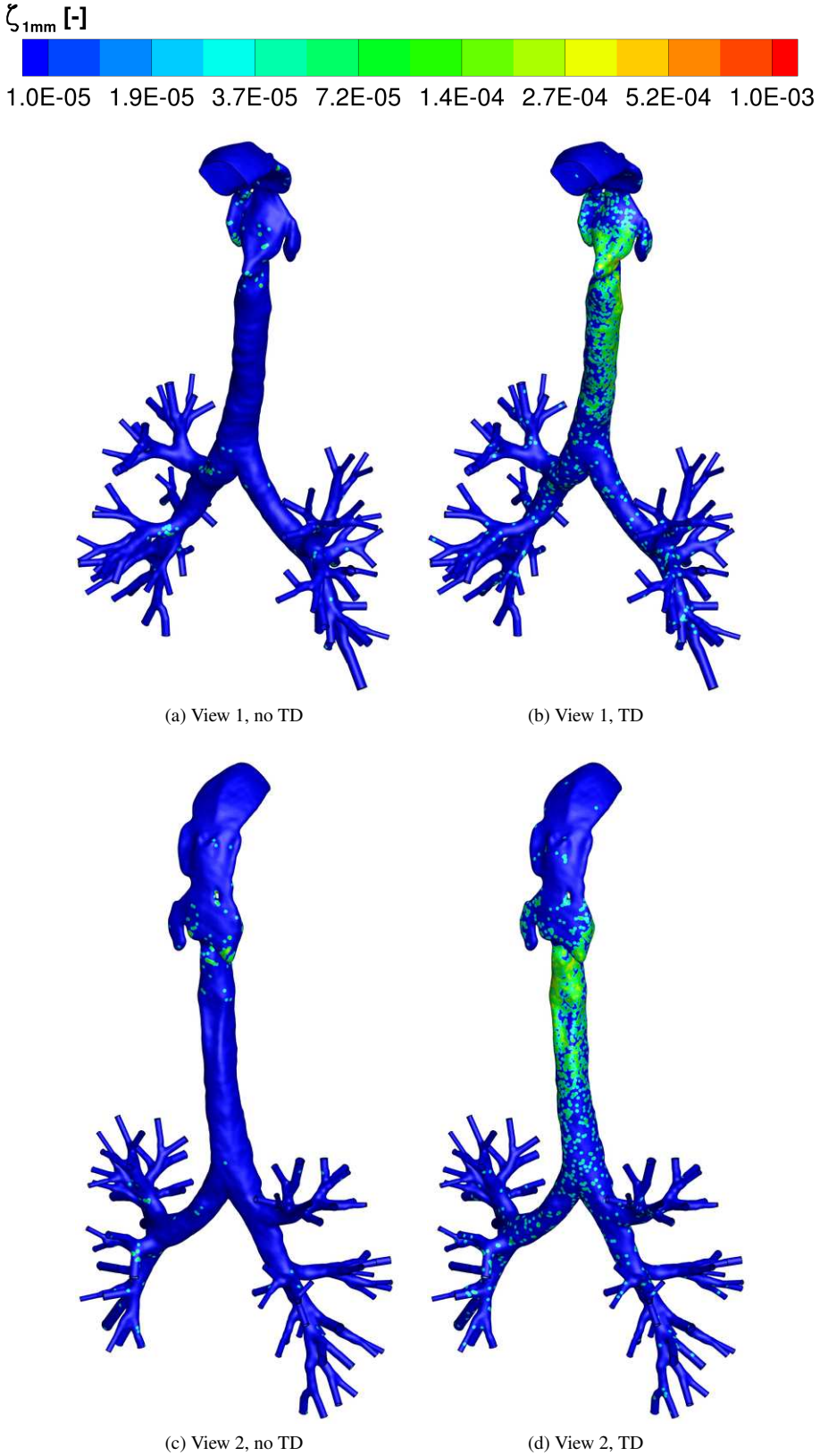

(a) View 1, no TD

(b) View 1, TD

(c) View 2, no TD

(d) View 2, TD

Figure C.46: Contours of local deposition efficiency $\zeta_{1\text{ mm}}$ from particle deposition with turbulent dispersion disabled (a,c) and enabled (b,d) for St = 4.8×10^{-3}.

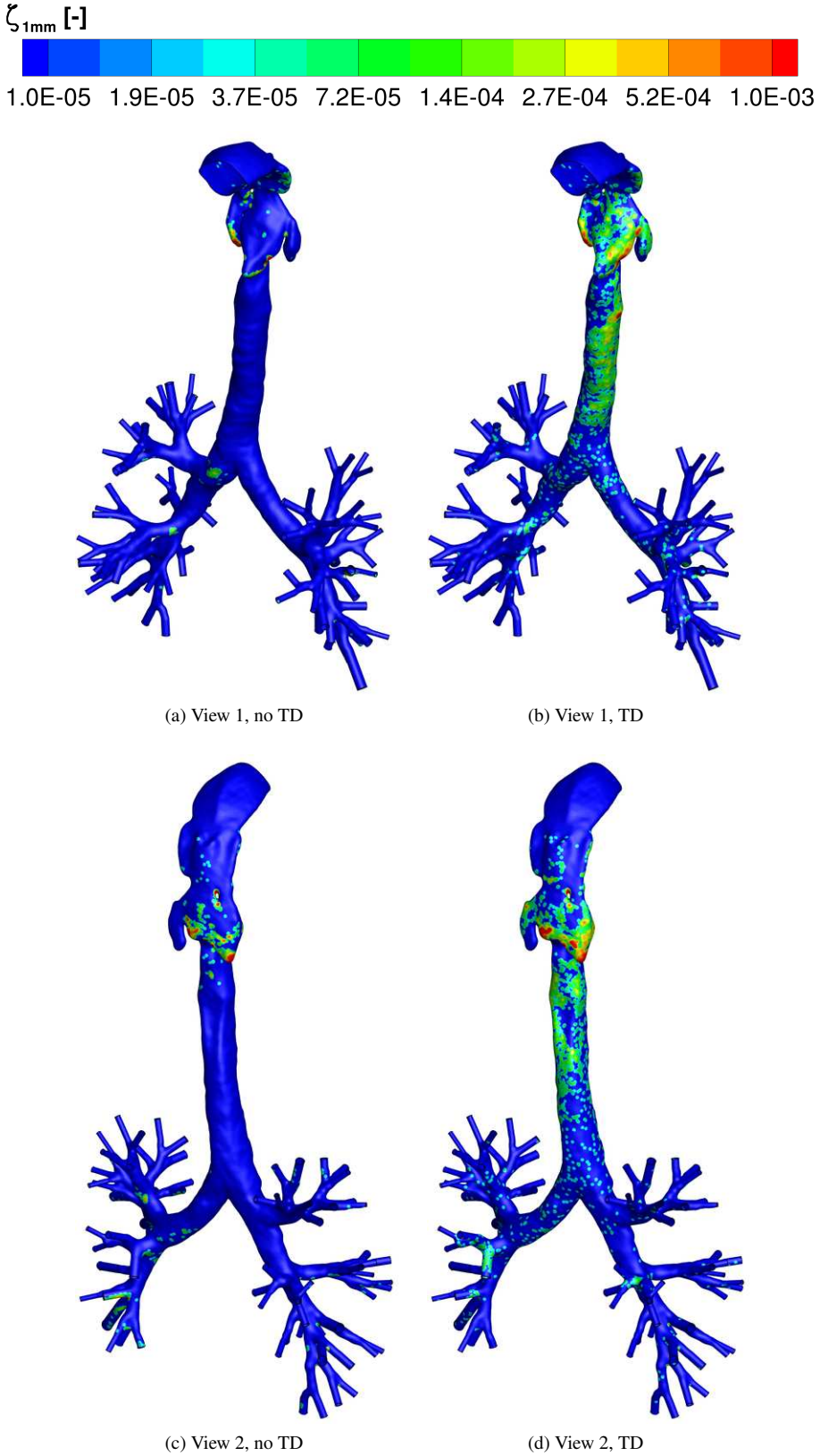

(a) View 1, no TD

(b) View 1, TD

(c) View 2, no TD

(d) View 2, TD

Figure C.47: Contours of local deposition efficiency $\zeta_{1\text{ mm}}$ from particle deposition with turbulent dispersion disabled (a,c) and enabled (b,d) for St = 4.3×10^{-2}.

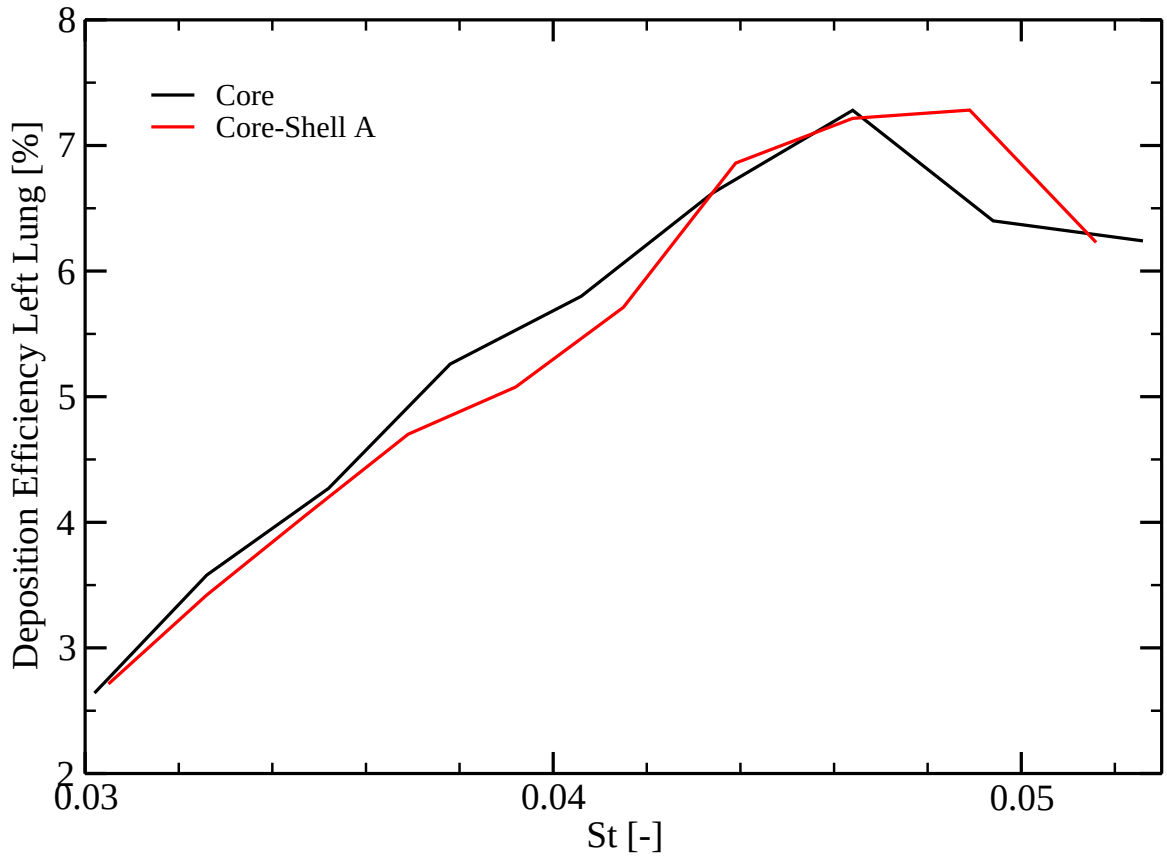

Figure C.48: Investigation of the bump when performing particle deposition with turbulent dispersion turned off.

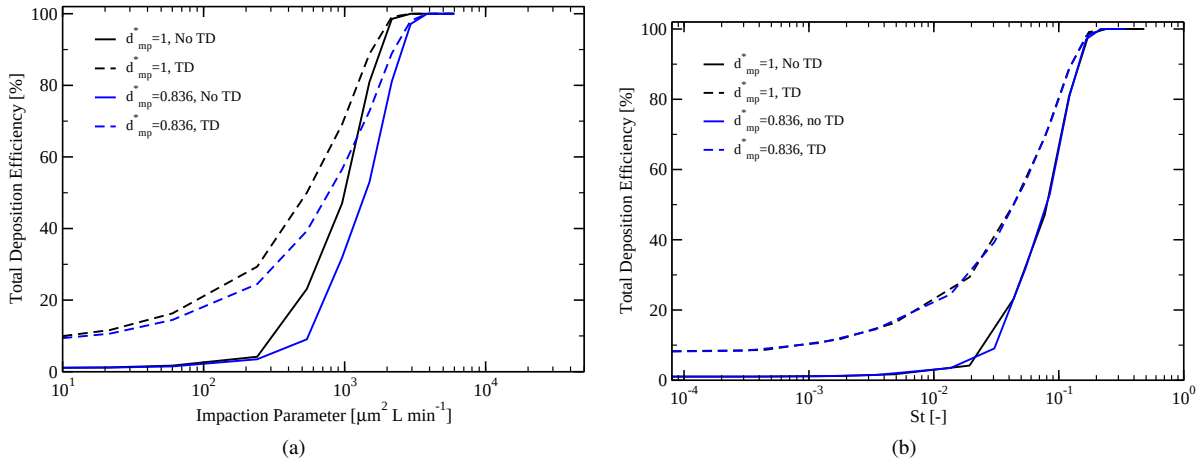

Figure C.49: Figure which illustrates the limitation of the impaction parameter namely the lack of particle density.

C.4.1 No gravity

In this section the results for the passive particle deposition without gravity are reported. It must be noted that for the scatter plots of the particles on a surface, a relatively small sample size was used to make the it more visible to the reader and thus the positions may change when re-running this simulation, especially for areas on the wall where only one or two particles deposit.

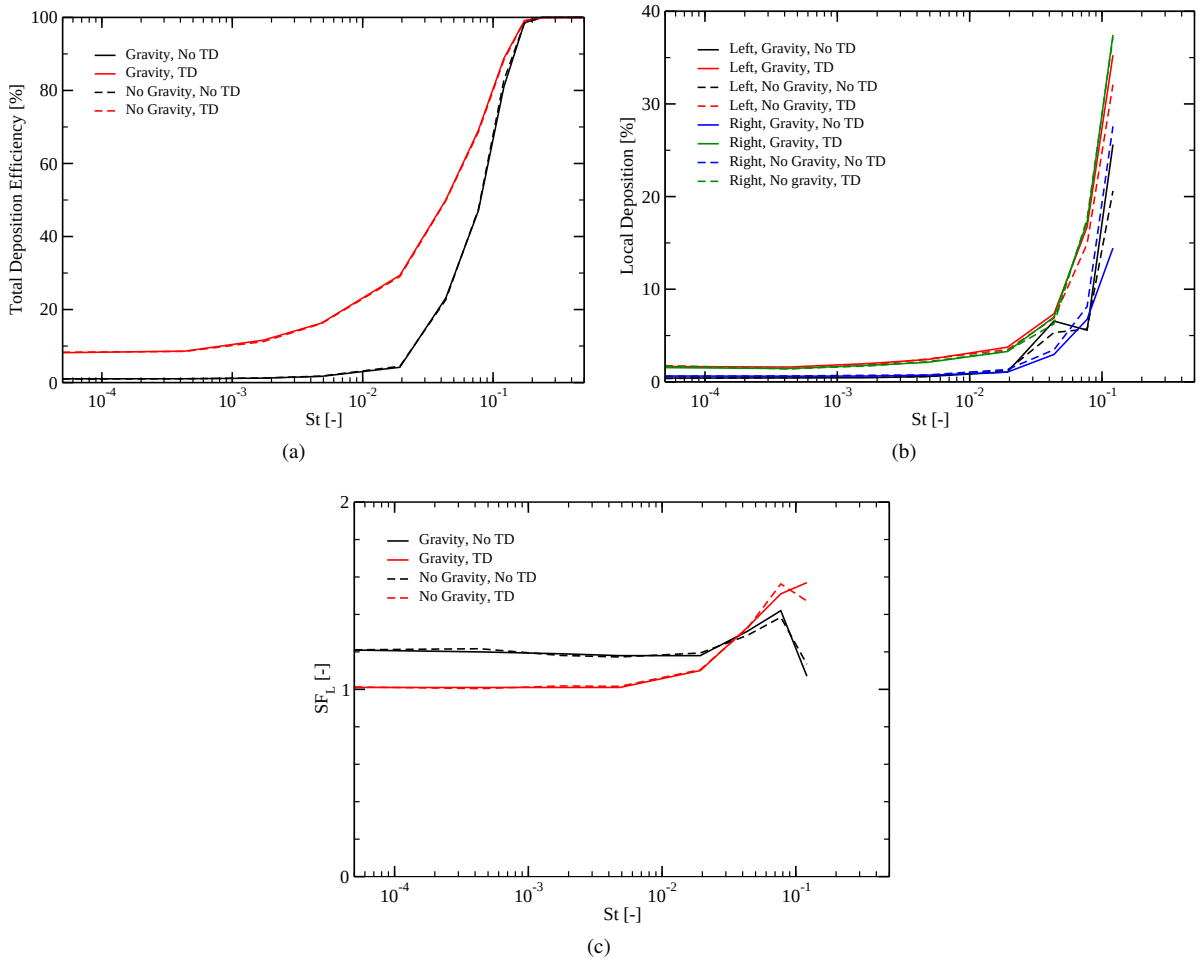

Figure C.50: Comparison between passive particle deposition with and without gravity. Note that the sample size used here for the no gravity simulations is smaller than that of the simulations with gravity.

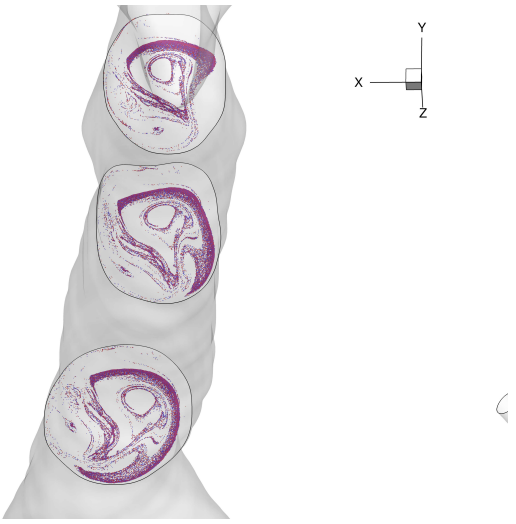

(a) St = St = 4.3×10^{-2}

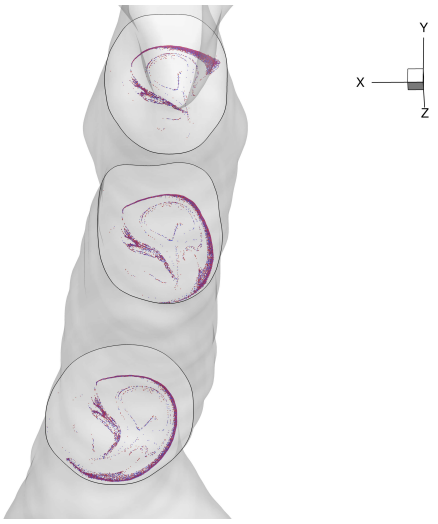

(b) St = 7.7×10^{-2}

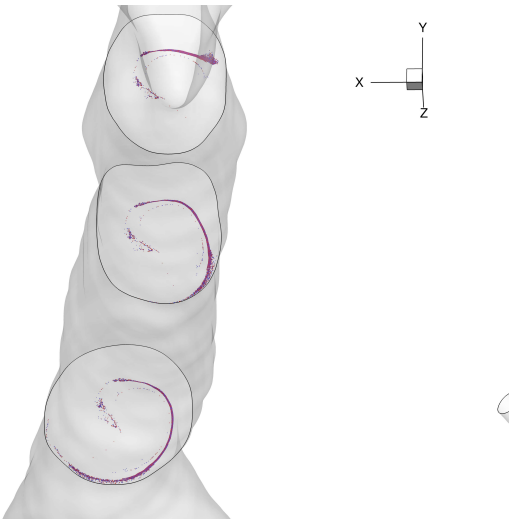

(c) St = 1.2×10^{-1}

Figure C.51: Effect of gravity on the particle distributions in planes 1, 2 and 3 for (a) St = 4.3×10^{-2}, (b) St = 7.7×10^{-2} and (c) St = 1.2×10^{-1} (particle diameter is 3, 4 and 5 micrometer respectively). Particles which experience gravity are coloured blue. Turbulent dispersion is turned off. The number of particles released at the inlet is 3×10^{4} for both simulations.

In the following figures, the particle distributions on the wall are compared. For the lower St particles, the gravity is negligible and thus the deposition patterns match closely, this is roughly the case until St = 4.8×10^{-3}, however when increasing the St the gravity effect is also increased and thus the deposition patterns start to differ. The same plots were performed with a larger sample size for the gravity simulations and the same behaviour is observed only these figures were omitted due to visibility issues in a static image.

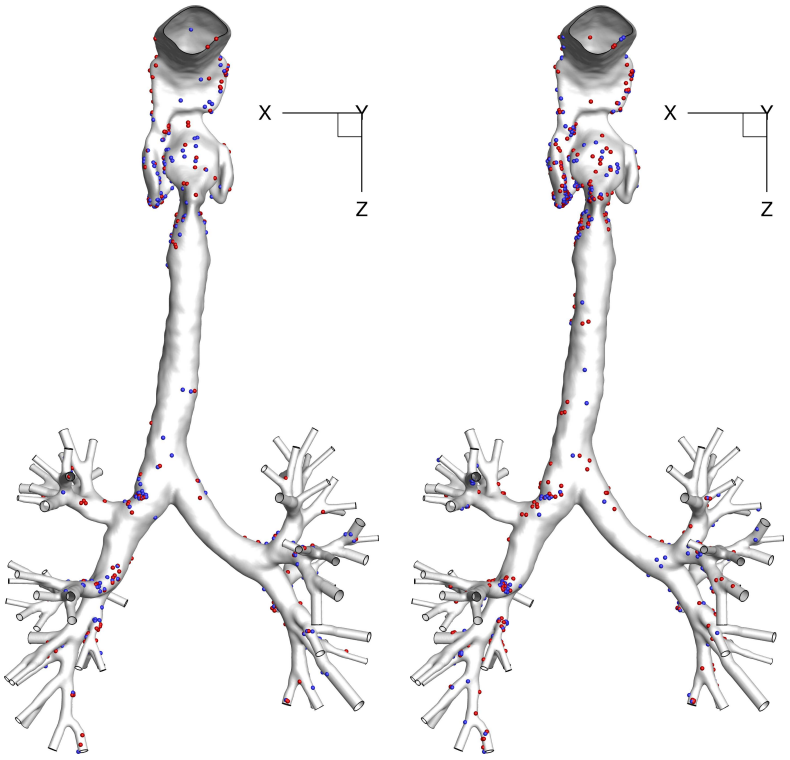

(a) St = 4.8×10^{-5}

(b) St = 4.8×10^{-3}

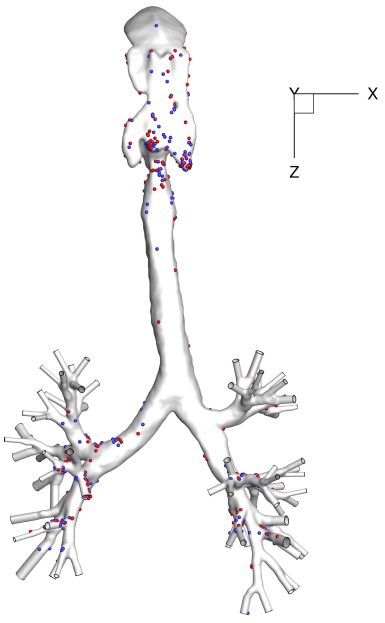

(c) St = 4.8×10^{-5}

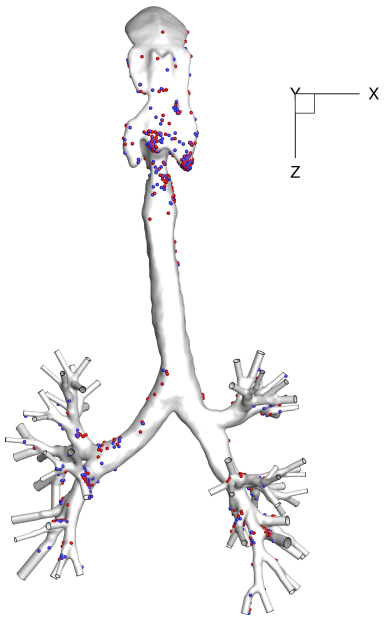

(d) St = 4.8×10^{-3}

Figure C.52: Particle distribution on the surface of the lung. Particles which experience gravity are coloured blue.

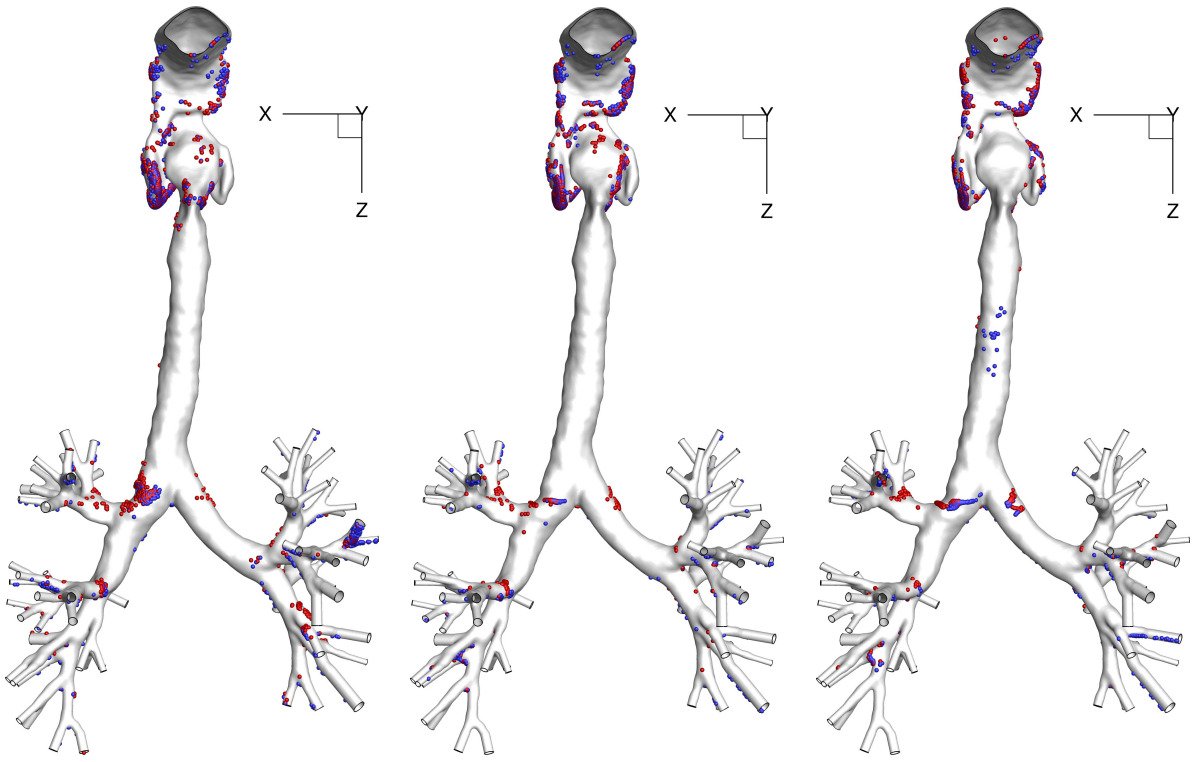

(a) St = 4.3×10^{-2} (b) St = 7.7×10^{-2} (c) St = 1.2×10^{-1}

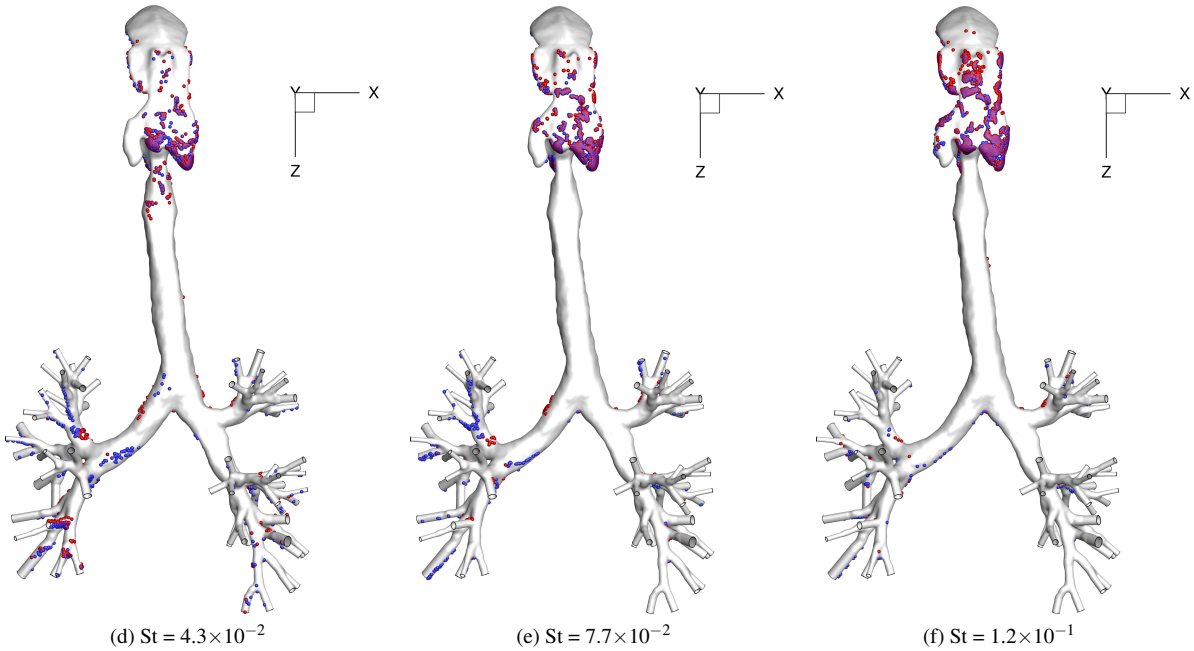

(d) St = 4.3×10^{-2} (e) St = 7.7×10^{-2} (f) St = 1.2×10^{-1}

Figure C.53: Particle distribution on the surface of the lung. Particles which experience gravity are coloured blue.

C.5 Magnetically Enhanced Particle Deposition

In table 8.8 below the list of wire positions can be found.

Table C.2: Overview of the wire positions with the names, reference position, displacement from the reference position and the direction of displacement.

Wire	**Reference position x [m]**	**Reference position z [m]**	**Distance [cm]**	**Direction**
Position 1	-0.252	0.269	1	-x
Position 2	-0.252	0.269	10	-x
Position 3	-0.258	0.287	1	-x
Position 4	-0.258	0.287	10	-x
Position 1′	-0.234	0.269	1	+x
Position 2′	-0.234	0.269	10	+x
Position 3′	-0.229	0.287	1	+x
Position 4′	-0.229	0.287	10	+x

Table C.3: Overview of the particles used in the patient specific deposition studies.

Particle	**d_{mp} [-]**	**Average density [kg/m^3]**
Core	1	4860
Core-shell A	0.84	3412
Core-shell B	0.20	1032

In the following sections among figures some tables are given, the data from these tables was copied directly from the results file. This means that there are some values present for example for the SF_L and SF_{pen} which were redacted in the main body of the report due to lack of sampling size (this can be quickly seen by looking at the deposition efficiency at the top).

C.5.1 Fully Magnetic Particles

Table C.4: Particle deposition efficiencies and steering factor for fully magnetic particles under the influence of a magnetic field caused by a wire at position 1, with turbulent dispersion (TD) either enabled or disabled. The number of particles released is around 3×10^5.

TD	St_{ref} [-]	Mnp_{ref} [-]	DE_{top} [%]	DE_{bot} [%]	DE_{LL} [%]	DE_{RL} [%]	SF_L [-]	SF_{pen} [-]
No	4.8×10^{-5}	0	0.56	0.52	0.39	0.67	1.21	1.21
Yes	4.8×10^{-5}	0	6.49	1.61	1.67	1.55	1.01	1.00
No	4.8×10^{-5}	1.9×10^{-4}	0.63	0.54	0.49	0.61	1.20	1.20
Yes	4.8×10^{-5}	1.9×10^{-4}	6.77	1.60	1.68	1.51	1.00	1.00
No	4.8×10^{-3}	0	1.10	0.61	0.55	0.69	1.18	1.18
Yes	4.8×10^{-3}	0	14.28	2.27	7.30	3.91	0.98	1.02
No	4.8×10^{-3}	1.9×10^{-2}	10.76	4.16	4.99	3.16	1.21	1.19
Yes	4.8×10^{-3}	1.9×10^{-2}	24.48	5.59	7.30	3.91	0.98	0.95
No	4.3×10^{-2}	0	19.09	4.95	6.41	3.02	1.31	1.27
Yes	4.3×10^{-2}	0	45.84	7.02	7.15	6.84	1.32	1.31
No	4.3×10^{-2}	1.7×10^{-1}	80.84	23.54	24.32	18.67	6.25	5.82
Yes	4.3×10^{-2}	1.7×10^{-1}	84.79	28.36	30.66	24.25	1.79	1.63
No	1.2×10^{-1}	0	76.09	20.35	25.82	14.53	1.07	0.92
Yes	1.2×10^{-1}	0	82.40	35.89	35.34	36.74	1.55	1.58
No	1.2×10^{-1}	4.7×10^{-1}	100.00	-	-	-	-	-
Yes	1.2×10^{-1}	4.7×10^{-1}	99.96	71.79	71.55	100.00	116.00	-

Table C.5: Particle deposition efficiencies and steering factor for fully magnetic particles under the influence of a magnetic field caused by a wire at position 2, with turbulent dispersion (TD) either enabled or disabled. The number of particles released is around 3×10^5.

TD	St_{ref} [-]	Mnp_{ref} [-]	DE_{top} [%]	DE_{bot} [%]	DE_{LL} [%]	DE_{RL} [%]	SF_L [-]	SF_{pen} [-]
No	4.8×10^{-5}	0	0.56	0.52	0.39	0.67	1.21	1.21
Yes	4.8×10^{-5}	0	6.49	1.61	1.67	1.55	1.01	1.00
No	4.8×10^{-5}	6.3×10^{-6}	0.53	0.53	0.42	0.65	1.21	1.21
Yes	4.8×10^{-5}	6.3×10^{-6}	6.65	1.56	1.64	1.48	1.01	1.01
No	4.8×10^{-3}	0	1.10	0.61	0.55	0.69	1.18	1.18
Yes	4.8×10^{-3}	0	14.28	2.27	7.30	3.91	0.98	1.02
No	4.8×10^{-3}	6.3×10^{-4}	1.83	2.97	4.31	1.39	1.18	1.15
Yes	4.8×10^{-3}	6.3×10^{-4}	15.69	4.22	6.15	2.30	0.99	0.95
No	4.3×10^{-2}	0	19.09	4.95	6.41	3.02	1.31	1.27
Yes	4.3×10^{-2}	0	45.84	7.02	7.15	6.84	1.32	1.31
No	4.3×10^{-2}	5.6×10^{-3}	26.47	25.79	37.77	6.20	1.63	1.08
Yes	4.3×10^{-2}	5.6×10^{-3}	54.81	25.69	33.90	15.04	1.30	1.01
No	1.2×10^{-1}	0	76.09	20.35	25.82	14.53	1.07	0.92
Yes	1.2×10^{-1}	0	82.40	35.89	35.34	36.74	1.55	1.58
No	1.2×10^{-1}	1.6×10^{-2}	85.41	71.58	75.57	31.20	10.15	3.60
Yes	1.2×10^{-1}	1.6×10^{-2}	88.68	62.45	69.05	47.33	2.29	1.35

Table C.6: Particle deposition efficiencies and steering factor for fully magnetic particles under the influence of a magnetic field caused by a wire at position 3, with turbulent dispersion (TD) either enabled or disabled. The number of particles released is around 3×10^5.

TD	St_{ref} [-]	Mnp_{ref} [-]	DE_{top} [%]	DE_{bot} [%]	DE_{LL} [%]	DE_{RL} [%]	SF_L [-]	SF_{pen} [-]
No	4.8×10^{-5}	0	0.53	0.51	0.41	0.63	1.21	1.21
Yes	4.8×10^{-5}	0	6.68	1.59	1.73	1.45	1.01	1.00
No	4.8×10^{-5}	1.9×10^{-4}	0.59	0.66	0.64	0.67	1.19	1.19
Yes	4.8×10^{-5}	1.9×10^{-4}	6.79	1.65	1.81	1.49	1.00	1.00
No	4.8×10^{-3}	0	1.06	0.63	0.55	0.72	1.18	1.18
Yes	4.8×10^{-3}	0	14.25	2.24	16.10	5.23	1.00	1.02
No	4.8×10^{-3}	1.9×10^{-2}	4.52	9.05	13.17	3.96	1.23	1.12
Yes	4.8×10^{-3}	1.9×10^{-2}	19.34	10.66	16.10	5.23	1.00	0.89
No	4.3×10^{-2}	0	19.11	5.04	6.59	3.02	1.32	1.27
Yes	4.3×10^{-2}	0	45.93	7.05	7.23	6.81	1.32	1.32
No	4.3×10^{-2}	1.7×10^{-1}	59.34	51.57	63.72	33.20	1.51	0.82
Yes	4.3×10^{-2}	1.7×10^{-1}	67.47	57.16	70.07	34.56	1.75	0.80
No	1.2×10^{-1}	0	75.99	20.32	25.57	14.67	1.08	0.94
Yes	1.2×10^{-1}	0	82.25	35.91	35.08	37.22	1.56	1.61
No	1.2×10^{-1}	4.7×10^{-1}	99.02	100.00	100.00	-	inf	-
Yes	1.2×10^{-1}	4.7×10^{-1}	96.94	98.59	99.47	86.01	14.41	0.55

Table C.7: Particle deposition efficiencies and steering factor for fully magnetic particles under the influence of a magnetic field caused by a wire at position 4, with turbulent dispersion (TD) either enabled or disabled. The number of particles released is around 3×10^5.

TD	St_{ref} [-]	Mnp_{ref} [-]	DE_{top} [%]	DE_{bot} [%]	DE_{LL} [%]	DE_{RL} [%]	SF_L [-]	SF_{pen} [-]
No	4.8×10^{-5}	0	0.53	0.51	0.41	0.63	1.21	1.21
Yes	4.8×10^{-5}	0	6.68	1.59	1.73	1.45	1.01	1.00
No	4.8×10^{-5}	6.3×10^{-6}	0.53	0.50	0.41	0.62	1.21	1.21
Yes	4.8×10^{-5}	6.3×10^{-6}	6.76	1.63	1.67	1.59	1.01	1.00
No	4.8×10^{-3}	0	1.06	0.63	0.55	0.72	1.18	1.18
Yes	4.8×10^{-3}	0	14.25	2.24	16.10	5.23	1.00	1.02
No	4.8×10^{-3}	6.3×10^{-4}	1.59	3.54	5.30	1.47	1.18	1.13
Yes	4.8×10^{-3}	6.3×10^{-4}	15.35	4.61	6.82	2.41	1.00	0.95
No	4.3×10^{-2}	0	19.11	5.04	6.59	3.02	1.32	1.27
Yes	4.3×10^{-2}	0	45.93	7.05	7.23	6.81	1.32	1.32
No	4.3×10^{-2}	5.6×10^{-3}	23.73	28.30	42.21	6.53	1.56	0.97
Yes	4.3×10^{-2}	5.6×10^{-3}	53.62	28.09	38.31	15.06	1.28	0.93
No	1.2×10^{-1}	0	75.99	20.32	25.57	14.67	1.08	0.94
Yes	1.2×10^{-1}	0	82.25	35.91	35.08	37.22	1.56	1.61
No	1.2×10^{-1}	1.6×10^{-2}	82.88	76.63	81.93	15.92	11.46	2.46
Yes	1.2×10^{-1}	1.6×10^{-2}	87.74	65.62	74.00	47.71	2.14	1.06

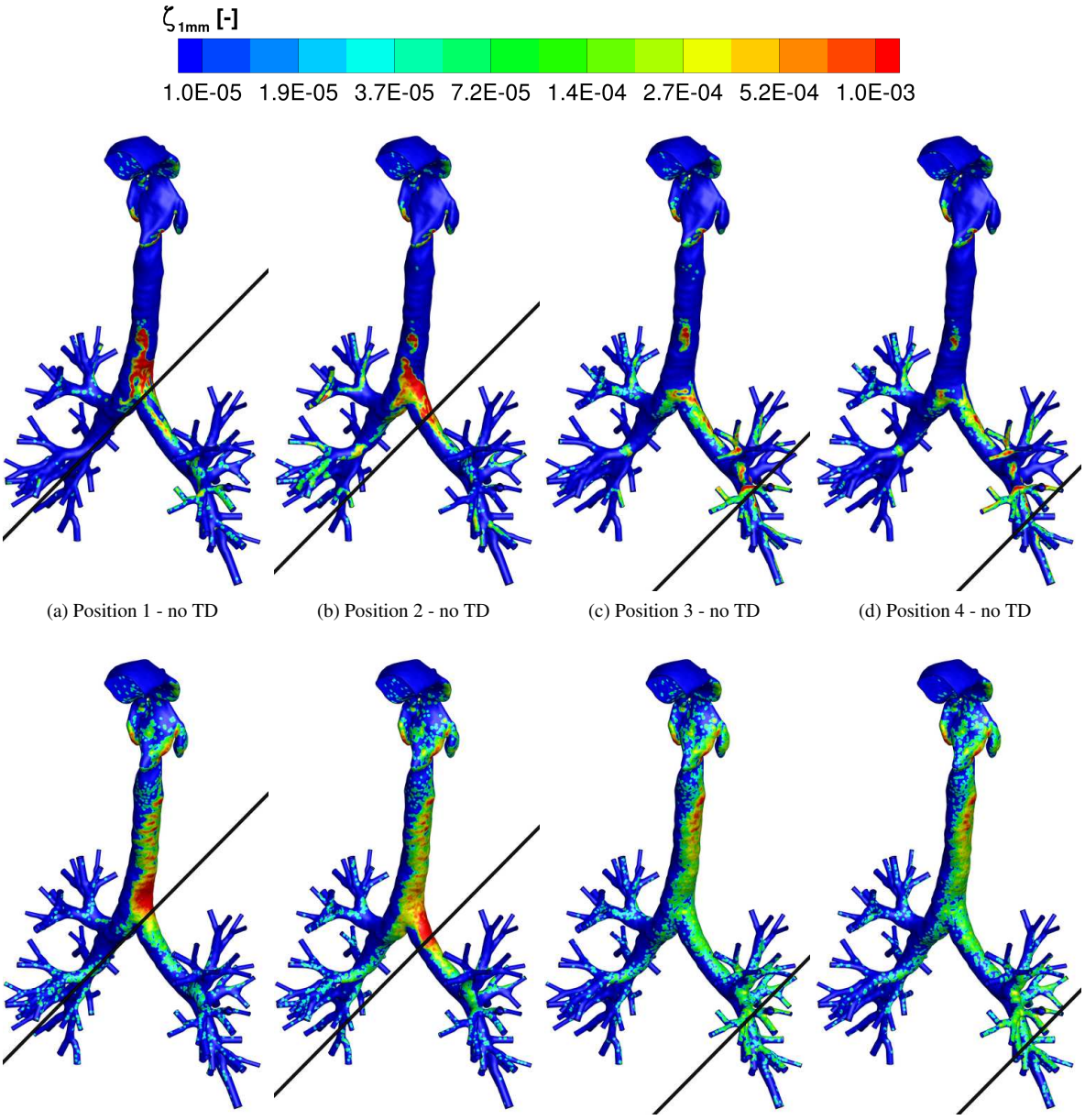

(a) Position 1 - no TD (b) Position 2 - no TD (c) Position 3 - no TD (d) Position 4 - no TD

(e) Position 1 - TD (f) Position 2 - TD (g) Position 3 - TD (h) Position 4 - TD

Figure C.54: Contours of local deposition efficiency $\zeta_{1\ \mathrm{mm}}$ of core particles with St = 4.3×10^{-2}, Mnp = 1.7×10^{-1} (position 1 and 2) and Mnp = 5.6×10^{-3} (positions 3 and 4) for simulations without turbulent dispersion (a-d) and with turbulent dispersion (e-h) for (a,e) wire position 1, (b,f) wire position 3, (c,g) wire position 2 and (d,h) wire position 4. The other view of the same results can be found in figure C.55.

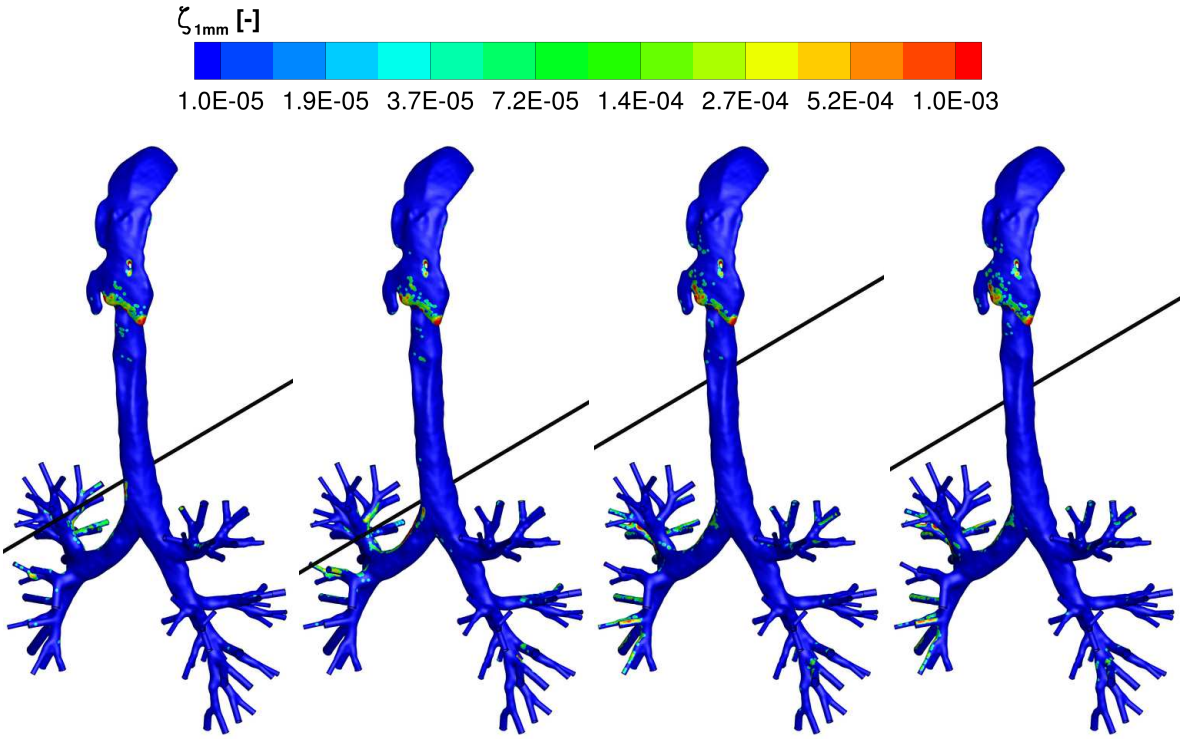

(a) Position 1 - no TD (b) Position 2 - no TD (c) Position 3 - no TD (d) Position 4 - no TD

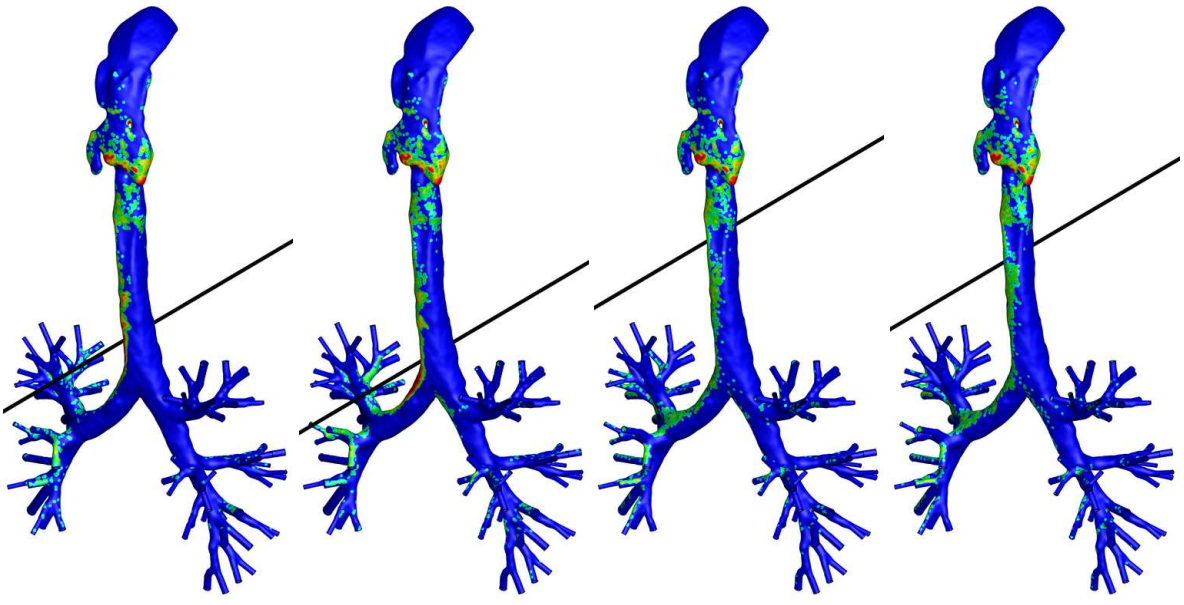

(e) Position 1 - TD (f) Position 2 - TD (g) Position 3 - TD (h) Position 4 - TD

Figure C.55: Contours of local deposition efficiency $\zeta_{1\,\mathrm{mm}}$ of core particles with St = 4.3×10^{-2} with a current through the wire of current I = 1×10^{5} A. (a) Wire position 1 without turbulent dispersion, (b) wire position 3 without turbulent dispersion, (c) wire position 1 with turbulent dispersion, (d) wire position 3 with turbulent dispersion. The first view of the same results can be found in figure C.54.

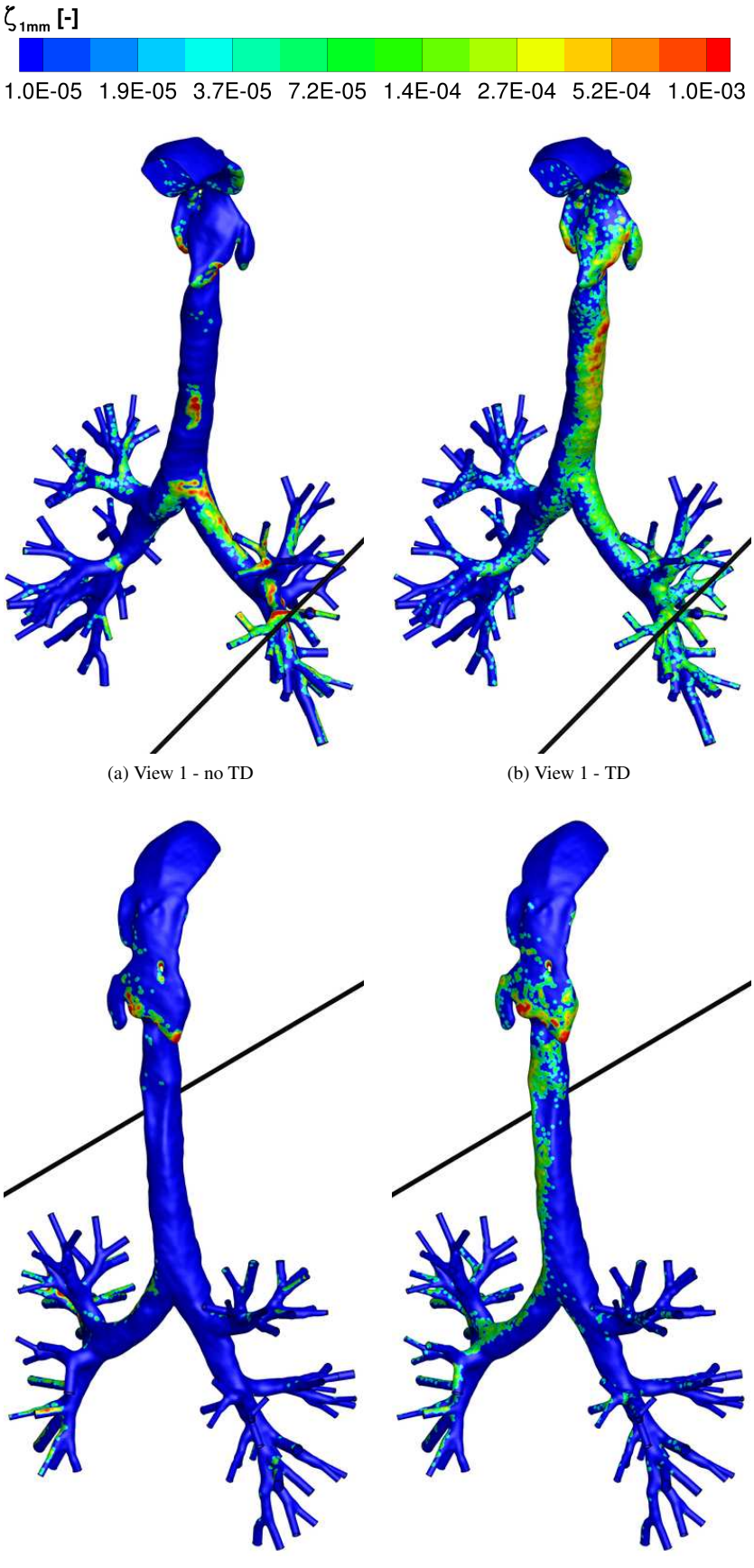

(a) View 1 - no TD

(b) View 1 - TD

(c) View 2 - No TD

(d) View 2 - TD

Figure C.56: Contours of local deposition efficiency $\zeta_{1\text{ mm}}$ of core particles with St = 4.3×10^{-2} with the wire (current I = 1×10^{5} A) displaced 10 cm in the negative x-direction with respect to reference point A.

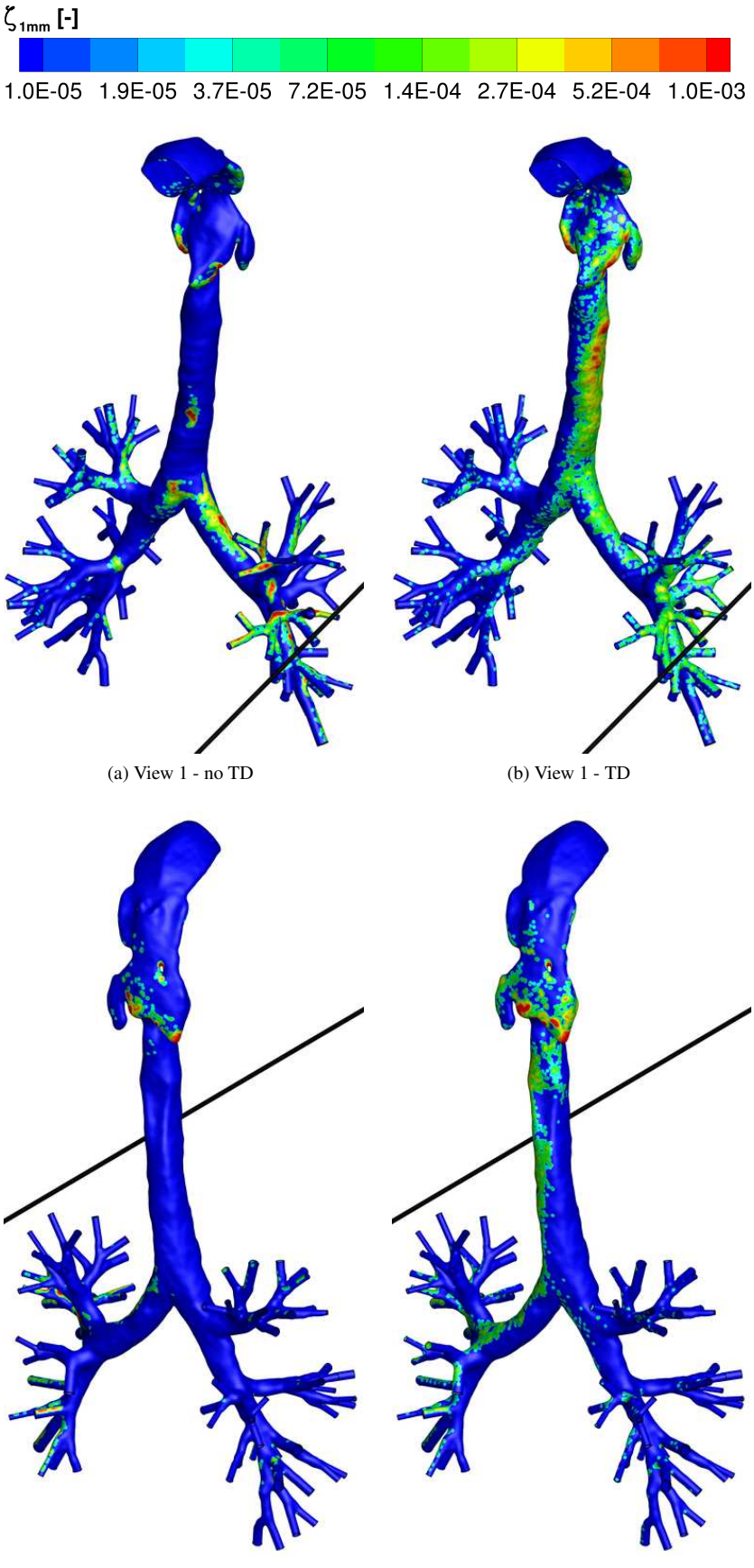

(a) View 1 - no TD

(b) View 1 - TD

(c) View 2 - No TD

(d) View 2 - TD

Figure C.57: Contours of local deposition efficiency $\zeta_{1\text{ mm}}$ of core particles with St = 4.3×10^{-2} with the wire (current I = 1×10^{5} A) displaced 10 cm in the negative x-direction with respect to reference point B.

C.5.2 High Magnetic Volume Fraction Core-Shell Particles

C.6 Figures and Tables

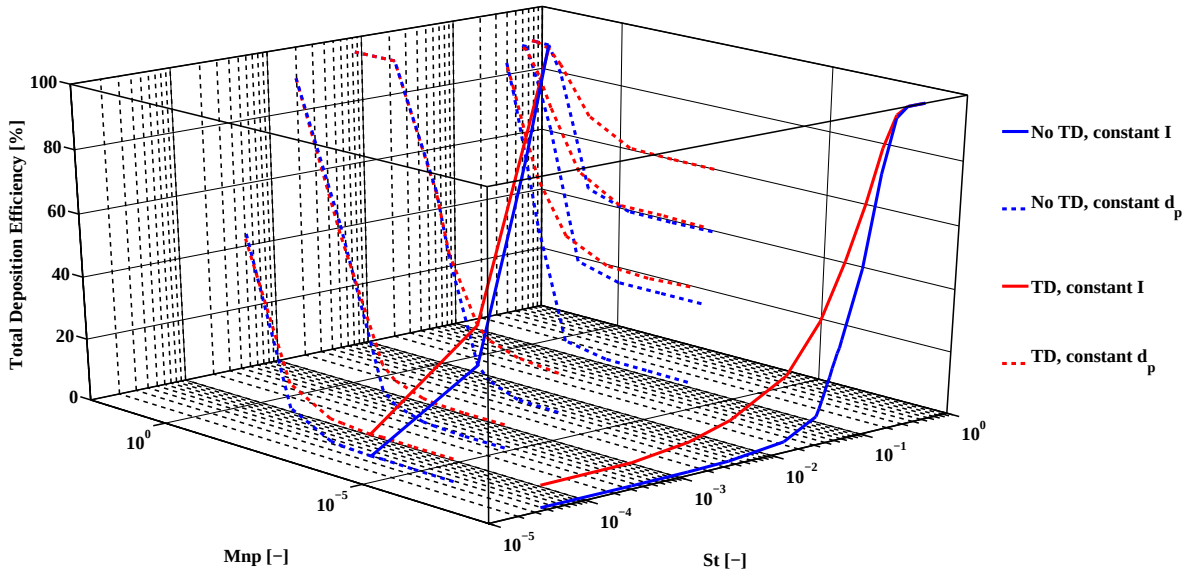

Figure C.58: Total deposition efficiency of fully magnetic particles as a function of St and Mnp for wire position 1. Note that the simulation with Mnp = 1×10^{-8} is actually Mnp = 0, a small number was added to make the series visible.

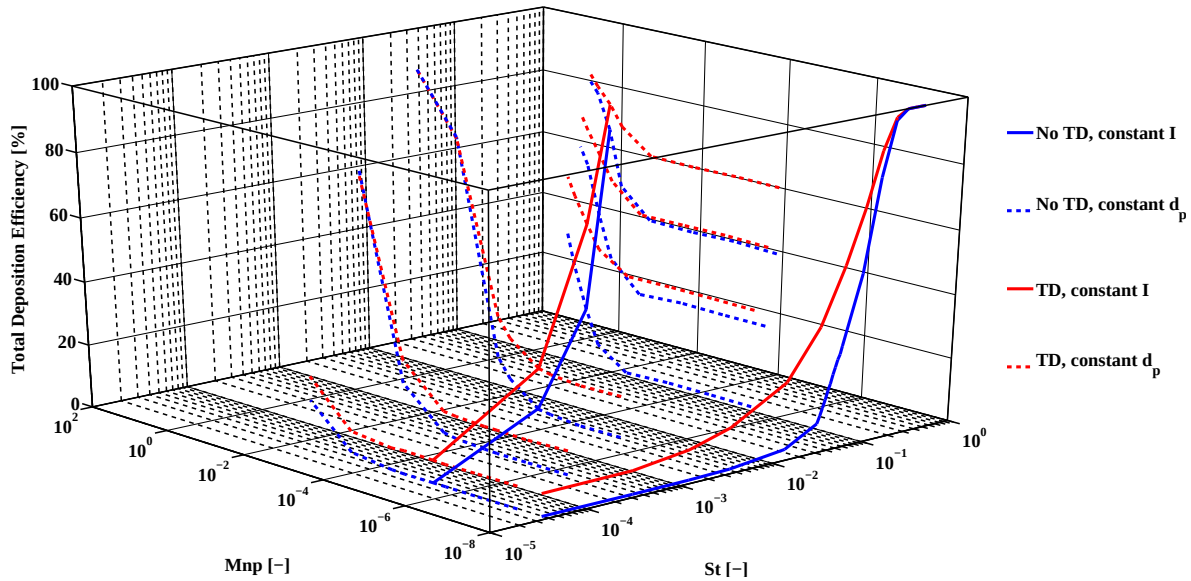

Figure C.59: Steering factor SF_L of fully magnetic particles as a function of St and Mnp for wire position 2. Note that the simulation with Mnp = 1×10^{-8} is actually Mnp = 0, a small number was added to make the series visible.

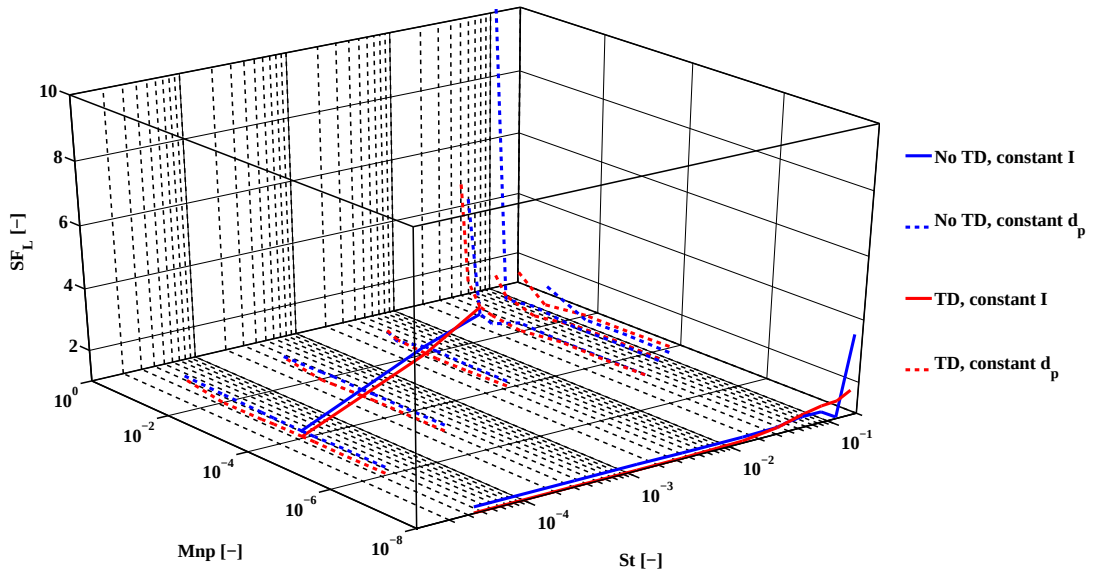

Figure C.60: Total deposition efficiency of fully magnetic particles as a function of St and Mnp for wire position 1. Note that the simulation with Mnp = 1×10^{-8} is actually Mnp = 0, a small number was added to make the series visible.

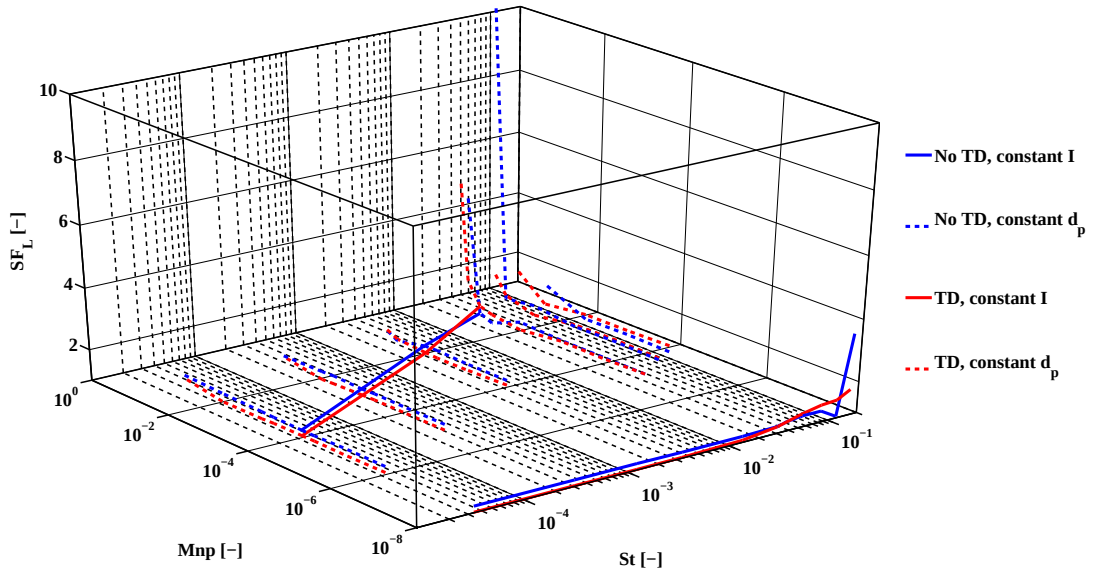

Figure C.61: Steering factor SF_L of fully magnetic particles as a function of St and Mnp for wire position 2. Note that the simulation with Mnp = 1×10^{-8} is actually Mnp = 0, a small number was added to make the series visible.

Table C.8: Particle deposition efficiencies and steering factor for core-shell A particles under the influence of a magnetic field caused by a wire at position 1, with turbulent dispersion (TD) either enabled or disabled. The number of particles released is around 3×10^5.

TD	St_{ref} [-]	Mnp_{ref} [-]	DE_{top} [%]	DE_{bot} [%]	DE_{LL} [%]	DE_{RL} [%]	SF_L [-]	SF_{pen} [-]
No	3.4×10^{-5}	0	0.51	0.50	0.39	0.63	1.21	1.21
Yes	3.4×10^{-5}	0	6.59	1.61	1.69	1.53	1.00	1.00
No	3.4×10^{-5}	1.1×10^{-4}	0.59	0.54	0.44	0.65	1.20	1.21
Yes	3.4×10^{-5}	1.1×10^{-4}	6.69	1.60	1.70	1.51	1.01	1.01
No	3.4×10^{-3}	0	0.89	0.57	0.51	0.64	1.18	1.18
Yes	3.4×10^{-3}	0	12.53	2.11	5.08	2.72	0.96	1.02
No	3.4×10^{-3}	1.1×10^{-2}	5.99	3.67	4.78	2.32	1.23	1.20
Yes	3.4×10^{-3}	1.1×10^{-2}	19.48	3.88	5.08	2.72	0.96	0.94
No	3.1×10^{-2}	0	7.03	2.36	2.82	1.79	1.22	1.21
Yes	3.1×10^{-2}	0	36.38	4.84	5.06	4.57	1.18	1.18
No	3.1×10^{-2}	9.9×10^{-2}	62.01	14.21	17.88	10.37	1.04	0.96
Yes	3.1×10^{-2}	9.9×10^{-2}	67.88	20.35	23.35	16.50	1.28	1.18
No	8.5×10^{-2}	0	47.89	9.32	8.74	10.11	1.35	1.37
Yes	8.5×10^{-2}	0	66.05	20.06	19.59	20.79	1.53	1.55
No	8.5×10^{-2}	2.8×10^{-1}	98.06	87.15	87.15	-	Inf	-
Yes	8.5×10^{-2}	2.8×10^{-1}	97.62	45.28	46.07	41.48	4.79	4.41

Table C.9: Particle deposition efficiencies and steering factor for core-shell A particles under the influence of a magnetic field caused by a wire at position 2, with turbulent dispersion (TD) either enabled or disabled. The number of particles released is around 3×10^5.

TD	**St_{ref} [-]**	**Mnp_{ref} [-]**	**DE_{top} [%]**	**DE_{bot} [%]**	**DE_{LL} [%]**	**DE_{RL} [%]**	**SF_L [-]**	**SF_{pen} [-]**
No	3.4×10^{-5}	0	0.51	0.50	0.39	0.63	1.21	1.21
Yes	3.4×10^{-5}	0	6.59	1.61	1.69	1.53	1.00	1.00
No	3.4×10^{-5}	3.7×10^{-6}	0.55	0.51	0.40	0.65	1.20	1.20
Yes	3.4×10^{-5}	3.7×10^{-6}	6.61	1.65	1.74	1.56	1.01	1.00
No	3.4×10^{-3}	0	0.89	0.57	0.51	0.64	1.18	1.18
Yes	3.4×10^{-3}	0	12.53	2.11	5.08	2.72	0.96	1.02
No	3.4×10^{-3}	3.7×10^{-4}	1.25	1.90	2.63	1.01	1.20	1.18
Yes	3.4×10^{-3}	3.7×10^{-4}	13.23	3.14	4.16	2.12	1.00	0.98
No	3.1×10^{-2}	0	7.03	2.36	2.82	1.79	1.22	1.21
Yes	3.1×10^{-2}	0	36.38	4.84	5.06	4.57	1.18	1.18
No	3.1×10^{-2}	3.3×10^{-3}	12.45	15.01	22.47	4.75	1.38	1.12
Yes	3.1×10^{-2}	3.3×10^{-3}	43.01	17.00	24.20	8.95	1.12	0.93
No	8.5×10^{-2}	0	47.89	9.32	8.74	10.11	1.35	1.37
Yes	8.5×10^{-2}	0	66.05	20.06	19.59	20.79	1.53	1.55
No	8.5×10^{-2}	9.1×10^{-3}	57.43	48.67	62.05	11.09	2.81	1.20
Yes	8.5×10^{-2}	9.1×10^{-3}	75.13	43.64	50.72	31.12	1.77	1.27

Table C.10: Particle deposition efficiencies and steering factor for core-shell A particles under the influence of a magnetic field caused by a wire at position 3, with turbulent dispersion (TD) either enabled or disabled. The number of particles released is around 3×10^5.

TD	St_{ref} [-]	Mnp_{ref} [-]	DE_{top} [%]	DE_{bot} [%]	DE_{LL} [%]	DE_{RL} [%]	SF_L [-]	SF_{pen} [-]
No	3.4×10^{-5}	0	0.51	0.49	0.39	0.61	1.20	1.20
Yes	3.4×10^{-5}	0	6.62	1.62	1.67	1.56	1.01	1.00
No	3.4×10^{-5}	1.1×10^{-4}	0.55	0.58	0.57	0.60	1.21	1.21
Yes	3.4×10^{-5}	1.1×10^{-4}	6.71	1.65	1.73	1.57	1.01	1.01
No	3.4×10^{-3}	0	0.86	0.61	0.57	0.65	1.19	1.19
Yes	3.4×10^{-3}	0	12.53	2.14	11.18	3.40	0.98	1.01
No	3.4×10^{-3}	1.1×10^{-2}	3.04	6.31	9.22	2.80	1.21	1.13
Yes	3.4×10^{-3}	1.1×10^{-2}	16.08	7.25	11.18	3.40	0.98	0.90
No	3.1×10^{-2}	0	6.84	2.28	2.75	1.72	1.20	1.19
Yes	3.1×10^{-2}	0	36.55	4.80	5.09	4.46	1.20	1.19
No	3.1×10^{-2}	9.9×10^{-2}	34.98	37.58	58.75	12.63	1.18	0.56
Yes	3.1×10^{-2}	9.9×10^{-2}	52.25	39.66	51.51	24.15	1.31	0.84
No	8.5×10^{-2}	0	47.82	9.43	8.88	10.17	1.34	1.36
Yes	8.5×10^{-2}	0	66.05	19.70	19.34	20.25	1.53	1.54
No	8.5×10^{-2}	2.8×10^{-1}	88.48	57.81	57.66	60.75	19.26	20.78
Yes	8.5×10^{-2}	2.8×10^{-1}	87.13	82.14	88.88	59.53	3.35	0.92

Table C.11: Particle deposition efficiencies and steering factor for core-shell A particles under the influence of a magnetic field caused by a wire at position 4, with turbulent dispersion (TD) either enabled or disabled. The number of particles released is around 3×10^5.

TD	St_{ref} [-]	Mnp_{ref} [-]	DE_{top} [%]	DE_{bot} [%]	DE_{LL} [%]	DE_{RL} [%]	SF_L [-]	SF_{pen} [-]
No	3.4×10^{-5}	0	0.51	0.49	0.39	0.61	1.20	1.20
Yes	3.4×10^{-5}	0	6.62	1.62	1.67	1.56	1.01	1.00
No	3.4×10^{-5}	3.7×10^{-6}	0.53	0.47	0.39	0.57	1.20	1.20
Yes	3.4×10^{-5}	3.7×10^{-6}	6.61	1.63	1.68	1.59	1.01	1.01
No	3.4×10^{-3}	0	0.86	0.61	0.57	0.65	1.19	1.19
Yes	3.4×10^{-3}	0	12.53	2.14	11.18	3.40	0.98	1.01
No	3.4×10^{-3}	3.7×10^{-4}	1.20	2.18	3.16	1.01	1.19	1.16
Yes	3.4×10^{-3}	3.7×10^{-4}	13.03	3.35	4.62	2.08	1.00	0.98
No	3.1×10^{-2}	0	6.84	2.28	2.75	1.72	1.20	1.19
Yes	3.1×10^{-2}	0	36.55	4.80	5.09	4.46	1.20	1.19
No	3.1×10^{-2}	3.3×10^{-3}	10.50	16.90	25.96	4.90	1.33	1.03
Yes	3.1×10^{-2}	3.3×10^{-3}	42.22	18.90	27.66	9.10	1.12	0.89
No	8.5×10^{-2}	0	47.82	9.43	8.88	10.17	1.34	1.36
Yes	8.5×10^{-2}	0	66.05	19.70	19.34	20.25	1.53	1.54
No	8.5×10^{-2}	9.1×10^{-3}	51.53	47.79	67.11	10.17	1.95	0.71
Yes	8.5×10^{-2}	9.1×10^{-3}	73.87	46.68	56.02	30.56	1.73	1.09

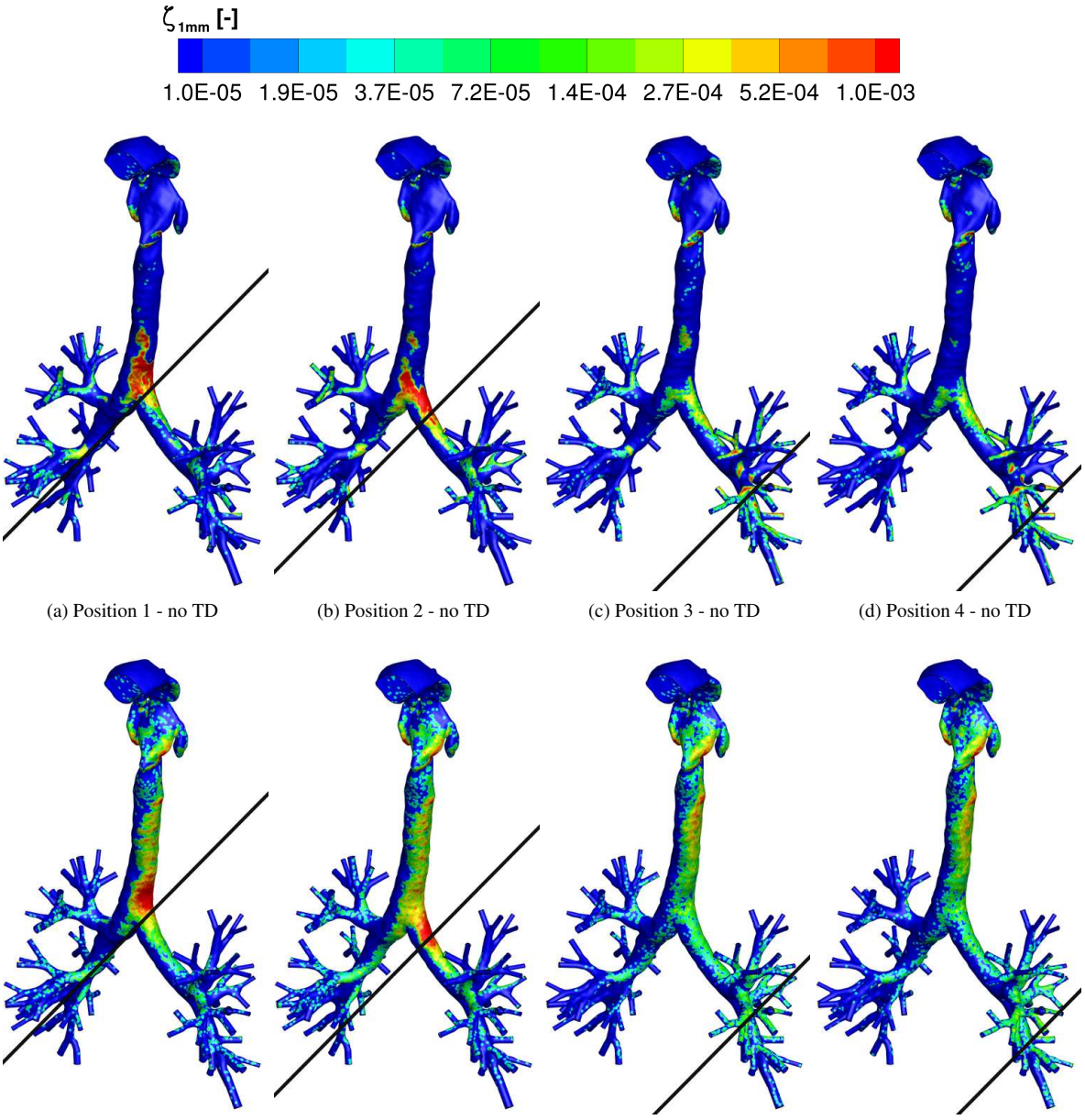

(a) Position 1 - no TD (b) Position 2 - no TD (c) Position 3 - no TD (d) Position 4 - no TD

(e) Position 1 - TD (f) Position 2 - TD (g) Position 3 - TD (h) Position 4 - TD

Figure C.62: Contours of local deposition efficiency $\zeta_{1\text{ mm}}$ of core particles with St = 3.1×10^{-2} with a current I = 1×10^{5} A. (a) Wire position 1 without turbulent dispersion, (b) wire position 3 without turbulent dispersion, (c) wire position 1 with turbulent dispersion, (d) wire position 3 with turbulent dispersion. The other view of the same results can be found in figure C.63.

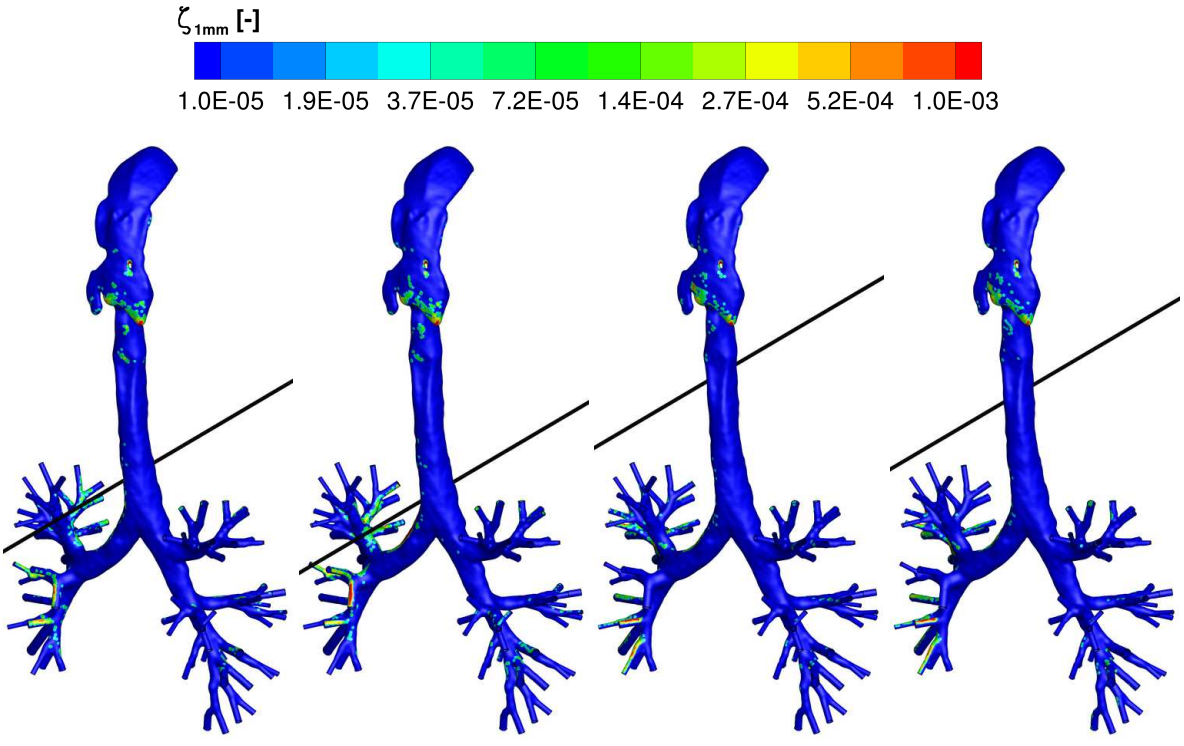

(a) Position 1 - no TD (b) Position 2 - no TD (c) Position 3 - no TD (d) Position 4 - no TD

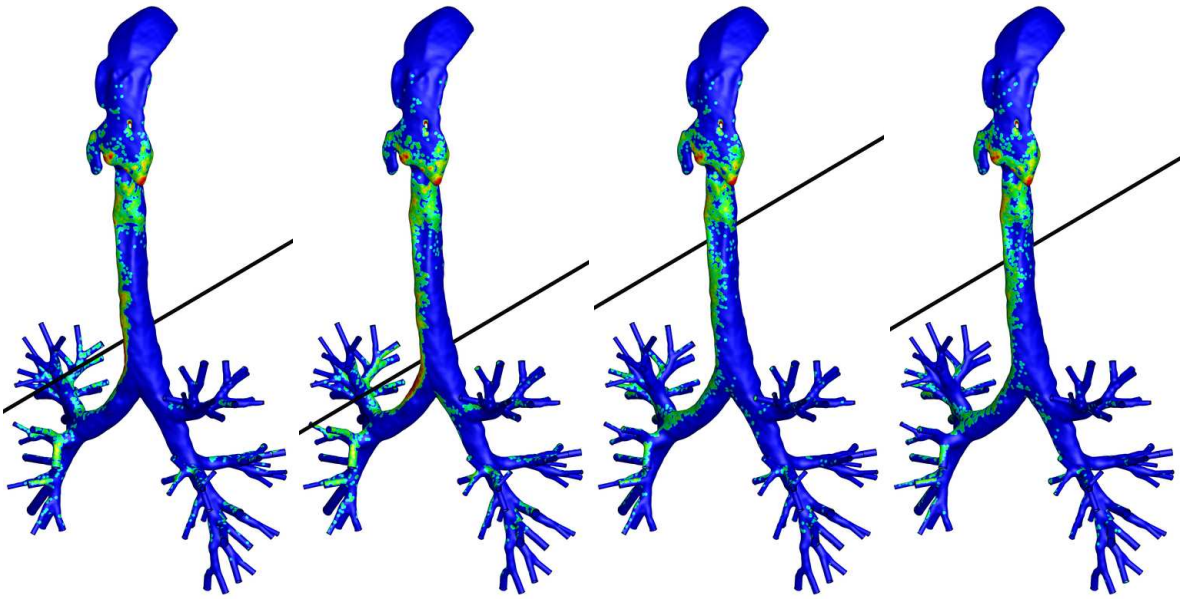

(e) Position 1 - TD (f) Position 2 - TD (g) Position 3 - TD (h) Position 4 - TD

Figure C.63: Contours of local deposition efficiency $\zeta_{1\,\mathrm{mm}}$ of core particles with St = 3.1×10^{-2} with a current I = 1×10^{5} A. (a) Wire position 1 without turbulent dispersion, (b) wire position 3 without turbulent dispersion, (c) wire position 1 with turbulent dispersion, (d) wire position 3 with turbulent dispersion. The first view of the same results can be found in figure C.62.

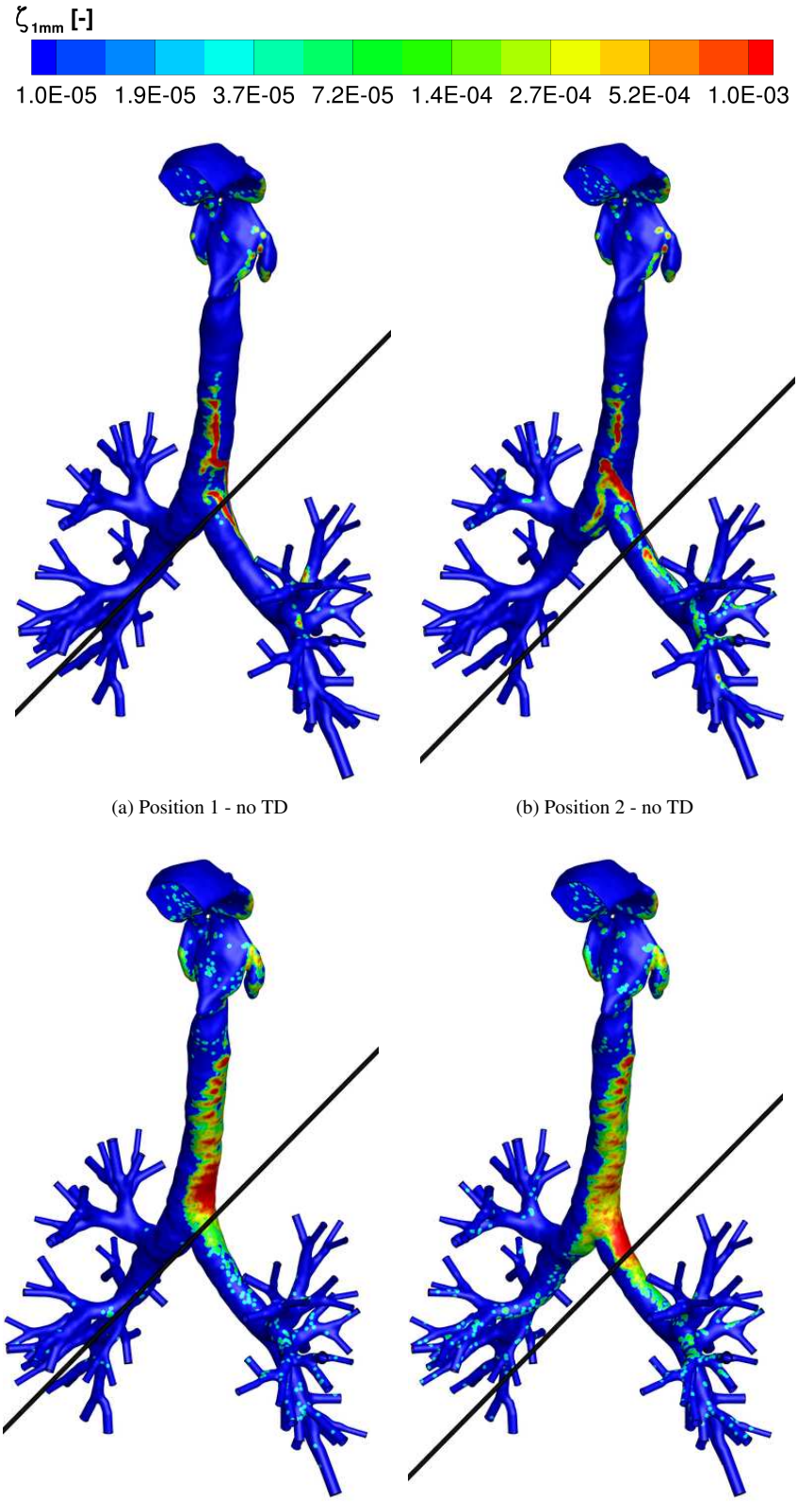

(a) Position 1 - no TD

(b) Position 2 - no TD

(c) Position 1 - TD

(d) Position 2 - TD

Figure C.64: Contours of local deposition efficiency $\zeta_{1\ \mathrm{mm}}$ of core-shell A particles with St = 3.1×10^{-2} with a current I = 1×10^{5} A. (a) Wire position 1 without turbulent dispersion, (b) wire position 3 without turbulent dispersion, (c) wire position 1 with turbulent dispersion, (d) wire position 3 with turbulent dispersion

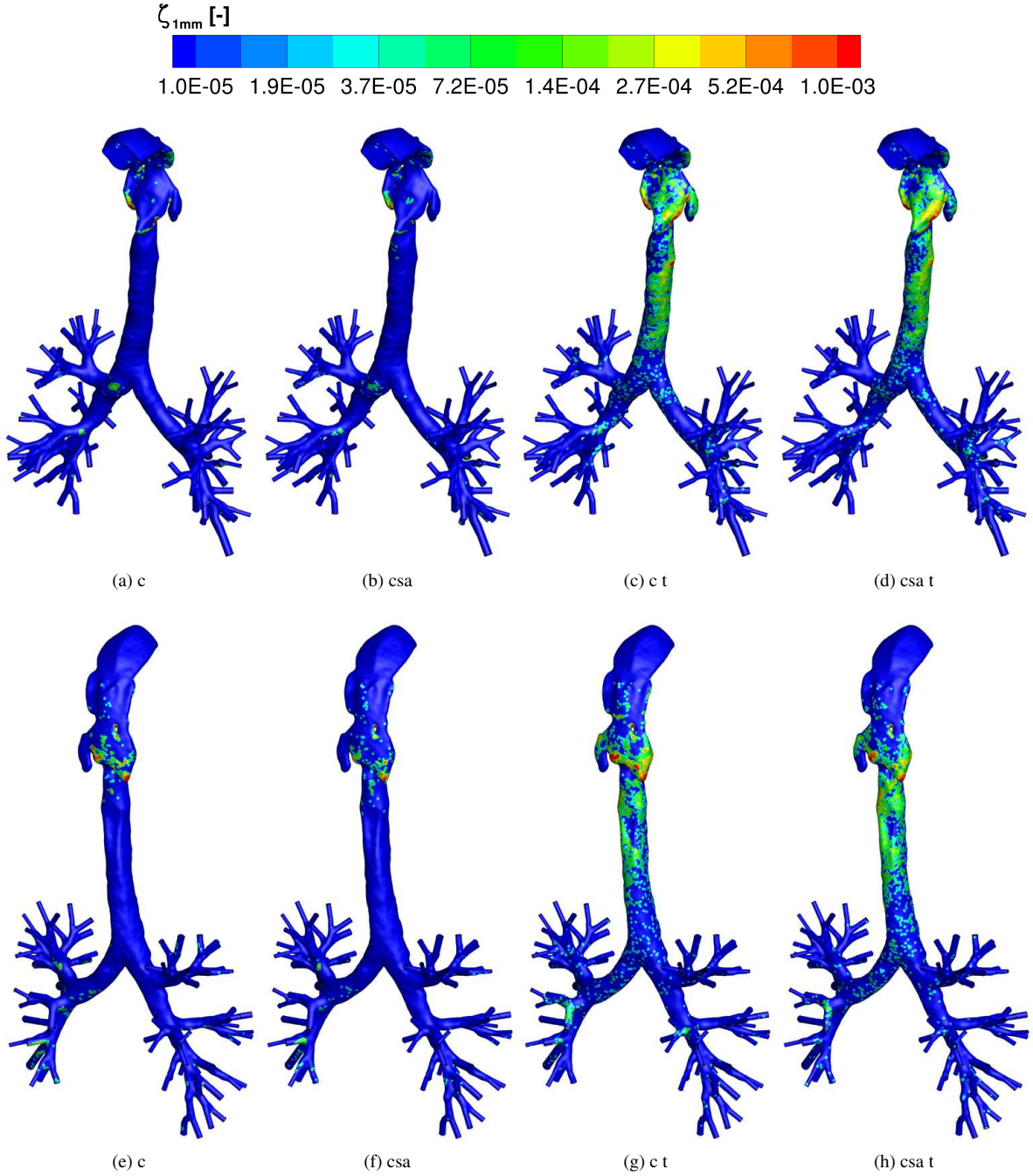

Figure C.65: Comparison of the particle deposition for fully magnetic particles and core-shell A particles for the same total particle size ($3\mu m$), $St_{fmp} = 4.3 \times 10^{-2}$, $St_{csA} = 3.1 \times 10^{-2}$.

C.6.1 Low Magnetic Volume Fraction Core-Shell Particles

The aerosols used by Dames et al. (2007), which consist of tiny magnetic particle dispersed in a liquid phase, are modelled as a solid particle with a representative magnetic volume fraction. These 'representative' particles have a d^*_{mp}=0.2 and since the magnetic force scales with d^3_{mp} these particles experience a magnetic force 125 times lower than fully magnetic particles (d^*_{mp}=1) and 73 times lower than the core-shell A particles (d^*_{mp}=0.836). Moreover, these particles have a density roughly 5 times lower than fully magnetic particles and thus the St decreases by a factor 5, making them less likely to be

In magnetic targeting, the magnetic force is, of course, of great importance. Because the magnetic force scales with the d^3_{mp} (magnetic volume fraction) halving the magnetic core diameter reduces the magnetic force by a factor of 8.

For example, the droplets used by Dames et al. (2007) which correspond to core-shell B particles in table 8.7 have a d_{mp}=0.2 and thus the magnetic force is 125 times lower than a fully magnetic particle and 73 times lower than a core-shell A particle.
While the particles have a sufficiently large magnetic volume fraction for targeting in mice, as indicated by their experimental results, but are insufficient for human purposes as illustrated by the results in table C.12: only for Mnp_{ref}=0.2 has the deposition measurably increased. This indicates that the drug particles should be carefully designed to deliver the right amount of medicine while also having a large of enough core but they cannot be too large since based on our results particles with high St will be filtered by the mouth/upper airway region. From the same table we can see that enabling turbulent dispersion the deposition is greatly enhanced due to the isotropic modelling of the velocity fluctuations, and also in regions near the wall.

Table C.12: Particle deposition efficiencies and steering factor for core-shell B particles under the influence of a magnetic field caused by a wire at position 1, with turbulent dispersion (TD) either enabled or disabled. The number of particles released is around 26×10^3.

TD	St_{ref} [-]	Mnp_{ref} [-]	DE_{top} [%]	DE_{bot} [%]	DE_{LL} [%]	DE_{RL} [%]	SF_L [-]
No	1.0×10^{-5}	0	0.96	0.34	0.33	0.35	0.77
Yes	1.0×10^{-5}	0	5.06	1.50	1.57	1.46	0.70
No	1.0×10^{-5}	1.6×10^{-6}	1.07	0.38	0.45	0.32	0.77
Yes	1.0×10^{-5}	1.6×10^{-6}	4.95	1.46	1.52	1.41	0.71
No	1.0×10^{-3}	0	1.04	0.41	0.50	0.34	0.79
Yes	1.0×10^{-3}	0	6.35	1.57	1.98	1.30	0.68
No	1.0×10^{-3}	1.6×10^{-4}	1.09	0.48	0.58	0.40	0.77
Yes	1.0×10^{-3}	1.6×10^{-4}	6.34	1.68	1.80	1.61	0.68
No	9.2×10^{-3}	0	1.22	0.84	0.99	0.72	0.78
Yes	9.2×10^{-3}	0	12.59	2.47	2.85	2.20	0.70
No	9.2×10^{-3}	1.5×10^{-3}	1.92	0.97	1.43	0.61	0.79
Yes	9.2×10^{-3}	1.5×10^{-3}	12.88	2.33	2.68	2.09	0.69
No	2.6×10^{-2}	0	2.06	1.80	1.79	1.81	0.76
Yes	2.6×10^{-2}	0	16.69	3.80	4.07	3.62	0.70
No	2.6×10^{-2}	4.0×10^{-3}	3.42	1.97	2.33	1.70	0.78
Yes	2.6×10^{-2}	4.0×10^{-3}	18.21	4.16	5.00	3.61	0.67

C.6.2 Alternative Cases

Wire positions on the other side were also simulated, these wires are located at the same z-coordinates as wire positions 1-4, but are located 1 cm or 10 cm away from the opposite wall. These positions are dubbed position $1'$ - $4'$. The data was hardly processed and therefore did not warrant an inclusion of the results in the main report. The only data reported here will be tables of the deposition efficiencies and steering factors, as well as some particle distribution plots in plane 1-3 (after figures 8.31, C.42 and C.43).

From the tables below and the plane distributions it can be concluded that particles can also be steered towards the right lung.

Table C.13: Particle deposition efficiencies and steering factor for fully magnetic particles under the influence of a magnetic field caused by a wire at position $1'$, with turbulent dispersion (TD) either enabled or disabled. The number of particles released is around 29×10^3.

TD	St_{ref} [-]	Mnp_{ref} [-]	DE_{top} [%]	DE_{bot} [%]	DE_{LL} [%]	DE_{RL} [%]	SF_L [-]	SF_{pen} [-]
No	4.8×10^{-5}	0	0.51	0.47	0.36	0.60	1.20	1.21
Yes	4.8×10^{-5}	0	6.73	1.52	1.58	1.45	1.02	1.02
No	4.8×10^{-5}	1.9×10^{-4}	0.59	0.61	0.46	0.80	1.19	1.19
Yes	4.8×10^{-5}	1.9×10^{-4}	6.77	1.65	1.78	1.51	1.02	1.02
No	4.8×10^{-3}	0	1.08	0.73	0.61	0.87	1.18	1.18
Yes	4.8×10^{-3}	0	14.39	2.34	3.56	8.48	1.13	1.03
No	4.8×10^{-3}	1.9×10^{-2}	7.93	4.87	2.56	7.66	1.20	1.27
Yes	4.8×10^{-3}	1.9×10^{-2}	21.10	5.87	3.56	8.48	1.13	1.19
No	4.3×10^{-2}	0	18.72	4.91	6.39	3.02	1.28	1.24
Yes	4.3×10^{-2}	0	45.68	7.33	7.42	7.21	1.33	1.33
No	4.3×10^{-2}	1.7×10^{-1}	51.33	15.62	5.12	32.84	1.64	2.32
Yes	4.3×10^{-2}	1.7×10^{-1}	63.75	28.65	19.19	38.01	0.99	1.29
No	1.2×10^{-1}	0	75.92	20.60	25.92	14.91	1.07	0.93
Yes	1.2×10^{-1}	0	82.77	36.05	36.88	34.78	1.52	1.47
No	1.2×10^{-1}	4.7×10^{-1}	95.01	93.2	-	93.2	0	0
Yes	1.2×10^{-1}	4.7×10^{-1}	95.10	69.51	54.31	70.86	0.09	0.14

Table C.14: Particle deposition efficiencies and steering factors for fully magnetic particles under the influence of a magnetic field caused by a wire at position 2′, with turbulent dispersion (TD) either enabled or disabled. The number of particles released is around 29×10^3.

TD	St_{ref} [-]	Mnp_{ref} [-]	DE_{top} [%]	DE_{bot} [%]	DE_{LL} [%]	DE_{RL} [%]	SF_L [-]	SF_{pen} [-]
No	4.8×10^{-5}	0	0.51	0.47	0.36	0.60	1.20	1.21
Yes	4.8×10^{-5}	0	6.73	1.52	1.58	1.45	1.02	1.02
No	4.8×10^{-5}	6.3×10^{-6}	0.61	0.51	0.45	0.60	1.23	1.23
Yes	4.8×10^{-5}	6.3×10^{-6}	6.74	1.56	1.58	1.53	1.00	1.00
No	4.8×10^{-3}	0	1.08	0.73	0.61	0.87	1.18	1.18
Yes	4.8×10^{-3}	0	14.39	2.34	3.56	8.48	1.13	1.03
No	4.8×10^{-3}	6.3×10^{-4}	1.97	2.14	1.11	3.37	1.20	1.27
Yes	4.8×10^{-3}	6.3×10^{-4}	14.70	3.15	2.37	3.96	1.02	1.04
No	4.3×10^{-2}	0	18.72	4.91	6.39	3.02	1.28	1.24
Yes	4.3×10^{-2}	0	45.68	7.33	7.42	7.21	1.33	1.33
No	4.3×10^{-2}	5.6×10^{-3}	24.00	12.89	6.72	21.57	1.41	1.67
Yes	4.3×10^{-2}	5.6×10^{-3}	46.32	19.55	12.37	30.51	1.53	1.92
No	1.2×10^{-1}	0	75.92	20.60	25.92	14.91	1.07	0.93
Yes	1.2×10^{-1}	0	82.77	36.05	36.88	34.78	1.52	1.47
No	1.2×10^{-1}	1.6×10^{-2}	77.74	51.22	24.46	80.19	1.08	4.13
Yes	1.2×10^{-1}	1.6×10^{-2}	80.67	55.06	41.17	74.77	1.42	3.31

Table C.15: Particle deposition efficiencies and steering factors for fully magnetic particles under the influence of a magnetic field caused by a wire at position 3′, with turbulent dispersion (TD) either enabled or disabled. The number of particles released is around 29×10^3.

TD	St_{ref} [-]	Mnp_{ref} [-]	DE_{top} [%]	DE_{bot} [%]	DE_{LL} [%]	DE_{RL} [%]	SF_L [-]	SF_{pen} [-]
No	4.8×10^{-5}	0	0.52	0.54	0.39	0.72	1.21	1.21
Yes	4.8×10^{-5}	0	6.72	1.55	1.65	1.45	0.99	0.99
No	4.8×10^{-5}	1.9×10^{-4}	0.71	0.71	0.44	1.04	1.21	1.22
Yes	4.8×10^{-5}	1.9×10^{-4}	6.71	1.68	1.64	1.73	1.00	1.00
No	4.8×10^{-3}	0	0.92	0.61	0.55	0.69	1.19	1.19
Yes	4.8×10^{-3}	0	14.42	2.38	4.74	19.85	1.12	1.03
No	4.8×10^{-3}	1.9×10^{-2}	5.85	9.79	3.29	17.64	1.21	1.42
Yes	4.8×10^{-3}	1.9×10^{-2}	19.39	11.86	4.74	19.85	1.12	1.33
No	4.3×10^{-2}	0	19.37	5.09	6.39	3.35	1.35	1.30
Yes	4.3×10^{-2}	0	45.80	7.32	7.30	7.36	1.36	1.36
No	4.3×10^{-2}	1.7×10^{-1}	33.25	41.87	13.08	76.11	1.19	4.33
Yes	4.3×10^{-2}	1.7×10^{-1}	53.20	47.90	27.81	69.02	1.05	2.45
No	1.2×10^{-1}	0	76.41	19.96	25.35	14.12	1.08	0.94
Yes	1.2×10^{-1}	0	82.76	36.67	36.33	37.23	1.61	1.63
No	1.2×10^{-1}	4.7×10^{-1}	82.37	94.60	-	84.60	0	0
Yes	1.2×10^{-1}	4.7×10^{-1}	85.50	92.84	81.05	96.03	0.27	1.29

Table C.16: Particle deposition efficiencies and steering factors for fully magnetic particles under the influence of a magnetic field caused by a wire at position 4′, with turbulent dispersion (TD) either enabled or disabled. The number of particles released is around 29×10^3.

TD	St_{ref} [-]	Mnp_{ref} [-]	DE_{top} [%]	DE_{bot} [%]	DE_{LL} [%]	DE_{RL} [%]	SF_L [-]	SF_{pen} [-]
No	4.8×10^{-5}	0	0.52	0.54	0.39	0.72	1.21	1.21
Yes	4.8×10^{-5}	0	6.72	1.55	1.65	1.45	0.99	0.99
No	4.8×10^{-5}	6.3×10^{-6}	0.49	0.50	0.41	0.61	1.21	1.21
Yes	4.8×10^{-5}	6.3×10^{-6}	6.66	1.70	1.91	1.49	1.00	0.99
No	4.8×10^{-3}	0	0.92	0.61	0.55	0.69	1.19	1.19
Yes	4.8×10^{-3}	0	14.42	2.38	4.74	19.85	1.12	1.03
No	4.8×10^{-3}	6.3×10^{-4}	1.66	2.13	1.20	3.25	1.22	1.24
Yes	4.8×10^{-3}	6.3×10^{-4}	14.78	3.59	2.60	4.64	1.06	1.08
No	4.3×10^{-2}	0	19.37	5.09	6.39	3.35	1.35	1.30
Yes	4.3×10^{-2}	0	45.80	7.32	7.30	7.36	1.36	1.36
No	4.3×10^{-2}	5.6×10^{-3}	23.74	13.53	6.89	23.18	1.45	1.76
Yes	4.3×10^{-2}	5.6×10^{-3}	46.43	21.11	13.10	33.64	1.56	2.05
No	1.2×10^{-1}	0	76.41	19.96	25.35	14.12	1.08	0.94
Yes	1.2×10^{-1}	0	82.76	36.67	36.33	37.23	1.61	1.63
No	1.2×10^{-1}	1.6×10^{-2}	78.32	53.40	23.02	88.98	1.17	8.18
Yes	1.2×10^{-1}	1.6×10^{-2}	81.03	56.84	42.00	78.14	1.44	3.81